DOE-ER-0313/44
Distribution
Categories
UC-423, -424

FUSION MATERIALS SEMIANNUAL PROGRESS REPORT FOR THE PERIOD ENDING

June 30, 2008

Prepared for
DOE Office of Fusion Energy Sciences
(AT 60 20 10 0)

DATE PUBLISHED: August 2008

Prepared for
OAK RIDGE NATIONAL LABORATORY
Oak Ridge, Tennessee 37831
Managed by
UT-Battelle, LLC
For the
U.S. DEPARTMENT OF ENERGY

FOREWORD

This is the forty-fourth in a series of semiannual technical progress reports on fusion materials science activities supported by the Fusion Energy Sciences Program of the U.S. Department of Energy. This report focuses on research addressing the effects of materials properties and performance from exposure to the neutronic, thermal and chemical environments anticipated in the chambers of fusion experiments and energy systems. This research is a major element of the national effort to establish the materials knowledge base of an economically and environmentally attractive fusion energy source. Research actives on issues related to the interaction of materials with plasmas are reported separately.

The results reported are the product of a national effort involving a number of national laboratories and universities. A large fraction of this work, particularly in relation to fission reactor irradiations, is carried out collaboratively with partners in Japan, Russia, and the European Union. The purpose of this series of reports is to provide a working technical record for the use of program participants, and to provide a means of communicating the efforts of fusion materials scientists to the broader fusion community, both nationally and worldwide.

This report has been compiled and edited under the guidance of F. W. (Bill) Wiffen and Renetta Godfrey, Oak Ridge National Laboratory. Their efforts, and the efforts of the many persons who made technical contributions, are gratefully acknowledged.

G. R. Nardella
Research Division
Office of Fusion Energy Sciences

TABLE OF CONTENTS

3 FERRITIC/MARTENSITIC STEELS

Microstructural evolutions in NFA under neutron-irradiation, at fusion relevant He/dpa ratios and dpa rates, were characterized using a novel in-situ $^{59}Ni(n,\alpha)$ reaction He-implanter technique. MA957 was irradiated at 500°C in HFIR to a nominal 9 dpa and 380 appm He. A high number density of ≈ 1 He-bubbles were observed. Comparisons of these results to the cavity structures in TMS F82H, described in a companion report, provide additional evidence that TMS may be susceptible to both low (fast fracture) and high (creep rupture) temperature embrittlement as well as void swelling at fusion relevant He concentrations, while NFA are much more resistant to these degradation phenomena.

Microstructural evolutions in TMS under neutron-irradiation, at fusion relevant He/dpa ratios and dpa rates, were characterized using a novel in-situ $^{59}Ni(n,\alpha)$ reaction He-implanter technique. F82H-mod3 was irradiated at 500°C in HFIR to a nominal 9 dpa and 190 or 380 appm He in both in the as-tempered (AT) and 20% cold-worked (CW) conditions. In all cases, a high number density of 1-2 nm He-bubbles were observed, along with a smaller number of larger faceted ≈ 10 nm cavities, which are likely voids. The He bubbles form preferentially on dislocations and various interfaces, including grain boundaries and at precipitates. A slightly larger number of smaller He bubbles were observed in the CW condition. The lower He/dpa ratio produced slightly smaller and fewer He bubbles. Estimates of the He content of the bubbles, assuming equilibrium capillary pressures, were in good agreement with the nominal implanted levels. Comparisons of these results to the cavity structures in nano-structured ferritic alloy (NFA) MA957, described in a companion report [1], provide additional evidence that TMS may be susceptible to both low (fast fracture) and high (creep rupture) temperature embrittlement as well as void swelling at fusion relevant He concentrations, while NFA are much more resistant to these degradation phenomena.

COMPRESSION TESTING OF V-4Cr-4Ti - M. B. Toloczko (Pacific Northwest National Laboratory)[1], R. M. Ermi[1], D. S. Gelles[1], R. J. Kurtz[1]

OBJECTIVE

The objective of this effort is to better understand the deformation behavior of vanadium alloys after irradiation.

ABSTRACT

The NIFS-1 heat and heat 832665 of V-4Cr-4Ti, irradiated to 3.7 dpa at 425°C and tested in compression at temperatures of 25°C and ~420°C, were compared to compression tests at similar temperatures on unirradiated material. The yield strength increased by a factor of two, and the upper/lower yield point that was observed in the unirradiated material was not present in the irradiated material test traces. The strain hardening exponent of the irradiated material was 40-80% less than the unirradiated material. Transmission electron microscopy observations indicate the formation of a fine distribution of small defects and no dislocation channeling.

PROGRESS AND STATUS

Introduction

Vanadium alloys are of interest as potential first wall structural materials because of their good thermal conductivity, good elevated temperature tensile strength, good high temperature creep resistance, and relative resilience to becoming radioactive [1-12]. At low irradiation temperatures vanadium alloys experience very high hardening caused by a high density of small, but shearable defect clusters, that results in a type of deformation called "channel deformation" [3,4,9,12-15]. At the onset of yield in a tensile test, a dislocation may move through a grain shearing the obstacles and clearing out a channel. Subsequent dislocations may easily pass through this channel. As the test progresses, more channels form. Up to the point of tensile instability plastic deformation is confined to these channels. One important macroscopic result of this deformation behavior is the rapid onset of necking in a tensile test and very low uniform elongation. As a means to help understand the range of stress states where localized deformation may adversely affect macroscopic ductility in vanadium alloys, compression test specimens fabricated from two heats of V-4Cr-4Ti were irradiated in the High Flux Isotope Reactor (HFIR). The results of 25°C, ~250°C, and ~420°C compression tests on the unirradiated control materials and the irradiated materials are presented here and compared with uniaxial tensile values as possible.

Experimental Procedure

Cylindrical compression specimens were fabricated from V-4Cr-4Ti heats 832665 and NIFS-1. Heat 832665 is reported to have an oxygen content of 330 wppm, and the NIFS-1 heat is reported to have an oxygen content of 181 wppm [2]. The cylindrical specimens are 3 mm in diameter and 3.5 mm tall. Heat 832665 was received in a 40% cold-worked condition, while the NIFS-1 heat was received in a 98% cold-worked condition. Before testing, individual specimens from both heats were wrapped in tantalum and titanium foil and annealed in a vacuum furnace for 2 hours at 1000^{o}C at 1x10^{-6} torr or better. Identification codes were laser engraved onto one end of each specimen.

Compression tests were performed in a 10,000 lb screw-driven Instron test frame with either a 1000 lb or 2000 lb load cell. A special compression test fixture, as shown in Figure 1, was constructed for the testing. The upper and lower loading surfaces of the fixture were made from a high modulus tungsten carbide composite with a polished surface. The upper loading surface is in the form of a piston that is guided by a cylinder made from machineable carbide composite. A tight tolerance was maintained between the piston and cylinder to limit axial misalignment between the upper and lower loading surfaces. Silicon powder was used as a lubricant on upper

[1] Pacific Northwest National Laboratory (PNNL) is operated for the U.S. Department of Energy by Battelle Memorial Institute under contract DE-AC06-76RLO-1830.

and lower loading surfaces. Specimen displacement was monitored with a capacitance-type displacement transducer with a resolution better than 0.0002 mm (better than 0.006% strain).

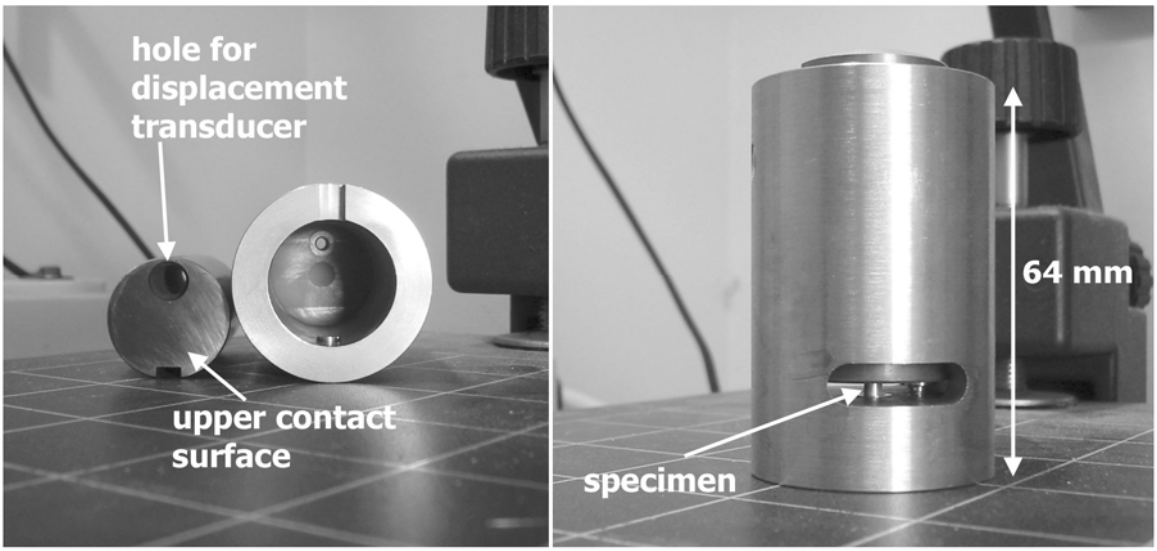

Figure 1. Pictures of the compression test fixture.

Compression tests were performed at constant crosshead speed and with an initial strain rate of $5x10^{-4}$ s^{-1}. The target test temperatures were room temperature (~25°C), 250°C, and 425°C. Heating was performed in a furnace capable of operation in an inert atmosphere or in a vacuum. Tests at 250°C were performed in 99.99% purity argon flowing at a rate of 2 L/min, and tests at 425°C were performed in a vacuum at 0.150 torr in an attempt to lower the partial pressure of oxygen during testing. Prior to testing, a thermocouple was placed below a dummy specimen in the fixture and a series of heating runs at different heating rates and target temperatures were performed to establish a correlation between specimen temperature and test chamber temperature. Preheating of the test chamber prior to the start of a test was done as quickly as possible (5.1°C/min for tests at 250°C and 9°C/min for tests at 425°C), and tests were performed while the temperature of the specimen was still changing, but at a rate where the increase in temperature during a test was limited to about 3°C. All data were monitored and recorded electronically. The 0.2% offset yield stress and, when present, the upper yield point were measured from engineering stress versus engineering strain plots. The power law strain hardening (PLSH) exponent was measured from true stress versus true plastic strain plots in the range of 1-3% true plastic strain.

Results

The actual test temperatures were 25°C, 250-255°C (unirradiated only), and 405-435°C. Engineering stress versus engineering strain curves for heat 832665 and the NIFS-1 heat in the unirradiated condition are shown in Figure 2. In most all of the tests, an upper and lower yield point was observed. The yield stress at 250°C was approximately 30% lower than at room temperature. The yield stress at ~415°C is essentially the same as at 250°C. Heat 832665 is consistently stronger than Heat NIFS-1 at all temperatures. All samples showed a continuous load increase during plastic deformation with a negative curvature up to the load limit of the load cell. Serrations from dynamic strain aging occurred only in CA06 (Heat 832665 tested at 430°C). As is common in a compression test, some barreling of the samples occurred. A typical amount of barreling for an unirradiated specimen is shown in Figure 3.

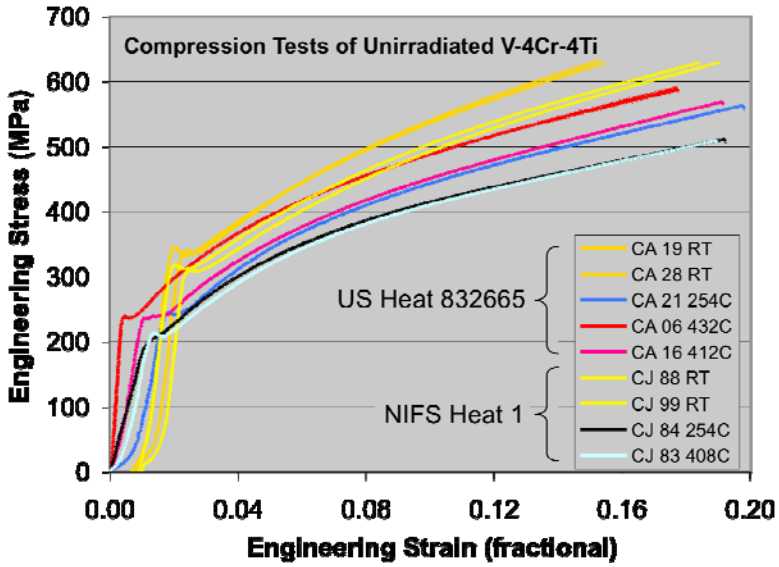

Figure 2. Engineering stress vs. engineering strain curves for unirradiated V-4Cr-4Ti at 25°C, 250°C, and ~420°C**.**

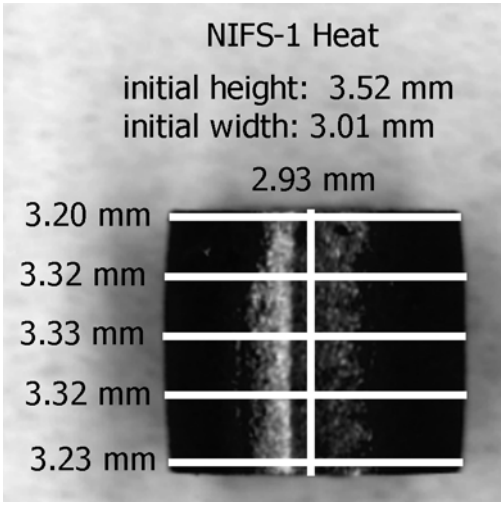

Figure 3. Typical amount of barreling in an unirradiated specimen tested to 20% engineering strain.

Engineering stress versus engineering strain curves for heat 832665 and the NIFS-1 heat in the irradiated condition are shown in Figure 4. The effects of irradiation are to raise the yield strength, eliminate the upper/lower yield point, and to change the strain hardening rate of curvature from negative to slightly positive. Strain serrations are apparent in both of the NIFS-1 specimens (CJ87, CJ89) tested at 425°C.

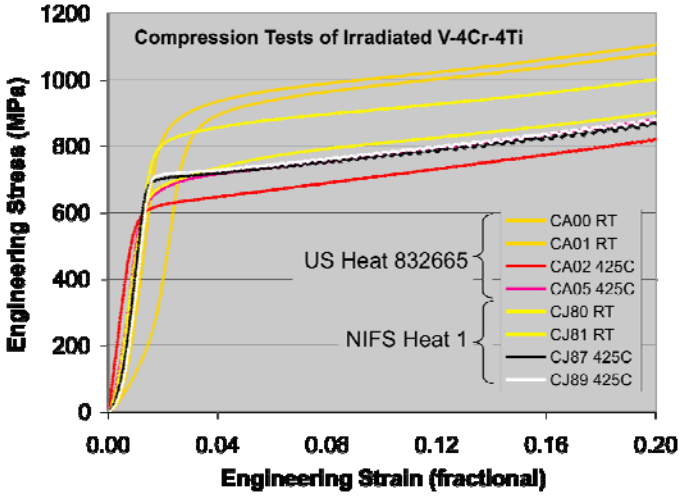

Figure 4. Engineering stress vs. engineering strain curves for irradiated V-4Cr-4Ti at 25°C and ~425°C**.**

Table 1 shows the average test temperature, 0.2% offset yield stress, upper yield point, and PLSH exponent. All values except temperature were calculated by hand. The upper yield point and 0.2% offset yield point were within 4 MPa for all tests where a yield point was observed. The 0.2% offset yield stress of the unirradiated heat 832665 samples remained approximately 22 MPa higher than the unirradiated NIFS-1 samples at all test temperatures as shown in Figure 5. The irradiated specimens have about twice the yield strength of their unirradiated counterparts. Strain hardening exponents were calculated from 0.01 to 0.03 true plastic strain following the reasoning from [16] and by assuming that V-4Cr-4Ti follows the power law strain hardening equation ($\sigma=k\varepsilon^n$). Figure 6 shows the strain hardening exponent versus temperature. Heat 832665 and the NIFS-1 heat both show similar deformation properties in either the unirradiated or irradiated condition with the effect of irradiation being to decrease the estimated strain hardening exponent by 40-80%.

Table 1. Compression test properties of unirradiated V-4Cr-4Ti at 25°C, 250°C, and ~420°C and irradiated V-4Cr-4Ti at 25°C and 425°C. CA = 832665 Heat and CJ = NIFS-1 Heat.

Specimen ID	Average Test Temp (°C)	0.2% Offset Yield Stress (MPa)	Upper Yield Point (MPa)	PLSH Exponent from $0.01 \leq \varepsilon_{pl} \leq 0.03$
Unirradiated				
CA·19	RT	340	340	0.17
CA·28	RT	344	344	0.16
CA·21	254	244	245	0.30
CA·06	432	236	240	0.25
CA·16	412	235	235	0.28
CJ·88	RT	310	310	0.16
CJ·99	RT	315	315	0.17
CJ·84	254	222	None	0.28
CJ·83	408	213	214	0.34
Irradiated·to·3.7·dpa·at~425°C				
CA00	RT	814	None	0.13
CA01	RT	820	None	0.09
CA02	425	570	None	0.06
CA05	425	623	None	0.08
CJ80	RT	632	None	0.11
CJ81	RT	771	None	0.07
CJ87	425	690	None	0.05
CJ89	425	705	None	0.05

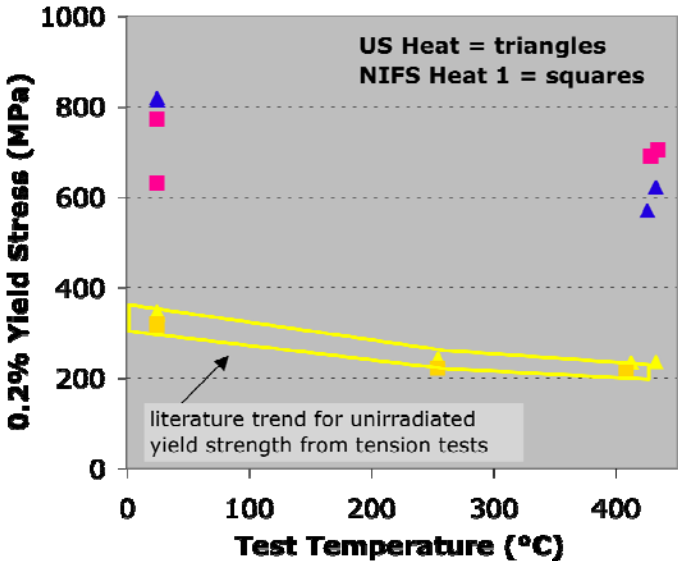

Figure 5. Temperature dependence at 25°C, 250°C, and ~425°C of 0.2% offset yield stress for unirradiated and irradiated V-4Cr-4Ti. Properties of the irradiated materials are blue and red symbols.

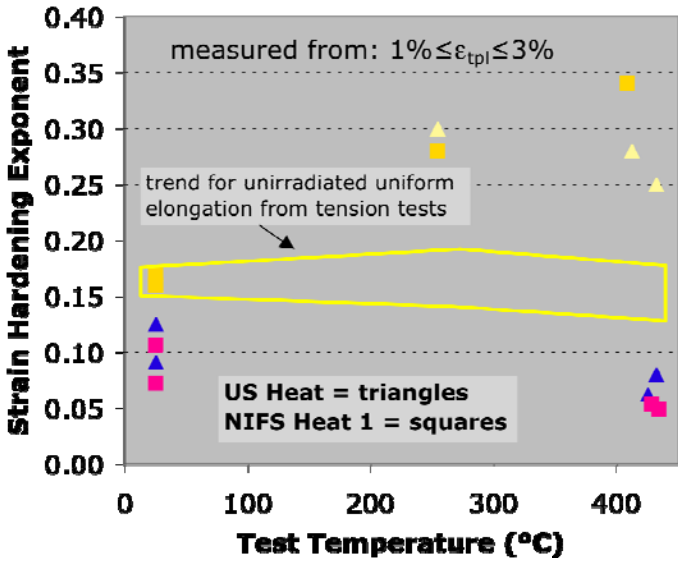

Figure 6. Temperature dependence at 25°C, 250°C, and ~425°C of the strain hardening exponent for unirradiated and irradiated V-4Cr-4Ti. Properties of the irradiated materials are blue and red symbols.

Discussion

Tests on Unirradiated Specimens

Yield stress values from the literature for uniaxial tensile tests on unirradiated heat 832665 are 315-355 MPa at 25°C, 220-260 MPa at 250°C, and 195-235 MPa at 400°C [8,9,11,12]. Unirradiated NIFS-1 yield stress values in tension were not found, but the NIFS-2 heat has a yield strength of around 300 MPa at 25°C [17]. Yield stress values from unirradiated heat 832665 and the NIFS-1 heat measured in compression fall within the range of values in the literature for these materials in tension as expected (Fig. 5) because polycrystalline vanadium with a random grain orientation should have isotropic deformation properties. Figure 5 shows that the elevated temperature yield stress in compression is about 30% lower than the room temperatureyield stress in

compression. Heat 832665 may be consistently stronger than the NIFS-1 heat due to heat 832665 having higher oxygen content [7, 18]. Strain serrations as exhibited in CA06 (heat 832665) are seen in uniaxial tensile data from 300-750°C [9], but were not seen in some other published V-4Cr-4Ti tensile traces [12]. Dynamic strain aging causes the strain serrations.

Necking does not occur in compression tests, so uniform elongation cannot be measured to compare with tensile data. The PLSH exponent, however, can be used to compare deformation behavior in a compression test to deformation behavior in a tensile test. If there is a sufficient amount of plastic strain during the test where the deformation along the length of the compression test specimen is uniform (i.e., minimal barreling for some part of the plastic deformation during the compression test), and if the true stress versus true plastic strain data fit well to the PLSH equation, then the PLSH exponent should be equal to the true uniform elongation (TUE) measured from an equivalent tensile test. The TUE from tensile data can be calculated from the engineering uniform elongation values in the literature using $\varepsilon_{UE}=\ln(e_{UE}+1)$ where ε_{UE} is the true uniform elongation and e_{UE} is the engineering uniform elongation. Literature values of tensile uniform elongation for heat 832665 are 0.14-0.20 at 25°C and 250°C, and 0.13-0.18 at 400°C [8,11,12]. Literature values for NIFS-1 are 0.18-0.2 for temperatures between 25°C and 400°C [19]. The TUE values are thus 0.13-0.18 at 250°C and 0.12-0.17 at 400°C for heat 832665 and approximately 0.18 for the NIFS-1 heat between 25°C and 400°C. A comparison of the measured PLSH exponent values from the compression tests with literature values of TUE from tensile tests are showing in Figure 6. For the 25°C compression tests, the PLSH exponent ranged from 0.16-0.18 which is in good agreement with the TUE values calculated from tensile data in the literature. For the compression tests at elevated temperature, the PLSH values were considerably higher than the TUE values calculated from tensile data in the literature. The reason for this is not clear and will be investigated further.

Tests on Irradiated Specimens

The goal of the research was to look at ductility response in compression for a material undergoing channel deformation. The irradiation temperature for this experiment is near the upper limit to create a microstructure that promotes channel deformation. As yet unreported tensile data from this same experiment show very high strength and low ductility which are strong indicators that channel deformation occurred during those tensile tests. A similar large increase in strength and concurrent reduction in strain hardening exponent in the compression tests are also suggestive of the possibility that the irradiation temperature may have been low enough to cause the formation of a microstructure in these compression specimens that allows channel deformation to occur.

It is interesting to use compression specimens to study channel deformation because it is thought that a specimen that undergoes channel deformation when tested under compression would have better measured ductility than a material undergoing channel deformation when tested in tension. The reason is that the induced increase in cross sectional area during a compression test (geometric hardening) in regions where channel deformation is occurring could make up for the softening that occurs in the channel deformation regions.Transmission electron microscopy was performed on selected untested, partially tested, and fully tested specimens in both the unirradiated and irradiated condition to observe the effect of irradiation on microstructure [20]. Unirradiated specimens were found to have a very low density of observable precipitates while the irradiated specimens had a high density of small defects as shown in Figures 7 and 8, respectively. The defects in the irradiated material may be a combination small dislocation loops, precipitates, and network dislocations, , but of greater interest is the lack of any clear dislocation channels. Figures 8 and 9 show the microstructure of two irradiated specimens tested to 2% and 20% plastic strain, respectively, at room temperature. Neither micrograph shows any signs of channel deformation. There are several possible reasons for a lack of channel deformation. The first is that it may be possible that the irradiation temperature was too high, resulting in a microstructure that does not allow channel deformation to occur. Alternatively, it may be possible that the deformation induced during a compression test may not allow channel deformation. More microscopy, compression tests, and examination of V-4Cr-4Ti tensile specimens from the same irradiation experiment will be needed to determine why no channel deformation was observed here.

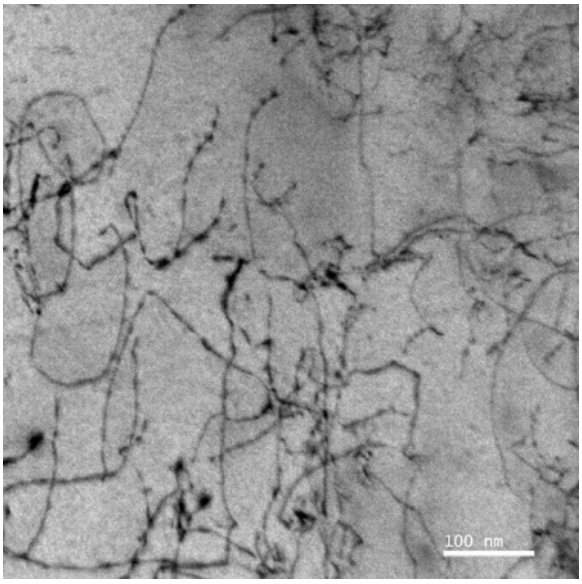

Figure 7. Microstructure observed in an unirradiated V-4Cr-4Ti compression specimen.

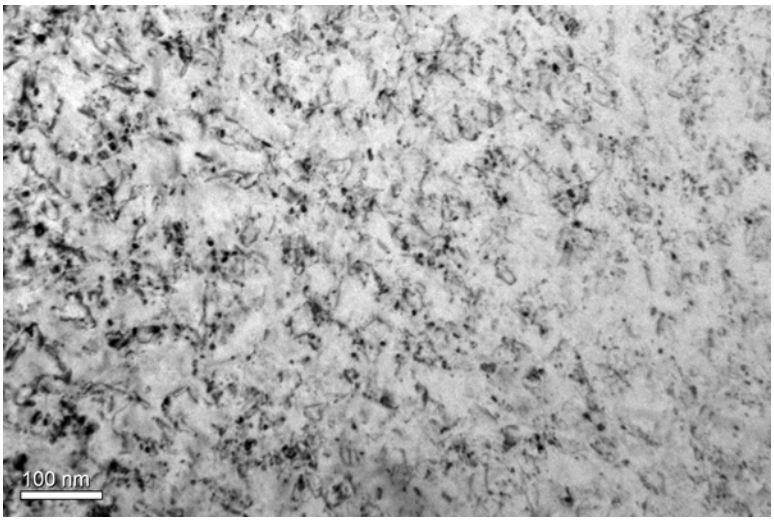

Figure 8. Dislocation and precipitate microstructure of a specimen tested in compression to 2% strain. No deformation channels are present.

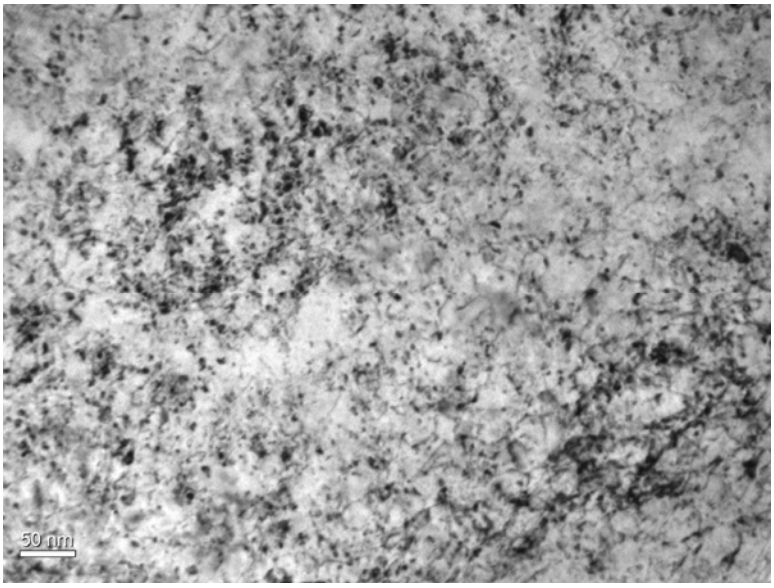

Figure 9. Dislocation and precipitate microstructure of a specimen tested in compression to 20% strain. No deformation channels are present.

Conclusions

Compression tests were performed on unirradiated V-4Cr-4Ti as part of a larger program to better understand the deformation behavior of irradiated V-4Cr-4Ti after irradiation. The effect of irradiation at 425°C on the compression test specimens was to cause a large increase in yield strength and concurrent strong reduction in strain hardening exponent which are both indicators of the possibility that channel deformation is occurring. However, microstructural examinations did not reveal the presence of channel deformation. Several reasons for this are possible, and further examination of compression and tensile specimens are needed to fully understand the response of the material under compression.

Future Work

To better understand the deformation response under compression, several actions are planned which include compression testing of irradiated specimens at 250°C, more microstructural studies of tested compression specimens and tested companion tensile specimens from the same irradiation experiment.

References

[1] R.J. Kurtz, K. Abe, V.M. Chernov, D.T. Hoelzer, H. Matsui, T. Muroga, G.R. Odette, “Recent Progress on Development of Vanadium Alloys for Fusion,” Journal of Nuclear Materials, vol. 329-333, 2004, pp. 47-55.

[2] T. Muroga, T. Nagasaka, K. Abe, V.M. Chernov, H. Matsui, D.L. Smith, Z.-Y. Xu, S.J. Zinkle, “Vanadium Alloys – Overview and Recent Results,” Journal of Nuclear Materials, vol. 307-311, 2002, pp. 547-554.

[3] H. Tsai, L.J. Nowicki, M.C. Billone, H.M. Chung, D.L. Smith, “Tensile and Impact Properties of Vanadium-Base Alloys Irradiated at Low Temperatures in the ATR-A1 Experiment,” Fusion Materials Semiannual Progress Report, vol. 23, Dec., 1997, pp. 70-76.

[4] D.J. Alexander, L.L. Snead, S.J. Zinkle, A.N. Gubbi, A.F. Rowcliffe, E.E. Bloom, “Effects of Irradiation at Low Temperature on V-4Cr-4Ti,” Fusion Materials Semiannual Progress Report, vol. 20, Jun., 1996, pp. 87-95.

[5] T.S. Bray, H. Tsai, L.J. Nowicki, M.C. Billone, D.L. Smith, W.R. Johnson, P.W. Trester, “Tensile and Impact Properties of V-4Cr-4Ti Alloy Heats 832665 and 832864,” Journal of Nuclear Materials, vol. 283-287, 2000, pp. 633-636.

[6] K. Natesan, W.K. Soppet, M. Uz, “Effects of Oxygen and Oxidation on Tensile Behavior of V-4Cr-4Ti,” Journal of Nuclear Materials, vol. 258-263, 1998, pp. 1476-1481.

[7] N.J. Heo, T. Nagasaka, T. Muroga, H. Matsui, “Effect of Impurity Levels on Precipitation Behavior in the Low-activation V-4Cr-4Ti Alloys,” Journal of Nuclear Materials, vol. 307-311, 2002, pp. 620-624.

[8] A.N. Gubbi, A.F. Rowcliffe, W.S. Eatherly, L.T. Gibson, “Effects of Strain Rate, Test Temperature and Test Environment on Tensile Properties of Vanadium Alloys,” Fusion Materials Semiannual Progress Report, vol. 20, Jun., pp. 38-52, 1996.

[9] A.F. Rowcliffe, S.J. Zinkle, D.T. Hoelzer, “Effect of Strain Rate on the Tensile Properties of Unirradiated and Irradiated V-4Cr-4Ti,” Journal of Nuclear Materials, vol. 283-287, 2000, pp. 508-512.

[10] E.V. van Osch and M.I. de Vries, “Irradiation Hardening of V-4Cr-4Ti,” Journal of Nuclear Materials, vol. 271&272, 1999, pp. 162-166.

[11] A.F. Rowcliffe, D.T. Hoelzer, and S.J. Zinkle, “High Temperature Tensile Properties and Deformation Behavior of V-4Cr-4Ti,” Fusion Materials Semiannual Progress Report, vol. 26, Jun., 1999, pp. 25-32.

[12] M.C. Billone, “Revised ANL-Reported Tensile Data for Unirradiated and Irradiated (FFTF, HFIR) V-Ti and V-Cr-Ti Alloys,” Fusion Materials Semiannual Progress Report, vol. 23, Dec., 1997, pp. 3-61.

[13] L.L. Snead, S.J. Zinkle, D.J. Alexander, A.F. Rowcliffe, J.P. Robertson, W.S. Eatherly, “Summary of the Investigation of Low Temperature, Low Dose Radiation Effects on the V-4Cr-4Ti Alloy,” Fusion Materials Semiannual Progress Report, vol. 23, Dec., 1997, pp. 81-98.

[14] S.J. Zinkle, L. L. Snead, A.F. Rowcliffe, D.J. Alexander, L.T. Gibson, “Effect of Irradiation Temperature and Strain Rate on the Mechanical Properties of V-4Cr-4Ti Irradiated to Low Doses in Fission Reactors,” Fusion Materials Semiannual Progress Report, vol. 24, Jun., 1998, pp. 33-40.

[15] S.J. Zinkle, L.L. Snead, J.P. Robertson, A.F. Rowcliffe, “Strain Rate Dependence of the Tensile Properties of V-(4-5%)Cr-(4-5%)Ti Irradiated in EBR-II and HFBR,” Fusion Materials Semiannual Progress Report, vol. 23, Dec., 1997, pp. 77-80.

[16] M.B. Toloczko and R.J. Kurtz, “Room Temperature Compression Properties of Two Heats of Unirradiated V-4Cr-4Ti,” Fusion Materials Semiannual Progress Report, vol. 36, Jun., 2004, pp. 13-18.

[17] A. Nishimura, T. Nagasaka, T. Muroga, "Fracture properties of high-purity V-4Cr-4Ti alloy (NIFS-HEAT-2) at room temperature", Journal of Nuclear Materials, Vols. 307-311, 2002, pp. 571-575.

[18] D.L. Harrod and R.E. Gold, “Mechanical Properties of Vanadium and Vanadium-based Alloys,” International Metals Reviews, No. 4, 1980, pp. 163-221.

[19] K. Fukumoto, T. Yamamoto, N. Nakao, S. Takahashi, H. Matsui, “High Temperature Performance of Highly Purified V-4Cr-4Ti Alloy, NIFS-Heat 1,” Journal of Nuclear Materials, vol. 307-311, 2002, pp. 610-614.

ADDITIONAL CHARACTERIZATION OF V-4Cr-4Ti AND MHD COATINGS EXPOSED TO FLOWING Li
– B. A. Pint (Oak Ridge National Laboratory)

OBJECTIVE

Characterize specimens exposed to flowing Li in a thermal gradient to evaluate the effects on V-4Cr-4Ti and a multi-layer electrically-insulating coating needed to reduce the magneto hydrodynamic (MHD) force in the first wall of a lithium cooled blanket.

SUMMARY

Additional characterization is being performed on specimens exposed to flowing Li in a thermal gradient. These include 500°C tensile testing, measurement of changes in interstitial elements and characterization of the MHD coatings. To assist in the interpretation of these results, a group of specimens was annealed at 700°C for 2,350h in a quartz ampoule.

PROGRESS AND STATUS

Introduction

One critical unresolved issue for the vanadium-lithium blanket concept[1,2] (and any liquid metal concept) in a deuterium/tritium fueled fusion reactor[3,4] is the pressure drop associated with the magnetohydrodynamic (MHD) effect of a conducting liquid flowing across the magnetic field lines One proposed solution is to decouple the structural wall from the liquid metal with an electrically insulating coating or flow channel insert (FCI).[5] This coating application requires a thin, crack-free,[6] durable layer with a relatively high electrical resistance.[7] While a “self-healing” layer is possible in corrosion where a re-passivation can occur by the re-formation of a surface oxide, this concept is not applicable to functional (i.e. electrically resistant) coatings because a defect that shorts the coating is unlikely to “heal”. Therefore, a robust coating system or a FCI is needed for this application. Due to incompatibility between Li and virtually all candidate insulating oxides,[8-12] the current focus of the U.S. MHD coating program[10-12] is evaluating the compatibility of durable, multi-layer coatings[7,13] where a vanadium overlayer prevents direct contact between the insulating oxide layer and Li. This concept shifts the compatibility concern from the oxide layer to the thin vanadium overlayer. In order to verify that a thin, ~10μm, V layer is sufficiently compatible with Li to function in a long-term situation, a mono-metallic thermal convection loop was designed and built to expose specimens with thin V overlayers to flowing Li. The loop was operated at a peak temperature of ~700°C for 2,355h.[14,15] Initial characterization of the coatings and V-4Cr-4Ti specimens in the loop was previously reported.[15,16] Further progress with the characterization is reported here.

Experimental Procedure

Details of the loop exposure have been presented previously.[14-16] The specimens consisted of miniature tensile specimens (type SS-3: 25 x 4 x 0.9mm), tab specimens and specimens with a dual layer MHD coating.[14-16] Initial characterization of the specimens and tubing included metallographic cross-sections, hardness (Vickers, 300g) measurements, chemical analysis using combustion and inductively coupled plasma analysis, and room temperature and 500°C tensile testing at $10^{-3}s^{-1}$ strain rate. Selected specimens were examined using scanning electron microscopy (SEM) equipped with energy dispersive x-ray (EDX) analysis. The EB-PVD coatings were examined by SEM/EDX, contact profilometry and x-ray diffraction (XRD).

Results and Discussion

Sections of the V-4Cr-4Ti tubing were examined metallographically and the composition was analyzed. Figure 1 shows the tube hardness data at 6 locations compared to the initial hardness and the tab specimens at similar locations. The tubing started out with a lower hardness [17] compared to the tab specimens (which were not annealed prior to exposure in Li) but showed a similar trend in hardness after exposure, particularly at the highest temperature. Figure 2 shows the microstructure of the tubing after exposure at the bottom of the cold leg and the top of the hot leg. As expected, the grain size of the tubing from the hot section was larger but there was no obvious change in the microstructure of the surface layer in contact with Li.

Figure 3 compares the interstitial chemistry of the tube sections and tab specimens [15] after exposure. The initial O content in the tubing was somewhat higher than in the tab specimens which reflects the greater amount of O uptake during processing of the tubing. Both data sets show the same trends with the O content decreasing with temperature (due to O gettering by Li) and the N content increasing at the highest temperature (due to N gettering from the Li). Since the tubes were thicker than the tabs and only exposed to Li from one side, it is not surprising that the extent of O depletion or N uptake is not as great at the highest temperature. However, the C values show a different trend in the tube specimens. The C content decreased in the tube specimens while it increased slightly in the tab specimens. Decarburization was not expected at this temperature, and may reflect loss of C in the vacuum. The starting tube composition values are the average of 4 specimens.

The 500°C tensile tests to compliment the room temperature measurements are in progress. The vacuum tensile rig to conduct these measurements has been calibrated and the work is proceeding.

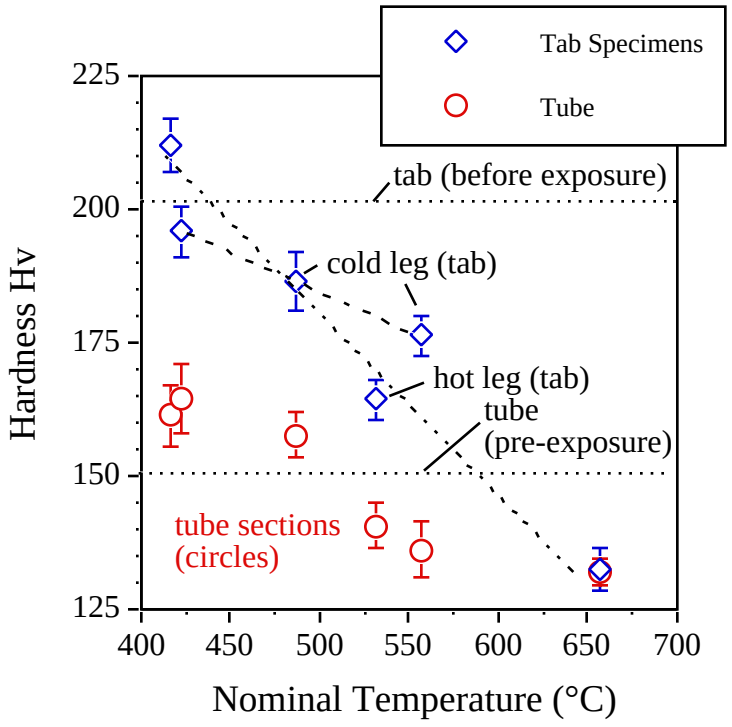

Figure 1. Average hardness measurements as a function of nominal exposure temperature along the hot and cold legs of the mono-metallic loop for tab specimens and tube specimens in similar locations.

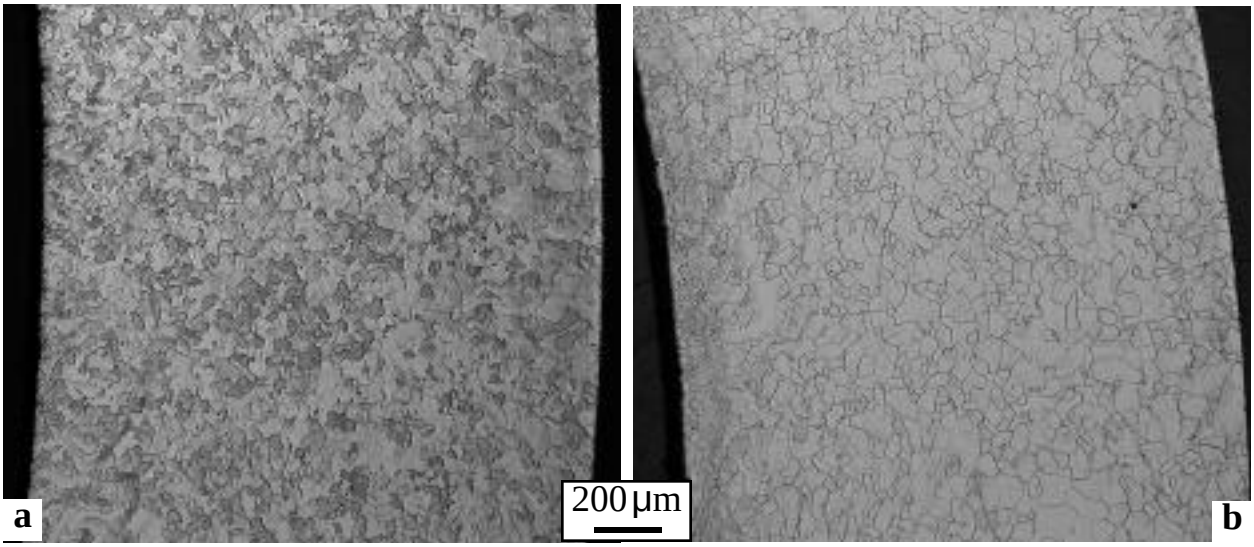

Figure 2. Light microscopy of the V-Cr-4Ti tubing in cross-section after exposure at (a) the bottom of the cold leg and (b) the top of the hot leg. The etchant was $60H_2O$-$30HNO_3$-10HF.

In order to assist in the interpretation of the results from Li exposure, a set of tensile, tab and one MHD coating were annealed for 2,350h at 700°C in a quartz ampoule. This provided a similar temperature as the hottest specimens in the loop without the Li exposure. Tensile specimens from that exposure did not change mass indicating no O uptake during the anneal. Initially, the microstructure of a tab specimen has been examined. Figure 4 shows the microstructure of the annealed tab compared to the tab specimen from the top of the hot leg. The grain growth and precipitate loss in the Li-exposed specimen was not evident in the annealed specimen. The curvature of the annealed MHD specimen was examined to

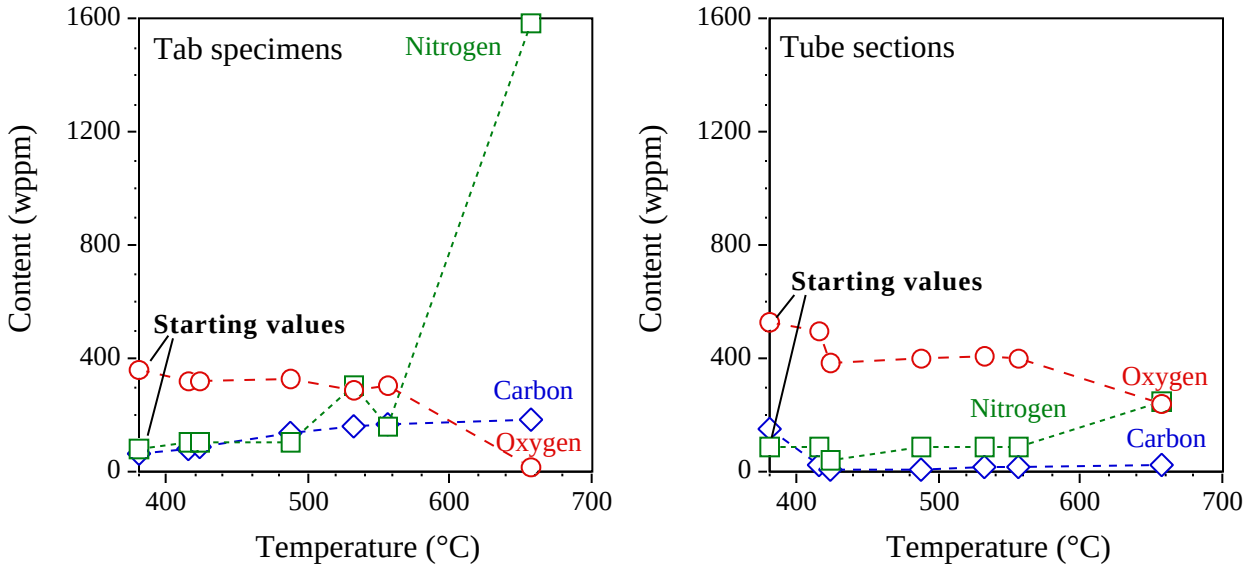

Figure 3. Measured O, C and N values for specimens at six locations in the loop (a) tab specimens and (b) tube specimens.

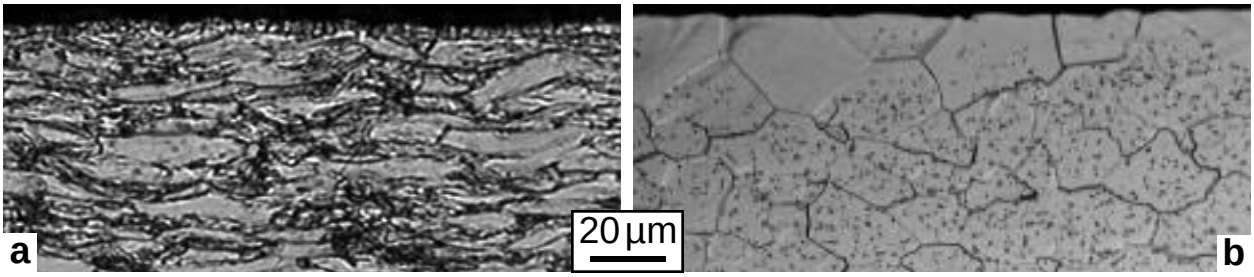

Figure 4. Light microscopy of cold-rolled V-4Cr-4Ti tab specimens (a) annealed for 2,350h at 700°C and (b) after exposure to flowing Li at the top of the hot leg (~655°C) where the surface grains appear depleted in precipitates.

compare to those exposed to Li. The annealed coating was from batch two and behaved similar to those coatings in the loop – the concave curvature increased after exposure. Batch 1 coatings which were exposed at the tops of the hot and cold legs, [16] changed curvature from concave to convex after exposure. The reason for the change in curvature has not been determined but likely reflects a change in the residual stress state of the coating and substrate.

References

[1] R. J. Kurtz, K. Abe, V. M. Chernov, D. T. Hoelzer, H. Matsui, T. Muroga and G. R. Odette, J. Nucl. Mater. 329-333 (2004) 47.
[2] T. Muroga, J. M. Chen, V. M. Chernov, K. Fukumoto, D. T. Hoelzer, R. J. Kurtz, T. Nagasaka, B. A. Pint, M. Satou, A. Suzuki and H. Watanabe, J. Nucl. Mater. 367-370 (2007) 780.
[3]. I. R. Kirillov, C. B. Reed, L. Barleon and K. Miyazaki, Fus. Eng. Design 27 (1995) 553.
[4] L. Barleon, V. Casal and L. Lenhart, Fus. Eng. Design 14 (1991) 401.
[5] S. Malang, H. U. Borgstedt E. H. Farnum, K. Natesan and I. V. Vitkovski, Fus. Eng. Design 27 (1995) 570.
[6] L. Bühler, Fus. Eng. Design, 27 (1995) 650.
[7] Y. Y. Liu and D. L. Smith, J. Nucl. Mat. 141-143 (1986) 38.
[8] J. E. Battles, Intern. Mater. Rev. 34 (1989) 1.
[9] T. Terai, et al., J. Nucl. Mater. 233-237 (1996) 1421.
[10] B. A. Pint, P. F. Tortorelli, A. Jankowski, J. Hayes, T. Muroga, A. Suzuki, O. I. Yeliseyeva and V. M. Chernov, J. Nucl. Mater. 329-333 (2004) 119.
[11] B. A. Pint J. L. Moser and P. F. Tortorelli, Fus. Eng. Des. 81 (2006) 901.
[12] B. A. Pint, J. L. Moser, A. Jankowski and J. Hayes, J. Nucl. Mater. 367-370 (2007) 1165.
[13] I. V. Vitkovsky, et al., Fus. Eng. Design, 61-62 (2002) 739.
[14] B. A. Pint, et al., DOE/ER-0313/42 (2007) 2.
[15] B. A. Pint, et al., J. Nucl. Mater. in press.
[16] B. A. Pint, et al., DOE/ER-0313/43 (2007) 2.
[17] B. A. Pint, S. J. Pawel and J. L. Moser, DOE/ER-0313/40 (2006) 2.

MECHANICAL, THERMAL, AND ELECTRICAL PROPERTIES OF NUCLEAR-GRADE SILICON CARBIDE COMPOSITES —R. Shinavski (Hyper-Therm HTC, Inc.), Y. Katoh and L. Snead (Oak Ridge National Laboratory)

OBJECTIVE

Objective of the present work was to acquire baseline properties data, including tensile properties, thermal conductivity, and electrical conductivity, of the reference nuclear grade material of silicon carbide fiber-reinforced, multilayered interphase, chemically vapor-infiltrated silicon carbide matrix (SiC/SiC) composite.

SUMMARY

Nuclear grade SiC/SiC composites combine the attributes of high temperature mechanical strength and toughness with a relative dimensional stability under high neutron fluences that address the primary requirement of survivability in application as a flow channel insert. Unirradiated, through-thickness thermal conductivity has been identified as one property that is not suitable for a flow channel insert. However calculations indicate that through architecturally creating a structure of the nuclear grade SiC/SiC that the targeted low thermal conductivity can be achieved. A database of properties is being developed on a number of nuclear grade SiC/SiC composite. This data accumulation has not yet measured all relevant properties, but has set out a methodology for generating these properties and statistically reducing the properties to a property that can be used for component design.

PROGRESS AND STATUS

Introduction

Nuclear grade silicon carbide fiber-reinforced silicon carbide matrix (SiC/SiC) composites have potential for use in components of fusion reactors subject to elevated temperatures and high neutron fluences. SiC/SiC composites are more suitable, than monolithic silicon carbide, for large structural components due to a significantly higher toughness, and resistance to catastrophic failure that is obtained by continuous fiber reinforcement. Such reinforcement results in nearly an order of magnitude improvement in failure strain. Thus due to Weibull effects, SiC/SiC composites are significantly more robust for producing larger components and structures.

Stoichiometric silicon carbide only has a small equilibrium dimensional change that occurs under neutron irradiation that makes these materials suitable for high neutron fluence environments. SiC/SiC composites composed of near stoichiometric SiC fibers (such as Hi-Nicalon Type S and Tyranno SA3) combined with a stoichiometric SiC matrix produced by chemical vapor infiltration have therefore been termed nuclear grade SiC/SiC. In particular, nuclear grade SiC/SiC is being considered as a candidate for the flow channel insert in fusion reactors.

Mechanical, thermal, and electrical property data for nuclear grade SiC/SiC are being accumulated to allow component design, and assess feasibility. Property databases for three configurations are being

gathered. The nuclear grade SiC/SiC constructions considered use either a fabric-based architecture, a braided architecture, or a near unidirectional architecture. All of the composites were produced by Hyper-Therm HTC (Huntington Beach, CA) The first two of these constructions can be suitable for producing a flow channel insert; while the third is suitable for making small diameter pins that can be used for joining and locating components.

Mechanical Properties

Mechanical properties are highly dependent on the orientation and the volume fraction of fibers oriented in the loading direction. Figure 1 shows the range of tensile stress-strain response that can be obtained. In general, all architectures result in a failure strain of 0.5%, while the ultimate strength and proportional limit strengths increase in proportion to the fraction of fiber oriented in the loading direction. The ultimate strength, for instance can be increased by a factor of nearly 4X. However, composites such as with a 0+/-55 triaxial braid architecture have closer to in-plane isotropic mechanical properties than a highly anisotropic unidirectional composite. Although the ultimate strengths can be tremendously different with different composite architectures, the in situ fiber strength (i.e. the ultimate strength of the composite divided by the fiber volume fraction oriented in the load direction or close to the load direction (<~30º) with correction for mis-orientation) obtained is always 2.3 +/-0.1 GPa. This consistency allows reasonable prediction of the expected ultimate strength of a composite architecture that is selected to maximize design margins for a given load case.

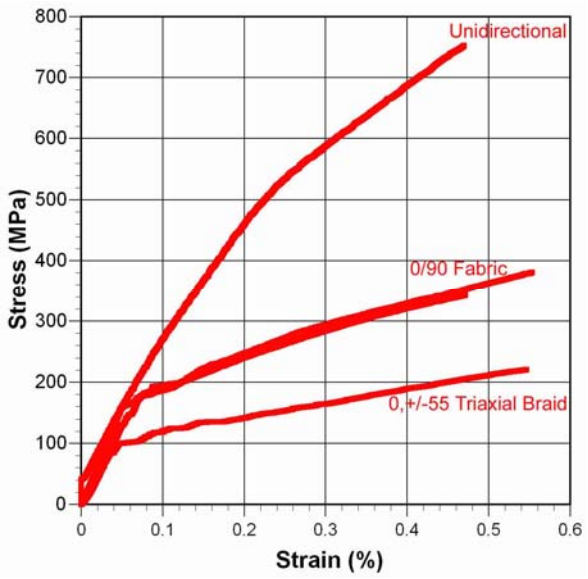

Fig. 1. Examples of the range of stress-strain response that can be obtained in nuclear grade SiC/SiC (Hi-Nicalon Type S/CVI SiC)

The mechanical test plan that is being performed consists of a significant number of room temperature and elevated temperature tensile tests such that a design allowable can be determined. Current status of the mechanical test effort is that a large fraction of the room temperature evaluations have been performed and a limited number of the elevated temperature tests have been performed. However the insensitivity of the nuclear grade SiC/SiC composites over the temperature range of interest (ambient to 800ºC) has been demonstrated to even higher temperatures (Figure 2). Table I presents a summary of the room temperature tensile testing that has been conducted for the respective architectures. Table II reduces these tensile properties to statistically acceptable B-basis allowable where there exists a 95% confidence that 90% of the material will be at or above this value. Further determination of a design allowable for a specific component must also be performed to take into consideration the size effect of the component on the mechanical properties. However in contrast to monolithic ceramics, fiber-reinforced composites have lower volume sensitivity. Additionally the desired factor of safety must also be considered. Similar testing will be completed at elevated temperatures in the upcoming year. Additionally further hoop direction tensile testing of the traixial braided geometry and the unidirectional architectures are required to improve the current statistical limitations in these orientations.

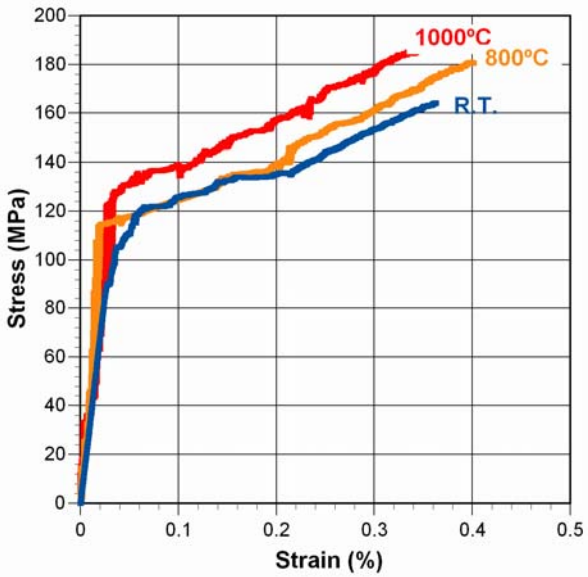

Fig. 2. Elevated temperature strength comparison of triaxially braided nuclear grade SiC/SiC tested in the axial direction as a function of temperature.

Table 1. Summary of the ambient tensile testing for nuclear grade SiC/SiC.

Material	Orientation	Elastic Modulus (GPa)	Ultimate Strength (MPa)	Failure Strain (%)	Prop. Limit Strength (MPa) 0.01% offset
Triaxial SiC/SiC	Axial	261+/-31 n=26	188+/-22 n=11	0.50+/-0.07 n=11	91+/-11 n=26
Triaxial SiC/SiC	Hoop	265+/-24 n=8	132+/-8 n=5	0.38+/-0.07 n=5	92+/-4 n=8
5 Harness Satin SiC/SiC	0/90	268+/-18 n=16	399+/-23 n=16	0.54+/-0.06 n=16	180+/-12 n=16
Unidirectional SiC/SiC	0	261+/-31 n=4	723+/-58 n=4	0.47+/-0.09 n=4	325+/-22 n=4

Table 2. B-basis statistical allowables for room temperature tension of nuclear grade SiC/SiC

Material	Orientation	Failure Stress (MPa)	Failure Strain (%)	Proportional Limit Stress 0.01% offset (MPa)
Triaxial SiC/SiC	Axial	138	0.23	72
Triaxial SiC/SiC	Hoop	94	0.10	79
5 Harness Satin SiC/SiC	0/90	344	0.39	157
Unidirectional SiC/SiC	0	481	0.08	232

Thermal Properties

Thermal conductivity and thermal expansion have been measured. These two properties are critical to application as a flow channel insert as a low thermal conductivity is required to adequately reduce the temperature of the ferritic steel blanket module, and differential thermal expansion combined with differential irradiation induced swelling dominate the induced stress in the flow channel insert. Table II shows the through-thickness thermal conductivity at three temperatures of interest. All values are the average of two measurements. In-plane thermal conductivities are ~2X the through-thickness values, which are more critical for application as a flow channel insert. The through-thickness thermal conductivity is higher than targeted for flow channel inserts by an order of magnitude in the unirradiated state. Achieving a 1-2 W/m/K thermal conductivity in the as-produced state presents the biggest challenge to using nuclear grade SiC/SiC composites for the flow channel insert. However recent calculations have indicated that by producing the SiC/SiC composite as a fluted core sandwich structure that the effective through-thickness conductivity can be reduced to as low as 1.2 W/m/K. Such a

structure will also provide a compliant layer between the hot and cold surfaces to allow accommodation of both the differential thermal expansion strains and the differential irradiation induced swelling strains. The feasibility of producing a fluted core sandwich structure has been demonstrated in other CMC systems, but producibility in nuclear grade SiC/SiC has not yet been demonstrated. This area is a subject of ongoing development.

Table 3. Through-thickness thermal conductivity of nuclear grade SiC/SiC

Material	Orientation	Thermal Conductivity (W/m/K)		
		20ºC	500ºC	800ºC
Triaxial SiC/SiC	Through-Thickness	27.6	21.5	18.2
5 Harness Satin SiC/SiC	Through-Thickness	21.8	17.0	14.2

Thermal expansion has been measured to be nearly isotropic (within 0.1 ppm/ºC) regardless of orientation or architectural construction. The mean thermal expansion coefficient from RT-500ºC is 3.9 ppm/ºC, and 4.3 ppm/ºC from RT to 800ºC.

Electrical Properties

Both through-thickness and in-plane electrical properties have been measured on the 5 harness satin fabric-based nuclear grade SiC/SiC. The electrical conductivity measurement in-plane and through-thickness are summarized in Table IV. In-plane electrical conductivity is significantly higher than through-thickness conductivity presumably due to the continuity of the highly conductive, but albeit thin, multilayer SiC fiber coating that contains carbon interlayers. The through-thickness electrical conductivities are in a suitable range for the flow channel insert to minimize magnetohydrodynamic pressure drops.

Table 4. Electrical properties of nuclear grade SiC/SiC (5 harness satin fabric-based)

Orientation	Electrical Conductivity (S/m)					
	20ºC	100ºC	280ºC	360ºC	500ºC	760ºC
Through-Thickness	0.02	0.10	0.27	0.75	not measured	not measured
In-Plane (0/90)	310	310	330	350	380	460

MICROSTRUCTURAL EXAMINATION OF SiC$_F$/SiC WOVEN FIBER COMPOSITES – D. S. Gelles and G. E. Youngblood (Pacific Northwest National Laboratory)*

OBJECTIVE

The primary objectives of this task are to: (1) assess the properties and behavior of SiC$_f$/SiC composites made from SiC fibers (with various SiC-type matrices, fiber coatings and architectures) before and after irradiation, and (2) develop analytic models that describe these properties as a function of temperature and dose as well as composite architecture. Recent efforts have focused on examining the electrical and thermal conductivity properties of SiC$_f$/SiC composites considered for application in flow channel insert-structures in support of the U.S. dual-coolant lead-lithium fusion reactor blanket concept.

SUMMARY

Electrical and thermal conduction in 2D-SiC$_f$/SiC composites exhibit lower than expected values in directions normal to the fiber weave plane. Transmission electron microscopy was used to carefully examine if micro-porosity possibly remaining at the impingement interface regions of the columnar SiC grains growing outwardly from adjacent SiC fiber surfaces could be partly responsible for the observed lower than expected transverse EC- and TC-values. Instead, in these regions no micro-porosity was observed; but rather a complete filling in of the vapor deposited SiC had occurred. The actual connectivity and amounts of the constituent phases (fibers, fiber coatings and CVI-SiC matrix) in each direction and the individual EC-values of the constituents govern the overall transverse and normal EC-values in 2D-SiC$_f$/SiC composite.

PROGRESS AND STATUS

Introduction

In the dual-coolant lead-lithium (DCLL) fusion reactor blanket concept, an important component called a flow channel insert provides electrical and thermal decoupling of the hot (~700°C) lead-lithium from the load-bearing, structural steel channel walls of the blanket. For application as an FCI component, a silicon carbide, fiber-reinforced composite material made by chemical vapor infiltration (SiC$_f$/CVI-SiC) is being investigated [1]. The SiC$_f$/CVI-SiC for this application should have low transverse electrical and thermal conductivity to reduce MHD-induced pressure drop in the flowing lead-lithium and to protect the steel channel walls from excessive temperature, respectively.

Electrical (and thermal) conductivity measurements on two dimensional or 2D-SiC$_f$/CVI-SiC composites made with stacked CVI fabric layers of woven SiC fibers exhibit significant anisotropy in directions normal and parallel to the fabric layers [2-3]. In Figure 1, typical electrical conductivity (EC) data in the in-plane and normal directions for three types of advanced 2D-SiC$_f$/SiC composites are shown as a function of temperature.

The in-plane EC-values, which lie above the typical range of EC-values for pure SiC, are governed by the amount (thickness) of the pyro-carbon (PyC) fiber coatings that provide continuous high conductivity pathways even though the amount of PyC is only ~1% overall. The normal EC-values, which lie below the range of values for pure monolithic CVD-SiC and also below the FCI-goal of <20 S/m, are greatly reduced by the limited electrical connectivity through the fiber PyC-coatings because most of the fibers are separated by CVI-SiC matrix in the transverse direction. Therefore, normal EC-values are governed primarily by conduction through the continuous portions of the SiC (a semi-conductor) matrix as suggested by a temperature dependence characteristic of thermal activation. However, these conduction pathways also are limited by the amount and orientation of the mostly in-plane, lamellar-shaped macro-

*Pacific Northwest National Laboratory (PNNL) is operated for the U.S. Department of Energy by Battelle Memorial Institute under contract DE-AC06-76RLO-1830.

porosity observed between fabric layers. It is also possible that some concentrations of micro-porosity may exist in the CVI-SiC matrix that might further contribute to the decrease in the transverse EC. Such micro-porosity could be formed during CVI-processing at the numerous impingement interfaces between intersecting SiC grain growth patterns surrounding adjacent SiC fibers. Many of these interfaces would lie normal to the conduction direction.

The purpose of this work then was to carefully examine and identify all possible micro-structural features peculiar to the CVI-SiC process that might reduce the transverse EC (and perhaps the transverse thermal conductivity) in 2D-SiC_f/SiC composites. Transmission electron microscopy (TEM) was used to carry out this examination.

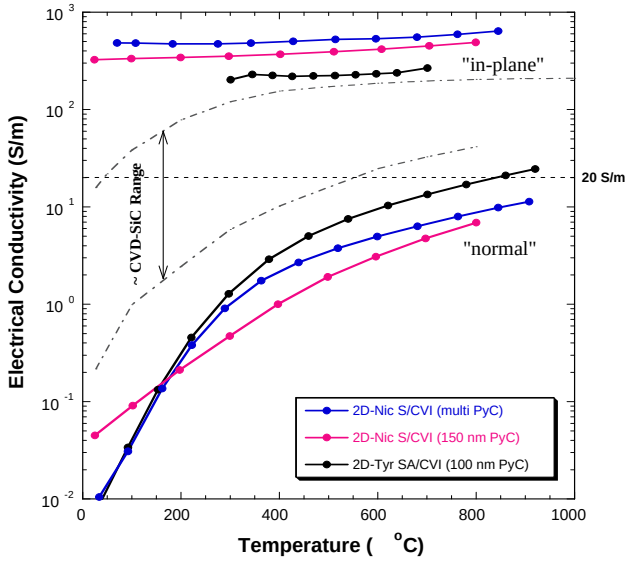

Figure 1. Electrical conductivity in two directions as a function of temperature for three types of advanced 2D-SiC_f/SiC composites. For comparison, an approximate range of EC-values for dense, high-purity monolithic CVD-SiC also is shown.

Experimental Procedure

The composite listed as 2D-Nic S/CVI (150 nm PyC) in Figure 1 was selected for detailed micro-structural examination by TEM. This commercially available composite was made by GE Power Systems using Hi Nicalon™ type S 5HS-0/90 woven fabric with relatively thin (nominally 150 nm) PyC fiber coatings. Results from previous testing of this material indicated that its quality was state of the art (e.g., 2.69 g/cc bulk density, 750 MPa and 284 GPa ultimate stress and elastic modulus at RT, respectively, and a transverse thermal conductivity of 27 W/mK at RT [4]). Little mechanical degradation occurred in this composite material after neutron irradiation for doses up to 10 dpa [5]. At 500°C, we measured transverse and in-plane EC-values of ~2 and 400 S/m, respectively for this material (see Figure 1). The transverse EC-value of 2 S/m is ~1/10th the goal for the FCI-application [6]. This composite exhibits about 10% open and connected porosity because of its layered woven fabric pattern and the required open pathways necessary for carrying out the matrix vapor infiltration process. However, the open porosity can be effectively sealed at plate surfaces by applying a thin, dense and adherent CVD-SiC “seal-coat” as a final step in the CVI-processing. This so-called advanced 2D-SiC_f/SiC best meets the requirements desired for application as a fusion reactor structural material, namely acceptable radiation resistance, mechanical strength and toughness as well as relatively high thermal conductivity, and is considered to be a reference SiC_f/SiC material. Except for its high values of transverse thermal conductivity (~20 W/mK unirradiated at 600°C), this material also meets the desired requirements for the FCI-application.

To examine porosity on a fine scale in such a material using transmission electron microscopy (TEM), two experimental requirements are needed. To view the pores, the specimen interfaces (perhaps containing pores) must be parallel to the electron beam and proper focusing conditions must be optimized. Therefore, several samples were prepared so that the cross-sectional view of at least one bundle of fibers in the 2D-weave pattern was parallel to the electron beam, and images were taken in an under-focused condition (~1000 nm under focused) so that porosity appears in strong white contrast. Two 3-mm diameter disks with the proper orientation were cut and thinned for electron microscopy by ion milling in a Precision Ion Polishing System (PIPS) from Gatan, Inc. using 5 KeV argon ions. Microstructure examinations by TEM were performed on a JEM 2010F analytical microscope operating at 200 KeV and equipped with an Oxford Instruments, Inc. X-ray spectrometer with INCA composition mapping software.

Results

In Figure 2, an optical microscopy view of a thinned sample illustrates the typical fiber arrangement in a 0/90 2D-SiC_f/SiC composite. In Figure 3, a TEM view at x18,000 illustrates the typical columnar grains growing outwardly from the fiber surfaces that were formed during CVI-SiC processing. The central triangular region is the cross-section of a needle-like cavity through which the deposition vapors flowed during processing. These needle-like pores run parallel between many of the fibers within a fiber bundle (500 filaments per yarn), but do not provide significant resistive barriers to EC in the in-plane direction. The curved light grey region surrounding each fiber is the pyro-carbon coating. Although nominally 150 nm thick, there appears to be significant variation in the coating thickness. Compositional mapping demonstrated that the carbon coating was securely attached to the fiber with no apparent separations between the fiber and its coating. However, some circumferential separations were observed within the pyro-carbon coatings themselves.

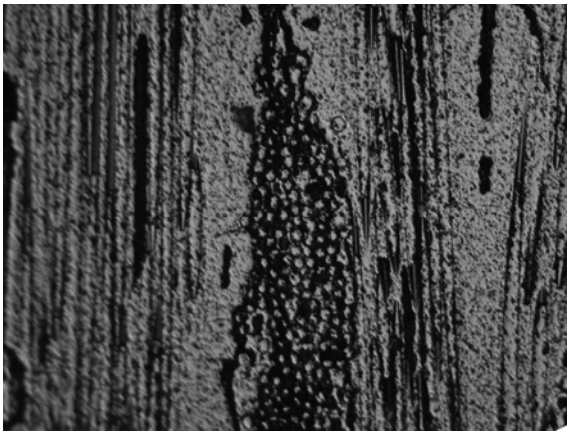

Figure 2. Optical micrograph showing the fiber bundle arrangement and microstructure of a typical 0/90 2D-SiC_f/CVI-SiC composite. The horizontal direction in the view plane is the transverse conduction direction.

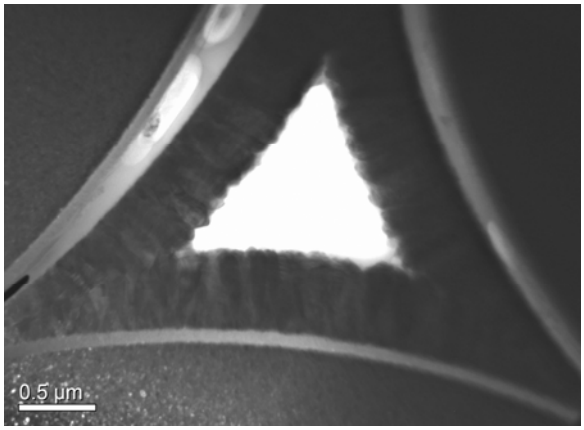

Figure 3. TEM micrograph showing typical columnar grains growing radially outward from the fiber surfaces that were formed during CVI-SiC processing. Also shown are the interface regions of interest between the intersecting growth patterns formed along three touching parallel fibers. The central triangular-shaped region is a cross-sectional view of a needle-like cavity through which the infiltration vapors flowed.

In Figure 4, a higher magnification view of the impingement region between the intersecting growth patterns shown on the lower left in Figure 3 is given. The columnar SiC grains are highly faulted, and their grain size is much larger than the grains in the Hi Nicalon™ type S fibers. Noticeably, the interface created between impinging columnar grain growth structures appears to be densely filled and cavity free.

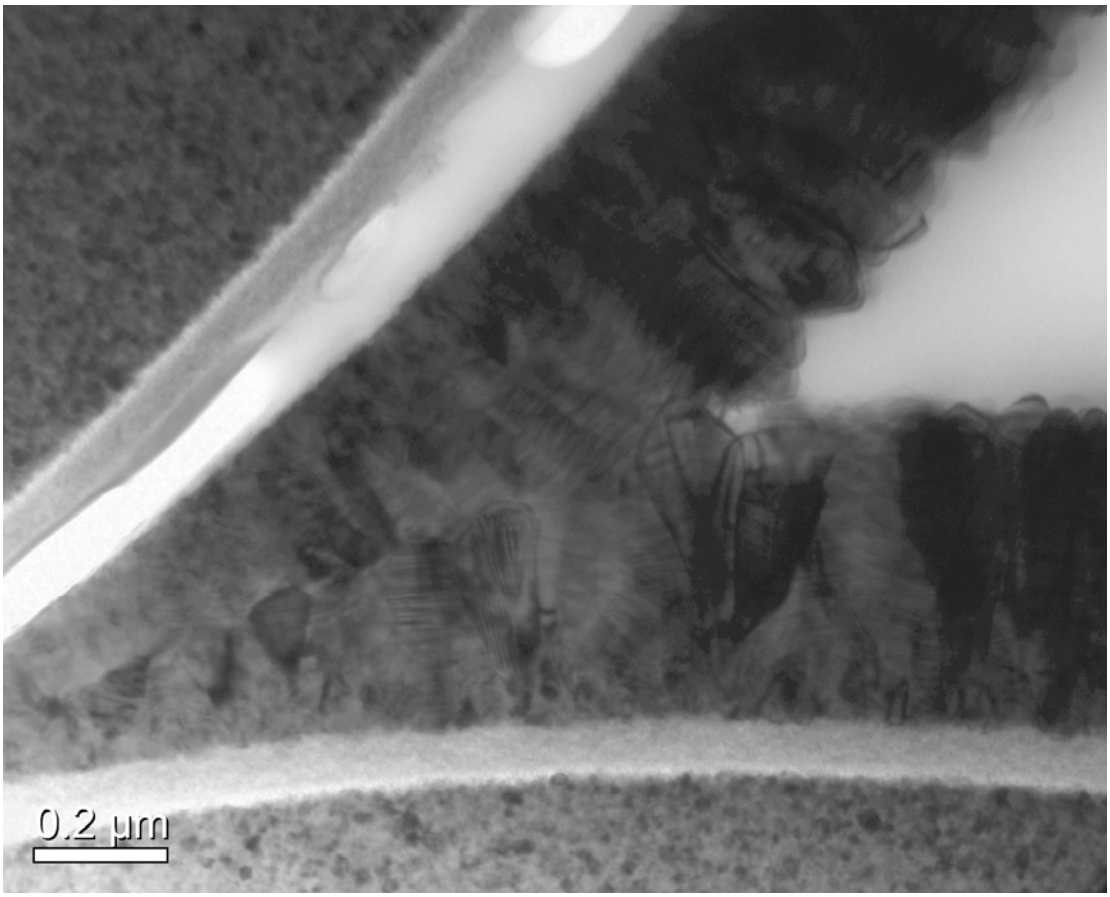

Figure 4. High magnification (x80,000) TEM edge-on view of the intersection interface region between impinging columnar grains growing outwardly from neighboring fiber surfaces as shown on the left side of Figure 3.

In order to make small pores or cavities visible, TEM images were under-focused (~1000nm) so that cavities, if they are present, should appear in stronger contrast. First, the region in the far left of Figure 4 is shown in Figure 5 at x100,000 magnification. The narrow white band shown in the upper-middle portion of Figure 5 is a separation (or crack) formed between the PyC coating and the CVI-SiC matrix. Note that it extends further between the coating and CVI-SiC matrix in Figure 4. Similar coating/matrix separations were observed in TEM views of other regions. In contrast, no separations were ever observed between the type S fiber/fiber coating interface. In a fiber-reinforced composite, this is a requirement to provide maximum protection of the fiber surface and to enhance the load transfer capability between fiber and matrix in a fiber-reinforced composite, and therefore the composite toughness and strength.

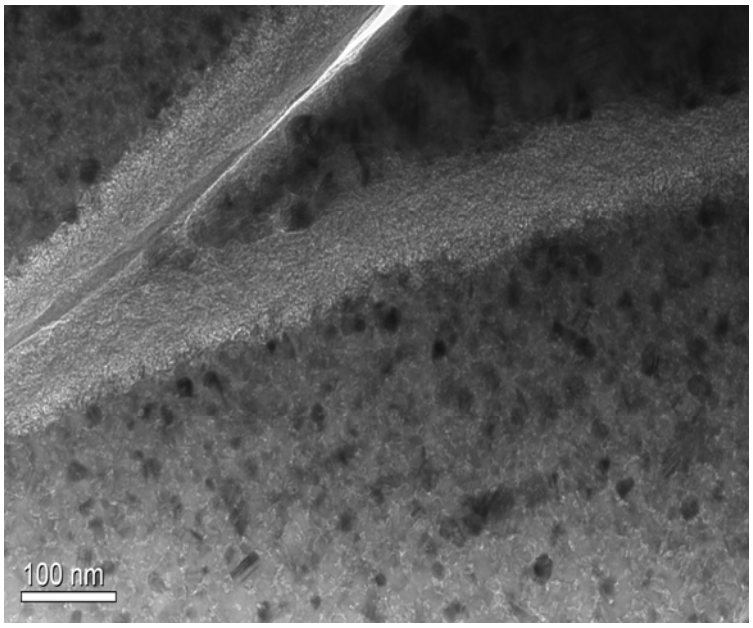

Figure 5. High magnification (x120,000) TEM micrograph of region near two touching fibers, under-focused. The two ~100-nm thick grey areas illustrate the turbostratic layered structure with <0001> texture of the PyC fiber coatings.

In Figure 6, another example of an under focused TEM view of the impingement interface at high magnification (x160,000) is shown. Again, no micro-porosity is revealed along the impingement interface.

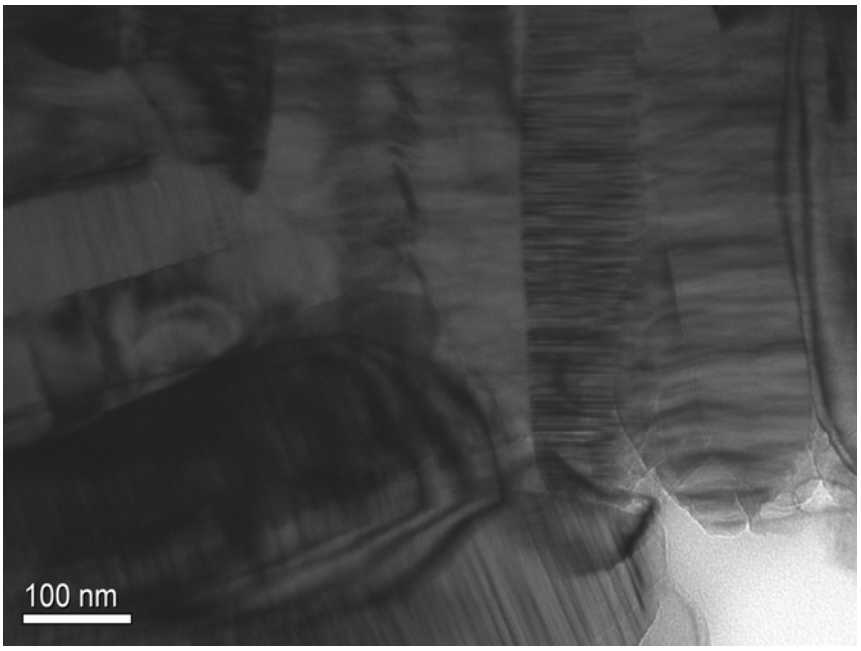

Figure 6. High magnification (x160,000) TEM view of another impingement interface region, under focused.

Discussion

In Reference [1], it was stated that simple parallel/series models based on constituent EC-values and geometry could not explain the observed highly anisotropic EC-values for the in-plane and normal directions in 2D-SiC_f/SiC (EC_x/EC_z > 100 where x and z are in the in-plane and transverse directions, respectively). It was conjectured that perhaps the many intersecting interfaces formed between the CVI-SiC columnar grains growing outwardly from neighboring fiber surfaces contained micro-porosity which could form barriers to conduction processes and could contribute to the lower than expected electrical conduction in the transverse direction. This region of the CVI-SiC pattern has received little attention until now. However, careful TEM examination of several interface regions did not reveal the presence of micro-porosity or cracking at these interfaces.

A search of the literature also did not identify such configurations. However, most micro structural examinations were primarily concerned with the fiber/coating and the coating/matrix interfaces as well as the nature of the PyC interphase itself [7-9]. In particular, most studies emphasized explaining the outstanding mechanical strength and toughness properties exhibited by SiC_f/SiC composites where the fibers were coated either with thin single layers of PyC or multiple C/SiC layers. Using SEM or TEM, the propagation of micro-cracks formed initially in the SiC matrix due to applied tensile stresses was examined in detail. It was revealed that the micro-cracks were blunted by deflection within single PyC fiber coatings or by branching between the multiple C/SiC coatings. However, no views of cracking along the intra-grain growth interfaces were ever shown, so apparently never observed.

In some sense, the negative results of this investigation looking for micro-porosity at grain growth interfaces in the CVI-SiC matrix explain why the thermal conduction in 2D-SiC_f/CVI-SiC is so high. The conduction path through the semi-continuous CVI-SiC matrix as well as across or through the nearly stoichiometric SiC fibers used in advanced SiC_f/SiC supports effective phonon conduction. Only the ~10% macro-porosity in the as-fabricated composites provides significant barriers to phonon conduction. Because of the shape and orientation of the macro-pores located primarily between the fiber bundles or fabric layers, these barriers have more than a linear influence on the transverse TC [10]. Likewise, the observed anisotropy of the thermal conduction (TC_x/TC_z ~ 2) for as-fabricated composite also is primarily due to the shape and orientation of the macro-porosity.

However, the electrical conduction for such composites is primarily due to electron conduction and the observed anisotropy is much larger (EC_x/EC_y ~100). Due to the much greater disparity between electronic conduction in SiC (a semi-conductor with EC-values in the $1\text{-}10^2$ S/m range and exhibiting a thermal activation temperature dependence) and the PyC coatings (a metallic conductor with EC-values in the $10^4\text{-}10^6$ S/m range and relatively independent of temperature), the overall transverse or in-plane EC-values of 2D-SiC_f/SiC depend on the actual connectivity and amounts of the constituent phases in each direction in these composites.

Finally, some evidence for separations within the PyC coating or at coating/CVI-SiC interfaces was observed by TEM. At this time, it is not known whether these observations are characteristic of the as-received GE composite, or were caused by the sample preparation. Further TEM examination of these regions in other samples of as-received composite must be carried out before any conclusions can be made concerning such separations.

Conclusions

No evidence for micro-porosity or cracking was observed by TEM in several views of the interface region formed between intersecting columnar SiC grains growing outwardly from neighboring fiber surfaces. In fact, rather complete fill-in of the CVI-SiC matrix occurred around the individual fibers except for the needle-like cavities (necessary for the flow of the CVI vapors) running parallel between many of the fibers in a bundle. The actual connectivity and amounts of the constituent phases (fibers, fiber coatings and

CVI-SiC matrix) in each direction and the individual EC-values of these phases determine the overall transverse and normal EC-values in 2D-SiC_f/SiC composite.

References

[1] G.E. Youngblood, R.J. Kurtz and R.H. Jones, "Development of SiC/SiC for application as a flow channel insert," pp 3-8 in Fusion Materials Semiannual Progress Report (FMSPR) for period ending Dec. 31, 2004 (DOE/ER-0313/37).

[2] G.E. Youngblood, E. Thomsen and G. Coffey, "Electrical conductivity of SiC/SiC," pp 46-51 in Fusion Materials Semiannual Progress Report (FMSPR) for period ending Dec. 31, 2005 (DOE/ER-0313/39).

[3] N.B. Morley, et al., "Recent research and development for the dual-coolant blanket concept in the US," Fus. Eng. And Design, in press.

[4] G.E. Youngblood and R.H. Jones, "Characterization of a 2D-SiC/SiC composite made by ICVI with Hi-Nicalon type S fabric, " pp 34-40 in FMSPR for period ending June 30, 2003 (DOE/ER-0313/34).

[5] T. Hinoki, et al., "The effect of high dose/high temperature irradiation on high purity fibers and their silicon carbide composites," J. of Nucl. Mater., 307-311 (2002) 1157-1162.

[6] N.B. Morley, et al., "Current understanding of feasibility of SiC/SiC composites for flow channel inserts in Dual Coolant Pb-17Li blankets," presented at TBM meeting, June 4, 2004, UCLA.

[7] R. Naslain, "Design, preparation and properties of non-oxide CMCs for applications in engines and nuclear reactors: an overview," Composite Sci. and Tech. 64 (2004) 155-170.

[8] R. Naslain, F. Langlais, R. Pailler and G. Vignoles, "Processing of SiC/SiC fibrous composites according to CVI-techniques," pp 19-37 in Advanced SiC/SiC Composites, eds. A. Kohyama, M. Singh, HT Lin and Y. Katoh, Ceramic Transactions 144 (2002), published by the American Ceramic Society, Westerville, Ohio.

[9] Gregory N. Morscher, et al., "Modeling stress-dependent matrix cracking and stress-strain behavior in 2D woven SiC fiber reinforced CVI SiC composites," Comp. Sci. and Tech. 67 (2007) 1009-1017.

[10] Gerald E. Youngblood, David J. Senor and Russell H. Jones, "Modeling the transverse thermal conductivity of 2D-SiC/SiC composites made with woven fabric," Fusion Sci. and Tech 45(4), (2004) 583-591.

DEVELOPMENT AND EVALUATION OF SILICON CARBIDE JOINTS FOR APPLICATIONS IN RADIATION ENVIRONMENT —Y. Katoh (Oak Ridge National Laboratory), T. Hinoki, H.C. Jung, J.S. Park, and S. Konishi (Kyoto University), and M. Ferraris (Politecnico di Torino)

OBJECTIVE

This work was intended to identify appropriate test method and specimen geometry, determine the effect of specimen size on apparent joint strength, and provide recommendation for a miniature specimen test scheme for silicon carbide joint strength in support of future neutron irradiation experiments. In the present report, recent development with regard to torsional shear strength evaluation is specifically discussed.

SUMMARY

Status of research and development of joining technology for silicon carbide-based ceramics and composites was surveyed and briefly summarized in terms of mechanical properties and anticipated stability in radiation environment. Several techniques which may be viable for joining silicon carbide-based materials for fusion and nuclear services were identified.

Test methods appropriate for testing shear properties of silicon carbide joints, including testing of neutron-irradiated specimens, was studied and identified. Torsional shear of solid cross-section specimens with hourglass-shaped fillet sections was selected as the method to be employed in the irradiation study in US-Japan TITAN program. Several miniature test specimen geometries were examined both by finite element analysis and by experiment. Joint specimen with a <~5 mm-diameter joint section and square grip sections was identified acceptable for the initial irradiation campaign. A few issues associated with the use of small and non-ideal geometry specimens were identified and adequately addressed.

PROGRESS AND STATUS

Introduction

Research and development of silicon carbide-based ceramics and composites for fusion energy are progressing from fundamental viability study to utilization technology development [1]. However, joining these materials is a significant challenge for their application in intense radiation environment anticipated [2]. Due to the lack of reliable and proven joining method developed so far for silicon carbide-based materials, mechanical/component designs for near-term applications such as flow channel insert in liquid metal blankets are avoiding the joining requirement [3]. However, if a reliable joining technology is readily available, that would provide substantially enhanced design flexibility. For long term application such as structural walls and coolant piping in blanket body, it is highly probable that silicon carbide-based components have to be joined each other and/or with other materials with robust, radiation-stable, and chemically compatible techniques [4]. Moreover, development of such techniques will greatly benefit other nuclear applications of silicon carbide-based materials, including fuel cladding for advanced light water reactors and gas-cooled thermal and fast spectrum reactors, and control rod structures in high temperature gas-cooled reactors.

This work was intended to survey the present status of joining research and development for silicon carbide-based materials for fusion energy, and to identify appropriate test method and specimen geometry, determine the effect of specimen size on apparent joint strength, and provide recommendation for a miniature specimen test scheme for silicon carbide joint strength in support of screening neutron irradiation campaign. In the present report, recent development with regard to torsional shear strength evaluation is specifically discussed.

R&D Status of Silicon Carbide Joining

Joining techniques presently considered promising include diffusion bonding using various active fillers [5], transient eutectic phase routes such as nano-infiltration and transient eutectic-phase (NITE) process [6, 7], selected area chemical vapor deposition [8], glass-ceramic joining [9, 10], reaction bonding [2, 11], and preceramic polymer routes [12]. Primary considerations specific to fusion application include resistance against neutron irradiation, mechanical properties such as strength and reliability during mechanical loading, compatibility of the processing condition with design requirement, and chemical compatibility with specific coolant, neutron breeder, or neutron multiplier. Techniques considered for the present study on silicon carbide to silicon carbide joining are summarized in Table 1. Several among these joining techniques are considered ready to proceed to a phase of neutron irradiation.

Table. 1. Potential methods for joining silicon carbide-based materials for radiation services.

Method	Typical strength	Anticipated radiation performance	On-going / recent R&D
Diffusion bonding w/ active metallic inserts	>~150 MPa shear	Good with adequate insert materials	NASA, Bettis, EU fusion
Transient eutectic-phase joining	~250 MPa tensile	Good with process optimization	Kyoto U., Dresden, etc.
Glass-ceramics Joining	~250 MPa flexural	Positive experimental result from EU Extremat program	POLITO
Brazing	N/A	Generally poor High induced activation	Snecma, ENEA, etc.
Reaction bonding (SiC+Si)	~200 MPa shear	Unstable due to residual silicon	NASA
Reaction bonding (TiSiC)	N/A	Unknown	PNNL
Polymer joining	~10 MPa shear	Unstable due to residual oxygen and nano-crystalline phase	PNNL, etc.
Transient Liquid Phase Metal Joining	N/A	Unknown	POLITO
Selective area CVD	N/A	As good as CVD SiC	U.Conn, etc.

Development of Miniature Specimen Test Technique

One of the difficult situations faced by the development effort for ceramic joints is the general lack of standard test methods which allow acquisition of mechanical properties data in a reliable and reproducible manner using specimens which are not prohibitively difficult and/or expensive to prepare . For example, simple methods of cantilever shear, double-notched shear, and asymmetric four point flexure are most frequently adopted for shear strength determination of ceramic joints. However, as shown in Table 2, which lists the methods applicable for shear properties evaluation of ceramic joints, none of those tests is able to produce reasonably pure shear stress state within the joint and the interfacing volumes which allows dependable determination of shear strength. Among the test methods shown in Table 2, only the Iosipescu shear, torsion, and V-notched rail shear tests enable the pure shear stress state in test specimens. It is highly preferred that one of such test methods is adopted in a consistent manner to enable meaningful comparison of joint properties from different processing techniques and before and after neutron irradiation.

Table 2. Methods of shear properties evaluation available for ceramic joints.

Method		ASTM Std.	Common for ceramic joint test	No severe flaw in stress state	Miniature specimen applicable	Remote testing practical
Short beam shear		D 2344	√			√
Lap shear		C 961				√
Iosipescu shear		D 5379	√	√		√
Off-axis tensile shear		D 3518			√	√
Rail shear		D 4255	√			
Cantilever shear		D 905	√		√√	√
Sandwich shear		C 273	√		√	√
Double-notched shear		D 3846	√		√	√
Torsion of thin tube		D 5448	√	√		√
Torsion of solid rod		F 734	√	√	√ √	√
Asymmetric four point		C 1469	√		√	√
V-notched rail shear		D 7078	√	√		
Off-axis Brazilian					√ √	√

Applicability of small specimens is a critical requirement in addition to the acceptable stress state. The requirement of small specimens is imposed by 1) the fact that the internal volume available in irradiation vehicle is generally very limited: in other words irradiating large specimens is more expensive and often cost-prohibitive, and the improved statistical quality by increased number of tests is often more beneficial for the same total specimen volume, and 2) the fact that the use of smaller specimens reduces the radioactivity, increasing flexibility of test procedures/techniques and reduces radiological concerns

associated with post-irradiation examination. Simple and robust test procedures are also preferred due to the same radiological reason, while other general benefits are obvious.

Above considerations eliminate Iosipescu and V-notched rail shear tests from the list of adequate methods for irradiated ceramic joints, although they may be considered adequate for the purpose of engineering data acquisition later for the purpose of materials qualification and database generation. Torsion of thin tube is also eliminated because preparation and handling of specimens involving thin-walled joint sections in miniature geometry is excessively challenging. By elimination, it is determined that torsion of solid specimens is the appropriate test method for post-irradiation shear properties of joints of silicon carbide-based materials.

The optimization of torsional specimen size and geometry is currently underway by collaboration among Oak Ridge National Laboratory, Kyoto University, and Politecnico di Torino. Figure 1 shows some of the miniature test sample geometries and dimensions which are being used for the preliminary study on the specimen size effect and considered for the irradiation study. The irradiation experiment currently under preparation in the US-Japan TITAN collaboration is supposed to be conducted using the rabbit capsules in High Flux Isotope Reactor of Oak Ridge National Laboratory, typically allowing interior volume of ~6 mm x ~6 mm X ~50 mm per capsule. Therefore, the largest specimen sizes are those with 6 mm x 6 mm grip cross-sections.

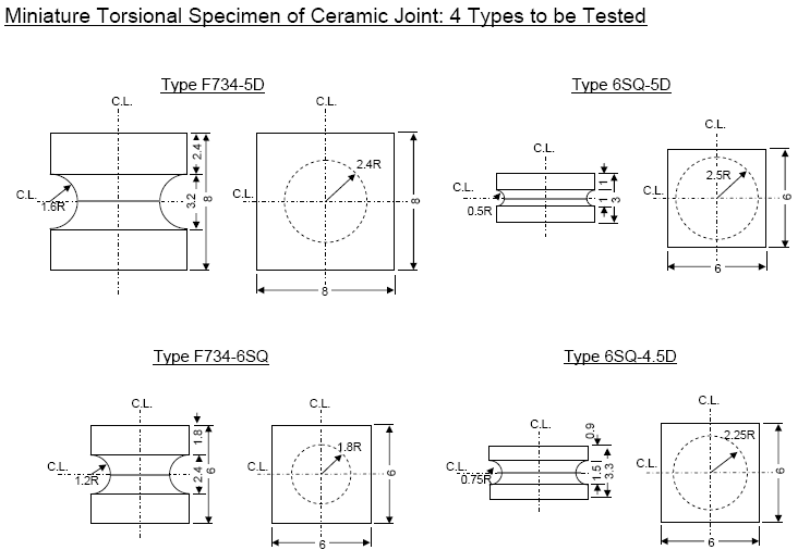

Fig. 1. Examples of miniature specimen geometries and dimensions for torsional testing of ceramic joints.

The potential drawbacks and associated issues for the miniature torsional specimens with very short fillet section length and polygonal grip sections are summarized: 1) non-linear stress distribution within the joint

layer with regard to the distance from torsional axis, 2) periodic variation of stress magnitude along the circumference due to the effect of grip shape, and 3) non-explicit correlation between the true and the

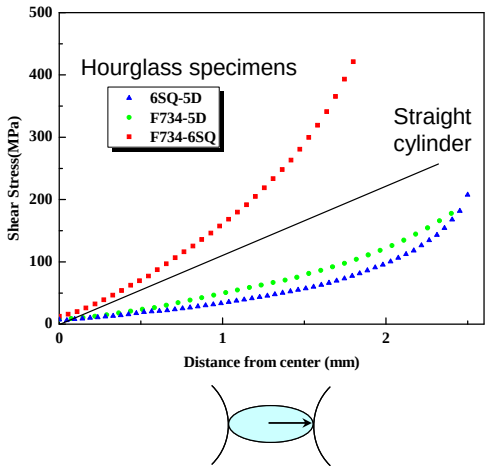

analytical maximum shear stresses due to 1 and 2.

Fig. 2. The influence of specimen geometry on radial distribution of shear stress magnitude within joint layer of torsional specimen.

Figure 2 depict the influences of fillet geometry on the radial distribution of shear stress in the joint layer calculated using a finite element model. The straight line indicating the ideal linear relationship between the stress magnitude and the distance from the torsional axis is for the case of straight rod specimen. In that case, the maximum shear stress that occurs at the specimen edge can be analytically derived as

$$\tau_{th} = 16T/\pi d^3 \qquad (1)$$

where T = applied torque and d = specimen (fillet) diameter. Clearly, stress distribution in the specimens with hourglass-shaped fillet sections deviates from linearity as the radial location approaches surface of the specimens. Such trend is apparent for the case of specimen geometry “F734-5D” and “F734-6SQ,” both based on ASTM Standard F734, and is more pronounced for the specimen geometry “6SQ-5D” which is with substantially smaller fillet curvature radius. The result indicates that a) the larger fillet curvature radius is preferred to minimize the stress distribution non-linearity, and b) true stress shall be determined based on finite element analysis rather than using the analytical equation, Eq. 1.

In Fig. 3, left, the influences of grip section geometry on the circumferential distribution of shear stress as calculated using a finite element analysis are presented. The circumferential stress distributions in specimens with square (black), octagonal (red), and circular (green) grip sections are compared for the same fillet curvature radius of 0.5 mm, indicating substantial (~±10%) stress variation for the case of square grip. Such circumferential variations in shear stress are believed to be caused by the fact that torque is transferred from the sockets to specimen only at the corners of the polygonal grip sections, when

rigid specimen is held in rigid sockets with a certain gap between them. Additional finite element analysis, result is shown on right, indicates that the circumferential stress variation can completely be mitigated when compliant filler material is inserted between the specimen and the sockets without leaving a space.

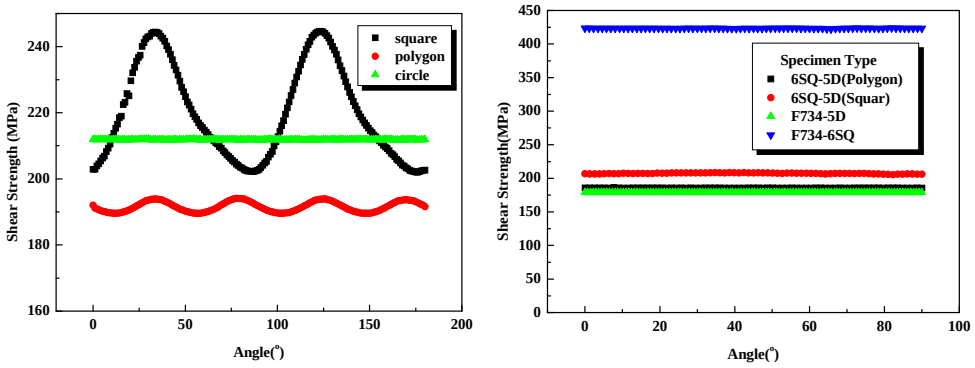

Fig. 3. The influences of geometry of grip section (left) and compliant socket insert (right) on circumferential distribution of shear stress in torsional joint specimens.

A torsional test instruments were developed and an experiment using it has been initiated at Kyoto University. The experimental setup, shown in Fig. 4, consists of the torsional loading mechanism driven by a universal mechanical test frame.

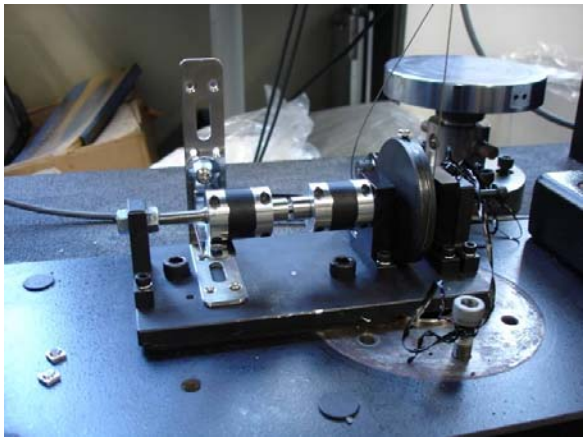

Fig. 4. Appearance of the miniature torsion test setup at Kyoto University.

Figure 5 shows the result of preliminary torsional shear test using the developed test setup and miniature specimens of chemically vapor-deposited silicon carbide (CVD SiC) joined with NITE™ joint. This result is considered to be showing incorrect strength of the NITE joint because the fracture appeared to be always initiating from within the base material. Moreover, the strength values shown are determined using Eq. 1, implying that the true shear strength is substantially higher. Nevertheless, the difference in apparent strength between two specimen types looks fairly reasonable considering the difference in extent of radial stress non-linearity.

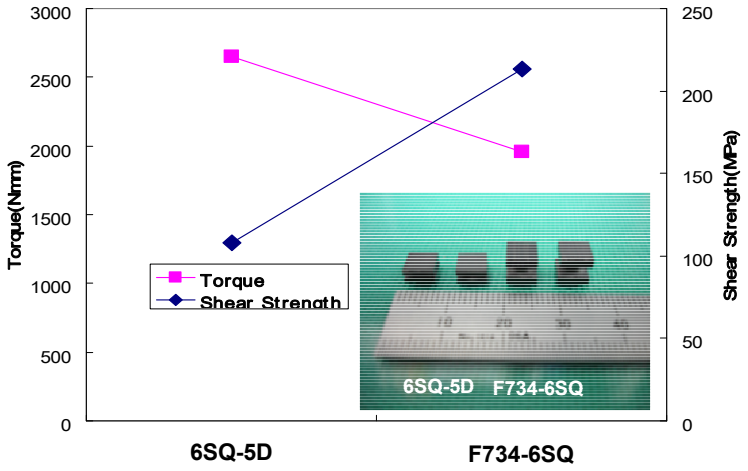

Fig. 5. Preliminary result of torsional strength test at room temperature using two different specimen types of NITE joint of CVD SiC. See text about evaluation of measured strength values.

References

1. Katoh, Y., et al., *Current status and critical issues for development of SiC composites for fusion applications.* Journal of Nuclear Materials, 2007. **367-370**: p. 659-671.
2. Lewinsohn, C.A., et al., *Joining of silicon carbide composites for fusion energy applications.* Journal of Nuclear Materials, 2000. **283**: p. 1258-1261.
3. Morley, N.B., et al., *Recent US research and development for the dual coolant blanket concept.* Fusion Engineering and Design, accepted.
4. Raffray, A.R., et al., *Design and material issues for high performance SiCf/SiC-based fusion power cores.* Fusion Engineering and Design, 2001. **55**(1): p. 55-95.
5. Cockeram, B.V., *Flexural Strength and Shear Strength of Silicon Carbide to Silicon Carbide Joints Fabricated by a Molybdenum Diffusion Bonding Technique.* Journal of the American Ceramic Society, 2005. **88**(7): p. 1892-1899.
6. Hinoki, T., et al., *Development of joining and coating tehnique for SiC and SiC/SiC Composites utilizing NITE processing.* Ceramic Engineering and Science Proceedings, 2005. **26**(2): p. 399-405.
7. Lippmann, W., et al., *Laser joining of silicon carbide—a new technology for ultra-high temperature resistant joints.* Nuclear Engineering and Design, 2004. **231**: p. 151-161.
8. Harrison, S. and H.L. Marcus, *Gas-phase selective area laser deposition (SALD) joining of SiC.* Materials and Design, 1999. **20**(2-3): p. 147-152.
9. Katoh, Y., et al., *Microstructure and mechanical properties of low-activation glass-ceramic joining and coating for SiC/SiC composites.* Journal of Nuclear Materials, 2000. **283**: p. 1262-1266.
10. Ferraris, M., et al., *Joining of machined SiC/SiC composites for thermonuclear fusion reactors.* Journal of Nuclear Materials, 2008. **375**: p. 410-415.
11. Lewinsohn, C.A., et al., *Silicon-Carbide-Based Joining Materials for Fusion Energy and Other High-Temperature Structural Applications.* Ceramic Engineering and Science Proceedings, 2001. **22**(4): p. 621-626.
12. Henager, C.H., et al. *Coating and joining for SiC/SiC composites using preceramic polymers*. in *The Sixth IEA International Workshop on SiC/SiC Ceramic Composites for Fusion Applications*. 2004. Boston, Massachusetts, USA.

CONCENTRIC RING ON RING TEST FOR UNIRRADIATED AND IRRADIATED MINIATURE SIC SPECIMENS - S. Kondo, Y. Katoh, and L.L. Snead (Oak Ridge National Laboratory)

OBJECTIVES

The objectives of this paper are to report on the development and qualification of a equibiaxial flexural strength test for miniature thin SiC samples, and obtain strength data of SiC irradiated at very high temperatures (>1100˚C).

SUMMARY

The flexure strength of miniature disk specimens was evaluated for both the unirradiated and irradiated CVD SiC by equibiaxial flexural test, where a disk specimen was supported on a ring and centrally loaded with a smaller loading ring. The obtained mean flexural strength and Weibull modulus were σ_f = 352 MPa and m = 5.0 for unirradiated specimen, respectively. Both of them are relatively smaller than the typical values of uniaxial tests such as 4 point bend test previously reported. However, no stress magnification at the loading ring, which is often concerned in the biaxial tests for the disk specimens, was indicated by the observation of fracture patterns. Above the irradiation temperature of 1100˚C, the flexural strength is almost same as the unirradiated values or slightly decreased at 1500˚C in contrast to the strengthening observed previously at 300-800˚C. It is clearly seen that the smooth cleavage of large grains were frequently observed in the sample irradiated at 1500˚C comparing to specimens irradiated at 1100˚C. A substantially lower population of finer defect clusters such as loops, vacancy, and vacancy clusters may be attributed to the inhibition of the strengthening at the higher irradiation temperatures. Although, many factors, such as the effective flaw populations subject to stress, may influence the relation between equibiaxial and uniaxial strength of ceramics, the simple and rapid procedure of the ring-on-ring test may be favored for the study on irradiation effects on the mechanical properties of SiC.

PROGRESS AND STATUS

Test apparatus

Although miniaturized disk specimens have been used for the post-irradiation mechanical tests, the stress concentrations associated with specific loading configurations such as ball-on-ring tests can be a significant problem for most ceramics because the fracture strength greatly depends on the effective loading area/volume and statistical distribution of the potential fracture origins. The equibiaxial flexural test in a ring-on-ring configuration, where a disk specimen on a support ring is loaded with a smaller coaxial loading ring, is often utilized to mitigate the stress concentration issues. For thin, high elastic modulus/strength (E/σ) ratio specimens, the uniform maximum stress occurs within the central region bounded by the loading ring.

In this study, the loading and supporting rings were designed to utilize miniature disk specimens in accordance with ASTM C1499-05 (Standard Test Method for Monotonic Equibiaxial Flexural Strength of Advanced Ceramics at Ambient Temperature [1]) as shown in Fig. 1. The equibiaxial stress is calculated as follows:

$$\sigma_f = \frac{3F}{2\pi h^2}\left[(1-\nu)\frac{D_S^2 - D_L^2}{2D^2} + (1+\nu)\ln\frac{D_S}{D_L}\right] \quad (1)$$

, where F [N] is the applied load, h [mm] is the specimen thickness, D_S [mm] is the supporting ring diameter, D_L [mm] is the loading ring diameter, D [mm] is the sample diameter, and ν is Poisson's ratio

(Test Method ASTM C1259). Both the outer diameter of loading and supporting fixtures is designed to be same as the specimen diameter for ease of alignment. No compliant layer, which is sometimes used to eliminate a stress concentration and frictional stress at the rings, were used for the present study. Alternatively, industrial lubricant was applied to the ring tips. The displacement rate was set at 0.1 mm/min. The crack patterns and fracture surfaces were examined after the tests.

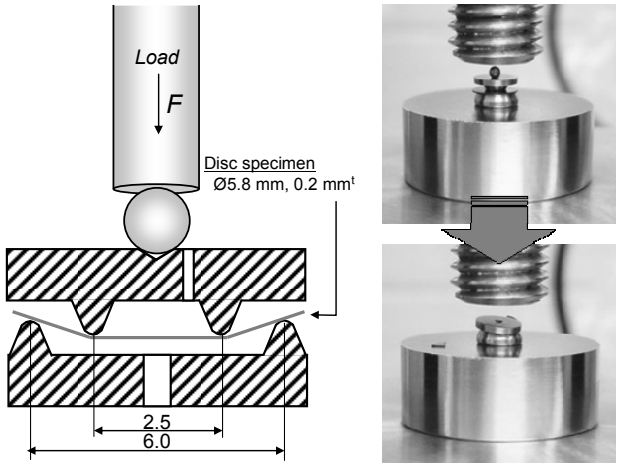

Fig. 1. Schematic and photos of concentric ring-on-ring test apparatus.

Materials

The material used for this work was poly crystalline β-SiC which was produced by chemically vapor deposition by Rohm and Haas Advanced Materials (Woburn, Massachusetts) [2]. The CVD material is extremely pure, with typical total impurity concentration of less than 5 wppm. The grain size is between 5 and 10 μm in the plane parallel to the deposition substrate, with the grains elongated in the <111> growth direction perpendicular to the substrate. The material is typically free of micro cracks or other large flaws, but atomic layer stacking faults on the {111} planes are common. There is no porosity in CVD SiC, and the material is generally considered to be of theoretical density (approximately 3.21 g/cm^3).

For the unirradiated case, 23 specimens, which were machined and polished in the same manner as described below for the irradiated samples, were tested. In addition to the unirradiated specimens, specimens irradiated in the High Flux Isotope Reactor at Oak Ridge National Laboratory were tested. The fluence for the specimen studied here ranged from 5.1 × 10^{25} to 9.7 × 10^{25} n/m^2 (E>0.1 MeV). Irradiation temperatures were 1100, 1300, and 1500˚C, which were estimated by post-irradiation viewing of melt wires inserted in both ends of each sub-capsule. Specimens of 5.8 mm diameter with 3.2 mm thickness were sliced into thin disks and lap finished aiming to ~200 μm thickness with 3 μm diamond suspension for both the surfaces. A minimum of 10 test specimens tested validly is, normally, required for the purpose of estimating a mean biaxial flexural strength. For the estimation of the Weibull parameters, a minimum of 30 test specimens validly tested is recommended. However, only 5 to 6 specimens were tested in the case of post-irradiation experiment. Therefore, the Weibull statistical analysis was not conducted for the irradiated specimens.

Results and discussion

Unirradiated SiC

The equibiaxial stresses are plotted as a function of the specimen thickness in Fig. 2, where the mean flexural stress is 352 MPa (Weibull mean; 357 MPa) and the standard deviation is 73 MPa. Although, the thicknesses of thin disks were varied in the range of 155-246 μm for unirradiated specimens, there was no evidence to prove a relation between the flexural stress and the thickness. The lowest flexural stress of 254 MPa was obtained for the specimen with 204 μm in thickness and the highest of 573 MPa was obtained for the specimen with 208 μm thickness. The significant scattered data points were generally found in a higher stress region as shown in Fig. 2. The edges of some specimens were slightly chipped, whereas the edge chip seemed not to affect the flexural strength in the present study.

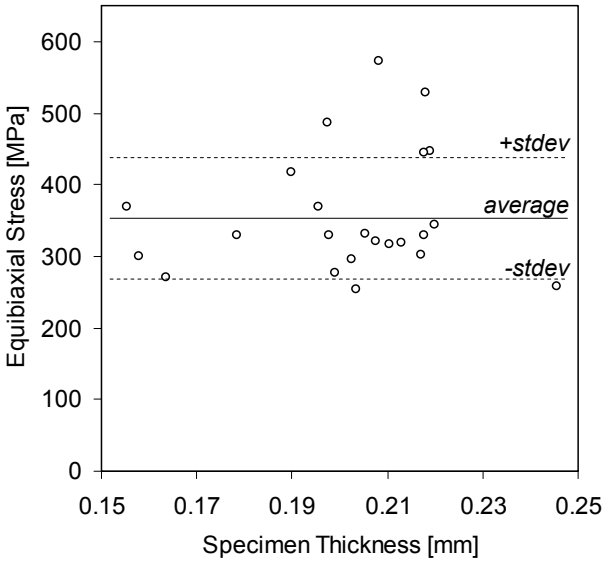

Fig. 2. Equibiaxial strength of unirradiated CVD SiC.

The room-temperature failure strength of β-SiC have been well reviewed in [3], which were mostly obtained by uniaxial and ring-compression tests and varied from 200 to over 3100 MPa. The failure strength of SiC particles is quite larger than that of the SiC bulk form. Such a large variation is due primarily to the specimen size effect. It is well known that the strength at the inner weakest flaw determines the overall strength of the brittle materials. The flaw population and distribution are strictly dependent on its volume as expressed by the Weibull distribution function. Byun et al. [4] investigated the size effect on tensile hoop strength for tubular alumina specimens using the internal pressurization and diametrical loading test techniques. A major conclusion in his work is that the failure strength of the tubular brittle specimens can be determined by the effective surface area rather than the volume [5]. Therefore, the strength obtained in the present work is strongly depended on the surface finish of the tension side. The likely thickness independent fracture strength indicates that the samples studied here were thick enough to avoid stress magnification at the loading ring. If the sample thickness is too small, the stress magnification and resultant localized deformation at the loading ring may occur due to the deviation from a linear relationship between load and displacement [6]. Although, many factors, such as the effective flaw populations subject to stress, may influence the relation between equibiaxial and

uniaxial strength of ceramics, the simple and rapid procedure of the ring-on-ring test may be favored for the study on irradiation effects on the mechanical properties of SiC.

In Fig. 3, Weibull stastical plots of the flexural strength of unirradiated samples are shown. The Weibull modulus of SiC at room-temperature is reported to be widely ranged from 2 to 12, depending on the condition of the SiC material [3]. The high Weibull modulus (m = 7–11) was often measured by the flexural and tensile tests, while the lower values (m = 3–9) were obtained in the ring compression test. Cockeram [7] assumed that the flaw distributions were quite different between a flexural bar and a small tubular (ring) specimen. The lower m values obtained by the ring compression test were therefore considered primarily as a consequence of the changed flaw distribution. Additionally, irregularity of the ring specimen [8] or surface roughness [4] would make a significant impact on the failure probability. The obtained Weibull modulus of 5.0 for the present study is within the data band of ring compression tests and is below the data band of tensile test results. More than one failure mechanism may be involved for the ring-on-ring tests because the array of plots in Fig. 3 has an upward knee.

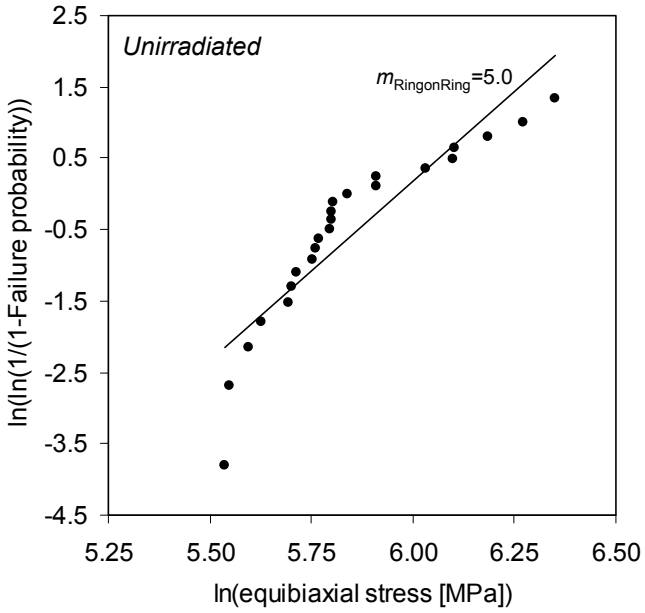

Fig. 3. Weibull plots of flexural strength of unirradiated CVD SiC.

Fractographic examination of the test specimens is recommended to determine the location of test specimen fracture [9]. Typical examples of the fracture patterns at the tensioned surface are shown in Fig. 4, where the possible contact lines of the supporting and loading rings are indicated as dotted circles. The fracture initiated likely in the area bounded by loading ring or just inside the loading ring in all samples, though the difference of the complexity of the fracture patterns were observed depending on the strength. For high strength case as Fig. 4 (a), primary crack plane is located near center line of the circular sample and significant flaw branching were observed. For intermediate strength case as Fig. 4 (b), likely crack origin was generally located near the center. These support that the successful avoidance of the stress magnification at the loading ring as stated above in the most cases. For low strength case as Fig. 4 (c), however, the primary crack was initiated just inside the loading ring, and samples were divided into only 4-5 pieces. This indicates that the results showing lower strength might be attributed to the stress magnification near the loading ring rather than the being of relatively large surface flaws that can be

uniformely distributed at the disk surfaces. The misalignment of the test fixtures and the sample may be suspected as one of the primary cause of the stress magnification, if any.

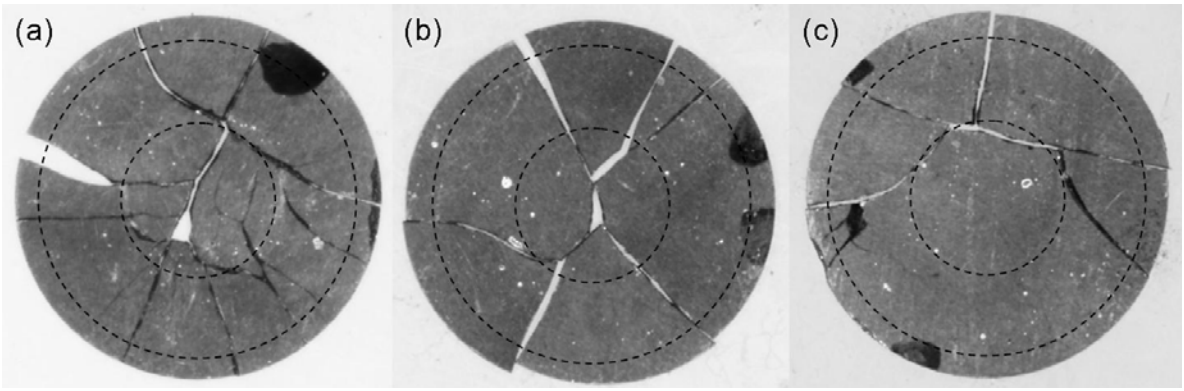

Fig. 4. Typical fracture patterns at the tensioned surface of unirradiated specimens showed a flexural strength of ; (a) σ_f = 573 MPa,(b) σ_f = 321 MPa, and (c) σ_f = 270 MPa.

Table 1 Irradiation conditions and test results

Sample ID	Irradiation Temperature	Irradiation Fluence	Mean Thickness	Mean Equibiaxial Stress	Std. Dev.	% Change	Weibull Modulus	Number of samples
	[degree C]	[dpa]	[mm]	[MPa]	[MPa]	[%]		
unirrad.	-	0	0.202	357	87	-	5.0	23
m14	1100	7.0	0.195	329	100	-7.8	-	6
m56	1300	5.1	0.205	345	61	-3.4	-	5
m20	1500	9.7	0.198	279	42	-22	-	5

Irradiated SiC

The irradiated flexural strengths normalized to unirradiated values are plotted with neutron data reported previously as a function of irradiation temperature in Fig. 5. Above 1100˚C, the flexural strength is almost same as the unirradiated values or slightly decreased at 1500˚C. Since the strength of irradiated SiC is strongly dependent on the form of the material tested, results except for pyrolytic β-SiC are excluded from the comparison. For all the case except for the present results, the values are for Weibull's mean with error bars indicating ±1 Weibull's standard deviation [10-13]. The irradiation-induced strengthening is statistically observed at 300-800˚C. The substantial increase of fracture energy was found to be primary cause of the strengthening [14]. The formation of strength peak was attributed to the reduction of the Young's modulus accompanied by point-defect swelling (lattice expansion) [14], which was generally observed in irradiated SiC at 300-800˚C [15]. The increase in effective fracture energy is probably due primary to the dense nano-sized defect clusters [16] such as interstitial-type faulted loops formed on {111} family planes, though the fracture energy increase may be attributable to the combined effect of a number of mechanisms operating simultaneously. Meanwhile, the damage microstructure above ~1000˚C was characterized by both the voids and much larger interstitial type faulted loops in contrast to the smaller defects densely formed below 1000˚C [17]. The significant reduction in the population of

irradiation-induced finer defects may prohibit the increase in fracture strength in addition to the less lattice expansion.

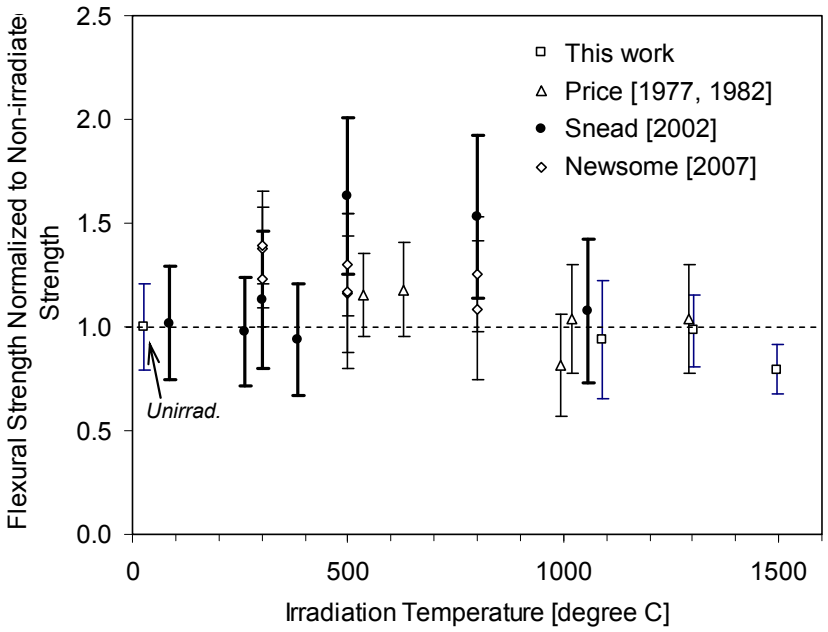

Fig. 5. Effect of irradiation temperature on normalized flexural strength of CVD SiC.

Fracture surfaces of a couple of samples tested were examined for each irradiation condition by scanning electron microscopy as typically shown in Fig. 6; irradiation temperature of 1000˚C for (a), and 1500˚C for (b), where tensioned surfaces are located on the upper side of the SEM images. In each case, fracture likely initiated at relatively large surface flaws indicated by black arrows. It is clearly seen that the smooth cleavage of large grains were frequently observed in the sample irradiated at 1500˚C as shown in Fig. 6 (b) compared to Fig. 6 (a). The same tendency of the frequent cleavage has been reported to be observed in bend-tested SiC without irradiation [14]. It has been also stated in [14] that the irradiation might increase the cleavage energy by the irradiation toughening and the Weibull modulus reduction at the irradiation temperatures ranging 300-800˚C. At 1500˚C, however, this mechanism may not be applicable because of the significant reduction of the defect cluster density. Fracture toughness and Young's modulus obtained by micro Vickers and nano-indentation techniques, respectively, were reported to be almost unchanged by the neutron-irradiation above 1100˚C. Therefore, it may be concluded that the modification of fracture energy by high temperature irradiation is also minimal for SiC as stated earlier. It suggests that the void-crack interaction, which has been observed by transmission electron microscope [18], also very limited in irradiated SiC. Furthermore, the array of voids with {111} facets, which is preferentially formed at stacking faults, may modify the fracture energy at the cleavage plane observed. Any significant differences of fracture patterns from unirradiated samples were not observed as shown in Fig. 7. It was confirmed that the ring-on-ring configuration may applicable to both the irradiated and unirradiated miniature SiC specimens. However, the sufficient number of samples to statistical analysis is strongly recommended for obtaining clear understanding of the irradiation effects due to the complex fracture mechanisms.

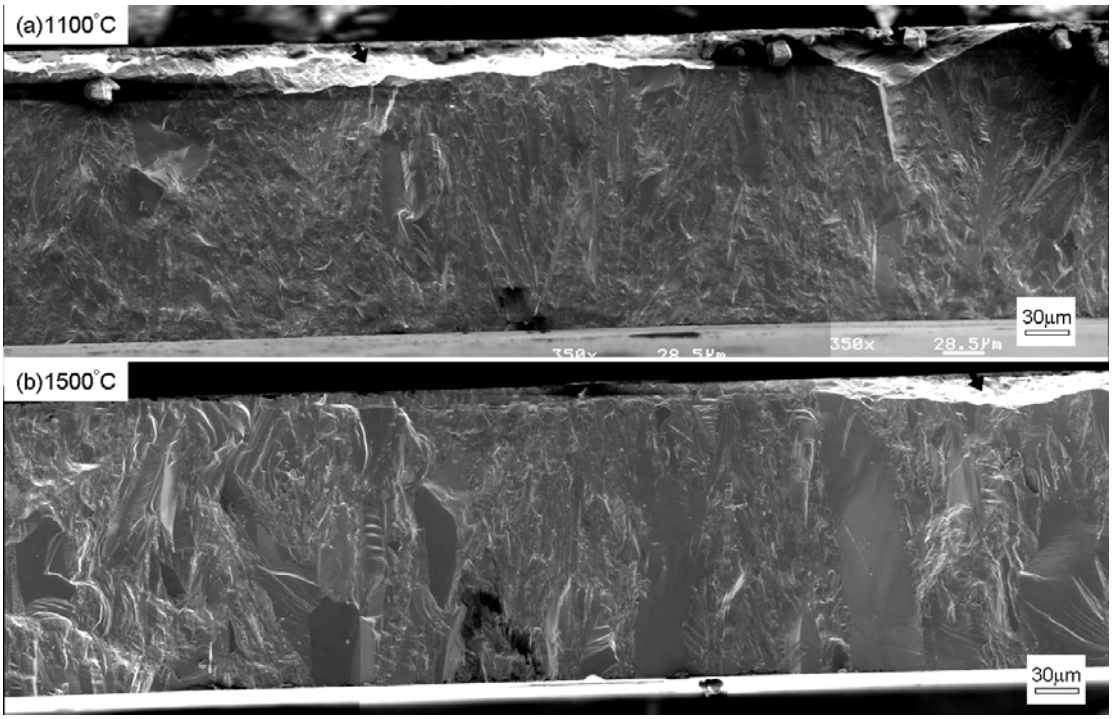

Fig. 6. Scanning electron microscope images of the fracture surface of the samples irradiated at (a) 1100˚C, and (b) 1500˚C.

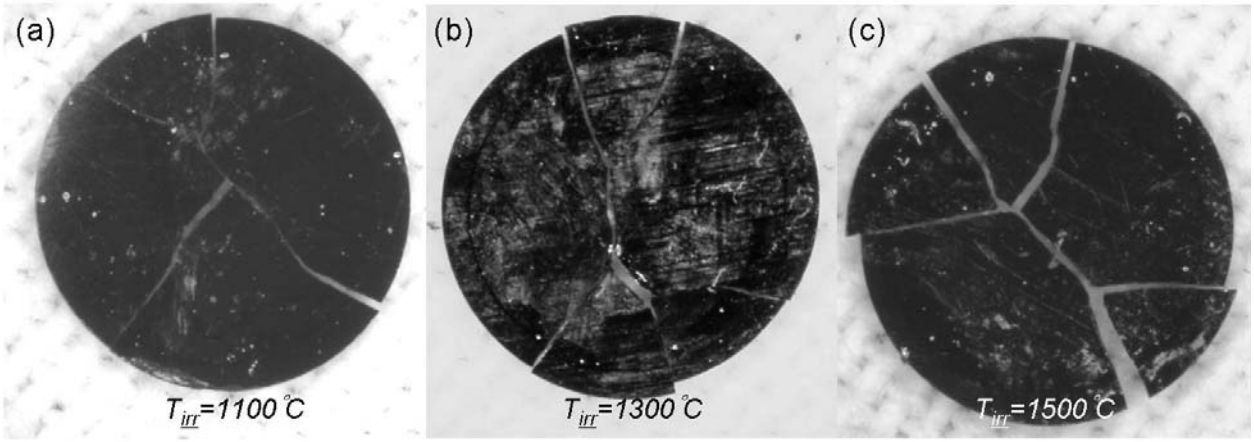

Fig. 7. Typical fracture patterns at the tensioned surface of unirradiated specimen; (a) T_{irr}= 1100˚C, σ_f = 314 MPa, (b) T_{irr}= 1300˚C, σ_f = 339 MPa, and (c) T_{irr}= 1500˚C, σ_f = 313 MPa.

References

[1] ASTM C 1499-05
[2] http://www.cvdmaterials.com/
[3] L.L. Snead, T. Nozawa, Y. Katoh, T.S. Byun, S. Kondo, D.A. Petti, J. Nucl. Mater. 371 (2007) 329-377.
[4] T.S. Byun, E. Lara-Curzio, R.A. Lowden, L.L. Snead, Y. Katoh, J. Nucl. Mater. 367-370 (2007) 653-658.
[5] Report CEGA-002820, Rev. 1 (July 1993).
[6] J.W. Kim (Private communication).
[7] B.V. Cockeram, J. Am. Ceram. Soc. 85 (2002) 603.
[8] K. Minato, K. Fukuda, K. Ikawa, J. Nucl. Sci. Technol. 19 (1982) 69.
[9] ASTM C 1322
[10] R. Price, Nucl. Technol. 35 (1977) 320-336.
[11] R.J. Price and G.R. Hopkins, J. Nucl. Mater. 108&109 (1982), 732-738.
[12] L.L. Snead, T. Hinoki, Y. Katoh, Report DOE/ER-0313/33 (2002).
[13] G. Newsome, L.L. Snead, T. Hinoki, Y. Katoh, D. Peters, J. Nucl. Mater. 371 (2007) 76-89.
[14] Y. Katoh, L.L. Snead, J. ASTM Intl. Paper ID JAI12377.
[15] Y. Katoh, H. Kishimoto, A. Kohyama, J. Nucl. Mater. 307-311 (2002) 1221.
[16] Y. Katoh, T. Hinoki, A. Kohyama, T. Shibayama, and H. Takahashi, Ceram. Eng. Sci. Proc. 20 (1999) 325-332.
[17] S. Kondo, et al., in proceedings of ICFRM-13, J. Nucl. Mater. (2008).
[18] F.W. Clinard, Jr., G.F. Hurley, R.A. Youngman, and L.W. Hobbs, J. Nucl. Mater. 133&134 (1985) 701-704.

A Comparison of Cavity Formation in Neutron Irradiated Nanostructured Ferritic Alloys and Tempered Martensitic Steels at High He/dpa Ratio – G.R. Odette, P. Miao, T. Yamamoto (Department of Mechanical Engineering, University of California Santa Barbara), D. J. Edwards, R Kurtz (Materials Science Division, Pacific Northwest National Laboratory) and H. Tanagawa (Japan Atomic Energy Agency)

OBJECTIVE

The objective of this work is to characterize the effects of high helium to dpa ratios (He/dpa) on irradiation induced microstructural evolutions in nanostructured ferritic alloys (NFA), in this case MA957, and to compare these results, to corresponding evolutions in normalized and tempered martensitic steels (TMS) at fusion relevant dpa rates.

SUMMARY

Microstructural evolutions in NFA under neutron-irradiation, at fusion relevant He/dpa ratios and dpa rates, were characterized using a novel in-situ $^{59}Ni(n,\alpha)$ reaction He-implanter technique. MA957 was irradiated at 500°C in HFIR to a nominal 9 dpa and 380 appm He. A high number density of ≈ 1 He-bubbles were observed. Comparisons of these results to the cavity structures in TMS F82H, described in a companion report [1], provide additional evidence that TMS may be susceptible to both low (fast fracture) and high (creep rupture) temperature embrittlement as well as void swelling at fusion relevant He concentrations, while NFA are much more resistant to these degradation phenomena.

PROGRESS AND STATUS

Introduction

Fusion neutron spectra produce ≈ 2000 appm He at 200 dpa, and the He/dpa ratio is even higher in spallation proton targets. Helium precipitates gas bubbles in the matrix and on dislocations, precipitate interfaces and grain boundaries [2]. Helium bubbles can act as formation sites for growing voids at lower irradiation temperature and creep cavities on stressed grain boundaries at high temperatures. Both 14Cr nanostructured ferritic alloys (NFA) and 9Cr tempered martensitic steels (TMS) are resistant, but not immune, to irradiation effects. For example, TMS are embrittled by irradiation hardening and grain boundary He at lower irradiation temperatures [3], and undergo significant void swelling at high He/dpa ratios in dual ion irradiations [4]. NFA are more resistant to irradiation damage at all temperatures. The irradiation damage resistance of NFA derives from their high sink densities, including stabilized dislocation structures, and large number of nm-scale Y-Ti-O enriched nanofeatures (NF) which trap He in small bubbles [2]. However, their overriding advantage is that NFA can operate at temperatures, up to 800°C, above the displacement damage-swelling regime [2]. At $T > 0.5T_m$, the primary irradiation damage issue is creep embrittlement due to accumulation of He on grain boundaries. The objective of this research is to characterize the transport, fate and consequences of He at spallation proton and fusion neutron relevant He/dpa ratios and dpa rates.

Experiment

A novel in-situ neutron irradiation He-implanter technique was used to characterize the effect of the He/dpa ratio on microstructural evolution in MA957, Eurofer97 [5,6] and F82H for irradiations in the High Flux Isotope Reactor (HFIR). Helium is uniformly implanted to a depth of 5 to 8 mm from thin NiAl coatings deposited on TEM discs. The He is produced by a two-stage thermal neutron (n_{th}) reaction sequence: $^{58}Ni(n_{th},\gamma)^{59}Ni(n_{th}, \alpha)$. The fast neutrons generate dpa at fusion relevant rates, and the corresponding He/dpa ratio can be easily adjusted from values of less than 1 to more than 50 appm He/dpa. The irradiated microstructure of MA957 [5] and Eurofer97 [6] and F82H irradiated in the HFIR JP26 experiment at 500°C to about 9 dpa and 380 appm He were characterized transmission electron microscopy (TEM). Eurofer97 was also characterized previously at ≈ 4.3 dpa and ≈ 90 appm He at 300 and 400°C.

Results

Previously published results showed a high density of $N_b \approx 3x10^{23}/m^3$ of very small $r_b \leq 1$ nm bubbles in MA957, primarily located on the NF interfaces [5]. A lower density $N_b \approx 1.5x10^{22}/m^3$ of larger $r_b \approx 4.3$ nm bubbles were found in companion TMS Eurofer97, along with even larger (>10 nm) faceted cavities, that are likely voids [5]. The NF are stable after a 9 dpa irradiation at 500 ºC and large bubbles do not form in the He implanted region of MA957. The estimated He contained in equilibrium bubbles was ≈ 130 appm in MA957, suggesting that N_b is underestimated, and ≈ 380 appm in Eurofer97, in agreement with the nominal amount. The bubble sizes decrease and number densities increase in Eurofer97 for irradiations at 400 and 300°C. Bubbles preferentially formed on dislocations in the TMS at all irradiation temperatures. Preliminary evidence suggests that loop formation in Eurofer97 is suppressed in the He implanted layer, compared to regions with low He [6].

The presence of a high number density of small bubbles in MA957 was recently confirmed, as shown in Figure 1a. These data are currently being quantified. As shown in Figure 1b, as in the case of Eurofer97, TMS F82H also show fewer ($\approx 1 \times 10^{23}/m^3$) and somewhat larger bubbles (2.0 nm) compared to MA957, along with what are likely polyhedral voids. Cold worked F82H had a slightly higher density of slightly smaller bubbles. The He bubbles are generally smaller and more numerous in F82H than in Eurofer97. The bubbles in F82H are estimated to contain about 340 appm He and are predominantly associated with dislocations and interfaces. Notably, Figure 1d shows that a boundary in F82H is highly decorated with small He bubbles, while a boundary in MA957, shown in Figure 1c, is relatively bubble free.

These preliminary observations strongly support the hypothesis that very high He concentrations can be managed in NFA. These studies are continuing, including comprehensive quantification of the irradiated alloy microstructures, as well as examination of additional alloys and irradiation conditions.

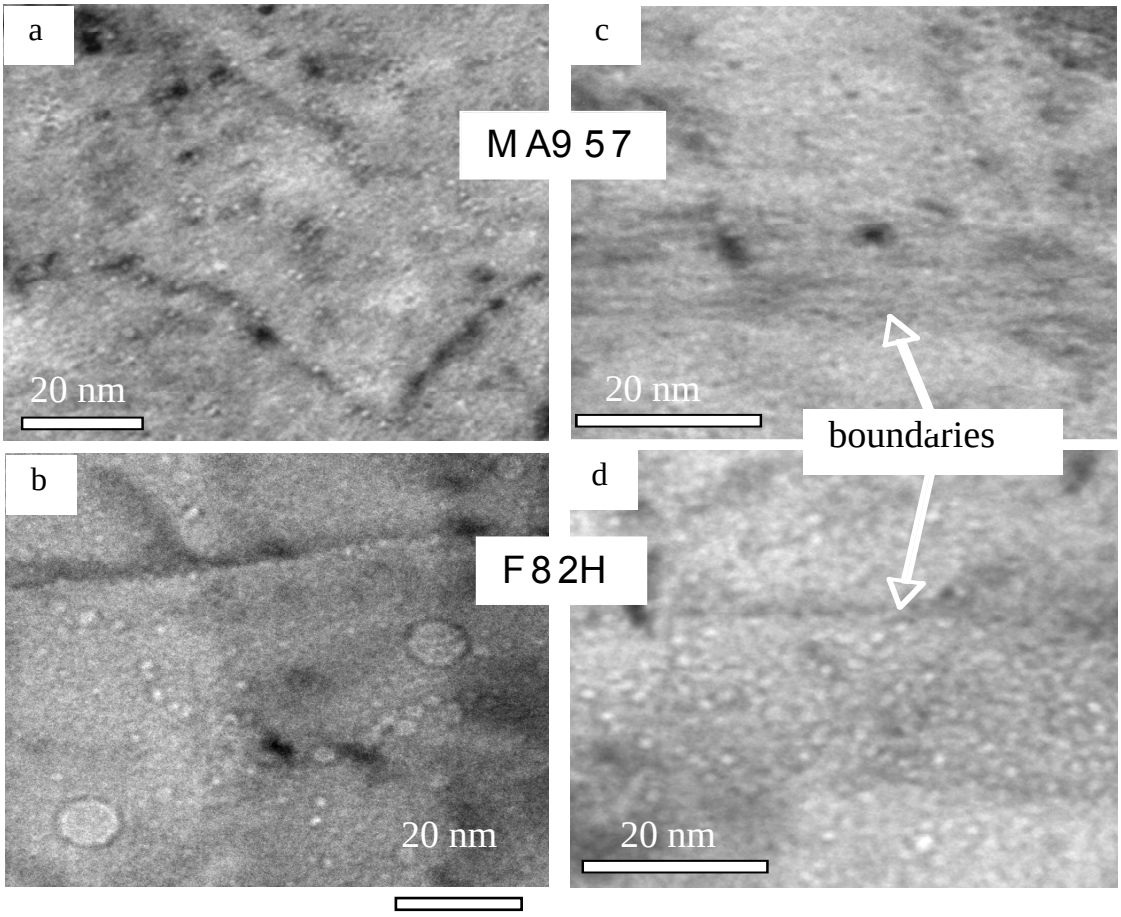

Figure 1 Cavity structures in NFA MA957 and TMS F82H: a and b) The (mostly) matrix cavities with smaller and more numerous bubbles in MA957 (a) compared to F82H (b); c and d) The boundary in F82H (d) has a high concentration of bubbles while the boundary in MA957 (c) is much cleaner.

Future Work

These results barely scratch the surface of what can be learned about the transport, fate and consequences of He using the in situ injection technique. Thus in addition to further characterization studies of the alloys and irradiation conditions described in this and previous publications, a major future effort will be directed at characterizing the large matrix of other alloys and irradiation conditions from the JP26 and JP27 experiments, that contained a total of ≈ 360 He injected TEM discs.

REFERENCES

1. T. YAMAMOTO, G. R. ODETTE, P. MIAO, D. J. EDWARDS AND R. J. KURTZ, Helium Effects on Microstructural Evolution In Tempered Martensitic Steels: In Situ Helium Implanter Studies In HFIR, this report

2. G.R. ODETTE, M.J. ALINGER, B. D. WIRTH, "Recent Developments in Irradiation Resistant Steels," Annual Reviews of Materials Research (in press)

3. T. YAMAMOTO, G.R. ODETTE, H. KISHIMOTO, J.W. RENSMAN, P.F. MIAO, "On the Effects of Irradiation on the Yield Stress Changes and Hardening and Non-hardening Embrittlement of 8Cr Tempered Martensitic Steels: Compilation and Analysis of Existing Data," *J. Nucl. Mater.* **356** 1-3 27-49 (2006).

4. K. YUTANI, H. KISHIMOTO, R. KASADA, A. KIMURA, "Evaluation of Helium Effects on Swelling Behavior of Oxide Dispersion Strengthened Ferritic Steels under Ion Irradiation," *Fusion Eng. Des.* **81** 1045 (2006).

5. T. YAMAMOTO. G. R. ODETTE, P. MIAO, D.T. HOELZER, J. BENTLEY, "The transport and fate of helium in nanostructured ferritic alloys at fusion relevant He/dpa ratios and dpa rates," *J Nucl. Mater.*, **367-370**, 399 (2007).

6. R.J. KURTZ, G.R. ODETTE, T. YAMAMOTO, D.S. GELLES, P. MIAO, B.M. OLIVER, "The transport and fate of helium in martensitic steels at fusion relevant He/dpa ratios and dpa rates," *J Nucl. Mater.*, **367-370**, 417 (2007).

HELIUM EFFECTS ON MICROSTRUCTURAL EVOLUTION IN TEMPERED MARTENSITIC STEELS: IN SITU HELIUM IMPLANTER STUDIES IN HFIR - T. Yamamoto, G. R. Odette and P. Miao (Mechanical Engineering Department and Materials Department, University of California, Santa Barbara), D. J. Edwards and R. J. Kurtz (Pacific Northwest National Laboratory)

OBJECTIVE

The objective of this work is to characterize the effects of high helium to dpa ratios (He/dpa) on irradiation induced microstructural evolutions in normalized and tempered martensitic steels (TMS) at fusion relevant dpa rates.

SUMMARY

Microstructural evolutions in TMS under neutron-irradiation, at fusion relevant He/dpa ratios and dpa rates, were characterized using a novel in-situ $^{59}Ni(n,\alpha)$ reaction He-implanter technique. F82H-mod3 was irradiated at 500°C in HFIR to a nominal 9 dpa and 190 or 380 appm He in both in the as-tempered (AT) and 20% cold-worked (CW) conditions. In all cases, a high number density of 1-2 nm He-bubbles were observed, along with a smaller number of larger faceted ≈ 10 nm cavities, which are likely voids. The He bubbles form preferentially on dislocations and various interfaces, including grain boundaries and at precipitates. A slightly larger number of smaller He bubbles were observed in the CW condition. The lower He/dpa ratio produced slightly smaller and fewer He bubbles. Estimates of the He content of the bubbles, assuming equilibrium capillary pressures, were in good agreement with the nominal implanted levels. Comparisons of these results to the cavity structures in nano-structured ferritic alloy (NFA) MA957, described in a companion report [1], provide additional evidence that TMS may be susceptible to both low (fast fracture) and high (creep rupture) temperature embrittlement as well as void swelling at fusion relevant He concentrations, while NFA are much more resistant to these degradation phenomena.

PROGRESS AND STATUS

Introduction

Predicting and mitigating the effects of a combination of large levels of transmutant He and displacement damage (dpa), produced by high energy neutrons, on the dimensional stability and mechanical properties of structural materials is one of the key challenges in the development of fusion energy. The fundamental overriding questions about He-dpa synergisms include: a) What are the basic interacting mechanisms controlling He and defect transport, fate and consequences, and how are they influenced by the starting microstructure and irradiation variables (dpa rate, He/dpa ratio, temperature and applied stress)? And, b) how can the detrimental effects of He-dpa synergisms be mitigated and managed by proper microstructural design?

We have previously demonstrated that in-situ He implantation in mixed spectrum fission reactor irradiations provides a very attractive approach to assessing the effects of He-dpa synergisms, while avoiding most of the confounding effects associated with Ni- or B-doping type experiments [2-4]. The basic idea is to use a thin Ni, B or Li-containing implanter layer to inject high-energy α-particles into an adjacent sample simultaneously undergoing neutron induced displacement damage. In this case, HFIR irradiations implant He uniformly to a depth of ≈ 5 to 8 μm from a μm-scale NiAl coating on TEM discs at a controlled He/dpa ratio 5 to 50 appm/dpa. The He implanted layer is sufficiently thick for low load Vickers microhardness and nanohardness measurements, as well as for making thinned specimens for extensive microstructural characterization by TEM, and potentially a variety of other techniques. We summarize here the results of microstructural characterization of TMS, F82H mod3 in both the as-tempered and 20% CW conditions for HFIR irradiations at 500°C to 9 dpa and 190 to 380 appm. These preliminary results focus on TEM characterization of the transport and fate of He in forming cavities (bubbles and voids) and the association of these cavities with dislocations and various interfaces.

Experimental Procedures

The TMS examined in this report is a high-Ta variant of F82H (so-called F82H-mod.3) [5]. The base chemical composition of F82H-IEA (nominally, 7.5%Cr 2%W 0.2%V 0.1%C 0.1%Si 0.02%Ta 60ppmN) was modified with high purification (14 ppm N and 0.001% Ti) and high 0.1% Ta [5]. The steel was austenitized at 1040ºC for 30 min, normalized (air-cooled), and tempered at 740ºC for 1.5 h. A wafer of the as-tempered (AT) F82H was also cold rolled to a 20% of thickness reduction. Three mm diameter, 0.2 mm thick TEM discs were irradiated in the HFIR JP26 experiment at 300, 400 and 500°C to produce a range of dpa and He/dpa for a large matrix of alloys, including the F82H conditions studied here. For the implantation studies, a thin NiAl intermetallic layer was electron beam co-deposited at the UCSB Materials Processing Laboratory on discs that were paired with adjacent uncoated discs. Nominal coating thicknesses of 1, 2 and 4 μm produced He/dpa ratios of 5, 20, and 40 at 9 dpa.

TEM specimens were prepared at PNNL using a cross-section thinning technique. This involved bonding the irradiated TEM discs between two half cylinders of Mo rod, and then slicing the composite rod to produce thin, 3-mm discs with a rectangular cross-section of the original irradiated disc in the center. Each composite disc was then dimple ground to thickness of ~100 μm centered on the implanted layer. The implanted region of the specimen foil was then thinned to electron transparency by ion milling with a Gatan Precision Ion Polishing System (PIPS). The PIPS was operated using a 5 keV ion beam in sector milling mode, meaning the ion milling was done only when the ion gun was perpendicular to the cross-section of the sample. This approach was found to offer the best chance of preserving the interface region between the NiAl layer and the TMS substrate. After the sample was thinned into the region of interest, a final ion polish was given using a 1.9 KeV ion beam for 20 minutes to remove any surface deposition of Ar. Microstructural examinations were performed on a JEOL 2010F instrument, operating at 200 KeV in transmission, with digitally recorded images. A variety of TEM imaging conditions were used, but the cavities were primarily characterized by the through-focus sequence method. Cavities appear as white regions surrounded by a dark ring in the under-focused condition (-512 to 1024 nm), as dark regions surrounded by white rings in the over-focused condition; the cavities are invisible in the focused condition.

Representative regions in the TEM micrographs, with a total area of ≈ 0.1 μm^2, were selected for detailed analysis of the cavity number densities and size distributions. The local foil thickness was measured by the convergent beam diffraction method. The grayscale micrographs were converted to black and white images. Cavities appear as white features on a black background. Image-J was used to determine cavity number densities and size distributions.

Results

All the irradiation and alloy conditions contained high concentrations of small cavities in the He-implanted regions. Figure 1a shows representative micrograph for the AT F82H implanted to 380 appm He (nominal He/dpa = 40 appm/dpa) imaged at a -768nm under-focus condition. The corresponding features identified as cavities by the through focus sequence examinations are shown in the white on black image in Figure 1b. Analysis of this, and other such images, showed that this irradiation condition produced ≈ $9.9 \times 10^{22}/m^3$ small bubbles with an average diameter of ≈ 1.7±0.8 (one standard deviation) nm. Figure 1 also shows much fewer but larger 10 nm scale polyhedral-faceted cavities. These features are almost certainly voids.

Note a bubble is defined as a near-equilibrium helium filled cavity, with a gas pressure $P_g \approx 3Z(P_g)mkT/4\pi r_b^3 \approx 2\gamma/r_b$ [6], where γ is the surface energy, r_b is the bubble radius, m is the number of He atoms in the bubble and $Z(P_g)$ is the compressibility factor (> 1) for high pressure He [6,7]. In contrast, voids are cavities that are unstably growing due to an excess flux of vacancies over self-interstitial atoms (SIA) flowing to them, arising from a bias of dislocation sinks for the SIA [7]. For a specified sink microstructure and irradiation condition, cavities grow as bubbles up to a critical helium content, m*, where they convert to growing voids, leading to bimodal cavity size distributions. Thus the incubation

dose, dpa_i, prior to the onset of rapid void swelling is governed by the requirement that a significant population of cavities reaches the m > m* condition. One corollary is that, for a given number of cavities, the incubation dose, dpa_i, scales inversely with the He/dpa ratio. Another corollary is, that at a specified He/dpa ratio, dpa_i scales with the number of bubbles. Further discussion of the elements of radiation damage resistance can be found in an Annual Review of Materials Research paper that will be published in 2008 [8].

Figure 1a also shows that visible dislocations are highly decorated with *string-of-pearls* like chains of bubbles. The dislocation bubble association is more clearly seen in Figure 1b, showing such chains in regions where dislocations are not observed in Figure 1a. In these cases, the dislocations may be invisible for the particular imaging condition, or they may have climbed away from previously attached bubbles. In either case, it is clear that a large fraction of the bubble population forms on dislocations. Figure 1 also suggests that the larger voids are associated with the chains of bubbles. If the dislocations are still attached, this observation suggests some interesting new physics of correlated bubble-void-dislocation evolutions that have not been considered previously.

Figure 2 shows the corresponding results for the CW F82H are generally similar. However, the bubbles are smaller and more numerous in this case, with a number density of $1.3x10^{23}/m^3$ and average diameter of 1.4±0.7 nm. Likewise, as expected, the AT F82H with a lower He content of 190 appm (nominal 20 appm/dpa) has fewer and smaller cavities, with number densities of $3.9x10^{22}$ and average diameters of 1.4±1.1 nm. Figure 3 summarizes the cavity size distributions in these three cases, clearly showing the bimodal bubble-void transition, especially for the lower He/dpa ratio ≈ 20 appm/dpa.

While the previous discussion has emphasized the dislocation-cavity (bubble and possibly void) associations, small bubbles are also observed on boundaries and matrix-precipitate interfaces. This is illustrated in Figure 4a and b showing under-focus cavity images of boundaries in CW F82H at 9 dpa and 380 appm He and AT F82H at 9 dpa and 190 appm, respectively. The slanted boundary between two precipitates in Figure 4a shows a very high density of uniformly distributed fine bubbles. The edge on view of a boundary in Figure 4b also shows a high concentration of fine bubbles along its entire length. Bubbles at precipitate interfaces are also observed in Figure 4. Another example of precipitate associated bubbles are shown in Figure 5. The number densities and size distributions of the boundary-interface associated bubbles have not yet been quantified. However, the observation of the collection of large amounts of helium on grain boundaries in TMS alloys, even in the CW condition, is rather alarming for reasons noted in the following section.

The number densities and size distributions for the He/dpa ration ≈ 40 appm/dpa for the AT and CW specimens were used to estimate the amount of He in the bubbles, assuming equilibrium capillary pressures, as described previously. The estimated value of 345±15 appm He is in good agreement with the nominal value of 380 appm He.

Summary, Discussion and Concluding Remarks

An in situ He injection technique was used to study the transport and fate of He in the F82H TMS in the AT and CW conditions for irradiation in HFIR to 9 dpa at 500°C at nominal He/dpa ratios of 20 and 40 appm/dpa. A high density of small bubbles, accompanied by a population of fewer and larger voids, was observed in all cases. A larger concentration of smaller bubbles was found in the CW alloy, and both the size and number densities increased at the higher He/dpa ratio. The bubbles were preferentially associated with dislocations, boundaries and precipitate interfaces. The presence of high concentrations of small bubbles on boundaries is a concern, since this may lead to enormous shifts in the ductile-to-brittle temperature for fast fracture at lower irradiation temperatures, in the hardening regime [9-11], and severe reductions in the creep ductility and rupture time at higher irradiation temperatures [12-13]. Both of these phenomena are related to the weakening of grain boundaries by high concentrations of He, albeit by different mechanisms. These degradation processes may reduce, or even close, the window for

application of TMS to fusion first wall structures beyond a dpa limit that may be far less than desired values in the range of 100 to 200 dpa.

It should be noted that similar bubble distributions were observed in a previous *in situ* He injection study of the TMS Eurofer97 [3]. However, the bubbles were somewhat smaller and more numerous in this case. More importantly, preliminary studies of the nanostructured ferritic alloy (NFA) MA957 show an even higher concentration of smaller bubbles compared to Eurofer97, that preferentially form in association with Y-Ti-O enriched nanofeatures (NF) [1,2,8,14]. Most significantly, a companion report shows preliminary evidence that the grain boundaries in NFA contain fewer bubbles than in TMS, and appears to be protected from accumulation of high quantities of He by the NF and associated bubbles.

Future Work

These results barely scratch the surface of what can be learned about the transport, fate and consequences of He using the in situ injection technique. Thus in addition to further characterization studies of the alloys and irradiation conditions described in this and previous publications, a major future effort will be directed at characterizing the large matrix of other alloys and irradiation conditions from the JP26 and JP27 experiments, that contained a total of ≈ 360 He injected TEM discs.

Acknowledgements

This research was supported by the U. S. Department of Energy, Office of Fusion Energy Sciences, under contracts DE-FG03-94ER54275 and DE-AC06-76RLO1830.

References

1. G.R. Odette, to be submitted to *Fusion Materials Semiannual Report 7/1 to 12/31/2007* DOE/ER-313/43
2. T. Yamamoto, G. R. Odette, P. Miao, D. T. Hoelzer, J. Bentley, N. Hashimoto, H. Tanigawa, R. J. Kurtz, *J. Nucl. Mater.* **367-370** (2007) 399.
3. R.J. Kurtz, G.R. Odette, T. Yamamoto, D.S. Gelles, P. Miao, B.M. Oliver, *J. Nucl. Mater.* **367-370** (2007) 417.
4. T. Yamamoto, G. R. Odette, L. R. Greenwood, *Fusion Materials Semiannual Report 1/1 to 6/30/2005* DOE/ER-313/38 (2005) 95.
5. K. Shiba, M. Enoeda, S. Jitsukawa, J. Nucl. Mater. **329-333** (2004) 243.
6. R. E. Stoller and G. R. Odette, J. Nucl. Mater. **131** (1985) 118.
7. G. R. Odette, J. Nucl. Mater. **155-157** (1988) 927.
8. G. R. Odette, M. J. Alinger, B. D. Wirth, Annual Review of Materials Research 38 (2008) in press.
9. T. Yamamoto, G. R. Odette, H. Kishimoto, J-W. Rensman, P. Miao, *J. Nucl. Mater.* **356** (2006) 27.
10. Y. Dai, submitted to J. Nucl. Mater.
11. T. Yamamoto, G. R. Odette, M. Salston, P. Miao, Y. Dai, *Trans. American Nuclear Society (in press)*
12. H. Trinkaus, J. Nucl. Mater. **118** (1983) 39.
13. G. R. Odette, J. Nucl. Mater. **122** (1984) 435.
14. G. R. Odette, P. Miao, T. Yamamoto, D. J. Edwards, H. Tanigawa, R. J. Kurtz, *Trans. American Nuclear Society* (in press)

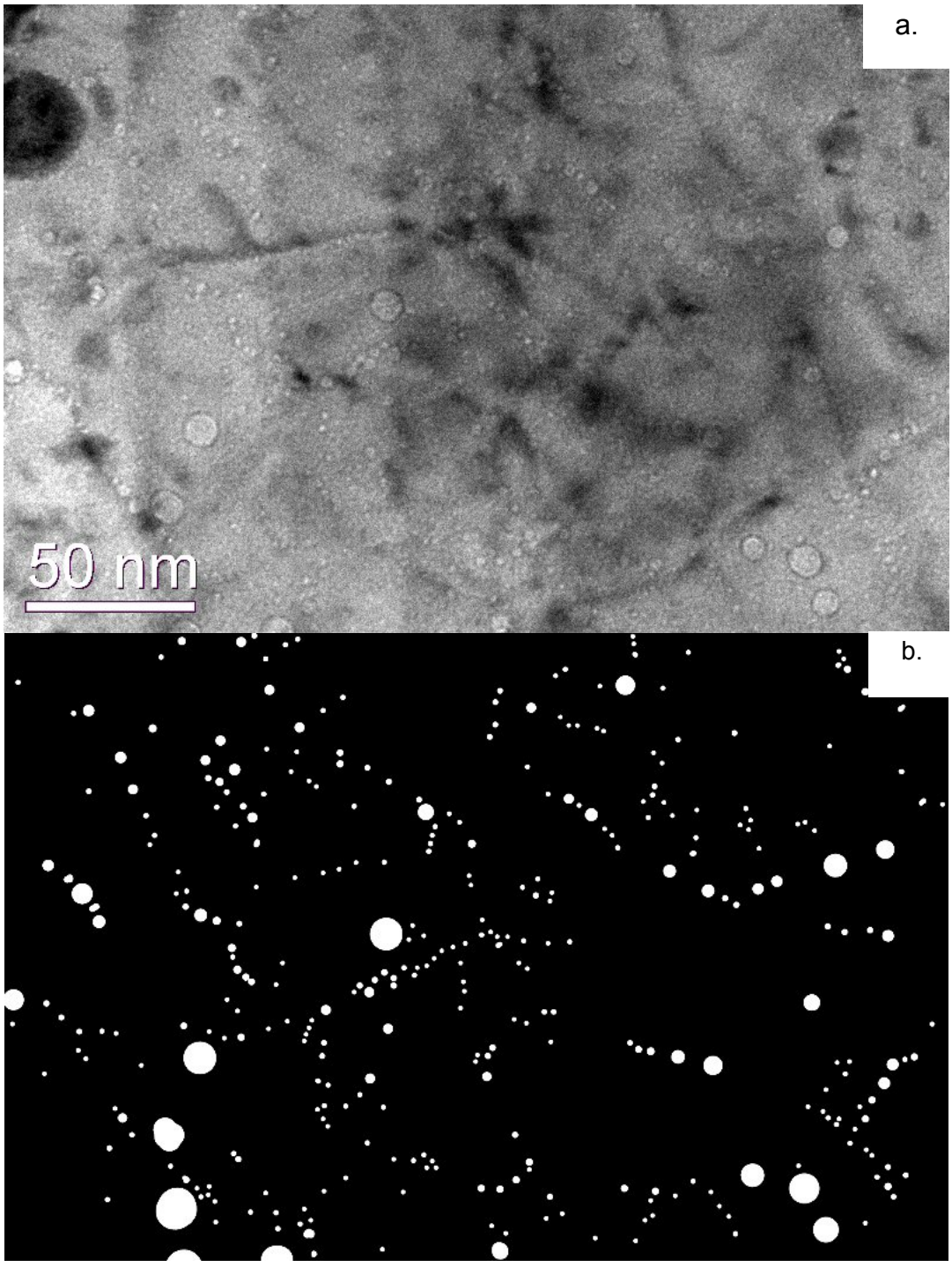

Figure 1 a) 512 nm under-focused TEM image for cavity structure in AT F82H-mod.3 irradiated to 9 dpa and He implanted to 380 appm at 500 ºC, and b) a map for the features identified as bubbles by through-focus image analysis

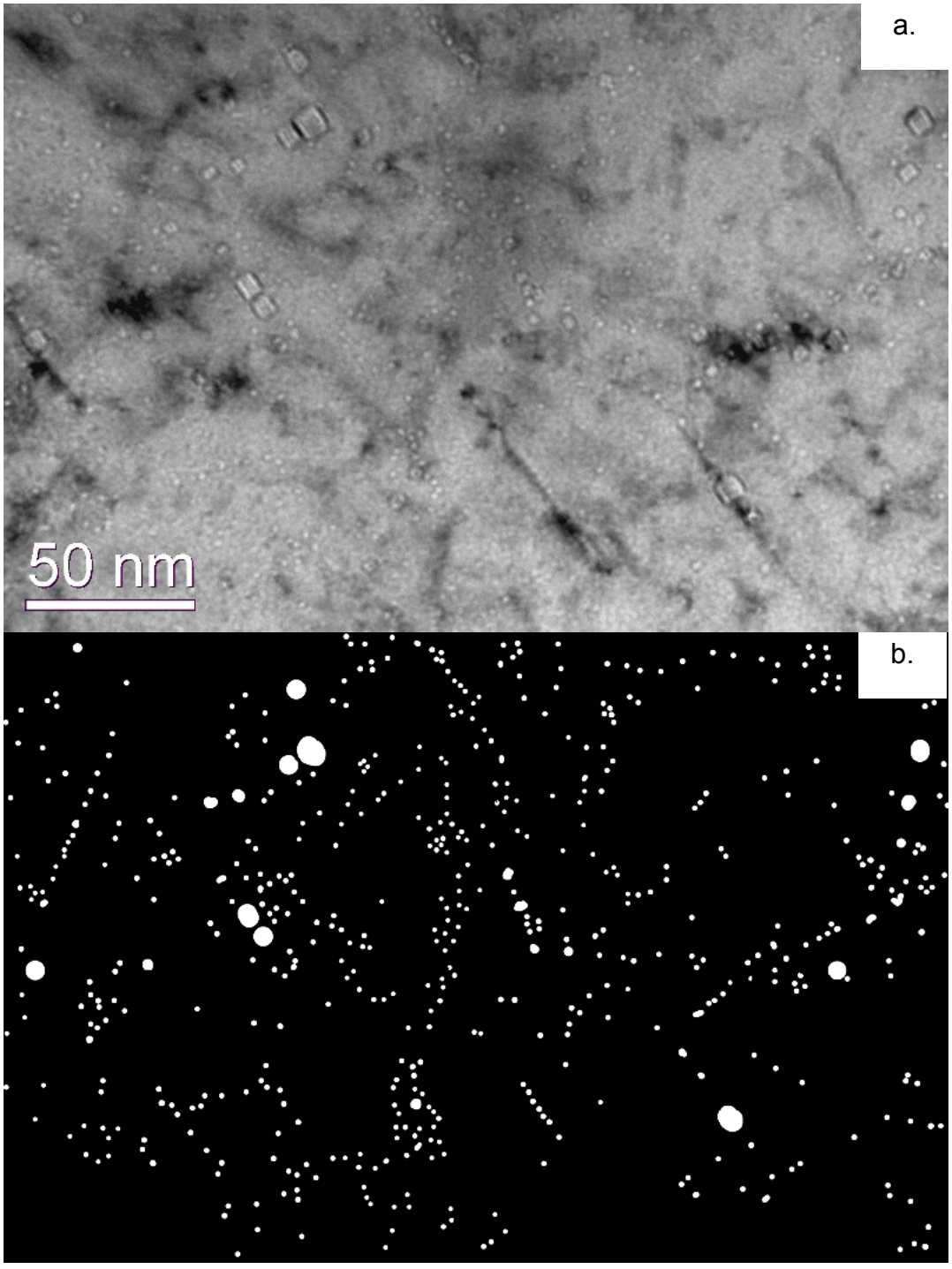

Figure 2 a) 512 nm under-focused TEM image for cavity structure in CW F82H-mod.3 irradiated to 9 dpa and He implanted to 380 appm at 500 ºC, and b) a map for the features identified as bubbles by through-focus image analysis

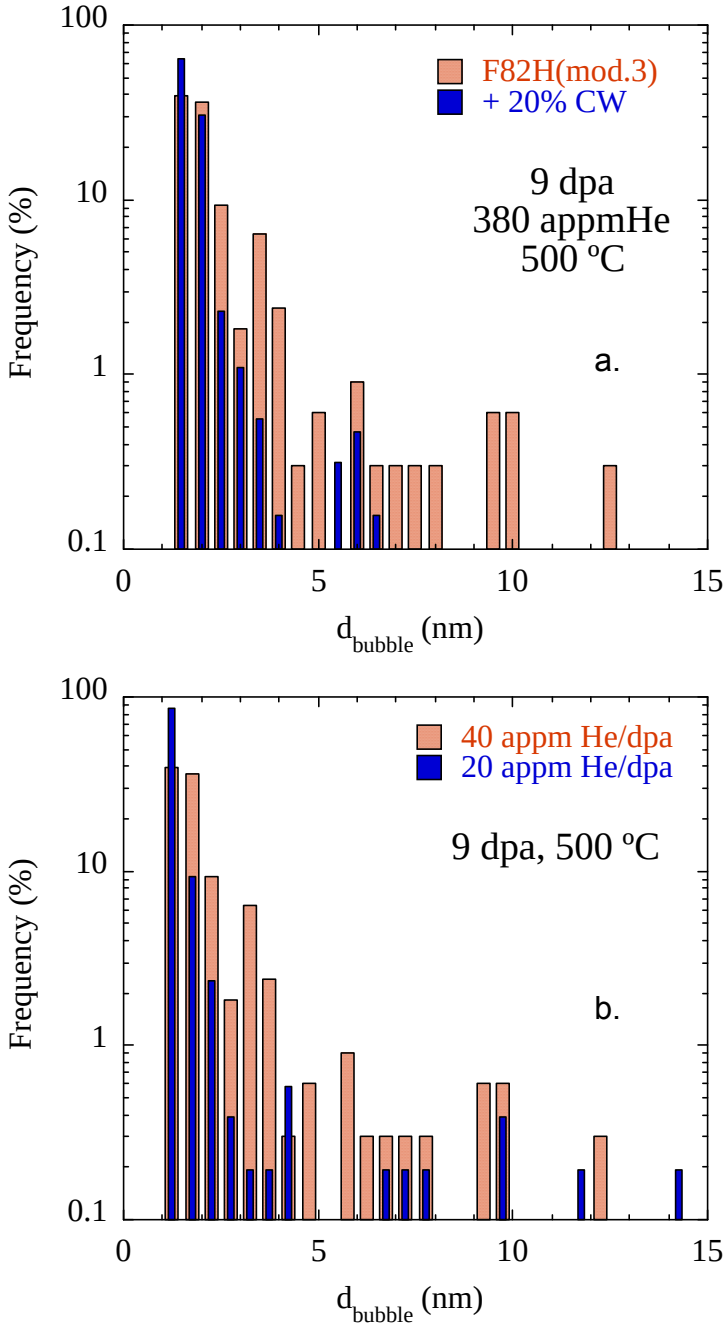

Figure 3 Cavity size distribution in a) AT and CW F82H mod.3 irradiated to 9 dpa and He-implanted to 380 appm at 500 ºC, and b) at two different He/dpa ratios in AT F82H mod.3 irradiated to 9 dpa at 500 ºC.

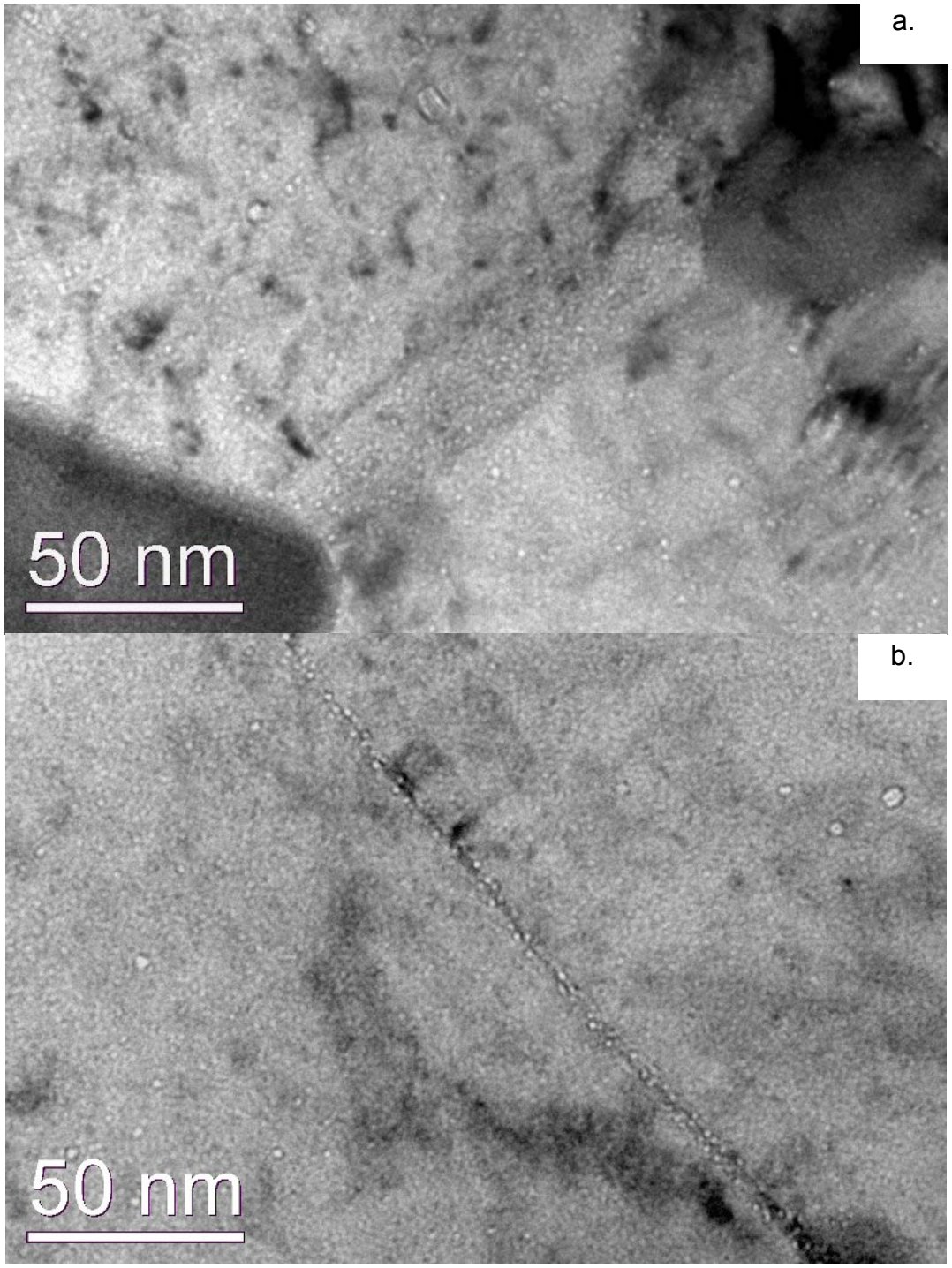

Figure 4 Cavity formation at grain boundaries in a) CW F82H mod.3 irradiated to 9 dpa and He-implanted to 380 appm at 500 ºC, and b) AT F82H mod.3 irradiated to 9 dpa and He-implanted to 190 appm at 500 ºC.

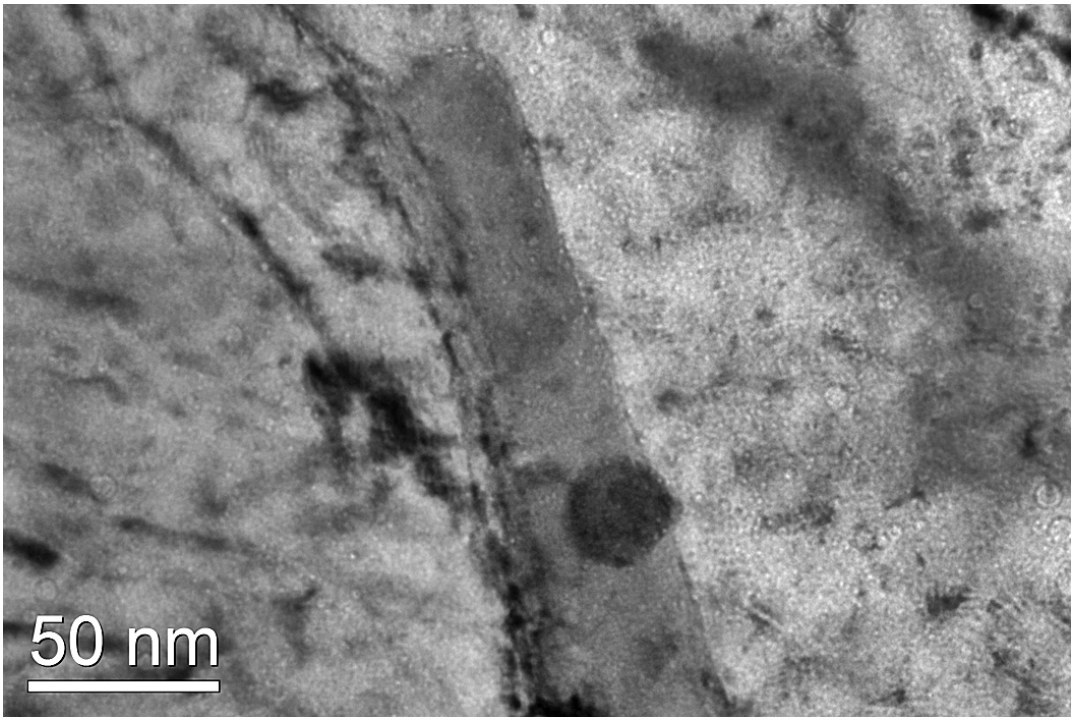

Figure 5 Cavity formation in the precipitate interface in AT F82H irradiated to 9 dpa and He-implanted to 380 appm at 500 ºC.

The Microstructural Stability of a Ruptured Thermal Creep Specimen of MA957 - D.T. Hoelzer, J.P. Shingledecker, R.L. Klueh, M.K. Miller, and J. Bentley (Oak Ridge National Laboratory)

OBJECTIVE

To report the results of several creep tests that were performed on MA957 in 2003 and the results of the microstructural analysis of a specimen that failed recently after 38,555 h at 800ºC in air and a 100 MPa load. A key focus of this study was to investigate the thermal stability of the Ti-, Y-, O-enriched nanoclusters that are present in MA957 after the long exposure time at 800ºC.

SUMMARY

A set of thermal creep tests were conducted on as-received MA957 starting in August 2003 shortly after discovering a high number density of Ti-, Y-, and O-enriched nanoclusters that were similar to those that had been discovered in 12YWT by APT in 1999. Four of the creep tests that were conducted at temperatures between 875ºC and 925ºC with 70 or 100 MPa loads ended with failure of the specimens before reaching 2000 h. On the other hand, two of the creep tests were conducted at lower temperatures of 800ºC (100 MPa) and 825ºC (70 MPa) and these lasted a considerably longer time. However, the specimen that was tested at 800ºC and 100 MPa recently failed after 38,555 h while the other specimen that was tested at 825ºC and 70 MPa is still in progress with more than 43,000 h logged to date. The microstructure of the recently failed creep specimen was investigated using optical microscopy and TEM, including Energy-Filtered TEM (EFTEM). The optical microscopy and TEM results showed that extensive porosity formed throughout the microstructure during the creep test. However, the significant discovery obtained by EFTEM revealed that the nanoclusters experienced no significant change in size, indicating that they are extremely stable at 800ºC (and 100 MPa) for very long periods of time.

PROGRESS AND STATUS

Background

There has been a renewed interest in the MA957 ferritic alloy that was patented by INCO in 1978 [1] following the discovery of a high number density of Ti-, Y-, and O-enriched nanoclusters (NC) by Atom Probe Tomography (APT) [2] and Small Angle Neutron Scattering (SANS) [3] during the FY02-05 I-NERI project between ORNL, plus UCSB subcontract, and CEA, Saclay, in France. The NC were found to have similar composition to those originally discovered by APT in 12YWT [4], which was developed in Japan during the 1990's [5]. The INERI project focused on 2 main tasks: (1) investigating the microstructure, with particular interest on the NC, and mechanical properties of the benchmark MA957 and 12YWT alloys, since they were produced by commercial companies (INCO and Kobe Steel, respectively) and (2) investigating the processing parameters toward development of the experimental 14YWT alloy.

The majority of recent results pertaining to microstructural analysis and mechanical properties testing of MA957 have been conducted on a thick walled tube sample that was provided to ORNL by CEA, Saclay in 2003 during the I-NERI project. Figure 1 shows the salient microstructural characteristics of the as-received MA957. The bright-field TEM micrograph in Figure 1a shows the general grain size and morphology observed in the microstructure at low-magnification. The grain size that was measured normal to the elongated grain direction was 654 +/- 79 nm and the grain length-to-width ratio, or aspect ratio (GAR), varied from ~3 to 10. The TEM analysis also revealed the presence of stringers of micron size Al_2O_3 oxide particles and low number densities of TiO_2 and $Ti_2Y_2O_7$ oxide particles with sizes typically >~20 nm. The Atom Probe Tomography (APT) results shown in Figure 1b reveal the Ti-, Y-, and O-enriched NC that are present in the as-received MA957. The analysis of the NC using the maximum separation envelope method [6] determined that the Guinier radius was r_g = 1.2 +/- 0.4 nm, the number density was ~2 x 10^{24} m^{-3}, and the average composition was 32.9 +/- 5.3 at.% Ti, 15.4 +/- 7.3% Y, 39.9 +/- 6.9% O, 1.7 +/- 1.7% Cr, 0.02 +/- 0.2% Mo, and remaining balance of Fe. The size and number

density of the NC determined from Small Angle Neutron Scattering (SANS) was r = 1.3 nm and ND = 0.7 x 10^{24} m^{-3} [3], which was in agreement with the APT results.

Following the discovery of NC in the as-received MA957, a total of 6 creep tests were initiated in August of 2003 to compare the creep properties with those of 12YWT, which had been completed on an earlier LDRD project at ORNL. The creep tests were conducted in air at temperatures ranging from 800ºC to 925ºC with loads of either 70 or 100 MPa. Four creep tests ended with specimen failures occurring within ~68 days of tests. All of these tests were conducted at 875ºC to 925ºC. Two of the tests (800ºC and 100 MPa and 825ºC and 70 MPa) continued without failure for more than 4 years. However, the specimen tested at 800ºC failed in early January, 2008 after 38,555 h, while the other specimen tested at 825ºC is still in progress with more than 43,000 h. The main objective of this report is to present the results of the creep test and the microstructural analysis of the specimen that recently failed after 38,555 h at 800ºC and 100 MPa.

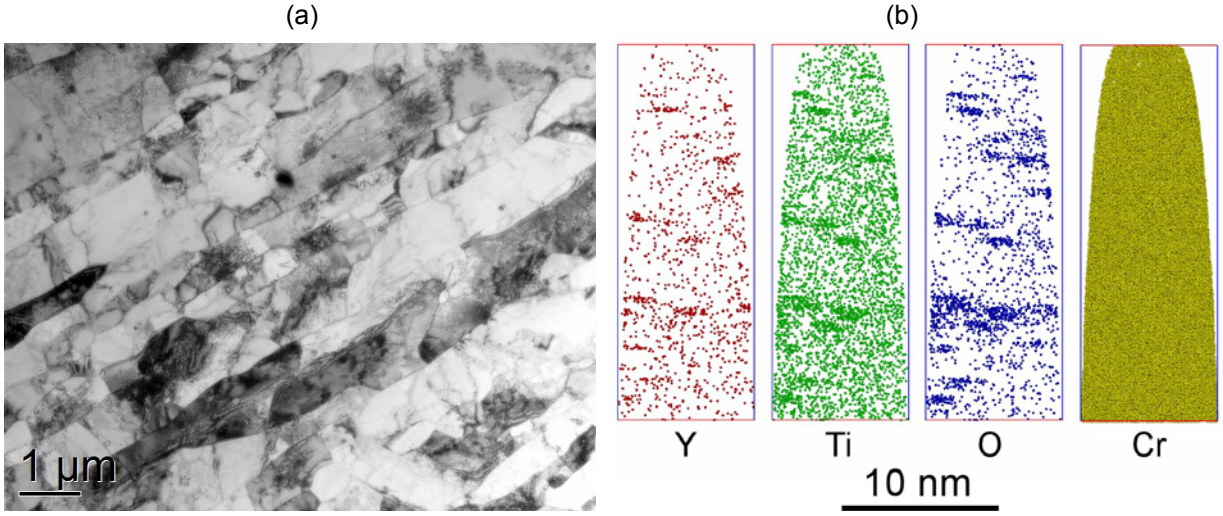

Figure 1. The as-received MA957 showing (a) bright-field TEM micrograph of the elongated grain structure and (b) APT of the Ti-, Y-, O-enriched nanoclusters including the solute Cr distribution.

Experimental Procedure

The sample of MA957 that was received in August, 2002 from CEA, Saclay consisted of a 100 mm long tube that had an external diameter of 65 mm and wall thickness of 9 mm. No information was provided on the fabrication history of this tube sample. A total of 7 creep specimens were machined from the tube wall section. The specimens were 3.0 in. long and had cylindrical gages, which were 0.8 in. long and 0.199 in. diameter. A total of 6 creep tests were started in August 2003. The temperatures and stresses used in these tests are shown in Table 1. All of the creep tests were conducted in air.

Results and Discussion

Thermal creep properties

The results of the 6 creep tests along with the test conditions are shown in Table 1. All of the specimens that were tested in the 875 to 925ºC temperature range failed within a short period of time, i.e. equivalent to ~1.5 to 68 days. At these temperatures, the protective Cr_2O_3 scale becomes unstable due to volatility of the CrO_3 phase [7] and oxidation of the specimens. These results show that lower test temperatures and stresses resulted in lower strains at failure and longer test durations. However, significantly longer time-spans resulted with the 2 specimens that were tested at the lower temperatures of 800ºC and 825ºC. As

shown in Table 1, the specimen that was tested at 800 ºC and 100 MPa recently failed after 38,555 h and the one tested at 825ºC and 70 MPa is still in progress.

Figure 2 shows the plot of the Larson-Miller Parameters (LMP) for the 6 additional creep tests conducted on MA957 and also those obtained in previous studies of the mechanically alloyed (MA) 12YWT ferritic alloy and advanced 9Cr-WMoVNb tempered martensitic steel (TMS) [7]. The 2 data points at 650ºC for MA957 were obtained from the INCO patent [1]. The temperature and time-to-failure are provided for the creep tests on 12YWT and MA957. The linear line fit through the data demonstrates that the overall creep properties of 12YWT are better than that of MA957, but both of these MA ferritic alloys show significant improvements over the 9Cr-WMoVNb TMS. The LMP data for 12YWT and MA957 are 4 to 6 orders of magnitude higher than that for the 9Cr-WMoVNb TMS at all stresses. Unfortunately, the LMP does not provide any information about the creep strain behavior and total strain at failure.

Table 1. Shows the test conditions and the results of the creep tests that were conducted on MA957.

Specimen	Stress (MPa)	Temperature (ºC)	Time (h)	Strain at Failure (%)	Status
1	100	900	37	1.8	Ruptured
2	70	925	165	4.2	Ruptured
3	70	875	1640	3.4	Ruptured
4	100	800	38,555	6.5	Ruptured
5	70	825	43,777	N/A	In Test
6	100	875	42	6.6	Ruptured

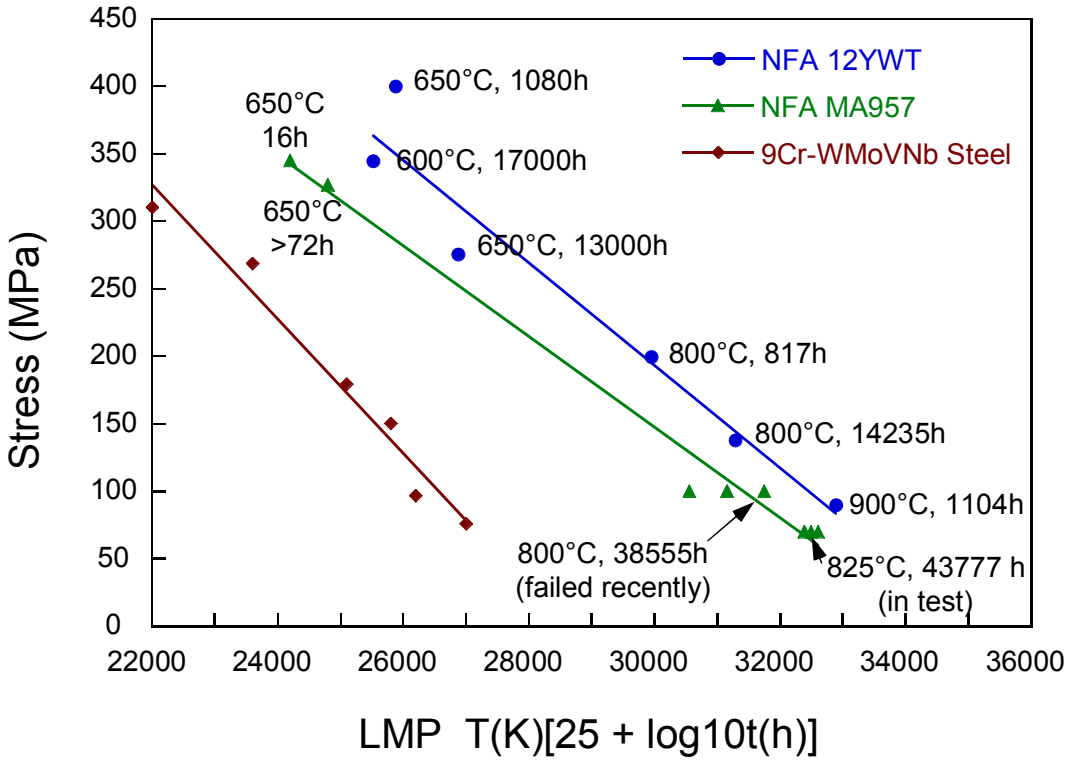

Figure 2. The Larson Miller Parameter plots of the new data for MA957 and of MA957, 12YWT and 9Cr-WMoVNb TMS from previous studies [1,7].

The results of the creep test for the specimen that failed after 38,555 h at 800ºC and 100 MPa are shown in Figure 3. This plot shows the creep strain as a function of time with the data processed to 100 points due to the very large number of data points for this test. Interestingly, the results do not show significant evidence of primary creep and tertiary creep behavior. The data follows nearly steady state creep rate from the beginning of the test to ~38,165 h. The results indicated that the vast majority of strain, ~6.14%, occurred in the last 0.1 h of the test. The extensometer creep strain prior to rupture was 0.361%, which corresponded to a displacement of ~0.003 in. for the 38,555 h test. The minimum creep rate was measured to be ~1.2 x 10^{-11} s^{-1} ($d\dot{\varepsilon}/dt$), which is a very low value.

Microstructural characterization

The digital image of the two ends of the ruptured test specimen is shown in Figure 4. The dark contrast visible on the external surface of the gages is from the oxide scale that formed during the creep test. In addition, the analysis of the fracture surfaces at the end of each gage section also showed dark contrast, which indicated that these surfaces had been exposed to the oxidizing atmosphere at 800ºC for a sufficient period of time before the specimen failed.

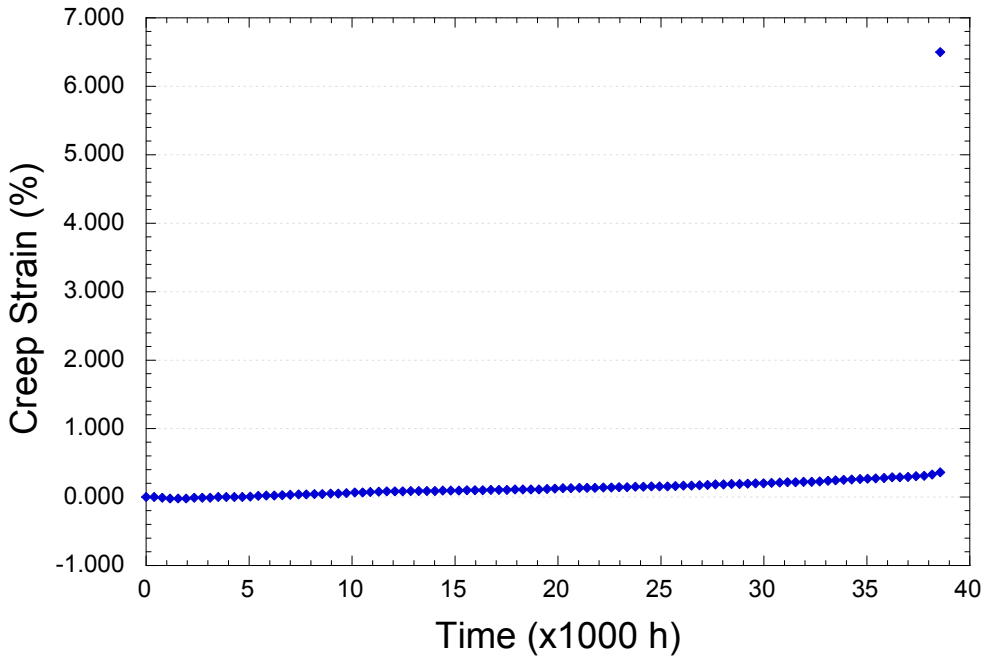

Figure 3. Results showing the creep strain as a function of time for the test conducted on the MA957 specimen at 800ºC in air and 100 MPa load.

Figure 4. Digital image showing the broken sections of the ruptured specimen of MA957.

The general microstructural investigation of the ruptured MA957 specimen was conducted using optical microscopy and transmission electron microscopy (TEM). A thin, ~1 mm thick, cylindrical-shaped sample was cut about 5 mm away from fracture surface of the longer gage section (the left gage section in Figure 4). This sample was mounted and polished for optical microscopy, and will be examined by SEM analysis in the future. Several 3 mm diameter TEM foils were prepared from another cylindrical-shaped sample that was cut from the same gage section. This sample was ~4 mm thick, which enabled the 3 mm diameter thin foil specimens to be prepared with an orientation that was parallel to the elongated grains, i.e. parallel to the gage. The foils were jet-polished in a Tenupol-3 using an electrolyte solution of 75% methanol and 25% nitric acid at 27ºC for TEM analysis.

The results of the microstructural analysis of the ruptured specimen using optical microscopy are shown in Figure 5. At low magnifications (Figure 5a), a complex surface oxide scale and extensive porosity throughout the microstructure are observed. The pores range in size from ~1 to ~20 μm and appear to be distributed in stringers. Similar porosity has been observed in other studies following exposure of ODS alloys to elevated temperatures during annealing of PM200 [9] and oxidation of ODS Fe-Cr alloys [10]. The reasons for explaining the formation of pores at high temperatures are not fully understood. Figure 5b shows the optical micrograph of the surface oxide scale at higher magnification. The surface oxide scale consists of several layers based on differences in contrast observed by optical microscopy. The outer layer varies considerably in thickness, from ~10 to 50 μm, and contains either a second phase or pores. This layer is most likely Cr_2O_3. A thinner layer that is ~5 mm thick lies below the top layer. This layer has a lighter contract that is similar to that of the base alloy. Below this layer lies another layer that is ~10 to 20 μm thick and has similar contrast to that of the top Cr_2O_3 layer. This region appears to contain large pores. Finally the bottom layer is ~15 to 20 μm thick and is consistent with internal oxidation of the alloy matrix since numerous oxide particles are present in this region.

Figure 6 shows a bright-field TEM micrograph of the microstructure observed in the ruptured specimen. This micrograph was obtained at very low magnification to show the stringers of pores. The pores have an elongated shape in the same orientation as the elongated grains in MA957 (Figure 1a). Unfortunately, the pores also prevented thin electron transparent regions from forming during electro-polishing.

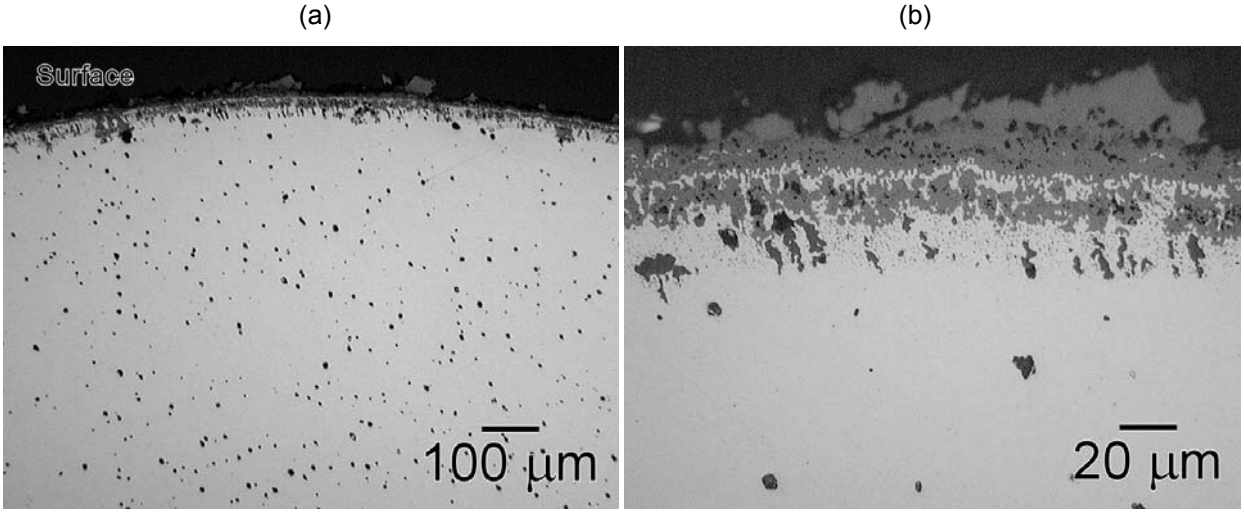

Figure 5. Optical micrographs showing the surface oxide scale and internal porosity that formed in the rupture MA957 specimen after exposure to 800ºC in air and 100 MPa load for 38,555 h. View is normal to gage of the test specimen.

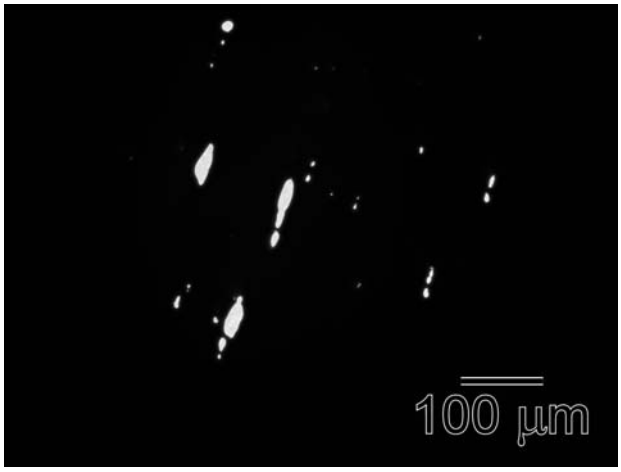

Figure 6. Bright-field TEM micrograph showing the porosity that was observed parallel the elongated grains in MA957 at a very low magnification (120 X).

Although no detailed analysis of the oxide phase in the surface scale has been conducted, this will be the focus of future research in order to investigate the possible link between the oxide scale formation and development of the porosity. Understanding these mechanisms is important since the formation of the large pores was most likely responsible for the failure mode of the creep specimen.

In order to investigate the thermal stability of the nanoclusters that were present initially in the as-received MA957 using Energy-Filtered TEM (EFTEM), which has been shown to be the most reliable electron microscopy method for imaging the nanoclusters [11], a different approach to specimen preparation was required to obtain very thin specimens. The method that finally provided the best specimen for EFTEM analysis was the lift-out method with the Focused Ion Beam (FIB) of a thin 10 μm x 10 μm specimen from the polished section of the jet-polished 3 mm dia. disc. The lift-out specimen was attached to a special grid and then thinned to electron transparency using the FIB.

The significant discovery that was obtained from the EFTEM analysis of the lift-out specimen was that the nanoclusters were still present in the ruptured specimen of MA957 and appeared to have undergone no significant change in size after 38,555 h at 800ºC and 100 MPa. Figure 7 shows 2 areas of the lift-out specimen that were analyzed using the EFTEM Fe-M jump ratio method. The results of analyzing several areas indicated that the particles showed a bi-modal size distribution and particle distribution was inhomogeneous. However, as shown in Figure 7a, the majority of the particles in the smaller size range are nanoclusters that have a size range of 2 to 4 nm. The larger particles are typically >10 nm and are usually distributed on grain boundaries, for example, the line of particles in the upper and lower region of Figure 7b. These particles are most likely an equilibrium oxide phase. However, no conclusive data was obtained that could verify this suggestion.

The results showed that the spatial distribution of the nanoclusters and larger oxide particles in the creep ruptured specimen of MA957 was relatively inhomogeneous. It was possible that this could have occurred during the creep tests. However, it was decided to have several 3 mm dia. specimens prepared from the as-received MA957 sample by jet-polishing in order to elucidate this possibility. Figure 8 shows the EFTEM Fe-M jump ratio images that were obtained from 2 regions in the as-received MA957 specimen. The results clearly showed that a bi-modal size distribution of the particles and an inhomogeneous distribution of the particles, including the nanoclusters present in the grains. Thus, these results proved that these are pre-existing characteristics of the particles dispersions in MA957 and that the nanoclusters are extremely stable very long exposures at 800ºC.

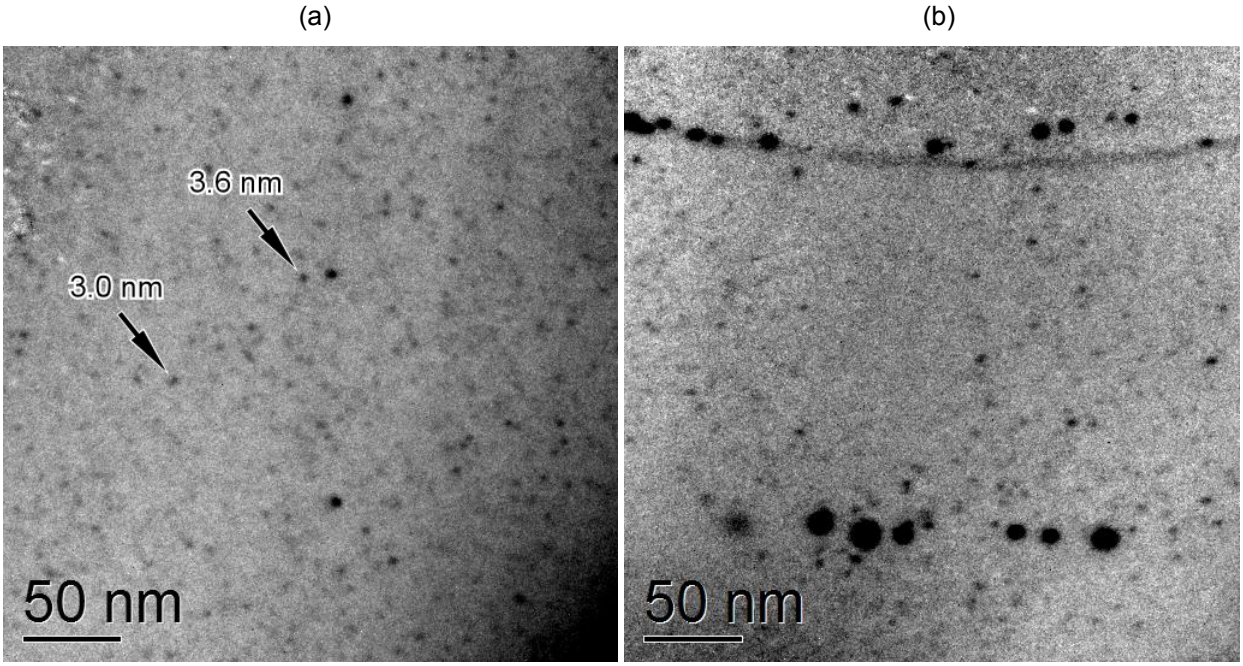

Figure 7. EFTEM Fe-M jump ratio maps of the ruptured creep specimen of MA957

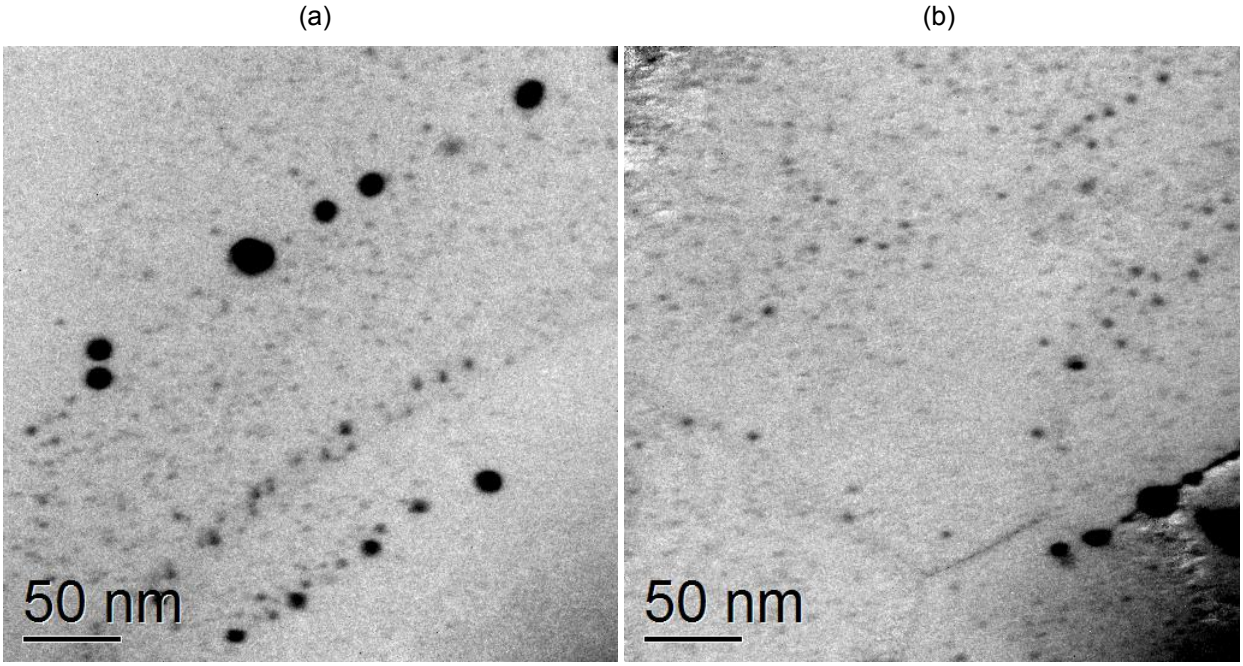

Figure 8. EFTEM Fe-M jump ratio maps of the as-received specimen of MA957.

Conclusions

- The results of the creep tests that were conducted on specimens prepared from the as-received MA7 in August 2003 showed that creep tests lasted more than 38,000 h for two of the specimens tested at

800ºC and 100 MPa and at 825ºC and 70 MPa. This was in contrast to the four specimens that were tested at temperatures between 875ºC and 925ºC with loads of either 70 MPa or 100 MPa.

- The creep results of the specimen that recently failed after 38,555 h at 800ºC and 100 MPa showed:
  - Essentially no primary or tertiary creep behavior occurred.
  - The total strain at failure was 6.5%. However, 6.14% of the strain occurred during the last 0.1 h prior to failure of the specimen, so that the steady state creep strain was only 0.361%. This corresponded to a displacement of ~0.003 in.
  - The minimum creep rate was measured to be ~1.2 x 10^{-11} s^{-1} ($d\dot{\varepsilon}/dt$).
- The microstructural analysis of the creep specimen that failed after 38,555 h at 800ºC and 100 MPa showed:
  - A complex multi-layer oxide scale formed on the surface of the creep specimen.
  - Extensive stringers of elongated shaped pores formed throughout the microstructure.
  - EFTEM revealed that the Ti-, Y-, O-enriched nanoclusters that were present initially in the as-received MA957 sample experienced no significant change in size, indicating that they are extremely stable at 800ºC (and 100 MPa) for very long periods of time.
  - The inhomogeneous distribution of the nanoclusters and larger oxide particles that was observed in the ruptured creep specimen was similar to that observed in specimens prepared from the as-received MA957, indicating that this was not due to the creep test conditions.

Future Work

The research that is planned for the future includes investigating the microstructure of the complex oxide scale that formed on the 800ºC creep specimen of MA957, which will involve the lift-out and FIB method for specimen preparation, and the reason for the extensive formation of porosity. The latter will include the microstructural investigation of the four creep specimens that failed with short times in the tests that were conducted at temperatures between 875ºC and 925ºC. These specimens may provide further insight into the formation of pores, stability of the nanoclusters, and specimen failure mode.

Acknowledgements

The author thanks J.R. Mayotte for the metallographic specimen preparation and D.W. Coffey and K.A. Thomas for preparing the lift-out/FIB and TEM thin foil specimens, respectively. This research was supported by the Office of Nuclear Energy, Science and Technology (INERI), by the Office of Fusion Energy Sciences, and at the SHaRE User Facility by the Scientific User Facilities Division, Office of Basic Energy Sciences, U.S. Department of Energy.

References

[1] J.J. Fisher, US Patent 4,075,010, issued 21 February 1978.
[2] M.K. Miller, D.T. Hoelzer, E.A. Kenik, and K.F. Russell, J. Nucl. Mater., Vol. 329-333 (2004) p. 338.
[3] M.J. Alinger, PhD Dissertation, University of California, Santa Barbara, September 2004.
[4] D.J. Larson, P.J. Maziasz, I.-S. Kim, and K. Miyahara, Scr. Mater., Vol. 44 (2001), p. 359.
[5] I.-S. Kim, B.-Y Choi, C.-Y Kang, T. Okuda, P.J. Maziasz, and K. Miyahara, ISIJ International, Vol. 43, No. 10, (2003), p. 1640.
[6] M.K. Miller, Atom Probe Tomography, Kluwer Academic/Plenum, New York, 2000.

[7] M. Brady, B. Gleeson, and I.G. Wright, JOM, Vol. 52, No. 1 (2000), p. 16.
[8] R.L. Klueh, P.J. Maziasz, I.S. Kim, L. Heatherly, D.T. Hoelzer, N. Hashimoto, E.A. Kenik, and M. Miyahara, J. Nucl. Mater., Vol. 307-311 (2002), p. 773.
[9] Z.Y. Gao, F.S. Han, J. Wu, and Q.Z. Wang, J. Alloys and Compounds, Vol. 419, (2006), p. 126.
[10] B.A. Pint and I.G. Wright, Oxidation of Metals, Vol. 63, No. 3-4 (2005), p. 193.
[11]. J. Bentley, D.T. Hoelzer, D.W. Coffey and K.A. Yarborough, Microsc. Microanal., Vol. 10 (Suppl. 2), (2004), p. 662.

ON THE STATIC AND CREEP STRENGTH OF MA957 FROM ROOM TEMPERATURE TO 1000ºC - M.C. Salston and G.R. Odette (*Department of Mechanical Engineering, University of California, Santa Barbara)*

OBJECTIVE

The objective of this work is to characterize the constitutive properties of MA957 and to analyze this data to assess the factors that control the tensile and creep strength of nanostructured ferritic alloys (NFA).

SUMMARY

Static tensile and creep tests were carried out on as-extruded (AE) MA957 from room temperature to 1000ºC. Comparison of these results to data taken from the literature show the yield stress (σ_y) and ultimate tensile strength of MA957 are generally higher than for 9 Cr tempered martensitic steels (TMS), like Eurofer97. However, the static tensile strength of MA957 varies by up to a factor of 2, or more, depending on the post extrusion thermal mechanical heat treatment (TMT) and specimen orientation with respect to the extrusion direction. The corresponding creep strength varies by up to a factor of ≈ 10. The AE and TMT variants of MA957 were fit to a threshold stress (σ_{tr}) model. The $\sigma_{tr}(T)$ for the AE MA957 is ≥ $0.4\sigma_y(T)$ up to 800°C and decreases at higher temperatures, approaching 0 at 1000°C.

PROGRESS AND STATUS

Introduction

Nano-structured ferritic alloys (NFA) offer great promise for advanced fission and fusion reactors. NFA are ferritic stainless steels that contain 12-14 Cr and are dispersion strengthened by a high density of nm-scale Y-Ti-O nanofeatures (NF) that result in remarkable high temperature creep strength and radiation damage resistance [1]. NFA are processed by mechanically alloying metal powders with Y_2O_3 by ball milling, followed by hot consolidation, usually by extrusion. Our objective is to characterize and model the constitutive properties of a commercial vendor NFA INCO MA957 in the as-extruded condition, and to compare this material to other NFA and MA957 conditions, as well as to a 9 Cr tempered martensitic steel (TMS) Eurofer97.

Experimental Procedures

The composition of MA957 is 14Cr-1Ti-0.3Mo-0.22Y_2O_3(wt.%). Tensile specimens (gauge dimensions 0.5x1.2 x 5 mm) were tested in air in the axial extrusion orientation on a MTS load frame at a strain rate (ε') of $1.33x10^{-3}$ s^{-1} in a furnace from ambient temperature to 1000°C. Corresponding strain-rate jump (SRJ) creep tests were carried from 600 to 1000°C, starting at a relatively low imposed ε', usually 10^{-7} s^{-1}, until a constant steady-state stress (σ) level was reached. The ε' was then changed, typically increasing by an order of magnitude, and held until a new steady-state σ was reached. A sequence of such SRJ were used to characterize $\sigma(T,\varepsilon')$. Creep tests were also carried out under constant load, and subsequently, under constant stress to rupture conditions.

Results

Tensile test data for several conditions of MA957 and TMS Eurofer97 [2,3,4] plotted in Figure 1a show: a) a wide range of σ_y in MA957, that vary by factors up to more than 2, depending on the alloy condition; and that b) MA957 is generally much stronger than Eurofer97. Figure 1b summarizes the corresponding creep strength for various MA957 conditions in a Larson-Miller Plot (LMP) for the creep rupture time (C = 30), along with data for Eurofer97 and NFA JYWT [3,4,5,6]. The various MA957 conditions and JYWT also show a wide range of creep strengths, up to a factor of ≈ 10. The NFA creep strengths are also generally much higher than for Eurofer97. However, the open cross symbols show the hoop strength biaxial creep tests of extruded tubing is much lower than for the other NFA, and is comparable to that for Eurofer97. Figure 2 shows a Larson-Miller plot for the inverse minimum creep rate for the AE MA957 data

as well as a data set reported by Wilshire et al. for a TMT condition of MA957 [5], which is much stronger than the AE alloy. The σ for constant load-stress tests is slightly higher than measured in the SRJ tests. This difference is likely due to the fact that accumulated strains in the constant load-stress case were higher, leading to larger dislocation densities and smaller cell sizes.

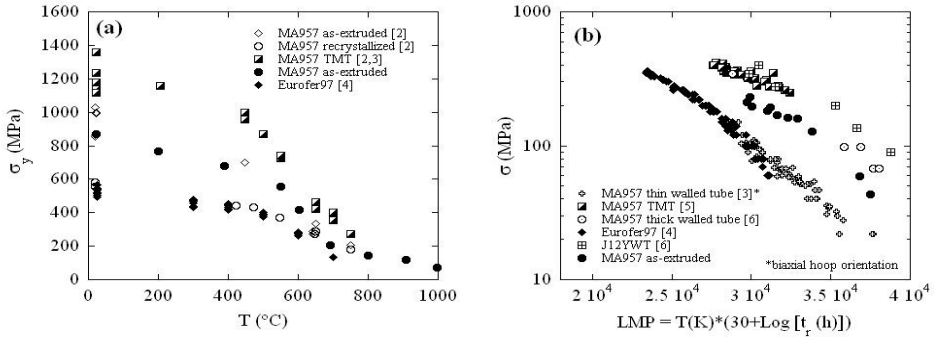

Figure 1 A comparison of: (a) $\sigma_y(T)$ for various alloys and alloy conditions; (b) creep rupture time LMP plots

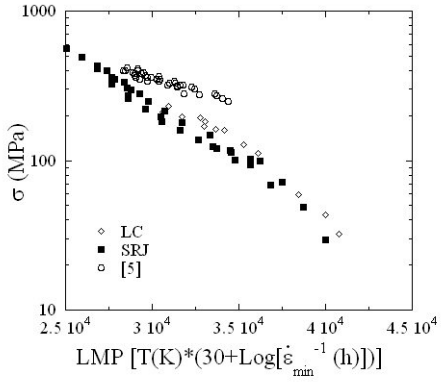

Figure 2 LMP for the inverse ε' for the AE MA957 SRJ tests, and CLS data for the AE and TMT MA957 [5].

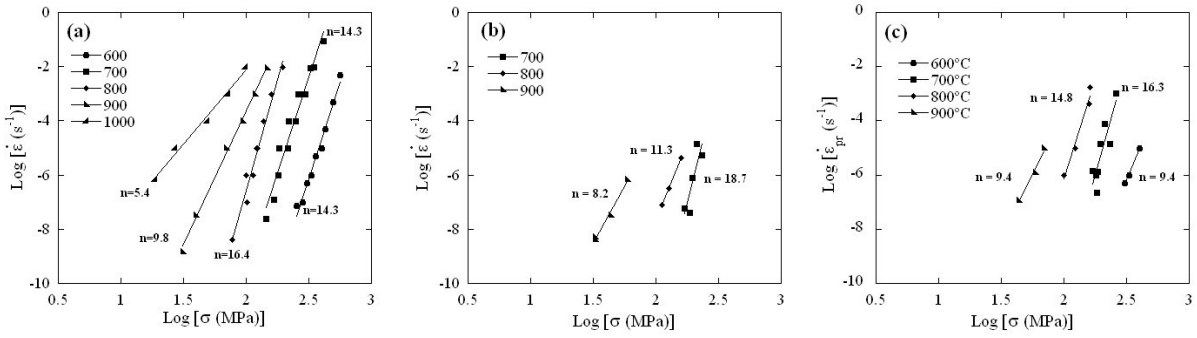

Figure 3 Log ε' versus log σ creep data for: (a) the SRJ tests; (b) the CLS tests; and, (c) the primary creep rate (ε'_{pr}) for CLS tests.

Figure 3a and b show plots of log ε' versus log σ data for the SRJ (3a) and constant load-stress (CLS) tests (3b) for the AE MA957, respectively. Figure 3c shows the corresponding primary average creep rates up to 0.5% from the CLS tests. The stress exponents (n) found by fitting the data to a standard

Norton power law creep model ($\varepsilon' \alpha \sigma^n$) are shown in the plots. The fitted n range from 14.3 to 16.4 for the SRJ data from 600 to 800°C shown in Figure 3a, and decrease to 9.8 and 5.4 at 900 and 100°C, respectively. The n for the CLS test data shown in Figure 3b are lower, but both the data and stress ranges are both more limited in this case. The corresponding n values for the primary creep rates are higher and closer to those observed in the SRJ tests.

As commonly observed for dispersion strengthened alloys the creep behavior of MA957 is consistent with the existence of a threshold stress $\sigma_{tr}(T)$, below which creep ceases [7]. Thus ε' can be better represented by

$$\varepsilon' = A\exp(-Q_{cr}/RT)\{[\sigma - \sigma_{tr}(T)]\}^n \quad (1)$$

The $\sigma_{tr}(T)$ were estimated by fitting Equation 1 to both the TMT MA957 literature data [5] and our measurements for AE condition. Typical n are ≈ 5 and Q_{cr} is the activation energy for creep which is expected to be close to the activation energy for self diffusion. Unconstrained fits resulted in somewhat higher and n and Q_{cr} than anticipated by the threshold stress model. Thus to estimate σ_{tr}, which only weakly depends of n and Q_{cr}, these parameters were fixed at n = 7, at the high end of a physically plausible range and restricted to nominal self diffusion values of 250 to 300 kJ/mole. The fitted σ_t for the AE condition are about 40 to 50% of σ_y from 600 to 800°C, decreasing to ≈ 18% at 900°C and approaching 0% at 1000°C and are shown in Figure 4. The exact $\sigma_y(T)$ for the TMT MA957 is not know, but the σ_{tr}/σ_y ratio is believed to be as high, or even higher, in this case.

The physical basis for the high σ_{tr} is that the NF result in a minimum stress for dislocation climb and glide. We only briefly note that the most successful σ_{tr} creep model was proposed by Artz and co-workers [7], based on the hypothesis that the underlying mechanism is detachment of dislocations from attractive obstacles. Understanding the physical basis for $\sigma_{tr}(T)$ and its relation to the alloy microstructure, is key to optimizing the creep strength of NFA.

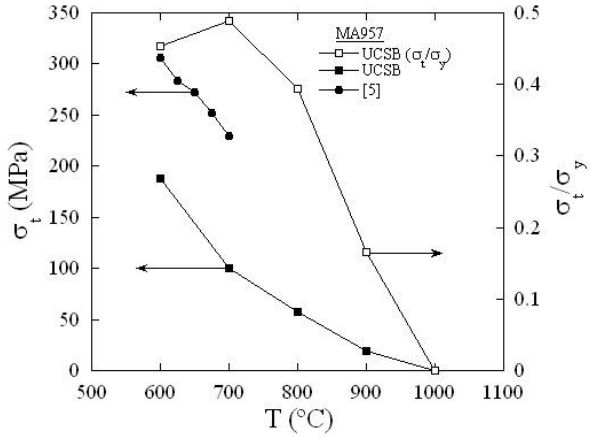

Figure 4 The $\sigma_{tr}(T)$ and σ_{tr}/σ_y for the TMT and AE MA957.

Figure 5 plots the primary creep (ε_{pr}) and creep rupture (ε_r) strains as a function of σ from 600 to 900°C for the constant load-stress tests. In both cases these strains tend to decrease with decreasing stress and increasing temperature.

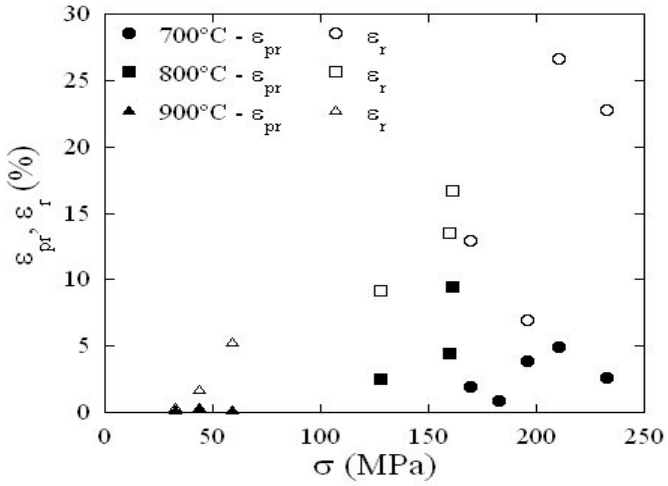

Figure 5 Primary and creep rupture strain data for CLS tests.

Figure 6 shows stress versus temperature plots for the 1000 h creep rupture time for TMT [5] and AE MA957. As well as the hoop stress for biaxial tests of extruded MA957 tubing [3] based on LMP fits. The TMT condition is about twice as strong as the AE MA957, which is about twice as strong as the tubing.

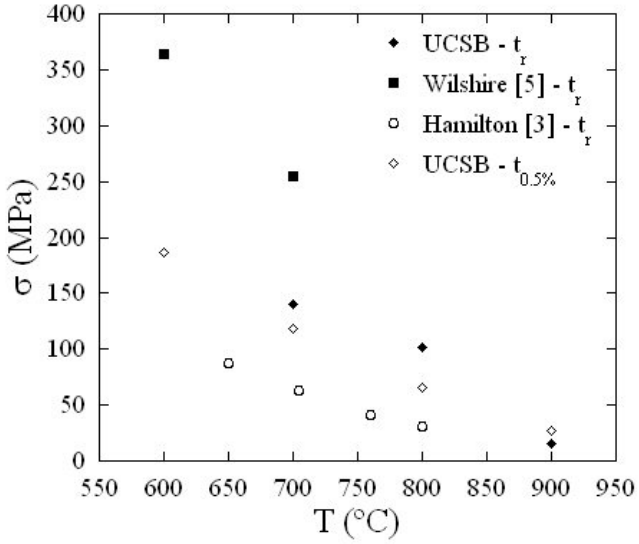

Figure 6 Predicted σ versus T plots for the 1000 h creep rupture and 0.5% primary strain times for various MA957 conditions and test orientations.

Summary and Future Work

The static and viscoplastic constitutive properties of AE MA957 were measured over a wide range of σ and T. Comparison of this data with that found in the literature shows that the strength of MA957 is generally higher than for TMS, but varies considerably, depending on the post-extrusion TMT and loading orientation relative to the extrusion direction. The creep data was fit the threshold stress model which shoes that was $\sigma_{tr} > 0.4\ \sigma_y$ up to 800°C. Testing and data analysis are continuing.

Acknowledgment

This research was partially funded by a DOE NERI Grant DE-FC07-05ID14663.

References

[1] G.R. Odette, M.J. Alinger, and B.D. Wirth "Recent Developments in Irradiation Resistant Steels," Annual Reviews of Materials Research (to be published) (2008).
[2] A. Alamo, V. Lambard, X. Averty, and M.H. Mathon, J. Nucl. Mater. 329-333 (2004) 333-337.
[3] M.L. Hamilton, D.S. Gelles, R.J. Lobsinger, G.D. Johnson, W.F. Brown, M.M Paxton, R.J. Puigh, C.R. Eiholzer, C. Martinez, and M.A. Blotter, "Fabrication Technological Development of the Oxide Dispersion Strengthened Alloy MA957 for Fast Reactor Applications," PNL-13168, Pacific Northwest National Laboratory, Richland, WA (2000).
[4] M. Rieth, M. Schirra, A. Falkenstein, P. Graf, S. Heger, H. Kempe, R. Lindau, and H. Zimmermann, "Eurofer97: Tensile, Charpy, Creep, and Structural Tests," FZKA6911, Forschungszentrum Karlsruhe (2003).
[5] B. Wilshire and T.D. Lieu, Materials Science and Engineering A 386 (2004) 81-90.
[6] D.T. Hoelzer, private communication.
[7] E. Arzt and D.S. Wilkinson, Acta Metall. 34 (1986) 1893-1898.

COMPATIBILITY OF MATERIALS EXPOSED TO ISOTHERMAL Pb-Li – B. A. Pint (Oak Ridge National Laboratory, USA)

OBJECTIVE

One proposed U.S. test blanket module (TBM) for ITER uses ferritic-martensitic alloys with both eutectic Pb-Li and He coolants at ~475°C. In order for this blanket concept to operate at higher temperatures (~700°C) for a DEMO-type reactor, several Pb-Li compatibility issues need to be addressed. Some of the issues being currently investigated are the use of corrosion resistant alloys and coatings, the transformation of alumina exposed to PbLi and the effect of impurities on dissolution of these materials.

SUMMARY

A series of six Pb-Li capsule experiments were conducted at 700° and 800°C for 1,000h using commercial purity Pb-17Li. The use of commercial Pb-Li with a higher O content did not reduce the amount of dissolution observed for type 316 stainless steel (316SS) at 700°C. The amount of dissolution for Fe-9Cr-2W (T92) was similar to 316SS at this temperature. However, when an Al-rich diffusion coating was applied to T92, the specimen mass loss was greatly reduced. The aluminized T92 specimen as well as a FeCrAl specimen formed $LiAlO_2$ on the surface. Exposures of FeCrAl and NiAl specimens at 700° and 800°C, pre-oxidized to form α-Al_2O_3, confirmed the prior observation that alumina transforms to $LiAlO_2$ during exposure to PbLi.

PROGRESS AND STATUS

Introduction

A recent focus of the U.S. fusion energy program has been on developing a proposal for a test blanket module (TBM) for ITER. The dual coolant Pb-Li (DCLL) TBM concept has both He and eutectic Pb-Li coolants and uses ferritic steel as the structural material with a SiC/SiC composite flow channel insert (FCI).[1] The interest in this concept has focused compatibility-related research on Pb-Li. Many materials have poor compatibility with liquid Li,[2] but the activity of Li is very low in Pb-17Li,[3] and this allows a wider range of materials to be considered. However, Pb-Li readily dissolves many conventional alloys above 500°C. While the TBM maximum operating temperature will be <500°C to limit compatibility issues, this blanket concept would be more attractive for a commercial reactor with a higher maximum operating temperature, perhaps >700°C if oxide dispersion strengthened (ODS) ferritic steels[4] were used. However, at these higher temperatures, compatibility is even more of a concern. Therefore, static capsule exposures have been conducted on materials at 700° and 800°C.[5,6] The use of Al-containing alloys and coatings has been studied as well as the transformation of α-Al_2O_3 to $LiAlO_2$.[7] Six capsule experiments were conducted to further study the behavior in Pb-Li and determine the effect of switching from high-purity Pb and Li to commercial purity Pb-17Li in the capsule.

Experimental Procedure

Static capsule tests were performed using Mo inner capsules and type 304 stainless steel outer capsules to protect the inner capsule from oxidation. Specimens were held inside the Mo capsule by a Mo wire. The capsules were loaded with 125g of commercial purity Pb-17Li in an argon-filled glove box. The difference between this Pb-Li and the higher purity Pb and Li used in prior work is mainly the interstitial elements: O, C and N, Table I. The specimens were ~1.5mm thick and 4-5cm^2 in surface area with a 0.3µm surface finish. The alloy chemical compositions are given in Table 2. Two specimens were pre-oxidized in dry, flowing O_2 to form an external Al_2O_3 scale under conditions shown in Table 3. One

Table 1. Chemical composition using inductively coupled plasma and combustion analysis of the starting Pb and commercial Pb-Li ingot (in ppma except for Li in atomic%).

	Li	Fe	Cr	Ni	Mn	Si	Al	Mo	C	O	N	S
Starting Pb	n.d.	<4	<4	<4	<4	<40	<8	<2	<170	1270	<40	<50
Comm. PbLi	14.3%	<30	<70	<30	<30	<120	<60	<40	750	4820	180	<50

Table 2. Alloy chemical compositions (atomic% or ppma) determined by inductively coupled plasma analysis and combustion analysis.

Material	Fe	Ni	Cr	Al	O	C	N	S	Other
316SS	65.1	8.9	19.9	0.02	490	3360	2380	68	1.94Si,1.67Mn, 1.38Mo,0.21Cu
T92 (9Cr-2W)	87.2	0.1	9.9	0.02	80	5120	2330	87	0.55W, 0.46Mn 0.30Mo,0.32Si
ODS FeCrAl	67.8	0.02	20.0	10.6	7430	340	210	50	0.44Ti,0.23Y 0.04Si, 0.04Mn
PM FeCrAl	65.2	0.1	21.3	9.7	1730	1320	1510	<	1.6Mo,1.1Si,0.15Y 0.07Hf,0.06Zr,0.02Ti
Ni-42.5Al+Hf	<	58.0	<	41.9	40	380	<	<	0.048Hf

< indicates below the detectability limit of <0.01% or <0.001% for interstitials

specimen of T92 was aluminized using chemical vapor deposition (CVD) for 6h at 900°C in a laboratory scale reactor. The process details and resulting coating microstructure are provided elsewhere.[8] These conditions produce a thin ~40µm thick coating with a maximum surface Al content of ~18at.%. Specimen mass was measured before and after exposure on a Mettler-Toledo balance with an accuracy of ±0.04 mg. Exposures were performed in resistively heated box furnaces for 1000 h. To remove residual Pb-Li on the surface, specimens were soaked in a 1:1:1 mixture of acetic acid, hydrogen peroxide and ethanol for up to 72 h. Post-test surfaces were initially examined using x-ray diffraction(XRD) and secondary electron microscopy (SEM).

Results and Discussion

Table 3 summarizes the mass change data for these capsule experiments. In Figure 1, the mass change results are compared to prior work.[5,6] The mass change for 316SS at 700°C was slightly higher in this exposure than in the previous exposure in high purity Pb-Li (-3.79 mg/cm^2). Therefore, the higher O content in the commercial Pb-Li did not have a beneficial effect on dissolution. While Ni is selectively

Table 3. Mass change of specimens after 1000h exposures in Pb-17Li with a Mo capsule.

Specimen	Pre-oxidation	Temperature	Mass Change (mg/cm^2)
316SS	none	700°C	- 5.06
T92	none	700°C	- 3.47
T92 + CVD Al	none	700°C	- 0.09
PM FeCrAl	none	800°C	- 1.93
ODS FeCrAl	2h at 1000°C	700°C	- 0.06
Ni-42.5Al+Hf	2h at 1200°C	800°C	- 0.51

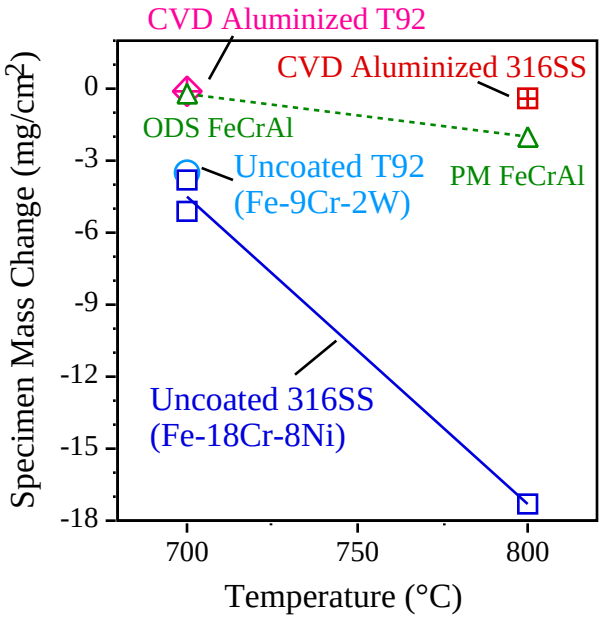

Figure 1. Specimen mass change as a function of exposure temperature in Pb-17Li for 1000h.

removed from stainless steel in Pb-Li, the mass loss for uncoated T92 (only 0.1%Ni) also was relatively high at 700°C. As expected, the thin Al-rich coating significantly reduced the mass loss for T92 at 700°C, similar to the previous results for ODS FeCrAl at 700°C and aluminized 316SS at 800°C, Figure 1.

Bare (i.e. no pre-oxidation) FeCrAl made by a powder metallurgy (PM) process (Kanthal alloy APMT) showed some mass loss at 800°C, higher than ODS FeCrAl (Plansee alloy PM2000) at 700°C. However, the mass loss was an order of magnitude less than the mass loss previously observed for uncoated 316SS at 800°C, Figure 1. The Al in PM FeCrAl formed a protective surface oxide that limited dissolution. As a result, this commercial tube alloy is a prime candidate for a metallic loop.

Finally, the pre-oxidized Hf-containing NiAl was exposed for two reasons. The first was to compare the result to NiAl without Hf that was exposed after a similar pre-oxidation.[5] The large mass loss for that specimen (-2.72 mg/cm^2) was attributed to poor adhesion of the pre-formed α-Al_2O_3 layer. The addition of Hf is known to improve alumina scale adhesion,[9] a similar effect as Y in the FeCrAl alloys, Table I. The lower mass loss for the Hf-containing NiAl specimen was attributed to better adhesion of the pre-formed alumina layer, however, as shown in Figure 2, the oxide was removed at the specimen edges after exposure. Dissolution of the metal where the oxide was removed likely explains the mass loss for this alloy. However, the pre-formed oxide layer did reduce the dissolution since this Ni-base material showed a lower mass loss than the Fe-base PM FeCrAl specimen, Table 3.

The second reason for the NiAl+Hf exposure was to confirm the earlier observation that pre-formed α-Al_2O_3 transforms to $LiAlO_2$ when exposed to Pb-Li.[7] All of the Al-containing specimens in this series were analyzed by XRD and all showed $LiAlO_2$ diffraction peaks and no α-Al_2O_3 peaks. This observation confirmed the earlier result for ODS FeCrAl at 800°C for a Ni-base alloy and on the same alloy at a lower temperature, 700°C. The surface oxide morphologies on ODS FeCrAl and NiAl+Hf before and after exposure are shown in Figure 3. Similar to the prior characterization,[6,7] the oxide grain size significantly increased due to the transformation on both specimens. The pre-formed oxide on NiAl+Hf showed the

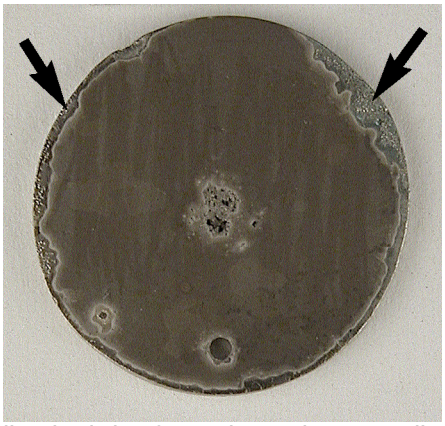

Figure 2. Photograph of pre-oxidized NiAl+Hf specimen (1.55cm diameter) after exposure to Pb-Li at 800°C for 1000h. The arrows show where the oxide was missing after exposure. There is a casting defect in the center of the disk and a hole at the bottom where the specimen was held with a Mo wire.

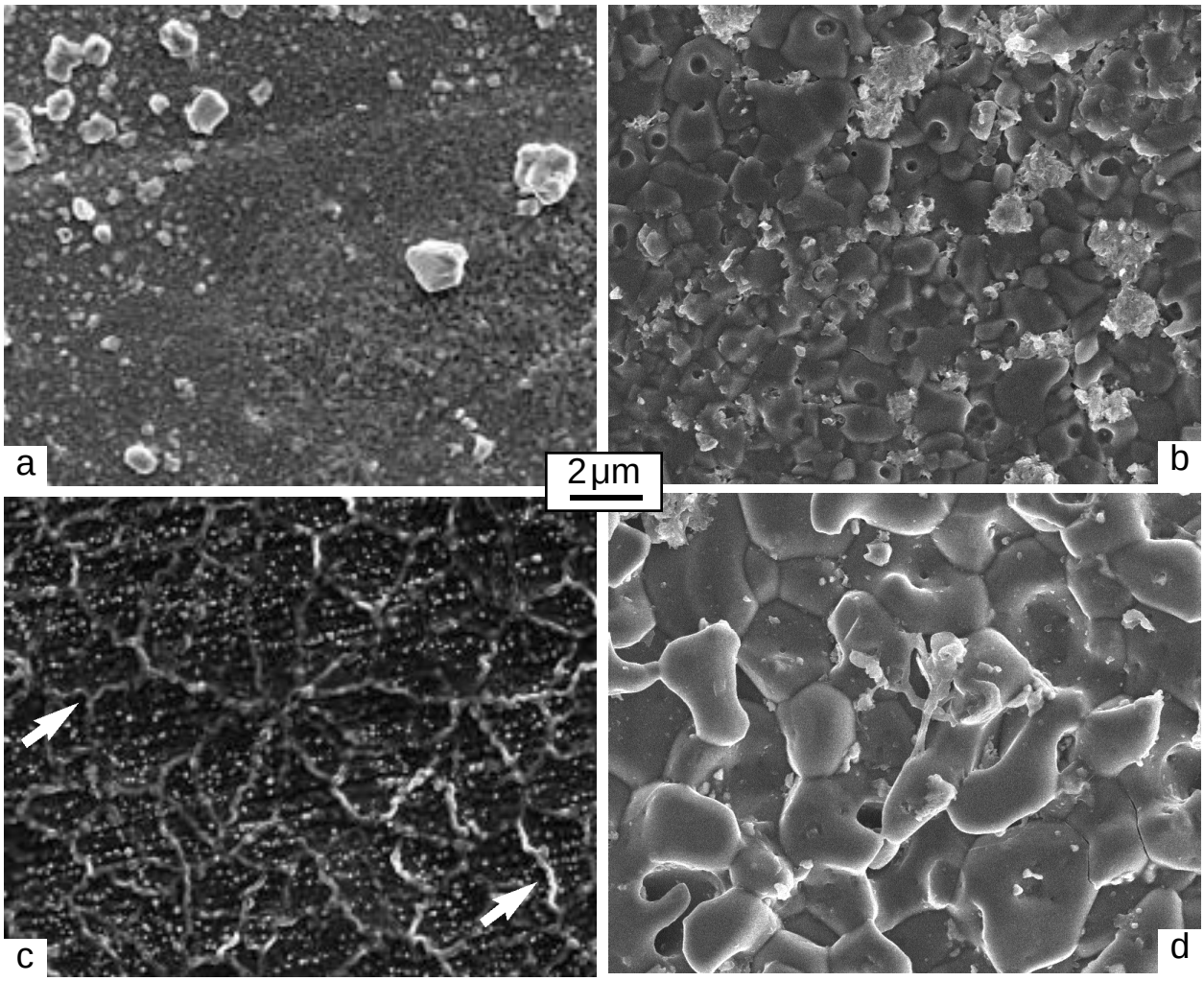

Figure 3. SEM plan view images of the reaction product before (a,c) and after (b,d) exposure to Pb-17Li at 700°C for 1,000h on ODS FeCrAl (a,b) and Hf-doped NiAl (c,d).

typical ridge structure (arrows in Figure 3c).[10] That structure was gone after exposure, Figure 3d. Further characterization of these specimens is in progress. After surface characterization is complete, the specimens will be metallographically sectioned to examine the oxide thickness, degree of alloy depletion and thickness of the coating layer.

To further study the effect of Pb-Li on oxides, the quartz ampoule that was filled with Pb-Li for exposure at 800°C is now being reexamined.[11] The quartz ampoule was used to determine if Si dissolved into Pb-Li as part of the evaluation of quartz as a potential loop material. Examining pieces of quartz by x-ray photoelectron spectroscopy (XPS) has indicated that a Li-Si-O likely formed on the surface and possibly Li carbonate. However, more work is needed to examine crystalline Li silicate standards in XPS to clarify which phases formed.

References

[1] M. Abdou, D. Sze, C. Wong, M. Sawan, A. Ying, N. B. Morley and S. Malang, Fus. Sci. Tech., 47 (2005) 475.
[2] J. E. Battles, Intern. Mater. Rev. 34 (1989) 1.
[3] P. Hubberstey, J. Nucl. Mater. 247 (1997) 208.
[4] S. Ukai and M. Fujiwara, J. Nucl. Mater. 307 (2002) 749.
[5] B. A. Pint, J. L. Moser and P. F. Tortorelli, J. Nucl. Mater. 367-370 (2007) 1150.
[6] B. A. Pint, Fus. Sci. Tech. 52 (2007) 829.
[7] B. A. Pint and K. L. More, J. Nucl. Mater. 376 (2008) 108.
[8] Y. Zhang, B. A. Pint, K. M. Cooley and J. A. Haynes, Surf. Coat. Tech. 202 (2008) 3839.
[9] B. A. Pint, Oxid. Met. 45 (1996) 1.
[10] J. L. Smialek, Met. Trans. 9A (1978) 309.
[11] B. A. Pint and J. L. Moser, DOE/ER-0313/40 (2006) 116.

SEVERE EMBRITTLEMENT OF NEUTRON IRRADIATED AUSTENITIC STEELS ARISING FROM HIGH VOID SWELLING – V. S. Neustroev (Research Institute of Atomic Reactors, Dimitrovgrad, Russia) and F. A. Garner (Pacific Northwest National Laboratory, Richland WA USA)

OBJECTIVE

The objective of this effort is to define the microstructural origins of radiation-induced embrittlement in stainless steels used to construct fission and fusion energy-producing devices.

SUMMARY

Data are presented from BOR-60 irradiations showing that significant radiation-induced swelling causes severe embrittlement in austenitic stainless steels, reducing the service life of structural components and introducing limitations on low temperature handling especially. It is shown that the degradation is actually a form of quasi-embrittlement arising from intense flow localized deformation with high levels of localized ductility involving micropore coalescence and void-to-void cracking. Voids initially serve as hardening components whose effect is overwhelmed by the void-induced reduction in shear and Young's moduli at high swelling levels. Thus the alloy appears to soften even as the ductility plunges toward zero on a macroscopic level although a large amount of deformation occurs microscopically at the failure site. Thus the failure is better characterized as "quasi-embrittlement" which is a suppression of uniform deformation. This case should be differentiated from that of real embrittlement which involves the complete suppression of the material's capability for plastic deformation.

PROGRESS AND STATUS

Introduction

It is known that a loss of ductility is expected in austenitic steels when void swelling arises in fast reactor, fusion and light water reactor environments [1]. The only data available at high swelling levels, however, has been drawn from examination of fuel pin claddings and fuel assembly wrappers from fast reactors such as BOR-60, BN-600 and various western reactors [1–15]. In this paper we concentrate on swelling data derived from fuel pin claddings and fuel assembly wrappers from BOR-60 to demonstrate the parametric dependencies of swelling-induced embrittlement in order to anticipate its behavior in fusion environments.

Experimental Details

Data were developed from conventional flat tensile specimens with gauge sections of $22.5 \times 5.5 \times 1$ mm cut from a hexagonal wrapper and from 2 mm wide ring-pull specimens cut from fuel cladding. Swelling values were determined using an immersion density technique in CCl_4 at room temperature with an accuracy of ±0.2%.

The wrapper was constructed from a titanium-stabilized Russian stainless steel designated Kh18H10T with nominal composition Fe-18Cr-10Ni-0.5Ti. This steel is used in Russian reactors for nuclear applications where AISI 304 would be used in Western reactors. The closest Western analog of the Russian steel is AISI 321 stainless steel. The duct wall was 1 mm thick. The duct was fabricated and then annealed at 800°C for 2 hours, followed by annealing at 600°C for 1 hour.

After removal of fuel and fission products from annealed Fe-16Cr-15Ni-3Mo-Nb cladding of fuel pins irradiated in BOR-60, ring-pull tests were conducted at room temperature using semi-circular mandrels inserted into the rings.

Experimental Observations

Wrapper Specimens

It was observed that the maximum embrittlement zone coincides with the maximum swelling zone in claddings and wrappers rather than with the location of the maximum fluence. This effect is particularly pronounced in fast reactors with lower inlet temperatures such as BOR-60 at 330°. As shown in Figure 1 brittle fracture (defined as strength reduction with zero plasticity) of a Fe-18Cr-10Ni-Ti stainless wrapper at 72 dpa maximum was observed at positions 25-125 mm higher than the core center-plane where the peak flux occurs. As expected, there appears that there is some decrease of strength with increasing irradiation temperature, but as shown in Figure 1 the primary strength reduction for specimens tested at the irradiation temperature arises from the magnitude of swelling.

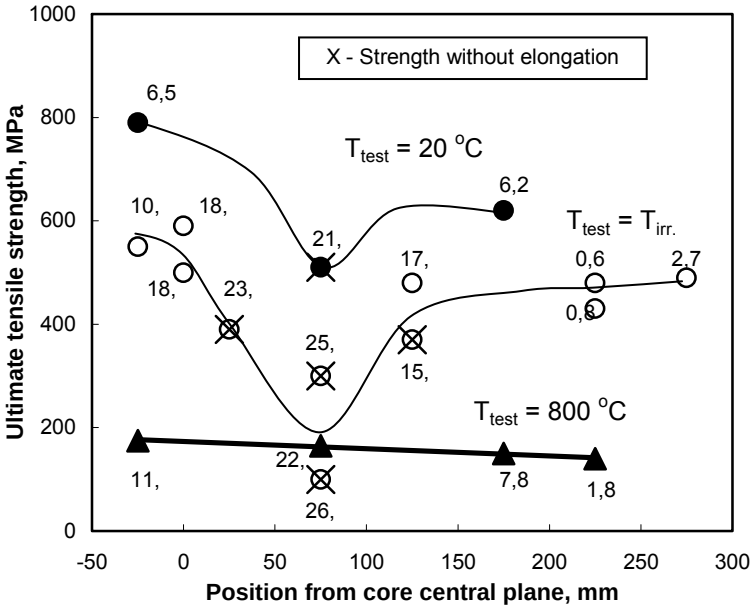

Figure 1. Ultimate tensile strength of Fe-18Cr-10Ni-Ti stainless steel wrapper specimens irradiated in the BOR-60 to a maximum dose of 72 dpa. Three tensile test temperatures are shown: ● – 20, o – 450-550, ▲ – 800°C Swelling values of each specimen are given near the points in units of %.

As also shown in Figure 1 testing at temperatures lower than the irradiation temperature (e.g., 20°C) demonstrates the same dependence on swelling and irradiation temperature but the strength and plasticity values are higher. As expected, the strengths for tests conducted at 800°C is uniformly much lower than that observed at lower temperatures, but there is an absence of any relationship between strength and swelling, with uniform elongation reaching saturation at ~1.2% for ≥10% swelling.

As shown in Figure 2, plotting the strength against swelling for a number of Fe-18Cr-10Ni-Ti wrappers [3, 7, 9, 12, 14] tested at temperatures at or below the irradiation temperature reveals that there is a critical value of swelling (15–20%) where the plasticity is essentially zero.

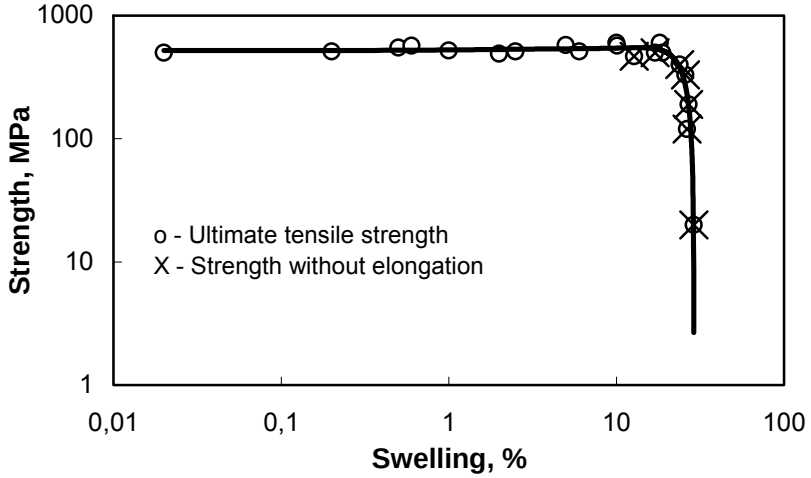

Figure 2. Strength characteristics as a function of swelling of Fe-18Cr-10Ni-Ti steel at irradiation temperatures of 400 to 500°C

The fracture surfaces of wrapper specimens with high swelling values exhibit characteristic features and well-defined zones. Secondary cracks were found along the grain boundaries (Figure 3) and within the grains [14]. A transgranular cup-cone morphology was observed on the fracture surface where failure proceeded by micropore coalescence arising from stress concentration between deforming voids (Figure 4). Similar fracture morphology has been observed in other studies on different stainless steels [1, 15].

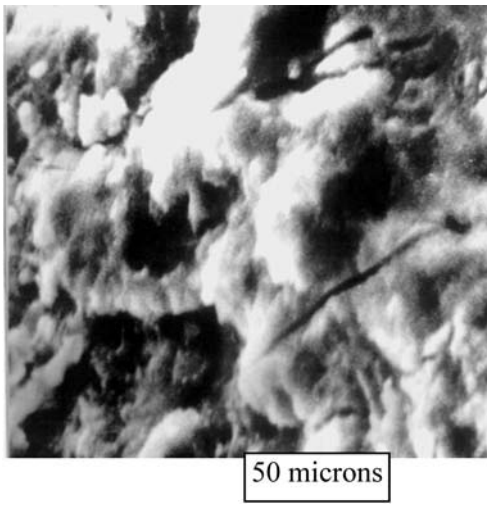

Figure 3. Microcracks on the BOR-60 wrapper fracture surface at the maximum swelling position of 21.7%

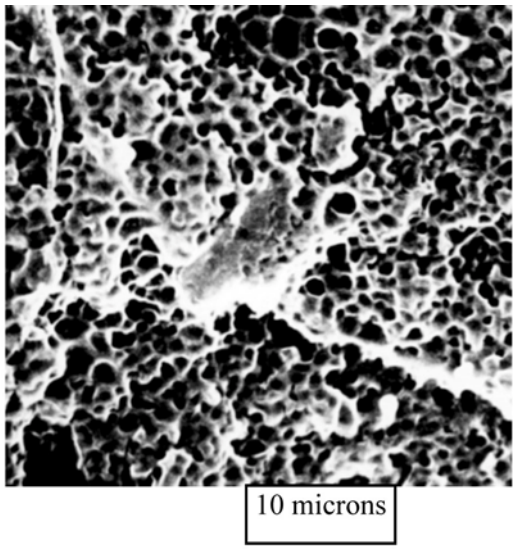

Fig.4. Nature of the fracture surface in the Fe-18Cr-10Ni-Ti stainless steel specimen at a swelling level of 30%

A short inter-particle distance (particles being defined as voids and precipitates) in [3] contributes to a quasi-brittle fracture mode such that as swelling approaches 20% the fracture surface rotates to become perpendicular to the strain axis as shown in Figure 5. In this case the stress-strain characteristics correspond to that of an entirely brittle material that is not capable of strain hardening. Note that the ratio of yield strength and ultimate strength approaches unity when swelling is about 5%.

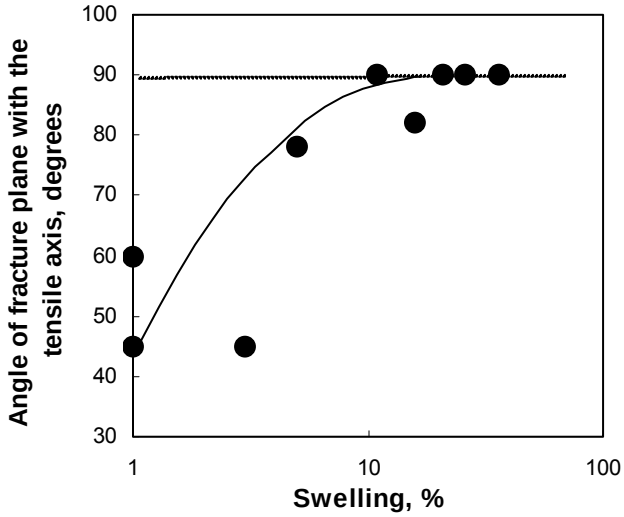

Figure 5. Angle of the fracture surface with the axis of specimen elongation against swelling of Fe-18Cr-10Ni-Ti stainless steel over the test temperature range of 20 to 500°C

Cladding Specimens

When using flat tensile specimens the fracture process in highly swollen steels occurs through crack initiation and growth with cracks often originating within the specimen. In ring-pull specimens tested using semicircular mandrels, the crack leading to failure is almost always observed to initiate on the

inside of the cladding. As shown in Figure 6 comparing tests on flat and ring specimens it is seen that swelling also reduces the ring strength but the critical swelling level is lower (5–10%) and the rate of decrease is not as steep as observed in the flat specimens.

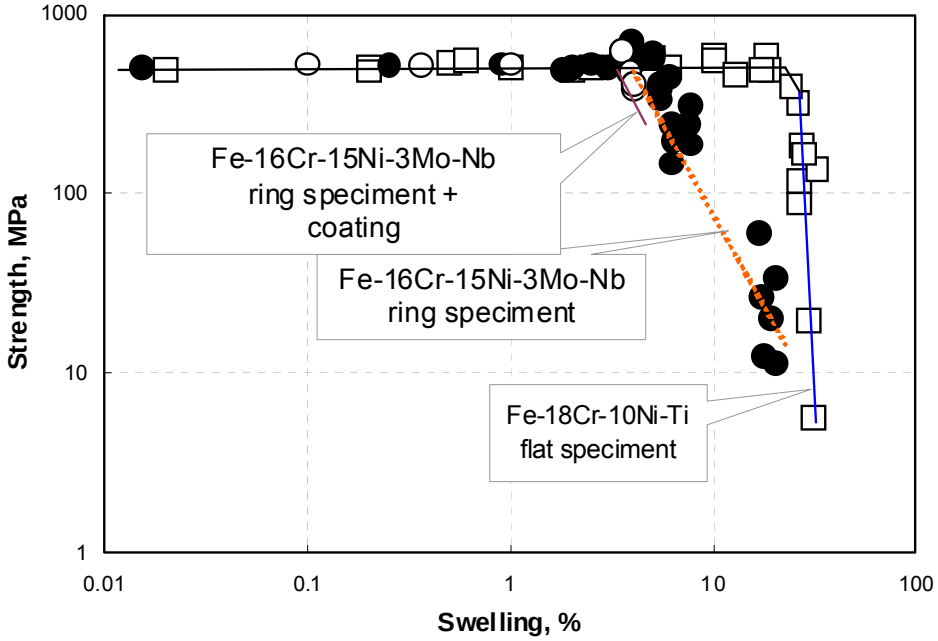

Figure 6. Ultimate strength of austenitic steels irradiated in BOR-60 at a temperature close to the maximum swelling temperature: Fe-16Cr-15Ni-3Mo-Nb stainless steel – ring-shaped specimens with coating (o), ring-shaped specimens without coating (●); Fe-18Cr-10Ni-Ti stainless steel – flat specimens (□)

The ring specimens are subjected to a number of processes that may promote cracking from the inside surface. First, it is known that a change of the surface state arising from a brittle coating can affect the stress-strain properties of the cladding [9]. Such coatings can arise from oxidation and fission product attack, as well as gas injection from neutron collisions with helium cover gas and fission gases. Second, as the test proceeds and the side walls are straightened, the inner surface is preferentially strained with estimates of the strain approaching 3–6%. Third, due to the large temperature gradient across the fuel cladding, the swelling is usually larger near the inner surface. Both the temperature and swelling gradients can result in tensile stresses in the inner layer leading to crack initiation as a rule along the grain boundaries on the inner surface of the fuel rod cladding [11, 13, 15].

Discussion

There are two major questions to address that arise from these studies. First, how general are the conclusions drawn from the current study concerning the behavior of steels in different chemical and thermal-mechanical conditions, especially when irradiated in different reactors at different temperatures and dpa rates? Is it certain that swelling is always the primary determinant of the embrittlement?

We have compiled data in Table 1 from a number of Russian studies [2, 3, 5-14] in the BOR-60 and higher-flux BN-350 fast reactors concerning swelling and stress-strain properties of various austenitic steels. In spite of differences in doses, temperatures and dpa rates the critical values of swelling for ring-shaped specimens cut from claddings made of different steels are nearly the same and within the range of 5 to 10%. This suggests that swelling is the dominant process to initiate cracking in both flat and ring

specimens, but ring specimens experience additional conditions not occurring in flat specimens. To the first order the difference is proposed to arise from the side-wall straightening characteristic of ring-pull tests.

Table 1. Relationship between the temperature extremums of the stress-strain properties and swelling of austenitic steel specimens cut out from cladding and wrappers of fast reactors BOR-60 and BN-600 [2, 3, 5-14]

Steel Grade	Thermal Treatment	Temperature of the Maximum Swelling, °C	Temperature of the Minimum Strength, °C	Temperature of the Minimum Plasticity, °C	Dose of the Drastic Strength Decrease, dpa	Swelling Corresponding to the Strength Decrease,%
Fe-16Cr-15Ni-3Mo-Nb	Annealed	500-520	500-550	400-650	35-40	8-10
Fe-16Cr-15Ni-3Mo-Nb-B	Annealed	500-520	500-530	450-600	55-60	8-10
Fe-16Cr-15Ni-3Mo-Nb-B + rare earths	Annealed	500-520	500-530	500-530	65-70	8-10
Fe-16Cr-15Ni-3Mo-Nb	Annealed	480	440-550	400-590	30-40	6-10
Fe-16Cr-15Ni-3Mo-Nb	Cold worked	445	430-570	430-570	55-60	5-8
Fe-16Cr-15Ni-3Mo-Nb	Cold worked	450	450-480	450-480	50	5-7
Fe-16Cr-15Ni-3Mo-Nb-B	Cold worked	450	500	450-480	60-65	5-9
Fe-16Cr-15Ni-2Mo-2Mn-Ti-V-B	Cold worked	480	440-500	400-500	60-70	5-10
Fe-18Cr-10Ni-Ti	Annealed	500-520	480-530	450-550	35-40	15-20

Note that one third of the critical swelling value (5-10%)/3 produces linear strains of ~ 2–3% for ring-shaped specimens and (15–20%)/3 = ~ 5–7% for flat specimen. The difference between the two sets of strain ranges is 3–4% which is comparable to the estimated side-wall straightening strains of 3–6%.

The second question involves the origin of the reduced strength and concurrent reduction in ductility. Although voids initially serve to harden the microstructure [16], large swelling levels allow previously second-order void effects to become dominant [17]. The most consequential of these second-order effects is the strong decrease of elastic moduli at high swelling levels. All of the elastic moduli are well-known to decrease initially at ~2% per each percent of void swelling [18–22]. At >15% swelling this leads to significant reduction in strength.

As a consequence the slope of the elastic region (Young's modulus) of the stress-strain curve decreases, and more even more importantly the barrier strengths of all sinks decrease as the shear modulus likewise decreases. Therefore the yield and ultimate strengths decrease with increasing swelling, even though the elongation strongly decreases. Similar behavior has also been observed in pure copper [23].

On a macroscopic level the elongation plunges toward zero although a large amount of deformation occurs locally at the failure site. Therefore we should characterize the failure as occurring by "quasi-embrittlement" which is a suppression of uniform deformation, and this mechanism should be differentiated from that of real embrittlement which involves the complete suppression of the material's capability for plastic deformation.

There is another late-term form of embrittlement that arises at the highest swelling levels. As shown by Hamilton and coworkers segregation of nickel to void surfaces causes martensitic instability in the matrix, especially at the crack tip. This in turn produces a tearing modulus of zero and transgranular failure with the failure surface completely coated with alpha martensite [24]. Others have noted this instability [15].

In this case there is total suppression of capability for plastic deformation. One of the consequences of this instability is that the failure surface becomes perpendicular to the strain direction as was also observed in this study. When this mechanism comes into play, however, the microstructure has already evolved to the point where failure is guaranteed.

Conclusions

While voids initially serve to harden the matrix of austenitic steels, increasing levels of swelling cause strong decreases in the elastic moduli, giving rise to a softening of strength in uniaxial tensile tests even as the plastic deformation plunges toward zero as a result of localized deformation. On the failure surface there is a large amount of deformation which proceeds via micropore coalescence upon reaching some critical swelling level. This in turn generates internal cracks that eventually lead to failure. In some situations such as in ring-pull specimens there are nonuniform strains developing during the test such that the critical swelling level for zero plasticity is lower than that of uniaxial tensile tests.

References

[1] F. A. Garner, Irradiation Performance of Cladding and Structural Steels in Liquid Metal Reactors, Materials Science and Technology: A Comprehensive Treatment, Volume 10A, VCH Publishers (1994), 419-543.

[2] V. S. Neustroev, V. N. Golovanov, A. V. Povstyanko and V. K. Shamardin, “Change of mechanical properties of the 0Х16Н15М3Б steel within the irradiation-induced swelling temperature range”. Preprint. RIAR - 30 (711) M.: TsNIIatominform, 1986.

[3] V. S. Neustroev, V. N. Golovanov and V. K. Shamardin, “Irradiation embrittlement of fuel rod cladding materials and fuel assembly wrappers in the temperature range of the maximum swelling,” Atomnaya Energiya 69 (1990) 223-226.

[4] A. Fissolo, R. Cauvin, J.-P. Hugot, V. Levy, “Influence of swelling on irradiated CW titanium modified 316 embrittlement,” Effects of Radiation on Materials: 14th International Symposium (Volume 2), ASTM STP 1046, American Society for Testing and Materials, Philadelphia, (1990) 700-713.

[5] S. A. Averin, V. A. Safonov and M. I. Solonin, “Physical aspects of fuel rod cladding damage in nuclear reactors,” VANT. Ser.: FRPiRM, edition 3(54), (1990) 62-68.

[6] V. Vorobiev, V. D. Dmitriev, A. G. Vakhtin etc., “Examination of mechanical properties of austenitic steels 0Х16Н15М3Б, 0Х16Н15М3БР, 0Х16Н15М2Г2ТР and ferritic-martensitic steel 1Х13М2БФР irradiated in BN-350,” “Radiation Material Science (Proceedings of the International Conference on Radiation Material Science, Alushta, 22-25 May, 1990). T. Z. Kharkov, 1990. pp. 110-118.

[7] V. S. Neustroev and V. K. Shamardin, “About the relationship between the microstructure and damage nature of the Х18Н10Т irradiated up to 70 dpa,” Atomnaya Energiya 71 (1991) 345-348.

[8] V. S. Neustroev, V. N. Golovanov, A. V. Povstyanko and V. K. Shamardin, “Microstructural aspects of embrittlement in irradiated austenitic steels and alloys,” VANT. Ser.: Material Science and New Materials, Edition 2(26), (1992) 58-64.

[9] V. S. Neustroev, T. M. Bulanova, A. V. Povstyanko and V. K. Shamardin, ‘Swelling-induced embrittlement of irradiated austenitic steels and alloys,” Proceedings of the Third Interindustry Conference on Reactor Material Science, Dimitrovgrad, 27-30 October 1992, , Dimitrovgrad, RIAR, 1994, Vol.2, pp.31-55.

[10] V. V. Chuev, V. N. Lanskikh, A. N. Ogorodov etc., “Service life of fast reactor fuel assemblies,” Examination of Structural Materials of Sodium-cooled Fast Reactor Core Components, Ekaterinburg, Ural Branch of the Russian Academy of Science, (1994) 85-140.

[11] S. A. Averin, Ye. A. Kinev and V. I. Barsanov, “Strength degradation of cold-worked austenitic steels after high dose irradiation,” Proceedings of the Third Interindustry Conference on Reactor Material Science, Dimitrovgrad: RIAR, (1994), 2:5-30.
[12] V. S. Neustroev and V. K. Shamardin,”Medium-temperature irradiation embrittlement of austenitic steels and alloys irradiated in fast reactors,” FMM, Vol.83, #5, (1997) 134-142.
[13] S. A. Averin, A. V. Kozlov and Ye. N. Shcherbakov, “Influence of high dose irradiation on the structure and damage of the 0Х16Н15М3Б steel”. Influence of High dose Irradiation on Core Structural and Fuel Materials in Advanced Reactors, IAEA-TECDOC-1039, VIENNA, (1998) 168-178.
[14] V. S. Neustroev, Z. Ye. Ostrovsky, V. K. Shamardin and V. V. Yakovlev, “Experimental investigation of damage of BOR-60 hexahedral fuel assembly wrappers,” Proceedings of the First Interindustry Conference on Reactor Material Science, Vol.2, Part 2, Dimitrovgrad, (1998) 42-66.
[15] S. I Porollo, A. N. Vorobyev, V. D. Dmitriev, Yu. K. Bibilashvili, I. S. Golovnin, G. V. Kalshnik, V. V. Romaneyev, “Post-irradiation examination of the BN-500 reflector pins,” Proceedings of conference on Fast Reactor Core and Fuel Structural Behaviour, BNES, London, (1990) 237-241.
[16] F. A. Garner, M. L. Hamilton, N. F. Panayotou and G. D. Johnson, "The Microstructural Origins of Yield Strength Changes in AISI 316 During Fission or Fusion Irradiation," J. Nucl. Mater., 103 and 104 (1981) 803-808.
[17] F. A. Garner and M. B. Toloczko, "High Dose Effects in Irradiated Face Centered Cubic Metals," J. Nucl. Mater., 206 (1993) 230-248.
[18] J. L. Straalsund and C. K. Day, Nuclear Technology, 20 (1973) 27.
[19] M. Marlowe and W. K. Appleby, Transactions ANS 16 (1973) 95-96.
[20] R. L. Trantow, “Ultrasonic Measurement of Elastic Properties in Irradiated 304 Stainless Steel,” Hanford Engineering Development Laboratory report HEDL-TME-73-92, 1973.
[21] I. I. Balachov, F. A. Garner, Y. Isobe, M. Sagisaka and H. T. Tang, “NDT Measurements of Irradiation Induced Void Swelling,” 11th International Conference on Environmental Degradation of Materials in Nuclear Power Systems – Water Reactors, (2003), 640-646.
[22] I. I. Balachov, E. N. Shcherbakov, A. V. Kozlov, I. A. Portnykh and F. A. Garner, “Influence of Irradiation-Induced Voids and Bubbles on Physical Properties of Austenitic Structural alloys,” J. Nucl. Mater. 329-333 (2004) 617-620.
[23] K. R. Anderson, F. A. Garner, M. L. Hamilton and J. F. Stubbins, "Mechanical Property Changes and Microstructures of Dispersion-Strengthened Copper Alloys After Neutron Irradiation at 411 and 529°C,” Proceedings 15th International Symposium on the Effects of Radiation on Materials, ASTM STP 1125, 1992, R. E. Stoller, A. S. Kumar and D. S. Gelles, Eds., pp. 854-874.
[24] M. L. Hamilton, F. H. Huang, W. J. S. Yang and F. A. Garner, "Mechanical Properties and Fracture Behavior of 20% Cold-Worked 316 Stainless Steel Irradiated to Very High Exposures," Effects of Radiation on Materials: Thirteenth International Symposium (Part II) Influence of Radiation on Material Properties, ASTM STP 956, F. A. Garner, N. Igata and C. H. Henager, Jr., Eds., ASTM Philadelphia, PA, (1987) 245-270.

UNUSUAL ENHANCEMENT OF DUCTILITY OBSERVED DURING EVOLUTION OF A DEFORMATION WAVE IN 12Cr18Ni10Ti STAINLESS STEEL IRRADIATED IN BN-350 – M. N. Gusev, N. S. Silniagina, I. S. Osipov, O. P. Maksimkin (Institute of Nuclear Physics, Almaty, Kazakhstan) and F. A. Garner (Pacific Northwest National Laboratory, Richland WA USA)

OBJECTIVE

The object of this effort is to determine all modes by which irradiated stainless steels respond to stress-induced deformation.

SUMMARY

Whereas most previous irradiation studies conducted at lower neutron exposures in the range 100–400°C have consistently produced strengthening and strongly reduced ductility in stainless steels, it now appears possible that higher exposures may lead to a reversal in ductility loss for some steels. A new radiation-induced phenomenon has been observed in 12Cr18Ni10Ti stainless steel irradiated to 26-55 dpa. It involves "a moving wave of plastic deformation" at 20–60°C that produces "anomalously" high values of engineering ductility, especially when compared to deformation occurring at lower neutron exposures. Due to the concentrated deformation occurring at the wave front, the wave moves much faster than the mechanically applied strain rate. However, when strained at 120°C the moving wave is not observed, indicating that the phenomenon operates at lower test temperatures.

Using the technique of digital optical extensometry the "true stress–true strain" curves were obtained. It appears that the moving wave of plastic deformation occurs as a result of an increase in the intensity of strain hardening, $d\sigma/d\varepsilon(\varepsilon)$. The increase in strain hardening is thought to arise from an irradiation-induced increase in the propensity of the $\gamma \rightarrow \alpha$ martensitic transformation.

PROGRESS AND STATUS

Introduction

It is generally accepted that irradiation of stainless steels at temperatures of 100–400ºC leads to a rapid increase in strength and to a concurrent reduction in both uniform and total elongation during deformation, a behavior that is clearly seen in "engineering" stress-strain curves and that is almost always associated with early flow localization leading to necking [1, 2].

Using a technique called "digital marker extensometry", however, we have shown recently that the stress-strain deformation characteristics (true stress-true deformation) continue unchanged in the necking region even though the remainder of the specimen no longer participates in the deformation process [3, 4].

Another well-accepted perception is that continued neutron exposure quickly leads to a saturation in mechanical properties that remains unchanged until significant void swelling is attained [5-9]. It now appears that this perception must be at least partially modified for relatively low irradiation temperature and very high fluence exposure, especially for steels prone to martensite instability. In this paper we demonstrate that the anticipated trend toward reduced elongation with increasing exposure is reversed at relatively high neutron dose (26-55 dpa).

Experimental details

A hexagonal wrapper constructed from 12Cr18Ni10Ti steel was removed from two spent fuel assemblies designated CC-19 and H-42 after irradiation in the reflector region of the BN-350 fast reactor. The wrapper walls were 2 mm thick with face-to-face distance of 96 mm. The wrapper was formed with a final cold deformation of 15 to 20%, followed by annealing at 800°C for an hour. The irradiation conditions of the examined regions are shown in Table 1.

Table 1. Position and irradiation conditions of investigated samples

Assembly	Distance from the center of the core, mm	Irradiation temperature, °C	Dose, dpa
H-42	-300	290	13
CC-19	+500	423	26
CC-19	-160	310	55

Hexagonal cross sections of 10 mm height were cut at various elevations between +500 mm and –160 mm measured relative to the core center-plane. From these sections flat rectangular specimens of size 20×2×0.3 mm were mechanically produced. Subsequently, mini-tensile specimens with gauge length of 7-10 mm, width 2 mm and thickness 0.3 mm were produced by mechanical grinding and electrolytic polishing to achieve the desired dimensions and surface quality.

Pneumatic grips were used for holding the specimen in an Instron-1195 tensile machine. Uniaxial tensile tests on both unirradiated and irradiated specimens were performed at strain rates of 8.3×10^{-3} sec^{-1}, 8.3×10^{-4} sec^{-1}, and 8.3×10^{-5} sec^{-1}. Most samples were tested at 20°C, but some experiments were conducted at elevated temperatures (up to 120°C).

A technique called “digital marker extensometry” was used which incorporates digital photo or video recording of the specimen during deformation. The surface of the specimen was marked with small (~0.3 mm) dots of dye in order to track the deformation on a local level. This technique was described in an earlier report and is especially useful in observing highly-irradiated miniature specimens subject to intense flow-localization [3, 4]. Application of this technique makes it possible to obtain the “true stress–true strain” behavior for a miniature specimen, as well as to identify the localized deformation region and to trace its evolving geometry during continuous deformation.

The first observation of the moving wave phenomenon was reported recently [10]. This current paper reports on a wider variety of tests conducted to examine this newly discovered deformation mode.

Results

The measured values of strength and ductility are shown in Table 2 for different test temperatures and applied strain rate. The data for strength agree well with most data found in the literature. The observed plasticity in the H-42 assembly (13 dpa) also agrees well with typical literature values.

Table 2. Mechanical properties of investigated samples

Assembly, level, mm	Dose, dpa	Test temperature, °C	Strain rate, s^{-1}	σ_{02}, MPa	σ_B, MPa	ε_u,%	ε_T,%	Presence of wave
H-42	13	20	8.3×10^{-4}	860	1060	<2	6-7	No
CC-19 +500	26	20	8.3×10^{-4}	780	930	18	18.5	Yes
CC-19 +500	26	20	8.3×10^{-3}	800	1030	48	48	Yes*
CC-19 +500	26	20	8.3×10^{-5}	790	950	21	21.5	Yes
CC-19 -160	55	20	8.3×10^{-4}	960	1070	20	22	Yes
CC-19 +500	55	60	8.3×10^{-4}	740	850	40	43	Yes*
CC-19 –160	55	120	8.3×10^{-4}	940	980	~1	<4	No

*Samples having two deformation waves are marked with a star.

In Figure 1 the engineering diagrams of four irradiated specimens are shown. The unirradiated steel is characterized by high ductility and high ability to strain harden with the ultimate strength, $\sigma_{B,}$ significantly greater than the yield strength, $\sigma_{02,}$. Following irradiation to ~13 dpa at 290ºC the yield strength of assembly H-42 strongly increases and a neck develops just after reaching the yield point. The uniform elongation ε_u is very small (<2%) and the total ductility ε_T falls to 6-7%.

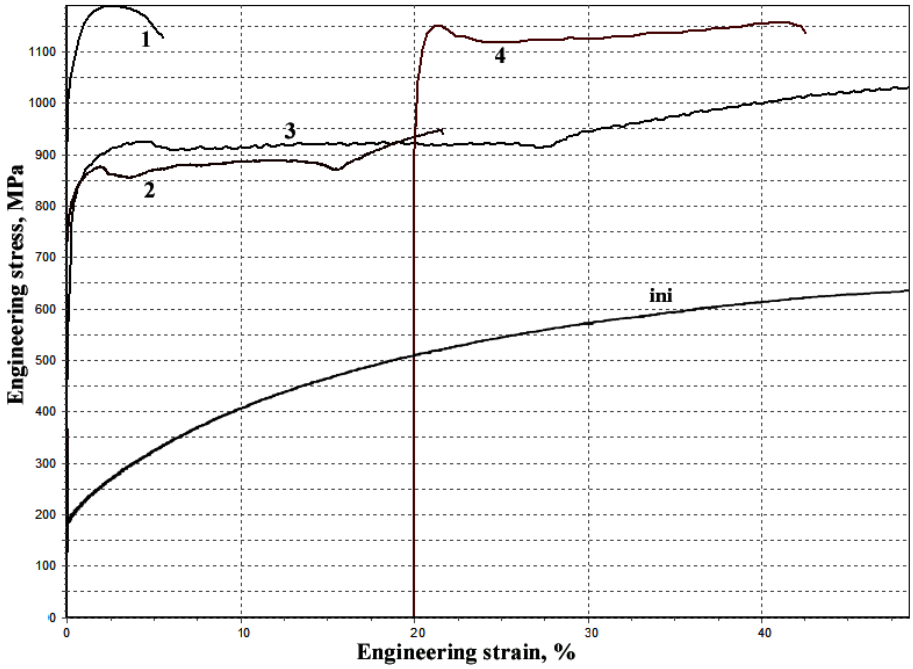

Figure 1. Engineering curves for irradiated samples tested at 20°C (#1 – 13.2 dpa, #s 2, 3 – 26 dpa, #4 – 55 dpa, (this curve was shifted to the right to avoid overlap). Curves 2 and 3 are at the same material and irradiation conditions, with curve 2 showing a single-wave case, and curve 3 showing a double-wave case (see comments in text). The curve designated "ini" is derived from an unirradiated specimen.

Based on current perceptions of saturation, one would expect that steel irradiated up to 55 dpa would achieve deformations <6–7%, even in the absence of void swelling. However, ductility levels of 19 to 48% were achieved in specimens tested at 20-60°C. This result was confirmed by other tests to be typical and not an anomaly. Note that after a small decrease in strength after yielding there is an extended plateau without significant increase in load. When tested at 120°C, however, the ductility fell to <4% and no moving wave was observed. Over the range tested there does not seem to be any significant influence of strain rate (see Table 2, CC-19 assembly, +500 level).

As shown in Figure 2, a series of freeze-frame video images taken during tensile testing at 20°C of a 55 dpa sample shows that localized deformation initially forms near the upper gripper position, most likely due to the stress concentration and triaxiality induced by the gripper. However, in contrast to irradiation to lower doses, a neck did not develop at either 26 or 55 dpa. The localized deformation band instead progressively extended its lower boundary, producing a moving deformation front (deformation wave) that moved down the specimen. The wave moved along ~2/3 of the specimen length producing total engineering deformation on the order of 20%. All of the deformation at a given instant appeared to occur at the wave front with material behind or in front of the wave essentially not participating in the deformation process.

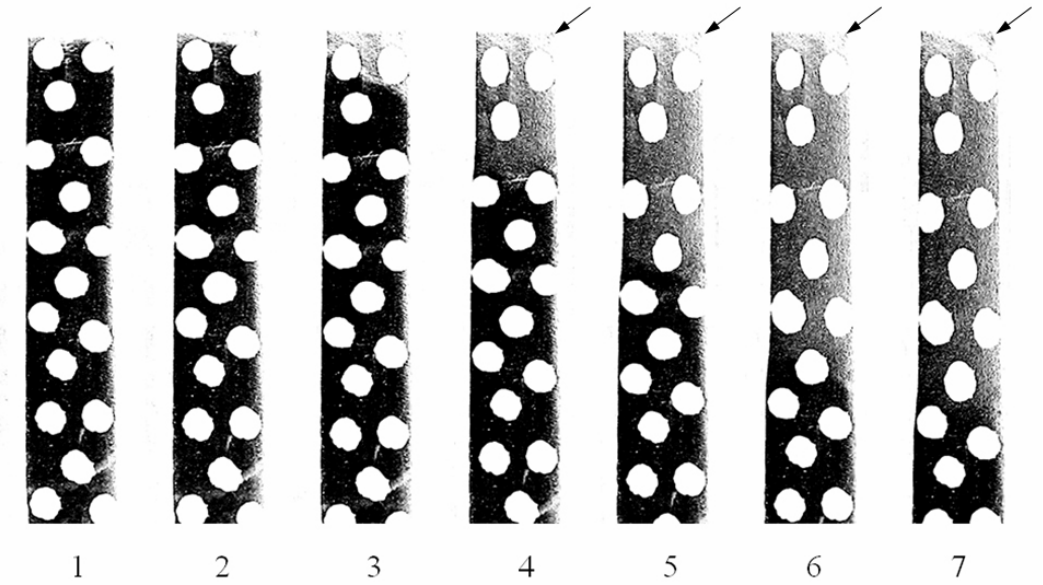

Fig. 2. Freeze frame images taken during deformation at 20°C of a specimen irradiated to 55 dpa. Photographs have been digitally processed to increase the contrast. The boundary between the lighter distorted and darker undistorted areas moves downward with time. Elongated dots behind the boundary also show the local distortion. Arrows on photos 4 through 7 show the second later-developing and immobile neck.

Due to the concentrated deformation occurring at the wave front, the wave moves much faster than the mechanically applied strain rate. For example, in the 55 dpa specimen tested at 20°C the wave front moved at ~0.04 mm/sec while the applied strain rate was only 0.008 mm/sec.

In some cases two deformation waves occurred on a specimen as illustrated in Figure 3. These waves started near each grip and progressed in opposite directions. Usually the second wave begins just after the first wave stops. There was one example, however, where simultaneous movement of two waves was observed. Two waves produced the highest total engineering deformation of 40–48%. In no case was the second wave observed to pass through the terminal position of the first wave.

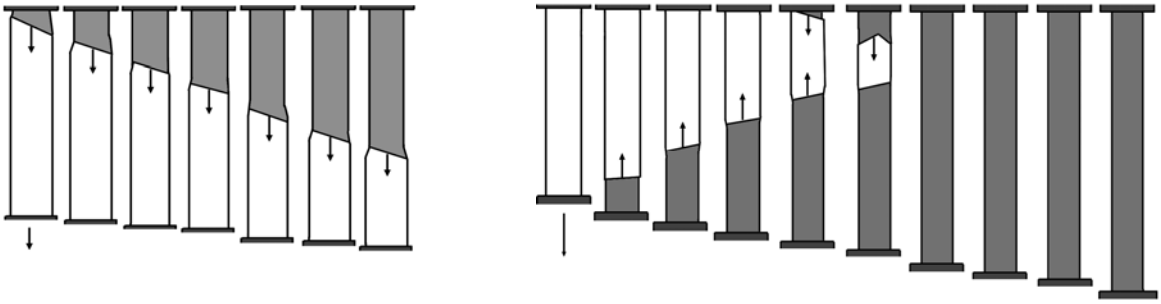

Figure 3. Schematic illustrations of deformation waves for single-wave (left) and double-wave (right) cases. Single wave starts moving from one grip and stops about 2/3 of sample length in both cases. Shortly after the first wave stops the second wave starts from the other grip. In the two-wave case there is no undeformed space remaining on the specimen.

Figure 4 shows the distribution of local deformation over length of a 55-dpa specimen as the test progressed. An abrupt increase in local deformation from zero up to 30 to 35% was observed at the moment the front passed that point. Failure with local deformation exceeding 60% occurred very near to the original place where the deformation wave appeared.

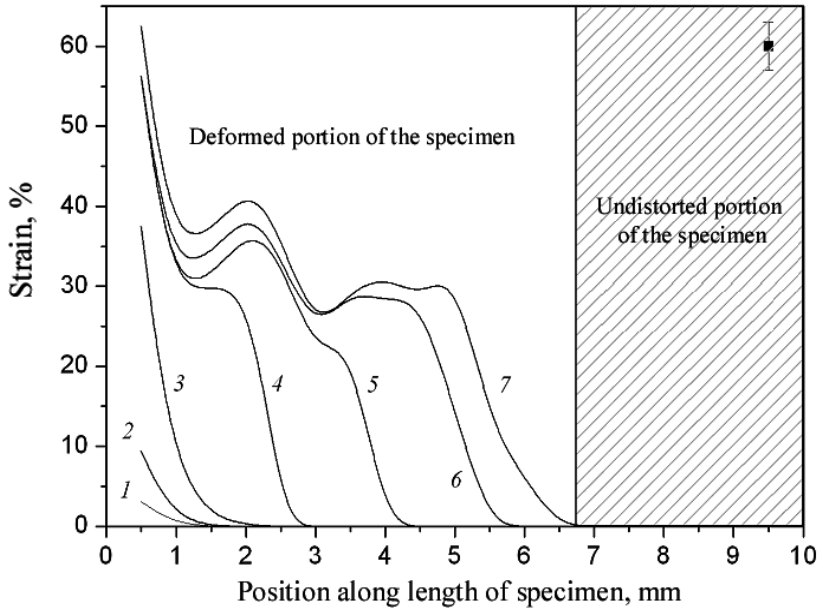

Figure 4. Distribution of local deformation along the length of the specimen irradiated to 55 dpa at various stages of the experiment.

Discussion

The condition for occurrence and development of localized deformation of the neck is [8, 9]

$$d\sigma/d\varepsilon \leq \sigma, \quad (1)$$

which can be rewritten in more convenient form:

$$d\sigma/d\varepsilon - \sigma \leq 0 \quad (2)$$

One can show that localization of deformation in compliance with a given condition starts at the moment when local strain hardening can no longer compensate for geometrical "softening" which occurs as a result of a decrease in the specimen cross section.

It was earlier shown by Byun [11] that for Cr-Ni steels the localized deformation occurs at a stress value σ_L~900 MPa and this value only weakly depends on damage dose. For samples investigated in this study the yield stress exceeds 900 MPa ($\sigma_{02}>\sigma_L$), so localization of deformation occurs immediately after the yield stress is reached.

It's clear that for cessation of local neck formation and displacement of the deformation into neighboring, less deformed space, the law which governs hardening must be altered, i.e., it is necessary that relation (2), on achieving a certain extent of deformation, becomes invalid. As a rule this does not happen in either unirradiated or neutron-irradiated pure metals, where $d\sigma/d\varepsilon$ always decreases as the strain

increases (see unirradiated curve labeled *ini* in Figure 5). If Luders bands are formed, as observed in pure iron, then an exception to this situation occurs.

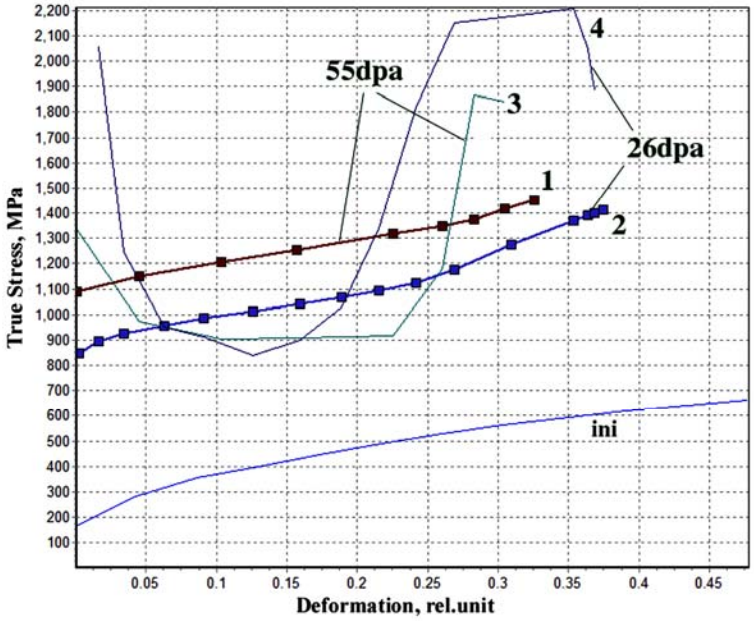

Figure 5. Curves of "σ–ε" (1, 2 , ini) and "dσ/dε-ε" (3, 4) for unirradiated 12Cr8Ni10Ti specimen (ini) and also for 26 dpa (2, 4) and 55 dpa (1 ,3) specimens. The dimensionless scale for dσ/dε-ε is defined as the true stress value divided by 1000 MPa.

Figure 5 presents "stress-deformation" curves obtained using the marker extensometry technique. Note that in 12Cr18Ni10Ti at 55 dpa the initial stage of deformation is close to that of 08Cr16Ni11Mo3 at ~15 dpa. Almost immediately on reaching the yield point, dσ/dε-ε reduces to negative values, and the neck develops. However, in contrast to other materials we have studied, at local deformations of ~25 to 30% a smooth upward trend is observed in the "σ-ε" curve. As dσ/dε increases the value of "dσ/dε-ε" becomes positive, indicating that strain hardening is increasing strongly.

Apparently it is the increase in dσ/dε that leads to suppression of development of a local neck, thereby displacing the deformation source to neighboring, undeformed space, generating the deformation wave. We consider it to be very significant that the second late-forming deformation band could not move through the previously deformed region. It is also significant that at the front of the wave local deformations are very large at >30%.

One potential source of the wave phenomenon is the $\gamma \rightarrow \alpha$ martensitic transformation. This low-nickel steel is known to be very sensitive to strain-induced martensite formation, especially during low temperature deformation, and to increase in propensity toward martensite with radiation-induced hardening and radiation-induced segregation [12, 13]. The fact that this behavior occurs at higher exposures but not at lower doses where saturation of strength had already occurred may reflect some second-order effect such as the progressive transmutation-induced loss of Mn or build-up of V, [14] or the progressive radiation-induced segregation of some other chemical elements. Nickel, in particular is known to segregate at microstructural sinks and chromium migrates away from these same sinks.

Increases in deformation speed from $8.3\times10^{-5}s^{-1}$ to $8.3\times10^{-3}s^{-1}$ (i.e., two orders of magnitude) might be expected to influence the formation of a deformation wave via strain-induced temperature increases, especially if a martensite transformation is occurring, a process known to be temperature-sensitive.

However, such an effect was not observed in this limited series of tests. It is significant, however, that at $8.3\times10^{-4}s^{-1}$ an increase in test temperature from 60 to 120°C led to a cessation of wave behavior.

Similar deformation behavior involving an increase in intensity of strain hardening has been observed in this same steel in the unirradiated condition during deformation at cryogenic temperatures [15]. Intense martensitic transformation was cited as the cause, but the digital marker extensometry technique was not used so it is not certain whether a deformation wave was associated with this behavior.

The possibility exists that this phenomenon may have been observed but not fully appreciated in an earlier study by Lapin and coworkers on this same steel when it was tested at 20°C after irradiation at 100-300°C [16]. They observed a tendency for elongation to exhibit a minimum at relatively low dpa levels and then tend to increase at higher dose. There were no observations made of the mode of elongation or details of the specimen post-tensile morphology, however.

Conclusions

A new radiation-induced phenomenon has been observed in steel 12Cr18Ni10Ti irradiated to 26 and 55 dpa. It involves "a moving wave of plastic deformation" at 20-60°C that produces "anomalously" high values of engineering ductility, especially when compared to deformation occurring at lower neutron exposures or for more stable steels. Using the technique of digital extensometry the "true stress –true strain" curves were obtained. It appears that the moving wave of plastic deformation occurs as a result of an increase in the strain hardening coefficient, $d\sigma/d\varepsilon(\varepsilon)$. The increase in strain hardening is thought to arise from an irradiation-induced increase in the propensity of the $\gamma\rightarrow\alpha$ martensitic transformation.

Acknowledgements

The Kazakh portion of this work was supported by the Ministry of Energy and Mineral Resources of the Republic of Kazakhstan. The United States portion was sponsored by the Office of Fusion Energy Sciences, U.S. Department of Energy under Contract DE-AC06-76RLO at Pacific Northwest National Laboratory.

References

[1] G. Was, Fundamentals of Radiation Materials Science, Springer, 2007.
[2] V.N. Voevodin and I.M. Neklyudov, "Evolution of the structure phase state and radiation resistance of structural materials," Kiev, Naukova Dumka, 2006.
[3] O. P. Maksimkin, M. N. Gusev, I. S. Osipov, "Deformation Extensometry during Mechanical Tests of Highly Radioactive Metal and Alloy Specimens," Information News of the National Nuclear Center of the Republic of Kazakhstan, 2005, Issue 1, pp. 46-52.
[4] M. N. Gusev, O. P. Maksimkin, I. S. Osipov and F. A. Garner, "Application of Digital Marker Extensometry to Determine the True Stress-Strain Behavior of Irradiated Metals and Alloys," Proceedings of 5th International Symposium on Small Specimen Test Technology," recently published in JAI.
[5] F. A. Garner, M. L. Hamilton, N. F. Panayotou and G. D. Johnson, "The Microstructural Origins of Yield Strength Changes in AISI 316 during Fission or Fusion Irradiation," J. Nucl. Mater., 103 and 104 (1981) 803-808.
[6] F. A. Garner, Chapter 6: "Irradiation Performance of Cladding and Structural Steels in Liquid Metal Reactors," Vol. 10A of Materials Science and Technology: A Comprehensive Treatment, VCH Publishers, 1994, pp. 419-543.
[7] M. L. Hamilton, F. H. Huang, W. J. S. Yang and F. A. Garner, "Mechanical Properties and Fracture Behavior of 20% Cold-Worked 316 Stainless Steel Irradiated to Very High Exposures," Effects of Radiation on Materials: Thirteenth International Symposium (Part II) Influence of Radiation on Material Properties, ASTM STP 956, F. A. Garner, N. Igata and C. H. Henager, Jr., Eds., ASTM Philadelphia, PA, 1987, pp. 245-270.

[8] A. M. Parshin, “Structure Resistibility and Radiation Damage in Corrosion-resistant Steels and Alloys,” Chelyabinsk, “Metallurgy,” Chelyabinsk Department, 1988, p. 656 (in Russian).
[9] V. Barabash, G. Kalinin et al., “Materials Challenges for ITER – Current Status and Future Activities,” J. Nucl. Mater. 367-370 (2007) 21-32.
[10] M.N. Gusev, O. P.Maksimkin, I.S. Osipov and F.A. Garner, “A new and unusual deformation behavior observed in 12Cr18Ni10Ti stainless steel irradiated at 307°C to 55 dpa in BN-350,” Proceeding of 13th International Conference on Fusion Reactor Materials, Nice, France, (in press).
[11] T.S. Byun, N. Hashimoto and K. Farrell “Deformation mode map of irradiated 316 stainless steel in true stress–dose space” Journal of Nuclear Materials 351 (2006) 303-315.
[12] O.P. Maksimkin, K.K. Kadyrzhanov , “Martensitic Transformations in Neutron Irradiated and Helium Implanted Stainless Steels,” 21st International Symposium on Effects of Radiation on Materials, ASTM STP1447, 2004, pp.105-118.
[13] E. Nagy, V. Mertinger, F. Tranta, J. Sólyom, “Deformation induced martensitic transformation in stainless steels,” Materials Science and Engineering A 378 (2004) 308–313.
[14] J. F. Bates, F. A. Garner and F. M. Mann, "The Effects of Solid Transmutation Products on Swelling in AISI 316 Stainless Steel," J. of Nucl. Mater., 103 and 104 (1981), p. 999.
[15] T.S Byun., N. Hashimoto, K. Farrell, “Temperature dependence of strain hardening and plastic instability behavior in austenitic stainless steels,” Acta Materialia 52 (2004), 3889-3899.
[16] A. N. Lapin, V. A. Nikolaev and I. A. Razov, Fiz. Khim. Obrab. Mater., No.1 (1970) 9-12.

MACROSCOPIC DEFORMATION MODES AND STRESS PARAMETERS IN METALLIC MATERIALS AFTER LOW TEMPERATURE IRRADIATION – T. S. Byun and K. Farrell (Oak Ridge National Laboratory) and M. Li (Argonne National Laboratory)

OBJECTIVE

The objective of this work is to produce macroscopic deformation mode maps for an extended set of irradiated metallic materials and to characterize the effects of radiation on macroscopic deformation modes and true stress parameters for each material group.

SUMMARY

Macroscopic deformation modes, elastic, uniform plastic, and unstable plastic deformation modes, are mapped in tensile true stress-dose space for more than two dozen metallic materials consisting of 13 bcc, 11 fcc, and 2 hcp metals irradiated at low temperatures (≤ 200^{o}C). The boundaries between different deformation regions are set by the yield stress (YS), plastic instability stress (PIS), and true fracture stress (FS) versus dose curves. The annealed fcc metals display large uniform plasticity regions, while unstable deformation regions are dominant in the harder bcc and hcp metals. The PIS values for all materials are independent of dose except for the precipitation-hardened IN718 alloy where the irradiation-induced phase change reduces its PIS. In the bcc materials for high temperature application, such as 9Cr ferritic/martensitic steels, sintered molybdenum, vanadium, and tantalum, the radiation-induced embrittlement is characterized in terms of FS decreasing with dose at relatively high doses. The FS is nearly dose-independent below the critical dose for the embrittlement. It is concluded that the tensile stress-based deformation mode maps effectively integrate mechanical property information and characterize differences in radiation effects between crystalline structures or material groups. Also, the analysis results indicate that the low temperature irradiation does not significantly change the strain-hardening rate of metallic materials. Such a dose independence in strain hardening behavior results in strong linear relationships between the true stress parameters.

PROGRESS AND STATUS

Introduction

Irradiation of metallic materials with high energy particles at low temperatures induces formation of numerous tiny defect clusters of nanometer size or larger [1-4]. Such clusters can act as strong obstacles to dislocation glide, and therefore, the microstructural change by low temperature irradiation leads to a significant increase of strength and is usually accompanied by reduction of ductility [2-14]. This report proposes an effective way to interpret and integrate such radiation-induced changes for different classes of materials.

Mapping deformation regimes and mechanisms on a coordinate plane has been regarded as a good method of displaying highly-integrated material property information. Thus far at least two types of deformation maps have been constructed for irradiated materials: Ashby-type deformation mechanism maps on stress-temperature plane [14-19] and Okada et al's strain localization map on strain-dose plane [20,21]. The Ashby deformation map displays the fields of normalized stress and temperature in which a particular mechanism of plastic flow is dominant and is constructed focusing on high temperature deformation, i.e., creep mechanisms. This type of map has been widely used for commercial materials for high temperature applications [17-19]. Recently, Zinkle and Lucas [14] have constructed Ashby-type deformation maps for irradiated and nonirradiated face-centered cubic (fcc) and body centered cubic (bcc) metals. It was concluded that the Ashby deformation maps were useful frameworks for categorizing the effects of irradiation on mechanical behaviors. Okada et al [20] have constructed maps to express irradiation-induced changes in deformation mechanisms on engineering strain-dose plane. Their mapping was based on transmission electron microscopy (TEM) results for pure nickel and gold, and it outlined the borders for localized deformation (channeling) and uniform deformation (dislocation tangling) mechanisms. Similar deformation mechanism maps have been published recently for commercial nuclear

structural alloys such as A533B steel, 316 stainless steel, and Zircaloy-4 [21]. In [20,21] the deformation temperature was fixed at room temperature.

Since deformation mechanisms are closely related to applied stress, the microstructure-based mapping was expected to be more effectively expressed on the true stress-dose plane rather than on the engineering strain-dose plane [13,22,23]. Further, a deformation mechanism map constructed in the true stress-dose coordinate system describes well the whole macroscopic deformation process consisting of elastic, uniform plastic, and unstable plastic deformation regimes [22]. Therefore, mapping tensile deformation modes without overlaying the microscopic mechanisms on them has been attempted for selected nuclear structural materials using true stress parameters such as yield stress (YS), plastic instability stress (PIS), and true fracture stress (FS) [13,23,24]. It was confirmed that the tensile data-based macroscopic mode maps could provide well-integrated information on the macroscopic deformation modes of irradiated and nonirradiated materials [23]. In this report the macroscopic deformation mode maps are presented for extended datasets for irradiated materials, which were produced through more than three dozen irradiation experiments [25-27]. The data are analyzed and integrated into 18 deformation mode maps for individual materials. Also, detailed analyses are performed for the individual dose and stress parameters and their relationships.

Experimental

Materials and Irradiation

This report selects and analyzes 39 datasets from room temperature tensile tests after low temperature irradiations (average irradiation temperature $\leq$ 200 ^{o}C) [26-28]. Table 1 lists those 39 cases and provides corresponding specimen types and irradiation temperatures and dose ranges. Three different types of miniature tensile specimens, SS-3, S-1, and BES/NERI types, were used for the experiments and their gage section dimensions are provided in the notes in Table 1.

Irradiation experiments were performed at two facilities: the Hydraulic Tube facility of the High Flux Isotope Reactor (HFIR) at Oak Ridge National Laboratory and the target area of the Los Alamos Neutron Scattering Center (LANSCE) accelerator at Los Alamos National Laboratory. In the HFIR irradiation facility, the tensile specimens were exposed to fast neutrons (E > 0.1 MeV) for different periods to achieve target damage levels [26]. The irradiation temperature in the HFIR irradiation facility was estimated to be in the range 60-100^{o}C. For the most part, the bare specimens were in direct contact with the flowing water coolant. Those materials that undergo corrosion in water, such as Fe, Cu, Zr, Zr-4, and A533B steel, were vacuum-sealed in aluminum foil envelopes that were compressed against the specimens by the hydraulic pressure during irradiation.

In the LANSCE accelerator, the tensile specimens were irradiated at different locations in the target-area to obtain different irradiation exposures to protons and spallation neutrons [27,28]. The kinetic energy of the incident protons was 800 MeV, and spallation reactions by the protons produced neutrons with a wide range of kinetic energy ($\leq$800 MeV). The protons produced most of displacement damage in specimens located at the front positions of target in the proton beam (p>n area) while the spallation neutrons made more or similar contributions to the damage at the back positions of the target (n>p area).

Specimens in the proton-dominant area, S-1 type specimens, received higher dpa values while those in the neutron-dominant area, SS-3 type specimens, got relatively low doses (< 1 dpa). Total doses for each alloy (from protons plus neutrons) are given in the displacements per atom (dpa) column in Table 1. The maximum temperatures measured by thermocouples were in the range 50-260^{o}C during irradiation.

The chemical compositions and heat treatment procedures are summarized in references [24,27] for the tested alloys and pure metals. Several metals and alloys were used in multiple irradiation experiments in the same or different heat treatment conditions. All tensile tests were conducted at room temperature in screw-driven machines at a strain rate of about 10^{-3} sec^{-1}. Since the differences in the specimen types and in the irradiation facilities did not lead to noticeable differences in the tensile properties [10], data for each material were assembled into a single map ignoring the differences in the procedures prior to tensile testing.

Table 1. Summary of irradiation experiments

Case #	Material	Specimen Type*	Irradiation Facility**	Dose Range, dpa	Irradiation Temperature, ^{o}C
1	A533B	BES/NERI	HFIR (n)	0 – 0.89	60 -100
2	A533B	SS-3	HFIR (n)	0 – 1.28	60 -100
3	9Cr-2WVTa	S-1	LANSCE (n<p)	0 – 10.15	50 - 160
4	9Cr-2WVTa	SS-3	LANSCE (n>p)	0 – 0.12	90 - 260
5	9Cr-1MoVNb	S-1	LANSCE (n<p)	0 – 10.15	50 - 160
6	9Cr-1MoVNb	SS-3	LANSCE (n>p)	0 – 0.12	90 - 260
7	Ta-1W	BES/NERI	HFIR (n)	0 – 0.14	60-100
8	Ta-1W	S-1	LANSCE (n<p)	0 – 7.52	50 - 160
9	Ta-1W	SS-3	LANSCE (n>p)	0 – 0.08	90 - 260
10	Ta-10W	S-1	LANSCE (n<p)	0 – 25.23	50 - 160
11	Ta-10W	SS-3	LANSCE (n>p)	0 – 0.08	90 - 260
12	Fe	BES/NERI	HFIR (n)	0 – 0.79	60 -100
13	Mo (LCAC)	SS-3	HFIR (n)	0 – 0.28	60 -100
14	Mo (PM)	BES/NERI	HFIR (n)	0 – 0.07	60 -100
15	Nb	BES/NERI	HFIR (n)	0 – 0.37	60 -100
16	V	BES/NERI	HFIR (n)	0 – 0.69	60 -100
17	Ta (Aesar-1)	BES/NERI	HFIR (n)	0 – 0.14	60 -100
18	Ta (Aesar-2)	BES/NERI	HFIR (n)	0 – 0.14	60 -100
19	Ta (ISIS)	BES/NERI	HFIR (n)	0 – 0.14	60 -100
20	316	BES/NERI	HFIR (n)	0 – 0.78	60 -100
21	EC316LN	S-1	LANSCE (n<p)	0 – 10.67	50 - 160
22	EC316LN	SS-3	LANSCE (n>p)	0 – 0.12	90 - 260
23	AL6XN	S-1	LANSCE (n<p)	0 – 10.67	50 - 160
24	AL6XN	SS-3	LANSCE (n>p)	0 – 0.12	90 - 260
25	HTUPS316	S-1	LANSCE (n<p)	0 – 4.0	50 - 160
26	HTUPS316	SS-3	LANSCE (n>p)	0 – 0.12	90 - 260
27	Fe-21Ni-16Cr (R)	S-1	LANSCE (n<p)	0 – 11.28	50 - 160
28	Fe-21Ni-16Cr (S)	S-1	LANSCE (n<p)	0 – 11.28	50 - 160
29	Al 1100-0	BES/NERI	HFIR (n)	0 – 1.11	60 -100
30	Al 6061-0	S-1	LANSCE (n<p)	0 – 0.14	50 - 160
31	Al 6061-T651	S-1	LANSCE (n<p)	0 – 0.14	50 - 160
32	IN718-PH	SS-3	HFIR (n)	0 – 1.2	60 -100
33	IN718-SA	SS-3	HFIR (n)	0 – 1.2	60 -100
34	Cu	BES/NERI	HFIR (n)	0 – 0.92	60 -100
35	Ni	BES/NERI	HFIR (n)	0 – 0.6	60 -100
36	Zr-4	BES/NERI	HFIR (n)	0 – 0.8	60 -100
37	Zr-4	S-1	LANSCE (n<p)	0 – 24.58	50 - 160
38	Zr-4	SS-3	LANSCE (n>p)	0 – 0.12	90 - 260
39	Zr	BES/NERI	HFIR (n)	0 – 0.63	60 -100

*Gage section dimensions for SS-3, S-1, and BES/NERI types are 0.76 ×1.52 × 7.62, 0.25 ×1.2 × 5, and 0.25 ×1.5 × 8 mm, respectively. **Irradiation particles: (n) – fast neutron irradiation; (n<p) – high energy protons dominant in the mixture of incident protons and spallation neutrons; (n>p) - fast neutrons dominant in the mixture of incident protons and spallation neutrons. SA - solution annealed; (R) - recrystallized; (S) – single crystal; others were produced by typical heat treatments for each metal or alloy [27].

Calculation of true stress boundaries

Developing a macroscopic deformation mode map in this study is actually a process of drawing boundaries between macroscopic deformation modes based on the tensile test data. Such boundaries are set by the true stress parameters, YS, PIS, and FS, plotted as functions of dose in true stress-dose coordinate system. The methods to obtain the values of these parameters are described in this section,

along with some latest findings and explanations [22-24]. First, the lowest stress parameter YS is obtained directly from tensile test data and it sets the boundary between elastic and plastic deformation regions. It is assumed that any micro-plasticity that occurs before the yield point is within the elastic regime. Throughout this study the lower yield stress is used for the YS if a yield drop occurred; otherwise, the 0.2% elongation offset yield stress is used.

Second, the PIS (σ_{PIS} in mathematical formula) is defined as the true stress version of the ultimate tensile strength (UTS), where the onset of plastic instability (necking) occurs, and sets the boundary between the uniform and unstable plastic flow modes. It is calculated from tensile test data, UTS (= S_{UTS} in equations) and uniform plastic strain ε_U^P , using a constant volume condition for plasticity [24]:

$$\sigma_{PIS} = S_{UTS} \times \exp(\varepsilon_U^P) \qquad (1)$$

For most of the materials studied here, it has been shown that below the critical dose for necking at yield the PIS is nearly independent of dose [24]. Thus, the PIS is regarded as a material-specific constant, or a criterion for plastic instability, for a material in both its irradiated and nonirradiated conditions; the engineering tensile curve after irradiation shows necking at yield when the yield stress is above the plastic instability stress of the nonirradiated material. This criterion was also confirmed to be valid for prestrained (cold-rolled) materials; addition of dislocations at a temperature lower than test temperature did not affect the PIS value [29]. Therefore, the PIS is believed to be independent of radiation-induced defect clusters and dislocation tangles. The dose-independent PIS is not defined when the plastic instability occurs at yield (YS > PIS). The dose at the critical point (YS = PIS) is defined as the dose to plastic instability at yield, D_C [24,30], above which there is no uniform deformation region and the YS and FS curves define the region for unstable (necking) deformation mode.

Third, approximations and iterative calculations are needed to obtain the highest stress parameter, FS, unless reduction-in-area values are measured or the specimen breaks in a fully brittle mode, since the dimension of the localized neck is necessary to calculate true strain at failure. After the onset of necking the stress state at the neck becomes triaxial, and therefore, the tensile stress defined by the load (P) divided by the minimum cross-sectional area of the neck (A_n) becomes the nominal (or axial) stress component in the tensile loading direction, which differs from the effective (or equivalent) stress. The axial and equivalent stresses are identical during uniform tensile deformation [31-33]. Since the stress components in the perpendicular directions are tensile but lower than the axial component, the effective stress is slightly lower than the axial component. A linear strain-hardening model for the effective stress gives an upper limit for the true stress-true strain curve for necking deformation [32]. In the present study, the nominal stress component (P/A_n) is used for true stress, instead of using effective stress, since the nominal stress component measured at fracture is usually regarded as the true fracture stress. A comparison of PIS and average strain-hardening rate (in normal stress units) led to the conclusion that the strain-hardening rate remains nearly unchanged at the PIS level during necking deformation [29]. It was also concluded [22] that the linear stress-strain curve during necking is a satisfactory approximation for the constitutive equation of necking deformation. Note that the equivalence of these two conclusions can be simply proved by applying Considere's instability criterion to the linear strain-hardening equation at the onset of necking.

In modeling a constitutive equation for unstable deformation, it should be considered that the true stress-true strain curve starts from the higher one of the YS or PIS, and the YS can be higher than the PIS after irradiation. Then, the above finding leads to the following linear true stress-true strain relationship in the necking strain range ($\varepsilon_U^P \le \varepsilon^P \le \varepsilon_F^P$) [22,23]:

$$\sigma(\varepsilon^P) = \max(\sigma_{YS}, \sigma_{PIS}) + \sigma_{PIS}(\varepsilon^P - \varepsilon_U^P) \qquad (2)$$

where ε^P, ε_U^P, ε_F^P, σ_{YS} and σ_{PIS} are the plastic strain, the true uniform plastic strain, the plastic strain at fracture, the yield stress, and the plastic instability stress, respectively. Then, the true fracture stress, σ_{FS}, can be calculated by replacing ε^P with ε_F^P in Eq. (2),

$$\sigma_{FS} = \max(\sigma_{YS}, \sigma_{PIS}) + \sigma_{PIS}(\varepsilon_F^P - \varepsilon_U^P) \quad (3)$$

(Note that the stress parameters, σ_{YS}, σ_{PIS}, and σ_{FS}, are defined for mathematical expressions only and are identical to YS, PIS, and FS, respectively.) Also, σ_{FS} can be calculated from the engineering fracture stress S_{FS} using the constant volume condition:

$$\sigma_{FS} = S_{FS} \times \exp(\varepsilon_F^P) . \quad (4)$$

The solution for ε_F^P and σ_{FS} can be obtained by iterative calculations using Equations (3) and (4) and measured tensile data: σ_{YS}, S_{UTS}, S_{FS}, and ε_U^P.

Results and discussion

Maps for bcc materials

Figures 1(a) -1(c) display macroscopic deformation maps for bcc materials based on the dose dependencies of true stress parameters [23]. The map for A533B steel, Fig. 1(a), shows that the YS increases with dose until it nearly saturates at ~ 1000 MPa above 0.1 dpa, making the elastic deformation region larger. The PIS is almost constant in the dose range of 0 – 0.02 dpa and it intersects the YS-dose curve at about 0.02 dpa, which was defined as the critical dose D_C [24,30] for the A533B steel. The A533B map shows that the FS is nearly independent of dose in the dose range of 0 - 1.3 dpa. It has an average value of ~1300 MPa with a large scatter; there is evidence of decrease with dose, which would have been perceived as a sign of embrittlement. Since the average PIS value (~700 MPa) is only about 1.5 times the YS of nonirradiated material (~470 MPa) and the YS increases with dose to make an intercept with the PIS line, the uniform deformation region which is defined by these two parameters is relatively small. This agrees with the relatively small uniform ductility observed in this steel before irradiation (~15%). The necking deformation region is typically a few times larger than the uniform deformation region.

For the ferritic/martensitic steels, 9Cr-1MoVNb and 9Cr-2WVTa, the true stress data after irradiation in spallation conditions to higher doses up to ~10 dpa are presented in Fig. 1(b). The small gap between the YS and the PIS produced a small region for uniform plasticity. The FS varied within a range over a dose range of 0 – 0.1 dpa, while it decreased with dose from the maximum at about 0.1 dpa until it experienced a complete embrittlement (fracture before yield) at 10.2 dpa. Such a decrease in FS indicates that the materials have been partially embrittled between 1 and 10.2 dpa. Since the FS is more than two times higher than the PIS prior to the embrittlement, the unstable deformation region is much larger than the narrow uniform plasticity region. This suggests that the necking deformation in bcc metals (maybe in all hard but ductile metals) should be given more attention in embrittlement analyses.

Figure 1(c) is the deformation mode map for Ta-1W alloy after neutron or neutron plus proton irradiation. Again, the PIS and the FS are nearly independent of dose, while the YS is strongly dose dependent. The PIS and FS values of Ta-1W alloy are in the range 450 – 490 MPa and 1200 – 1300 MPa, respectively. This large difference between the PIS and FS values produced a large plastic instability region. A notable feature found in the map of Ta-1W is that the YS line is far below the FS line at the highest dose 7.5 dpa. This indicates that the Ta-1W alloy may not experience radiation-induced embrittlement until its dose reaches beyond 10 dpa. It is, therefore, predicted that this alloy will retain decent fracture toughness to this dose level because of such high necking ductility.

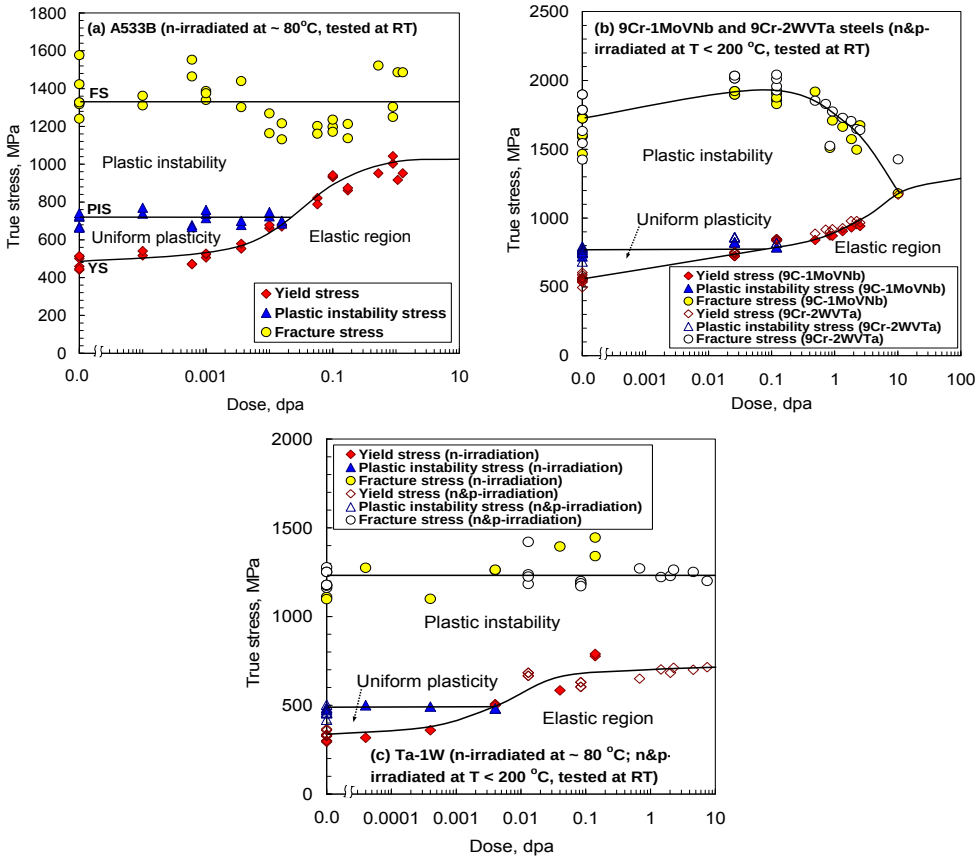

Figure 1. Deformation mode maps for bcc alloys after low temperature irradiation: (a) A533B, (b) 9Cr-1MoVNb and 9Cr-2WVTa, and (c) Ta-1W.

Comparing the sizes of the deformation regions in Fig 1, the deformation mode maps for these bcc materials are characterized by a relatively large plastic instability region and a narrow uniform deformation region. This reflects the common characteristics of bcc metals such as relatively high necking ductility and low strain-hardening rate or low strain-hardening exponent. Deformation maps for other pure bcc metals are presented in Figs. 2(a) – 2(f). In Fig. 2(a) high purity Fe shows rather mild hardening in YS. PIS value is constant at about 320 MPa until the PIS line intersects the YS-dose curve at about 0.2 dpa. Although the FS shows large scatter in the dose range of 0 – 0.79 dpa, the dose dependence is not evident in this range. The average FS is about 490 MPa and is about 1.5 times the average PIS. In keeping with this low FS/PIS ratio, the relative size of unstable plasticity region is smaller than those in the bcc steels described above.

As seen in Figs. 2(b) and 2(c), the map for low-carbon arc-cast wrought molybdenum (LCAC Mo) is a typical one for annealed bcc metal, while the map for sintered-and-wrought PM Mo has the features of a highly embrittled material. In both maps an increase of YS with dose is not observed until the dose reaches 0.001 dpa. Then the YS of LCAC Mo starts to increase until it saturates (or decrease slightly) above 0.1 dpa, while the YS of PM Mo starts to decrease due to severe embrittlement. In the LCAC Mo, both the PIS and FS are constant over the explored dose range. Fig. 2(c) indicates that the FS of PM Mo before irradiation, 860 MPa, is already much below the possible maximum fracture stress for the arc-cast pure Mo, ~1400 MPa, and the FS after irradiation continues to decrease with dose. It is observed in Figs. 1(b) and 2(c) that the FS value decreases with dose or with the degree of embrittlement. Grain boundary embrittlement is known as the main embrittlement mechanism of PM Mo and its alloys [34,35], and no abrupt drop of fracture stress was found in this study. This might indicate that the grain boundaries are

gradually weakening with dose. As a result, the map for this embrittled material has small regions of both stable and unstable deformations.

Other bcc refractory metals, Nb, V, and Ta, have similar maps to the earlier bcc maps, Figs. 2(d) – 2(f). Among these metals Nb has a relatively large uniform plasticity region due to its high strain-hardening capability. V and Ta show embrittlement at the highest doses, 0.69 and 0.14 dpa, respectively (only the ISIS Ta among the three pure Ta metals broke in a brittle mode at the dose). Both of these refractory metals have small uniform plasticity regions and much larger unstable plasticity regions, reflecting their low uniform ductility and high necking ductility. For V and Ta, the doses to plastic instability at yield are noticeably low, about 0.001 dpa, although the FS/PIS ratios are on the high side among the bcc metals, and therefore, most of their total plasticity occurs during necking.

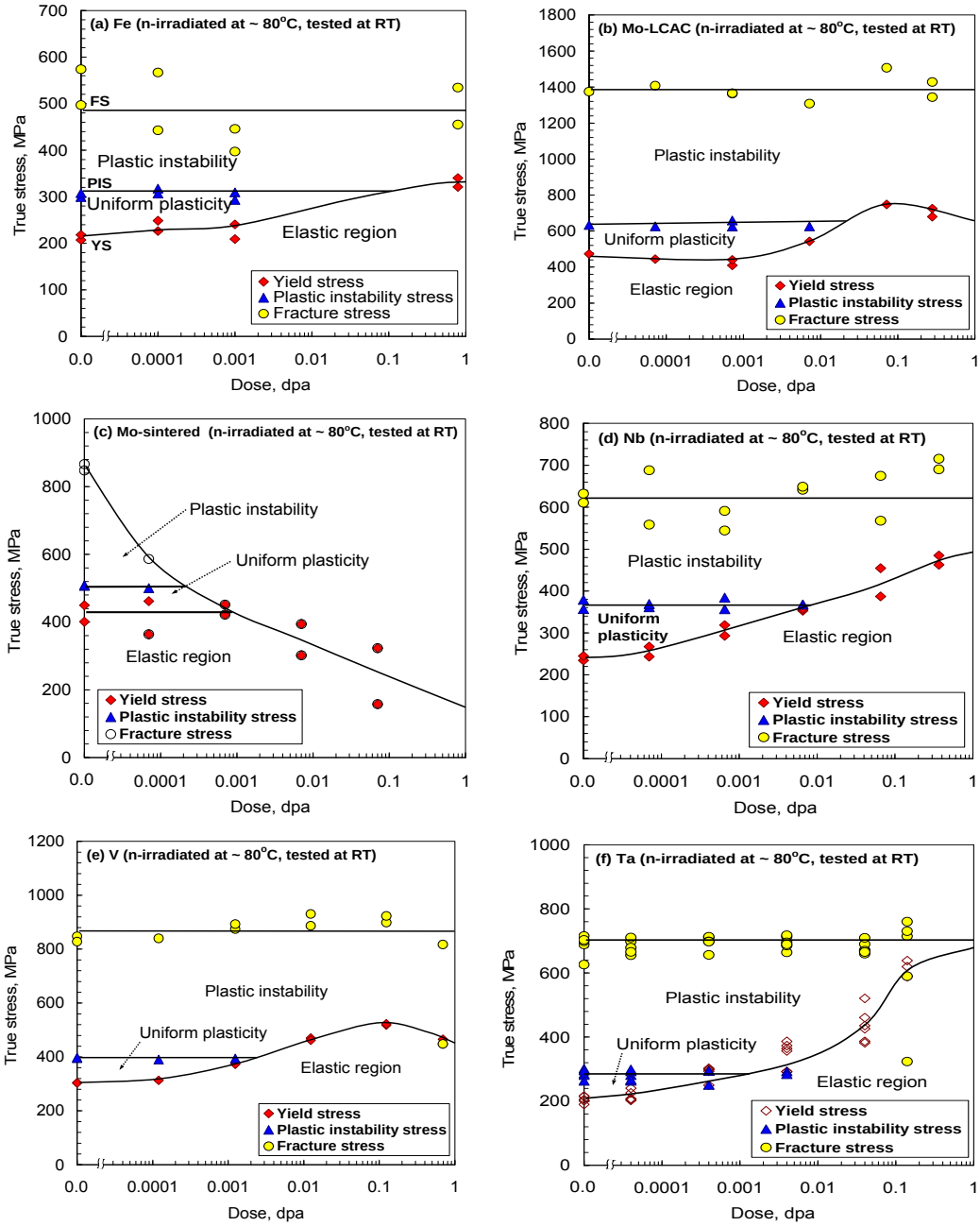

Figure 2. Deformation mode maps for pure bcc metals after low temperature irradiation: (a) Fe, (b) LCAC Mo, (c) sintered Mo, (d) Nb, (e) V, and (f) Ta (all Ta cases).

Maps for fcc materials

Figs. 3(a) – 3(d) present the maps for fcc alloys: annealed 316 and 316LN austenitic stainless steels [23] and solution annealed (SA) and precipitation hardened (PH) IN718 alloy. The PIS and FS values for the annealed alloys are nearly independent of dose, and the span between YS and PIS values before irradiation is wide; the YS values are in the range 230 – 320 MPa and the PIS values in the range 900 – 1300 MPa. This results in large uniform plasticity regions, almost as large as their plastic instability regions, and much larger than the uniform plasticity regions in the bcc metals. In the IN718-PH, however, the PIS decreases with dose in the middle dose range of 0.001 – 0.1 dpa and becomes close to the YS curve. Consequently, this precipitation-hardened material has a relatively small uniform deformation region. It is notable that the YS of this second phase hardened material is nearly stagnant over the test dose range.

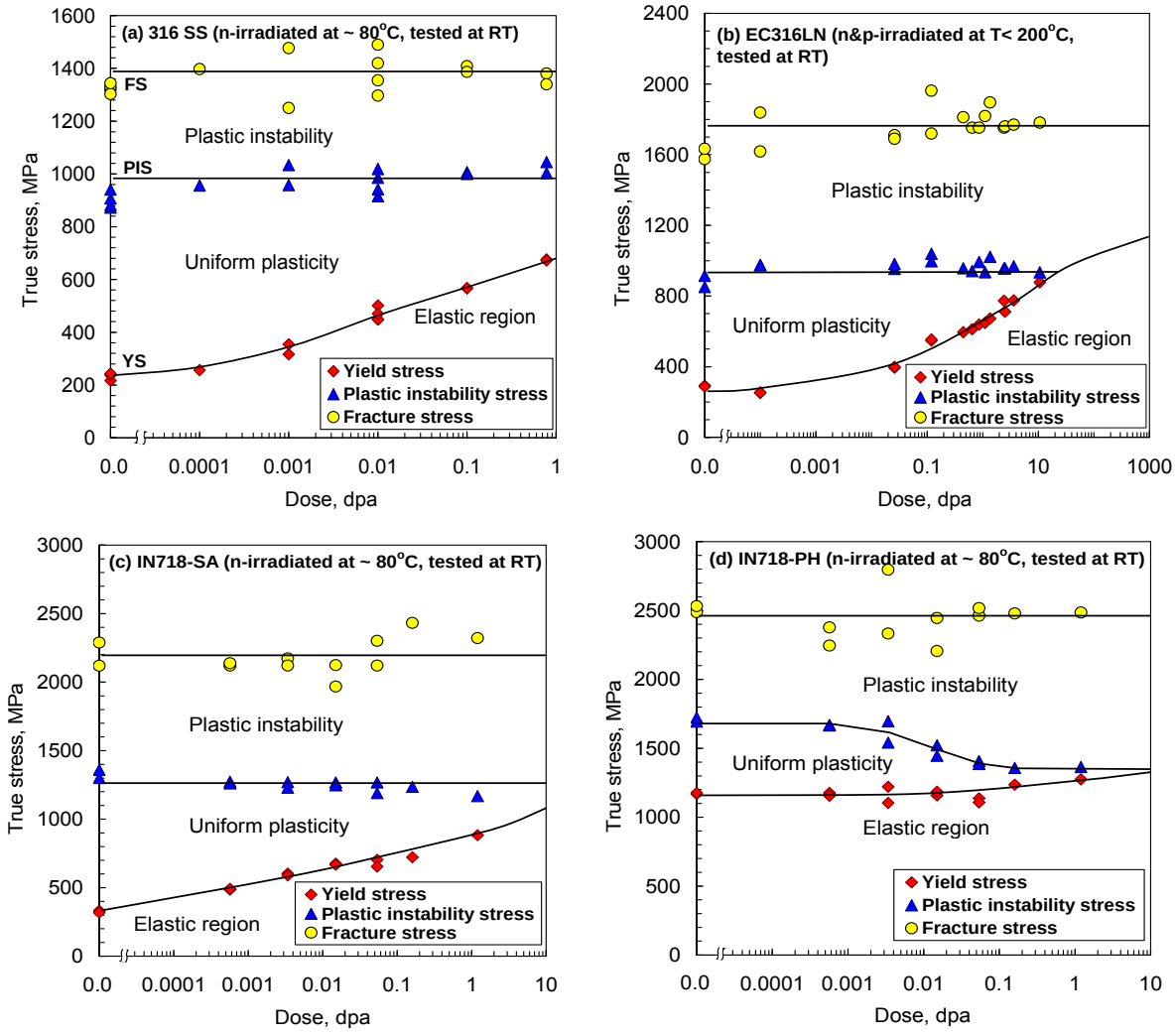

Figure 3. Deformation mode maps for fcc alloys after low temperature irradiation: (a) 316, (b) EC316LN, (c) IN718-SA, and (d) IN718-PH.

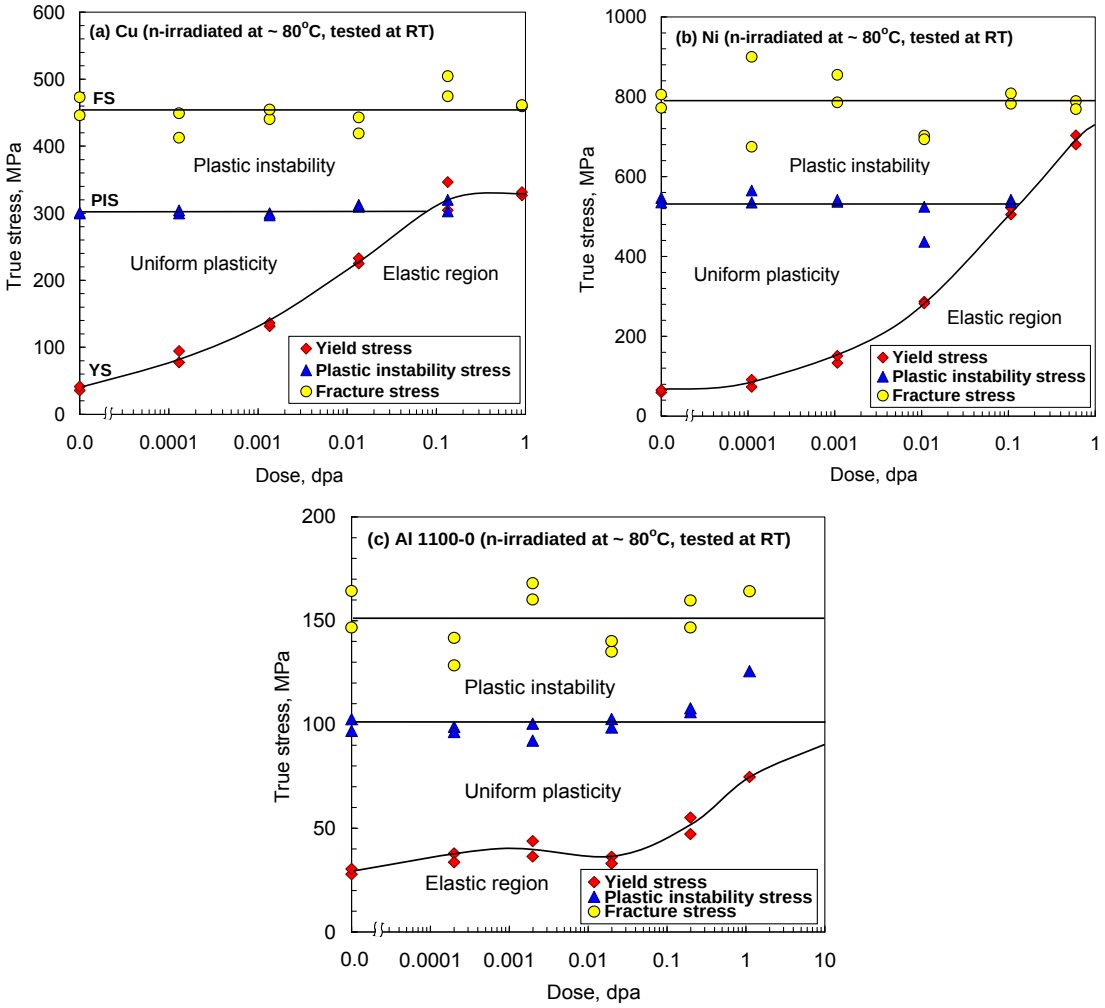

Figure 4. Deformation mode maps for pure fcc metals: (a) Cu, (b) Ni, and (c) Al.

It is also worth noting that the precipitation (or aging) heat treatment increased the YS of IN718-SA more than 3.7 times while it increased the PIS and FS just about 24% and 12%, respectively. These contrasting behaviors between IN718-SA and IN718-PH must be related to differences in microstructural changes occurring during irradiation. The IN718-SA is a single phase, solid solution-hardened material, while in the IN718-PH a high strength composite microstructure is developed during thermal aging by precipitation of spheroidal γ' ($Ni_3(Ti,Al)$) and disk-shaped γ'' (Ni_3Nb) phases in the fcc matrix [12,36]. Dissolution of the hard γ' and γ'' phases in IN718-PH during irradiation at low temperature is claimed to be responsible for holding the yield stress nearly constant with dose [12]. TEM images of the γ' and γ'' phases lost some of their intensity after irradiation to 0.1 dpa with protons and neutrons as disordering occurred in the second phases [36]. At a dose of 0.6 dpa, all evidence of the γ' and γ'' precipitates disappeared from diffraction patterns. Softening from these phase changes was presumably counterbalanced to a large extent by generation of radiation-induced point defect clusters, with a net effect of little change in flow stress [12].

Large uniform plasticity regions are also observed in the elemental fcc metals, Al, Cu, and Ni, Figs. 4(a) – 4(c). This is believed to result from the high strain-hardening capability of annealed fcc metals. Particularly in Cu and Ni, the PIS values are 7 – 9 times higher than their YS values before irradiation. The magnitude of irradiation hardening also extraordinarily high in those two metals; the maximum yield

stresses reached 8 – 11 times the YS values before irradiation. This provides evidence for the assertion that the dislocation tangles accumulated by plastic strain can resemble the damage structure produced by low temperature irradiations [37]. In the commercial grade Al, however, relatively lower hardening is observed, more comparable to those of annealed fcc alloys. Characteristics of necking deformation seem to be similar for all three metals; the distance between the FS-dose and PIS-dose curves are narrower than those in most of the bcc metals. In general, the soft fcc metals are characterized by high strain hardening but relatively rapid progress of necking when it commences.

Maps for hcp materials

Two datasets for Zircaloy-4 (Zr-4) are grouped into one map, Fig. 5(a), and cover a wide dose range of 0 – 24.6 dpa. This map has characteristics of bcc alloys, showing a relatively small uniform plasticity region and a large plastic instability region. The FS shows a small dose-dependence; it increases slightly with dose in the dose range 0 – 2 dpa and then it starts to decrease. As in the tempered martensite steels, this decrease of FS with dose is believed to be caused by a gradual approach of embrittlement. It is observed, however, that the YS is far below the FS even at the highest dose, 24.6 dpa. This implies that the Zr-4 experience a complete embrittlement only at a very high dose. As with the bcc and fcc metals, the PIS for Zr-4 does not show any dose dependence. For the dataset of Zr-4, the average PIS values for respective doses were in the range 500 – 530 MPa and the average FS values in the range 1050 – 1150 MPa; these stress values fall in narrow ranges although the data are obtained from different types of tensile specimens.

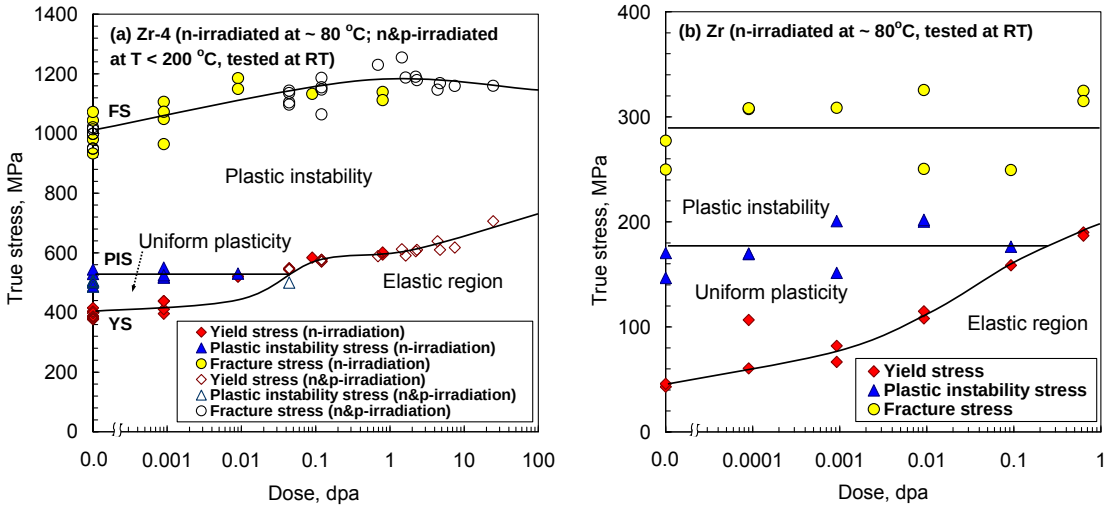

Figure 5. Deformation mode maps for hcp metals: (a) Zr-4 and (b) pure Zr.

Pure Zr is one of the softest materials in the test matrix, along with Al-1100 and Cu. The size of the uniform plasticity region in Zr is comparable to its unstable plasticity region, and the relative sizes of these deformation regions are similar to those of the low strength fcc metals. The PIS and FS of Zr are dose independent in the dose range 0 – 0.8 dpa although they show large scatters. The average PIS and FS values are much lower than those for Zr-4 alloy: 176 and 285 MPa, respectively.

Dose dependence of true strain parameters

Uniform strain and fracture strain data are presented in Fig. 6(a) to 6(c) for selected bcc, fcc, and hcp materials, respectively. In Fig. 6(a) it is observed that the fracture strains for bcc metals are in the range 0.8 – 1.5 before irradiation and start to decrease with dose after 0.001 – 0.1 dpa, while uniform strains never reach 0.2. As implied also in the stress-based deformation maps with the small uniform deformation region and large unstable deformation region, these bcc metals can be characterized by their relatively low uniform strains and predominantly large necking strains. Fracture strain remains almost unchanged over a relatively lower dose range and then started to decrease with dose; in A533B steel, for example, it decreased with dose above 0.001 dpa, and in 9Cr steels above about 0.1 dpa.

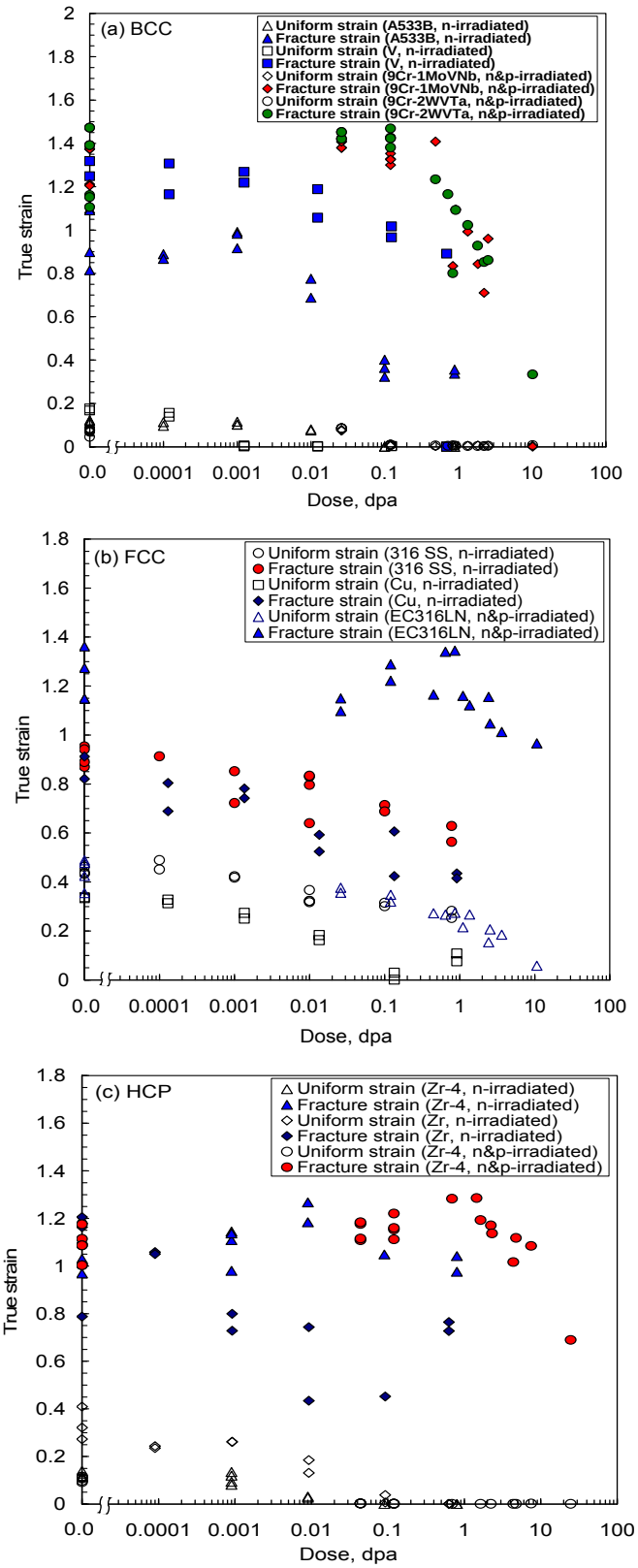

Figure 6. Dose dependence of true strain parameters for (a) bcc, (b) fcc, and (c) hcp materials.

In fcc metals, Fig. 6(b), the uniform strains are relatively higher than those for bcc metals, but fracture strains are similar to those for bcc metals. Also, the uniform and fracture strains for Cu, which is one of the softest materials, tend to be lower than those of stainless steels over the test dose range. As a group, the fcc materials are actually no more ductile than the other materials of different crystal types when compared in terms of true fracture strain. Many fcc metals grouped as highly ductile materials are possibly in an inadequate classification which overly relies on engineering strain terms such uniform and total elongations. The elongation during necking is a much shortened version of true necking strain, influenced largely by the degree of strain localization in the neck. It is also seen that the fracture strains of EC316LN are much higher than those of the standard 316 stainless steel although their uniform strains are nearly on the same trend line. It is believed that the addition of nitrogen in the EC316LN material has decreased its stacking fault energy, and thereby increased its tendency for twinning. In EC316LN the true stress during necking (> 900 MPa) is higher than the twinning stress for the steel, ~ 600 MPa, and therefore, twinning is a common deformation mechanism [38-42]. It is known that such mechanical twinning can increase strain-hardening capability and delay deformation localization and failure [24]. This observation also reminds that a true stress or true strain parameter reflecting both stable (uniform) and unstable deformations should be a consideration when an improved mechanical property is observed.

Fig. 6(c) shows that the dose dependences of the true strains for hcp metals are similar to those of bcc metals. For both pure metals and alloys, the uniform strains decrease to zero at about 0.1 dpa. The fracture strain of Zr-4 is maintained at about 1 up to about 10 dpa; it tends to decrease from about 1 dpa. No zero fracture strain or complete embrittlement was observed in the dataset. The pure zirconium actually shows lower fracture strains than the alloy although its uniform strains are higher. The amount of necking deformation is smaller in the softer pure metal. Before they decreased the fracture strains for these hcp metals were in the range of 0.8 – 1.2, similar to the bcc and fcc materials in Figs. 6(a) and 6(b). It may be a significant finding that the fracture strain is not strongly dependent on crystal structure; it seems to depend more on alloying and heat treatment.

The dose to plastic instability at yield

Since a simple increase of yield stress usually reduces uniform ductility [9], irradiation hardening almost always results in the loss of uniform ductility before embrittlement and eventually eliminates all ductility. It was found that engineering tensile curves showed necking at yield whenever the YS was higher than the dose-independent PIS [23-25,27]. This PIS criterion for plastic instability was also applied to other materials hardened by other types of defects such as dislocation tangles produced by cold working [29]. Thus, it is worth evaluating a parameter that can measure the critical amount of defect accumulation for the moment when the YS reaches the PIS. For irradiated materials, such a critical dose parameter D_C was named the dose to plastic instability (or prompt necking) at yield [24]. In the maps [27], the D_C values are graphically determined at the doses when the YS versus dose curve intercepts the PIS versus dose line. This dose parameter can be regarded as a lifetime for mechanical stability since the materials will show unstable plastic deformation above dose D_C. The D_C values are listed in Table 2, along with the data from earlier work [30,24]. Note that the D_C values beyond the irradiation dose ranges were obtained by extrapolation, and are tentative.

In bcc materials, D_C values ranged from ~0.001 to 0.2 except one pure Fe, which has an outstanding value of 6 dpa for the critical dose [24]. The large difference between the D_C values for the two pure irons is possibly due to their YS difference, which may be related to impurity levels. The YS values prior to irradiation were 213 and 104 MPa, respectively, for the Fe of case 12 and the other pure Fe [24], while their PIS values were similar at about 300 MPa. The bainitic and ferritic/martensitic steels have D_C values in the range of 0.015 – 0.12, which are relatively low when compared to the pure irons but are high when compared to the refractory metals whose values are always below 0.02. It was not possible to determine D_C for the molybdenum produced by powder metallurgy (PM) because of its prompt embrittlement and abnormal tensile behavior. The irradiation responses of the hcp metals, zirconium and Zircaloy-4, are similar to those of bcc metals: 0.004 and 0.009 dpa were obtained for Zircaloy-4 and 0.09 dpa for pure zirconium.

The fcc materials have relatively high D_C values in agreement with the general observation that the fcc materials have higher resistance to irradiation when compared to other crystal types; no D_C value was below 0.1 dpa. All the austenitic steels, cases 20 – 28, and the austenitic IN718 alloy, cases 32 and 33, show very high critical doses of at least 5 dpa. The aluminum alloys and the pure metals, Cu and Ni, have much smaller D_C values: 0.12 to 0.15 dpa. As indicated in the dose-dependence curves of YS and PIS, the critical dose D_C depends on how fast the irradiation hardening ($\Delta\sigma_{YS}$) progresses to bridge the difference that previously existed between the two stresses before irradiation. The deformation maps show that the fcc metals have generally wider uniform deformation regions compared to the bcc and fcc metals. This explains the result that the fcc metals generally take longer irradiation time or dose to reach their PIS values, indicating that in a ductile material its total work-hardening capability matters in the irradiation hardening process.

Table 2. List of the doses, D_C , to cause plastic instability at yield

Case # [Ref. #]	Material	Dose Range, dpa	D_C, dpa
1	A533B	0 - 0.89	0.02
[24]	A533B	0 - 1.2	0.015
2	A533B	0 - 1.28	0.02
[24]	3Cr-3WV	0 - 1.2	0.025
[24]	9Cr-1MoVNb	0 - 1.2	0.034
[24]	9Cr-2VWTa	0 - 1.2	0.054
[24]	9Cr-2WV	0 - 1.2	0.054
3,4	9Cr-2VWTa	0 - 10.2	0.12
5,6	Mod. 9Cr-1MoVNb	0 - 10.2	0.09
7,8,9	Ta-1W	0 – 7.52	0.005
10,11	Ta-10W	0 – 25.23	<0.01
12	Fe	0 - 0.79	0.2
[24]	Fe	0 - 1.07	6
13	Mo (LCAC)	0 – 0.28	0.02
14	Mo (PM)	0 – 0.07	>0.0007
15	Nb	0 - 0.37	0.007
16	V	0 - 0.69	0.0017
17,18,19	Ta	0 – 0.14	0.015
20	316	0 - 0.78	27
[24]	316	0 - 1.2	35
[24]	316LN	0 - 1.2	40
21,22	EC316LN	0 - 10.7	22
23,24	AL6XN	0 - 10.7	17
25,26	HTUPS316	0 - 10.7	5
27	Fe-21Ni-16Cr (R)	0 – 11.28	>11.28
28	Fe-21Ni-16Cr (S)	0 – 11.28	>11.28
29	Al1100-0	0 – 1.11	>1
30	Al6061-Ann	0 – 0.14	>>0.14
31	Al6061-T651	0 – 0.14	>0.14
32	IN718-PH	0 – 1.2	~10
33	IN718-SA	0 – 1.2	>10
34	Cu	0 - 0.92	0.12
35	Ni	0 - 0.6	0.15
36	Zr-4	0 - 0.8	0.009
37,38	Zr-4	0 - 24.6	0.004
39	Zr	0 - 0.63	0.09

Dose independence of strain-hardening behavior

As is displayed repeatedly on in the deformation mode maps [27], the PIS-dose and FS-dose lines are mostly parallel to each other if there is no embrittlement or phase change. This is an expected result from the conclusion of earlier works that the strain-hardening behavior at a given stress is nearly dose independent [23-24,27]. Figs. 3(a) to 3(c) present full true stress-true strain curves for A533B steel, EC316LN stainless steel, and Zircaloy-4, representing bcc, fcc, and hcp materials, respectively (the same curves up to onset of necking were presented in reference [24]). Here, the true stress-true strain curves up to onset of necking were obtained from tensile tests, and then the curves for the necking deformation were drawn by extending the uniform deformation curves to fracture by setting their strain-hardening rates at the PIS values. For each material, the curves for irradiated specimens were shifted along the curve for the unirradiated specimen in the positive strain direction until the irradiated YS intercepted the curve for the unirradiated specimen. As a reminder, the true stress in the unstable deformation region beyond the onset of necking (the straight lines extended to fracture in Fig. 3) is the principal stress component in the tensile direction, and consequently is slightly higher than the equivalent stress [31-33]. Thus, as assumed in the calculation (equation 2), the true stress-true strain curves after yield are close to each other. This close coincidence indicates that irradiation increases only the yield stress without significantly changing strain-hardening behavior afterwards [23,24,33]. An important outcome of this conclusion is that the loss in uniform elongation that accompanies irradiation hardening is not due to an irradiation-induced change in strain hardening behavior. It is caused simply because less strain is required to raise the heightened flow stress to the level of the unaltered plastic instability stress where necking begins.

No apparent embrittlement was observed in these three materials within the test dose ranges; if such embrittlement had occur it would have shortened the curves without changing their slopes or strain-hardening rates [23,33]. Therefore, in metals where no phase change occurs during irradiation, the irradiation effect on true stress-true strain curves can be described as: 1) increases in yield stress and no significant effects on subsequent plastic deformation, and 2) If embrittlement by non-ductile failure occurs, the fracture stress will decrease. These deductions confirm our earlier conclusion [9] that the ductility loss by low temperature irradiation is mostly due to the increase of yield stress, not to a decrease of strain-hardening rate. It can therefore be said that low temperature irradiation narrows the deformation window defined between yield stress and fracture stress. This view challenges the widely-held belief that the loss of uniform ductility after irradiation, prior to necking, is related to a reduction of strain-hardening rate or to the softening effect due to the clearance of radiation-induced defects by glide dislocations [21,30,42-53]. That belief is based largely on reading changes directly from the engineering tensile curves, or by comparing true stresses at a given strain.

Radiation-induced defect clusters such as dislocation loops, stacking fault tetrahedra, and other grown-in dislocations [1-4,45-53] have all dislocation characters such as displacement vectors and stress fields, and hence, they should produce resistance forces to dislocation glide in a similar manner to the strain hardening by dislocation tangles in nonirradiated materials [24]. This should result in similarity of irradiation hardening and strain hardening. Others [37,54-56] have reported the near-invariance of strain-hardening behavior after irradiation. They found that the strain-hardening portions of the flow curves for bcc materials after irradiation to various doses were very similar if compared at the same stress, and that they could be superimposed on the curve for unirradiated material by shifts along the strain axis.

Such near invariance of strain-hardening behavior after irradiation is considered as an unexpected phenomenon if we take into account the fact that the microscopic plastic deformation mechanism usually changes from uniform to localized deformation mode with increasing dose. Localized deformation mechanisms are dislocation channeling, and mechanical twinning. Channeling is found in most metallic materials [21,30,42,46-56]. Twinning is common in hcp, in some bcc metals at cryogenic temperatures, and in low-stacking fault energy materials like austenitic stainless steels [33,42,38-41,57-62]. In a channel a significant drop of local shear stress should occur because of defect clearance in the early stage of channel formation [42,45-53,59]. In twinning of stainless steels, which is developed by a successive glide of partial dislocations on consecutive slip planes, the stress to glide the first partial dislocation is greater

than that for the second and further partial dislocation because only movement of the first dislocation is needed to form the new stacking fault [40,57-59]. Both of these microscopic localization mechanisms can produce softening effects. However, a few earlier studies have shown that the change in deformation mechanism does not significantly affect macroscopic strain-hardening behavior if compared at the same true stresses [23,24,37,54-56,59]. In fact, the microscopic strain localization is believed to be a common phenomenon under any high stress deformation [24]. The localized (channeled) deformation has been reported for many nonirradiated but prestrained metals such as pure copper [50-53], molybdenum [45,60, 61] aluminum [62]. In these results, macroscopic strain-hardening rates were positive despite observation or prediction of localized (channeled) deformation. This implies that microscopic strain localization may coexist with more homogenous bulk deformation without causing significant macroscopic softening.

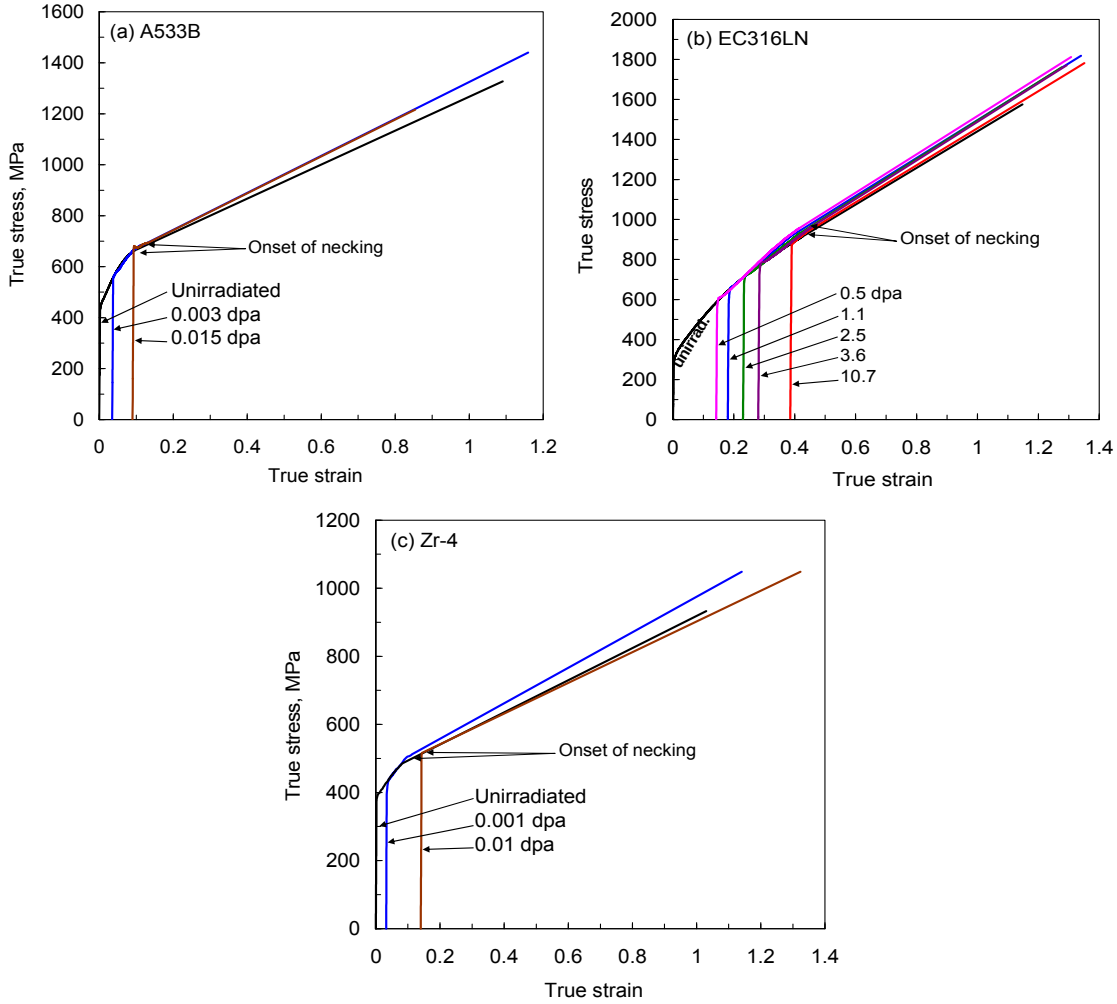

Figure 7. True stress-true strain curves extended to fracture: (a) A533B after neutron irradiation, (b) EC316LN after irradiation in spallation condition, and (c) Zr-4 after neutron irradiation.

A simplified theoretical model in terms of long-range back stress hardening [59,63] was offered to account for this concurrence of local and homogenous plastic deformation. It was devised to explain the strain-hardening behavior during strain localization in irradiated materials. Calculation results showed that in a localized band the local stress lowered by an initial localization process returned quickly to a stress level as high as those in adjacent regions, and the average stress continued to increase as the long-range back stress built up. The residual dislocations at each channel-grain boundary intercept could account for the strain-hardening rates as high as those for the microscopically-uniform deformation by dislocation tangling. This result states that the relatively-short range hardening stress from dislocation

tangling in uniform deformation is replaced by the long-range stress hardening as the plastic deformation is microscopically localized [63].

Linearity between true stress parameters

Since the two true stress parameters, PIS and FS, are nearly dose-independent in certain dose ranges, it should be possible to use the averages of the PIS and FS values as material constants for characterizing deformation of a material or a material group [25]. Also, the yield stress of nonirradiated material, YS(0), is a key property parameter for the reference material. In this section, therefore, an attempt is made to find any consistent behavior such as linearity between those parameters which can characterize material groups or crystal types. Hereafter, the three parameters, YS(0), PIS, and FS, indicate their average values.

As indicated on the macroscopic deformation maps, the strain-hardening capability of a metallic material is directly dependent on the interval between YS and PIS, and hence it is believed that the stress ratio, PIS/YS(0), is an effective parameter to present the capability. The PIS/YS(0) ratios are calculated and presented in Fig. 8 (see Table 3 for the values for individual materials). Fig. 8 displays two roughly linear lines, indicating that the materials can be classified into two groups. The first is a group of high strain-hardening capability with PIS/YS(0) ratios ranging from 3.3 – 8.4. The average PIS/YS(0) ratio was about 3.9 for this materials group, which is given as the slope of the linear line for the group. All annealed fcc metals and pure Zr (open square) belong to this materials group. Since a hcp metal (Zr) is included in this materials group, and the fcc alloys In718-PH and the hcp Zr-4 fall on the line for the bcc group, crystal type is not a sufficient criterion to determine whether a material belongs to a particular group; other factors must play a role.

The second materials group, or lower slope group, includes all bcc pure metals and alloys (thin dashed line), hcp alloy (Zr-4) (solid line), and precipitation hardened fcc alloys such as Al6061-T651 and IN718-PH (open squares). This materials group with lower strain-hardening capability showed PIS/YS(0) ratios ranging from 1.1 to 1.6, with an average of 1.4; which is just slightly above 1/3 of the average ratio for the softer materials group. The materials showing such low PIS/YS(0) ratios correspond to those with narrow uniform deformation region in the maps, Figs. 1 – 5.

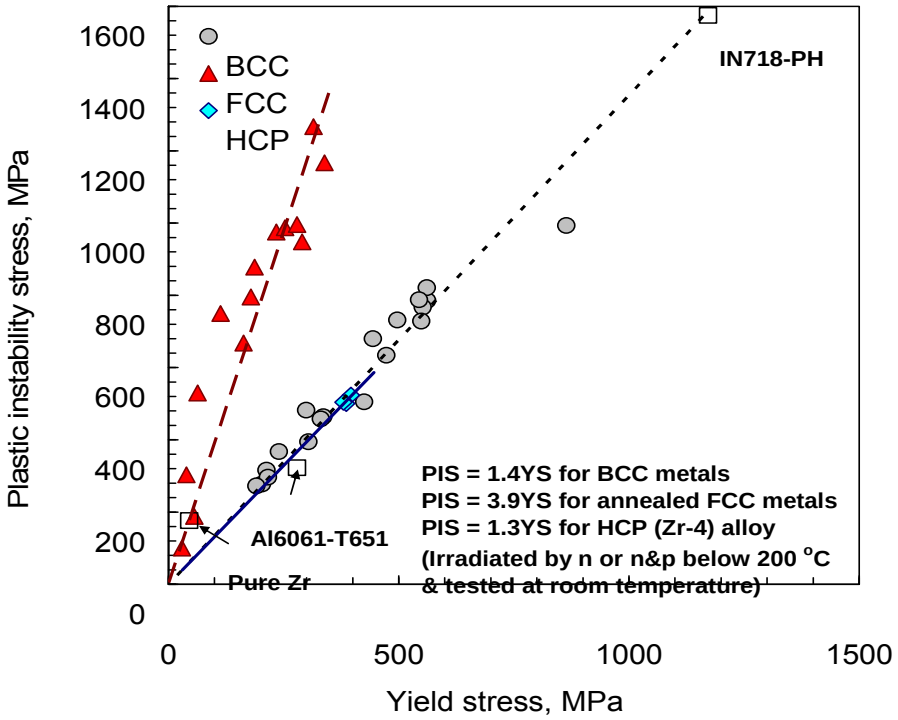

Figure 8. Linear relationship between YS and PIS.

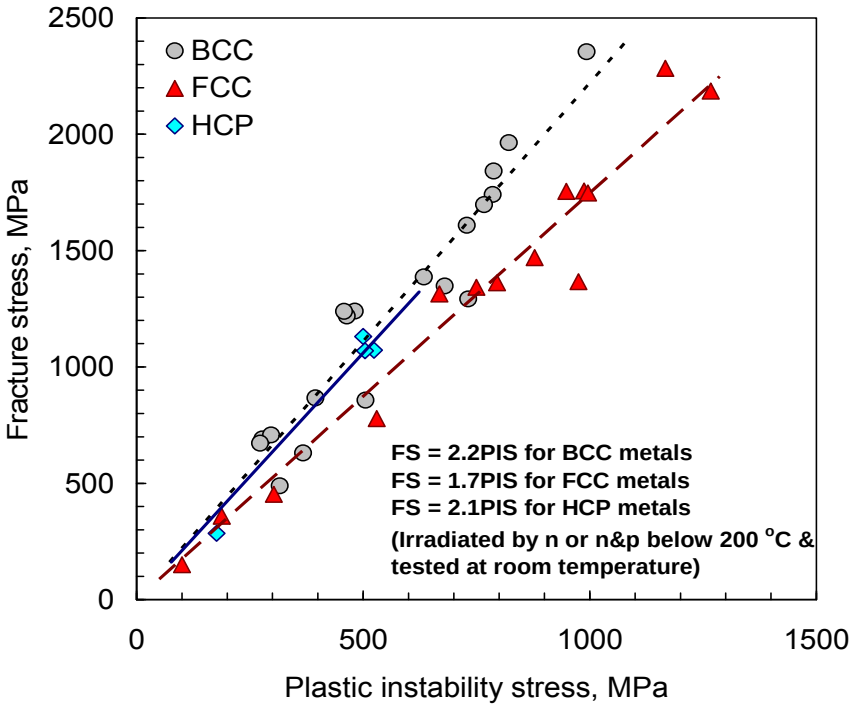

Figure 9. Linear relationship between PIS and FS.

The PIS and FS represent the start and finish of necking deformation, and the necking plasticity and strain-hardening rate will determine the ratio between the two parameters. It was concluded earlier that the strain-hardening rate was nearly independent of dose, and moreover, remained at the PIS during unstable deformation if no embrittlement occurred [23,33]. It is expected therefore that this simple hardening behavior during necking leads to a simple relationship between PIS and FS [23]. Indeed, the calculation results in Fig. 9 display a strong linear relationship between PIS and FS. The FS/PIS ratios for A533B steel, 9Cr steels, and pure refractory metals (Mo, Nb, and V) ranged from 1.7 to 2.4. Also, slightly higher values of 2.2 – 2.7 were calculated for the pure tantalums and the alloys Ta-1W and Ta-10W. Fe showed the lowest value,1.5, among the bcc metals tested.

Slightly lower FS/PIS ratios were calculated for fcc pure metals and alloys than for bcc and hcp metals, and the variations among fcc metals were also lower. The FS/PIS ratios for fcc metals ranged from 1.4 to 2.0. While the FS/PIS ratios obtained for hcp Zircaloy-4 (2.0, 2.1, and 2.3) are similar to those of typical bcc alloys, the ratio for pure Zr (1.6) is close to the lower end values of bcc metals. Thus, the fitting line given for hcp metals in Fig. 5 (solid line) almost coincides with the thin dashed line for bcc materials. As given in Fig. 5, the averages of FS/PIS ratios, or the slopes of fitting lines, were 2.2, 1.7, and 2.1, respectively, for the bcc, fcc, and hcp groupings. It is worth noting that among the tested materials the spread of the FS/PIS ratios over the range 1.4 – 2.7 is smaller than that of the PIS/YS(0) ratios in the range 1.1 – 8.4. This indicates that among the metallic materials less variation in the behavior of unstable tensile deformation is predicted than in the behavior of uniform deformation. This should be because the necking deformation is relatively unaffected by irradiation [25].

The strong relationship between PIS and FS should make it possible to predict FS from PIS, or vice versa. For most ductile materials, this predictability may be retained until the material is embrittled at high doses: for example, lower than 1 dpa for refractory metals, ~1 dpa for non-austenitic steels, and higher than 10 dpa for austenitic stainless steels. Considering that any experimental measurement on necking deformation is difficult, this predictability can be significant for practical use because it enables the prediction of whole necking and fracture process with reasonable accuracy from the uniform deformation

data and PIS value which can be easily obtained from routine tensile tests. If non-ductile failure occurs, however, the FS values decrease with dose and the linearity between PIS and FS will be broken. After a complete embrittlement, or when fracture occurs before the applied stress reaches the yield stress, the FS values may show wider statistical variation and become more sensitive to specimen conditions such as surface flaws, inclusions, geometrical irregularities, etc. No consistent correlation between PIS and FS is expected in such a circumstance.

Table 3. True stress data and stress ratios

Case #	Material	Dose Range, dpa	YS (at 0 dpa/at highest dose), MPa	Average PIS, MPa	Average FS, MPa	PIS/YS(0)	FS/PIS
1	A533B	0 – 0.89	497 / 1023	732	1292	1.5	1.8
2	A533B	0 – 1.28	444 / 952	680	1348	1.5	2.0
3*	9Cr-2WVTa	0 – 10.15	562 / 1170	786	1741	1.4	2.2
4	9Cr-2WVTa	0 – 0.12	561 / 846	821	1964	1.5	2.4
5*	9Cr-1MoVNb	0 – 10.15	552 / 1183	767	1698	1.4	2.2
6	9Cr-1MoVNb	0 – 0.12	544 / 839	788	1842	1.4	2.3
7	Ta-1W	0 – 0.14	299 / 783	482	1276	1.6	2.6
8	Ta-1W	0 – 7.52	336 / 715	464	1219	1.4	2.6
9	Ta-1W	0 – 0.08	331 / 617	458	1239	1.4	2.7
10	Ta-10W	0 – 25.23	864 / 1483	993	2355	1.1	2.4
11	Ta-10W	0 – 0.08	549 / 940	729	1609	1.3	2.2
12	Fe	0 – 0.79	213 / 281	316	489	1.5	1.5
13	Mo (LCAC)	0 – 0.28	473 / 723	634	1387	1.3	2.2
14*	Mo (PM)	0 – 0.07	425 / -	505	857	1.2	1.7
15	Nb	0 – 0.37	240 / 474	368	630	1.5	1.7
16*	V	0 – 0.69	304 / 457	395	867	1.3	2.2
17	Ta (Aesar-1)	0 – 0.14	203 / 595	278	636	1.4	2.3
18	Ta (Aesar-2)	0 – 0.14	216 / 629	297	802	1.4	2.7
19	Ta (ISIS)	0 – 0.14	191 / 590	273	638	1.4	2.3
20	316	0 – 0.78	234 / 674	975	1367	4.2	1.4
21	EC316LN	0 – 10.67	290 / 877	948	1755	3.3	1.9
22	EC316LN	0 – 0.12	253 / 551	987	1757	3.9	1.8
23	AL6XN	0 – 10.67	279 / 980	996	1747	3.6	1.8
24	AL6XN	0 – 0.12	339 / 629	1167	2284	3.4	2.0
25	HTUPS316	0 – 4.0	179 / 791	795	1362	4.4	1.7
26	HTUPS316	0 – 0.12	187 / 517	878	1470	4.7	1.7
27	Fe-21Ni-16Cr(R)	0 – 11.28	113 / 641	750	1343	6.6	1.8
28	Fe-21Ni-16Cr(S)	0 – 11.28	163 / 591	668	1314	4.1	2.0
29	Al 1100-0	0 – 1.11	29 / 97	100	151	3.5	1.5
30	Al 6061-Ann	0 – 0.14	56 / 72	188	359	3.4	1.9
31	Al 6061-T651	0 – 0.14	279 / 279	323	629	1.2	1.9
32	IN718-PH	0 – 1.2	1172 / 1275	1575	2447	1.3	1.6
33	IN718-SA	0 – 1.2	315 / 883	1267	2186	4.0	1.7
34	Cu	0 – 0.92	39 / 329	303	453	7.8	1.5
35	Ni	0 – 0.6	63 / 692	530	778	8.4	1.5
36	Zr-4	0 – 0.8	396 / 598	524	1072	1.3	2.0
37	Zr-4	0 – 24.58	386 / 706	500	1131	1.3	2.3
38	Zr-4	0 – 0.12	380 / 574	504	1069	1.3	2.1
39	Zr	0 – 0.63	45 / 189	176	285	3.9	1.6

* Data for ductile failure only; averages excluded data from embrittled specimens.

Conclusions

The irradiation dose dependencies of the true stress parameters for bcc, fcc, and hcp pure metals and alloys were integrated into 18 deformation mode maps. Conclusions on the maps and true stress parameters are:

[1] Drawing a true stress parameter-based deformation mode map on a true stress-dose plane is an effective way of displaying the deformation data of an irradiated material. The macroscopic deformation mode maps reflect well the characteristics of irradiation effects on mechanical behaviors for individual materials or material groups.

[2] Comparing the extents of deformation regions, the uniform plasticity regions were generally large and dominant in annealed fcc metals, while the unstable plasticity regions were dominant in harder bcc and hcp metals. Large uniform deformation regions in fcc metals were attributed to their higher strain-hardening capability.

[3] The dose independencies of PIS and FS were demonstrated for all the test materials that did not exhibit a phase change or embrittlement. YS increased with dose in all the materials except the IN718-PH where a radiation-induced phase change was suspected to have interfered, as inferred by a decrease of PIS. In some materials signs of radiation-induced embrittlement were indicated by a decrease of FS with dose at high doses.

[4] No obvious dependence of fracture strains on crystal structure was observed, while uniform strains were generally larger in annealed fcc metals than in bcc or hcp metals. Alloys tended to retain fracture strains after irradiation as high as those of softer pure base metals.

[5] Comparison of true stress-true strain curves extended to fracture and overlapped at the same stresses showed that the major effect of low temperature irradiation is to increase the yield stress while not significantly changing the strain-hardening rate. Uniform ductility is shortened because less strain is required to raise the flow stress (the heightened yield stress) to the level of the plastic instability stress where necking begins. Irradiation decreases the fracture stress when non-ductile failure occurs. The insensitivity of strain hardening to irradiation was explained by the result that the relatively-short range hardening stress from dislocation tangling in uniform deformation was replaced by the longer-range stress hardening as the plastic deformation was microscopically localized.

[6] The near dose independences of PIS and FS resulted in strong linear relationships between true stress parameters: average PIS/YS(0) ratios were about 1.4, 3.9, and 1.3 for bcc metals (and precipitation hardened alloys), annealed fcc metals (and pure Zr), and hcp alloy, respectively. The FS/PIS ratios were calculated to be 2.2, 1.7, and 2.1, for bcc, fcc, hcp materials, respectively. These numbers confirm that the annealed fcc metals have larger uniform ductility but smaller necking ductility when compared to the other materials.

Acknowledgements

This research was sponsored by U.S. Department of Energy, Offices of Fusion Energy Sciences and Basic Energy Science, under Contract DE-AC05-00OR22725 with UT-Battelle, LLC. The author expresses special thanks to (Drs. R. L. Klueh and J. T. Busby) for technical reviews and thoughtful comments.

References

[1] Lee EH, Hunn JD, Hashimoto N, Mansur LK. J Nucl Mater **278** (2000) 266.
[2] Singh BN, Foreman AJE, Trinkaus H. J Nucl Mater **249** (1997) 103.
[3] Victoria M, Baluc N, Bailat C, Dai Y, Luppo MI, Schaublin R, Singh BN. J Nucl Mater **276** (2000) 114.
[4] Eldrup M, Singh BN, Zinkle SJ, Byun TS, Farrell, K. J Nucl Mater **307-311** (2002) 912.
[5] Singh BN, Edwards DJ, Toft P. J Nucl Mater **238** (1996) 244.
[6] Koppenaal TJ, Arsenault RJ. Metals Rev **157** (1971) 175.
[7] Pawel JE, Rowcliffe AF, Alexander DJ, Grossbeck ML, Shiba K. J Nucl Mater **233-237** (1996) 202.
[8] Farrell K, Byun TS. J Nucl Mater **296** (2001) 129.
[9] Byun TS, Farrell K, Lee EH, Hunn JD, Mansur LK. J Nucl Mater **298** (2001) 269.
[10] Byun TS, Farrell K, Lee EH, Mansur LK, Maloy SA. James MR, WR Johnson. J Nucl Mater **303** (2002) 34.
[11] Farrell K, Byun TS. J Nucl Mater **318** (2003) 274.
[12] Byun TS, Farrell K. J Nucl Mater **318** (2003) 292.
[13] Byun TS, Hashimoto N. Nucl & Engi Tech **38** (2006) 619.
[14] Zinkle SJ, Lucas GE. Fusion Mater Semiann Prog Rep **DOE/ER-0313/21** (2003)101.
[15] Ashby MF. Acta Met **20** (1972) 887.
[16] Stocker RL, Ashby MF. Rev Geophys Space Phys **11** (1973) 391.
[17] Ashby MF. The Microstructure and Design of Alloys, The Inst Metals and The Iron and Steel Inst, London, **2** (1973) 8.
[18] Frost HJ, Ashby MF. Deformation-Mechanism Maps, Pergamon Press, 1982.
[19] Ashby MF, Materials Selection in Mechanical Design, Pergamon Press, 1992.
[20] Okada A, Kanao K, Yoshiie T, Kojima S. Mater Trans JIM **30** (1989) 265.
[21] Farrell K, Byun TS, Hashimoto N. J Nucl Mater **335** (2004) 471.
[22] Byun TS, Hashimoto N, Farrell K. J Nucl Mater **351** (2006) 303.
[23] Byun TS. J Nucl Mater **361** (2007) 239.
[24] Byun TS, Farrell K. Acta Mater **52** (2004) 597.
[25] Byun TS, Farrell K, M. Li, Acta Mater **56** (2008) 1056.
[26] Farrell K, Byun TS, Hashimoto N. Mapping flow localization processes in deformation of irradiated reactor structural alloys, Oak Ridge National Lab., **ORNL/TM-2003/63** (2003).
[27] Byun TS, Farrell K, Li M, Acta Mater. **56** (2008) 1044.
[28] Farrell K, Byun TS. Tensile properties of candidate SNS materials after irradiation in two neutron areas in the LANSCE accelerator, Oak Ridge National Lab. **SNS/TR-211** (2001).
[29] Byun TS, Hashimoto N, Farrell K. Acta Mater **52** (2004) 3889.
[30] Byun TS, Farrell K. J Nucl Mater **326** (2004) 86.
[31] Bridgman PW. Studies in Large Plastic Flow and Fracture, McGraw-Hill, NY, 1952.
[32] Ling Y, AMP J Tech **5** (1996) 37.
[33] Scheider I, Brocks W, Cornec A. Trans. ASME **126** (2004)70.
[34] Bryhan AJ. Welding Research Council Bulletin **312** (1986).
[35] Miller MK, Kenik EA, Mousa MS, Russell KF, Bryhan AJ. Scripta Mater **46** (2002) 299.
[36] Hashimoto N, Hunn JD, Byun TS, Mansur LK. J Nucl Mater **318** (2003) 300.
[37] DiMelfi RJ, Alexander DE, Rehn LE. J Nucl Mater **252** (1998)171.
[38] Lee EH, Byun TS, Hunn JD, Yoo MH, Farrell K, Mansur LK. Acta Mater **49** (2001) 3269.
[39] Lee EH, Yoo MH, Byun TS, Hunn JD, Farrell K, Mansur LK. Acta Mater **49** (2001) 3277.
[40] Byun TS. Acta Mater **51** (2003) 3036.
[41] Byun TS, Lee EH, Hunn JD. J Nucl Mater **321** (2003) 29.

[42] Byun TS. Hashimoto N, Farrell K. J Nucl Mater **349** (2006) 251.
[43] Tucker RP, Wechsler MS, Ohr SM, J Appl Phys **40** (1969) 400.
[44] Li M, Hashimoto N, Byun TS, Snead LL, Zinkle SJ, J. of Nucl. Mater **367-370** (2007) 817.
[45] Luft A. Pro Mater Sci **35** (1991) 97.
[46] Smidt FA, Jr. Dislocation Channeling in Irradiated Metals, Naval Res. Lab., Washington D.C. **NRL Report 7078** (1970).
[47] Wechsler MS. Dislocation Channeling in Irradiated and Quenched Metals (Ch.2), in: The Inhomogeneity of Plastic Deformation, Amer. Soc. for Metals, Metals Park, Ohio, (1971) 19-54.
[48] Makin MJ, Sharp JV. Phys Stat Sol **9** (1965)109.
[49] Sharp JV. Phil Mag **16** (1967) 77.
[50] Sharp JV. Acta Metal **22** (1974) 449.
[51] Hashimoto N, Byun TS, Farrell K, Zinkle SJ. J Nucl Mater **336** (2005) 225.
[52] Hashimoto N, Byun TS, Farrell K. J Nucl Mater **329-333** (2004) 947.
[53] Hashimoto N, Byun TS, Farrell K. J Nucl Mater **351** (2006) 295.
[54] Mogford IL, Hull D. J Iron & Steel Inst **201** (1963) 55.
[55] Ohr SM. Scripta Metall **2** (1968) 213.
[56] Van Osch EV, DeVries MI. J Nucl Mater **271&272** (1991)162.
[57] Jin Z, Bieler TR. Phil Mag A **72** (1995) 1201.
[58] Jin Z, Bieler TR. Phil Mag A **71** (1995) 925.
[59] Byun TS, Hashimoto N. J ASTM Inter **4** (2007).
[60] Brenner B, Luft A. Mater Sci Engi **52** (1982) 229.
[61] Ritschel C, Luft A, Schulze D. Kristall und Technik **13** (1978) 791.
[62] Cottrell AH, Stokes RJ. Proc Roy Soc **A233** (1955) 17.
[63] Byun TS, Hashimoto N. J Nucl Mater **354** (2006)123

DISSOCIATION OF MIGRATING PARTICLES FROM TRAPS WITH A LONG-RANGE INTERACTION FIELD.- A.V. Barashev (The University of Liverpool), S.I. Golubov (Oak Ridge National Laboratory, *University of Tennessee*), Yu.N. Osetsky and R.E. Stoller (Oak Ridge National Laboratory)

OBJECTIVE

Some lattice defects, such as dislocations, interact with migrating species, e.g. vacancies, interstitial atoms and their clusters, via long-range strain fields. In this paper, an equation for the mean dissociation time of a migrating particle from a trap is derived in terms of the potential well function for the interaction energy. The distribution of dissociation times is studied by the Monte Carlo method, and the problem of particle exchange between spatially separated traps is considered.

SUMMARY

The main results can be summarized as follows:

1. An equation for the mean dissociation time of a migrating particle from a trap has been derived. It is independent of the saddle point energy profile within the well.
2. Generally, the distribution of dissociation times deviates from an exponential function, especially in the regime of small dissociation times. The probability function at the mean time may differ significantly from $1-e^{-1}$, which is for a random process. The effect depends on the well shape (is stronger for shallower and/or wider wells) and on the saddle point energy profile within the well.
3. The exchange frequency for diffusing particles between spatially separated wells is generally many orders of magnitude smaller than the frequency for dissociation from the well, and this is due to correlated recapture of diffusing particles by the same well.

Note also that, in general, the information on the mean dissociation time alone and, hence, the effective binding energy associated with it, is not sufficient to characterise the process completely and the probability distribution function of dissociation times has to be taken into consideration. Work is currently in progress to investigate the description of complexes with a non-exponential distribution of dissociation times by chemical reaction rate equations.

PROGRESS AND STATUS

I. Introduction

Solving various problems of diffusion-reaction kinetics requires knowledge of the time a migrating particle spends trapped by lattice defects before dissociation. This information allows considering longer time and length scales using a rate theory[1] or a kinetic Monte Carlo approach, which treats complexes as single entities. These dissociation times have been or can readily be obtained only in simple cases, e.g. for vacancy-solute pairs with short-range bonding. In more complicated cases, the solution is generally unknown. A particular example of such a case is that of a vacancy executing three-dimensional (3-D) random walk, which is trapped inside a Cu precipitate in an iron matrix (see Refs. [2] to [5] for molecular dynamics results). Another example is that of a one-dimensionally migrating cluster of self-interstitial atoms trapped in a long-range field of an edge dislocation (see, e.g. Ref. [6] for observations in Ni and Mo). Yet another example is that of an interstitial cluster trapped between Cu precipitates in Fe; it can penetrate inside one of them and this requires overcoming an energy barrier (see Refs. [4] and [5] for molecular dynamics results). The importance of the processes mentioned above in microstructure evolution and changes of mechanical properties, especially under irradiation conditions, is discussed in Refs. [1] to [5] for Cu precipitation and, in Refs. [6] and [7], for dislocation decoration with interstitial clusters. In this paper, we first derive an equation for the mean dissociation time for a well of arbitrary shape in Sec. II. We start with a simpler case of one-dimensionally diffusing particles in Sec. II A, and then generalise to higher-D diffusion in Sec. II B. Some particular potential energy wells and limiting cases are considered in Sec. III. Monte Carlo calculations of the probability distribution of dissociation times are presented in Sec. IV for two particular 1-D wells. In Sec. V, we generalise the problem to the case of particle exchange between spatially separated wells for two particular cases: vacancy evaporation from void and interaction of interstitial clusters with dislocation. The conclusions are drawn in Sec. VI.

RESULTS

II. Mean Dissociation Time From Well

A. One-dimensional diffusion

Consider a particle that hops on a lattice containing a potential well $U(x_i)$ (interaction energy in equilibrium positions *i*, see Fig. 1a) in the diffusion direction and 'free' states. The 'free' states are those, where $U(x_i) = 0$ and all the migration barriers are the same as in perfect crystal. The mean time-delay between jumps in these states is denoted by τ. A dissociation event occurs when particle jumps from the well to a 'free' state and an association event is a reverse jump. The dissociation time τ_{diss} is the mean time from association to dissociation. (This definition is discussed further in Sec. IV C and Sec. V.)

Consider a well and one adjacent 'free' state in periodic boundary conditions. In this system, a dissociation event is followed by an association event, hence for each time that particle spends time τ_{diss} on average in the well region, it spends time τ in the 'free' state. Hence, the probability to find particle in the 'free' state is equal to

$$p_{\text{free}} = \frac{\tau}{\tau + \tau_{\text{diss}}}. \qquad (1)$$

The same probability can be written through the partition function of the canonical ensemble $Z = 1 + \sum_{\text{well}} e^{-\beta U(x_i)}$, where $\beta = 1/k_{\text{B}}T$, k_{B} is the Boltzmann constant, T is the temperature and unity corresponds to the 'free' state, where $U = 0$, (see, e.g. Ref. [8]) as:

$$p_{\text{free}} = \left(1 + \sum_{i=1}^{\text{N}} e^{-\beta U(x_i)}\right)^{-1}. \qquad (2)$$

In this equation and further in the text, the summation is taken over all N equilibrium states of the well. From Eqs. (1) and (2) one obtains

$$\tau_{\text{diss}} = \tau \sum_{i=1}^{\text{N}} e^{-\beta U(x_i)} = \tau \text{N} \left\langle e^{-\beta U(x_i)} \right\rangle_{\text{well}}, \qquad (3)$$

where the brackets denote averaging over sites representing equilibrium states of the well.

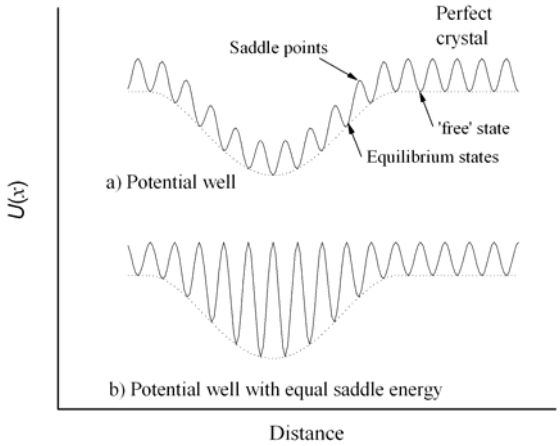

FIG. 1. Schematic diagram showing the potential energy profiles for a migrating particle in a crystal containing a) a potential well and b) a potential well, where all the saddle energies are equal. $U(x)$ is the interaction energy in equilibrium states.

B. Higher-dimensional diffusion

The analysis can readily be extended to two and three dimensionally diffusing particles. Consider a well $U(\mathbf{r}_i)$ of N states surrounded by a shell of adjacent 'free' states, m in total, each separated from the well by one jump distance. Assume that a particle in a 'free' state jumps successfully only to the well. This assumption does not influence the results but makes the derivation easier. It affects, however, the times spent by a particle in 'free' states. If the mean value of these times, τ_{free}, is known, the probability of finding the particle in a 'free' state can be written in two ways: as the ratio of times (left-hand side of the following equation) and via the partition function (right-hand side):

$$\frac{\tau_{\mathrm{free}}}{\tau_{\mathrm{free}}+\tau_{\mathrm{diss}}}=\frac{m}{m+\sum_{i=1}^{\mathrm{N}} e^{-\beta U(\mathbf{r}_i)}}. \qquad (4)$$

Hence, the dissociation time is given by

$$\tau_{\mathrm{diss}}=\frac{\tau_{\mathrm{free}}}{m}\mathrm{N}\left\langle e^{-\beta U(\mathbf{r}_i)}\right\rangle_{\mathrm{well}}. \qquad (5)$$

Now let us find τ_{free}. Under the assumption that a particle in a 'free' state jumps successfully only towards the well, the time spent on average by the particle in a 'free' state *i* before jumping back to the well is higher than τ by the ratio of the total number of jump directions z to the number of directions towards the well, n_i: $\tau_{\mathrm{free}}^{i}=\tau z/n_i$. The mean time is the sum of these times weighted with relative frequency of visiting these states, p_{free}^{i}, which is equal to the ratio of the number of directions from the well to this particular site, n_i, to the total number of directions from the well to 'free' sites, $\sum_{i=1}^{m} n_i$. Hence $p_{\mathrm{free}}^{i}=n_i/\sum_{i=1}^{m} n_i$ and

$$\tau_{\mathrm{free}}=\sum_{i=1}^{m}\tau_{\mathrm{free}}^{i}p_{\mathrm{free}}^{i}=\tau z/\left\langle n\right\rangle_{\mathrm{free}}, \qquad (6)$$

where the brackets denote averaging over adjacent 'free' states. Finally, by substituting Eq. (6) into Eq. (5), one obtains

$$\tau_{\mathrm{diss}}=\frac{z\mathrm{N}}{m\left\langle n\right\rangle_{\mathrm{free}}}\tau\left\langle e^{-\beta U(\mathbf{r}_i)}\right\rangle_{\mathrm{well}}. \qquad (7)$$

This is a general solution valid for any dimensionality of diffusion. In the case of 1-D diffusion, when the total number of jump directions is $z=2$, the number of directions from a 'free' state to the well is $n=1$ and the number of 'free' states adjacent to the well is $m=2$, Eq. (7) reduces to Eq. (3).

We emphasise that Eq. (7) depends on the energy of equilibrium states (the exponent is averaged over these states) but is *independent of the saddle point energy profile within the well*. Note that τ depends on the energy barrier in the perfect part of the crystal only. (Obviously, the probability distribution of dissociation times does depend on the saddle point energy and this is considered below in Sec. IV.)

III. Mean Dissociation Times for Particular Wells

A. 1-D square well

For a square well and coordinate *x* (in units of jump length a)

$$U(x) = \begin{cases} -E, & x_{\min} \le x \le x_{\max}, \\ 0, & x < x_{\min},\ x > x_{\max}. \end{cases} \tag{8}$$

Eq. (3) yields

$$\tau_{\text{diss}} = \mathrm{N}\tau e^{\beta E}, \tag{9}$$

where $\mathrm{N} = x_{\max} - x_{\min}$ is the total number of equilibrium positions inside the well. Hence the frequency of dissociation events is given by

$$\nu_{\text{diss}} = \tau_{\text{diss}}^{-1} = \left(\frac{2}{\mathrm{N}}\right)\frac{e^{-\beta E}}{2\tau}. \tag{10}$$

The physical significance of Eq. (10) can be understood as follows. The bracketed term stands for the probability to find a particle at one of the two well edges, τ^{-1} is the total jump frequency in perfect crystal in both directions, ½ describes the probability to jump towards the barrier and the exponential factor accounts for the decrease of the probability of successful jump due to the barrier.

B. 1-D triangular well

A particular case of a triangular shape well:

$$U(x) = \begin{cases} -E(1 - x / x_{\min}), & x_{\min} \le x < 0, \\ -E(1 - x / x_{\max}), & 0 \le x \le x_{\max} \end{cases} \tag{11}$$

is a more realistic approximation to real situations with no single energy. In this case:

$$\tau_{\text{tri}} = 2\tau e^{\beta E}\frac{\left[1 - e^{-\beta E(1 + x_{\max}^{-1})}\right]}{1 - e^{-\beta E / x_{\max}}}. \tag{12}$$

It can readily be shown that, for deep enough triangular wells, such that $e^{\beta E} >> 1$, the dissociation time is smaller than for a square well of the same depth and width by the ratio of the thermal energy to the well depth. This is due to a smaller effective binding energy.

C. Void

A void can be considered as a well for vacancies. Since vacancies are always at the void surface, $\mathrm{N} = m$ in Eq. (7). Hence, for a large void of radius r_0, such that $\langle n \rangle_{\text{free}} = z / 2$, and the vacancy binding energy $-U = E$, one obtains $\tau_{\text{diss}} \approx 2\tau e^{\beta E}$. The factor of two in this equation accounts for an increase of the time spent by a vacancy in the void, because successful jumps are only in the direction away from the void. The evaporation frequency is, hence, $\nu_{\text{diss}} = e^{-\beta E} / 2\tau$. In equilibrium conditions this frequency equals to that of

the void-vacancy association events: $C_{\mathrm{V}}^{\mathrm{e}} / 2\tau$, hence the equilibrium vacancy concentration near the void is $C_{\mathrm{V}}^{\mathrm{e}} = e^{-\beta E}$ (see Sec. V for derivation). This equilibrium concentration and Eq. (7) can be used to calculate the evaporation rate using the diffusion-reaction theory (see Sec. V below).

D. Vacancy in solute precipitate

For a vacancy and a large solute precipitate of radius r_0 with a constant interaction energy between the vacancy and any site within the precipitate $U = -E$: $\langle n \rangle_{\mathrm{free}} = z/2$, $\mathrm{N} = 4\pi r_0^3 / 3\Omega$, where Ω is the atomic volume, $m = 4\pi r_0^2 a / 2\Omega$, where the surface layer is assumed to be of thickness $a/2$, and, hence, $\nu_{\mathrm{diss}} \approx e^{-\beta E} a / r_0 \tau$. The ratio a / r_0 accounts for the probability to find a vacancy near the surface. Hence, the frequency of dissociation events is equal to the vacancy concentration near the surface times the frequency of jumps away from the precipitate, which seems to be an obvious description in such a simple case. To take into account the interaction energy profile $U(x_i)$ within the precipitate, one should use $\left\langle e^{-\beta U(\mathbf{r}_i)} \right\rangle_{\mathrm{well}}^{-1}$ for the probability of successful jump in this case. This is useful in calculations of an enhanced vacancy concentration inside precipitate.

For example, in conditions typical for thermal ageing, when the concentration in the matrix outside a precipitate is kept constant and equal to the equilibrium vacancy concentration, $C_{\mathrm{V}}^{\mathrm{e}}$, at given temperature, the enhanced mean vacancy concentration in the precipitate $\left\langle C^{\mathrm{in}} \right\rangle$ can be obtained using the detailed-balance condition at the precipitate surface. The frequency with which vacancies enter the precipitate is $C_{\mathrm{V}}^{\mathrm{e}} m \langle n_{\mathrm{free}} \rangle / z\tau$, while the frequency with which vacancies leave the precipitate is $\left\langle C^{\mathrm{in}} \right\rangle \mathrm{N} / \tau_{\mathrm{diss}}$. The equality of these frequencies implies that

$$\left\langle C^{\mathrm{in}} \right\rangle = C_{\mathrm{V}}^{\mathrm{e}} \left\langle e^{-\beta U(\mathbf{r}_i)} \right\rangle_{\mathrm{well}}. \qquad (13)$$

IV. Distribution Function of Dissociation Times

A. Definitions and Monte Carlo scheme

A more detailed description of the stochastic process of dissociation than by the statistical average value of dissociation time, Eqs. (3) and (7), is given by the probability density function of dissociation times, $dP(t)/dt$. Here, $P(t)$ is the probability that a dissociation event occurs before time t. For a random process without memory, such as the radioactive decay:

$$1 - P(t) = \exp(-t / \tau_{\mathrm{diss}}) \qquad (14)$$

and the probability density function is given by

$$dP(t)/dt = \exp(-t / \tau_{\mathrm{diss}}) / \tau_{\mathrm{diss}}. \qquad (15)$$

It will be shown below that this is valid in the cases characterised by a unique binding energy such as a single-site trap, but not for spatially distributed wells.

To study the influence of the well shape on the distribution of dissociation times, we performed Monte Carlo calculations of particle diffusion in the same system as used for derivation of the mean dissociation times in Sec. II, i.e. it consisted of a well and one 'free' state with periodic boundary conditions. Two particular cases are considered below, namely 1-D square and triangular wells (see Sec. III A and B). In the case of a square well, the jump frequencies of the diffusing particle in forward and backward directions, ν^+ and ν^-, were equal to those in perfect crystal: $\nu^+(x) = \nu^-(x) = (2\tau)^{-1}$ for all but two frequencies for two border sites,

where $\nu^{+}_{\text{right border}} = \nu^{-}_{\text{left border}} = e^{-\beta E} / \tau$. In the case of triangular wells, the frequencies were calculated as $\nu^{\pm}(x) = e^{\mp \beta \Delta U^{\pm}} / \tau$, where $\Delta U^{\pm} = \pm\left[U(x \pm 1) - U(x)\right] / 2$ are the changes of the migration barriers due to the interaction energy (see Fig. 2). The probabilities that particle jumps forward or backward are defined by ratios $\nu^{+} / \nu_{\text{total}}$ and $\nu^{-} / \nu_{\text{total}}$, where $\nu_{\text{total}} = \nu^{+} + \nu^{-}$ is the total jump frequency. The value $< t >= \nu^{-1}_{\text{total}}$ is the mean waiting time before a jump, which is generally site dependent. The value τ normally obeys the Arrhenius relationship for the temperature dependence with activation energy equal to the saddle point energy in perfect crystal (E_0 in Fig. 2). In most of our calculations, τ was a constant chosen to be the unit of time. Some calculations revealing influence of the saddle-point energy profile on the distribution function, thus with τ dependent on the position inside the well, are presented in Sec. IV D. The calculations were performed until a specified number of dissociation events occurred. The distribution of dissociation times was obtained as the number of dissociations within a specific time window (a bin of the distribution) divided by the total number of events and the bin width. In our calculations, the bin width was taken as $0.1\tau_{\text{diss}}$ and calculated using Eqs. (9) and (12) for the square and triangular wells, respectively. The main purpose of calculations was to compare the probabilities calculated with those described by Eq. (15). We use a dimensionless variable t / τ_{diss} and function $\tau_{\text{diss}} dP(t) / dt$ to represent the results, since they are independent of the mean dissociation time.

B. Results for 1-D square wells

The MC calculations were performed for wells of different width (50, 100 and 200 one jump distances) and depth (βE =3.87 and 7.74, which correspond to E =0.1 and 0.2 eV, respectively, at T =300K) and ~500,000 dissociation events were accumulated in each case. The range of well widths was chosen with a particular interest in the migration of a self-interstitial atom cluster in the long-range stress-field of an edge dislocation, see Refs. [6] and [7]. The calculations reproduced Eq. (9) with high accuracy, which was one of the tests for the code. The main aim of the following calculations was to study the deviation of $dP(t) / dt$ from Eq. (15). The results are presented in Fig. 3. Typical error bars are shown for one calculation (the upper parts of errors bars are omitted in order to keep presentation clear). As can be seen, for wells deep and/or narrow enough (e.g. for βE =7.74 or N =50), the probability density approaches Eq. (15), which is characteristic of a random process without memory. For shallow and/or wide wells, the distribution deviates from exponential dependence, especially at small times. More specifically, the deviation occurs for such wells, where the mean dissociation time is not significantly longer than $\tau_{\text{diff}} = \mathrm{N}^2 \tau / 2$, which is the time corresponding to the diffusion length equal to the half of the well width $l = \mathrm{N}a / 2$, where a is the jump distance. The diffusion length, i.e. the mean-free path, is defined from equation $l^2 = 2D\tau_{\text{diff}}$, where $D = a^2 / 2\tau$ is the diffusion coefficient in 1-D. The last column of the legend in Fig. 3 contains necessary ratios $\tau_{\text{diss}} / \tau_{\text{diff}}$. We note that wells for which $\tau_{\text{diss}} \approx \tau_{\text{diff}}$ can hardly be treated as traps at all. Thus, we conclude that for square wells strong enough to be considered as traps, i.e. with $\tau_{\text{diss}} >> \tau_{\text{diff}}$, the distribution under interest is described reasonably well by the exponential dependence.

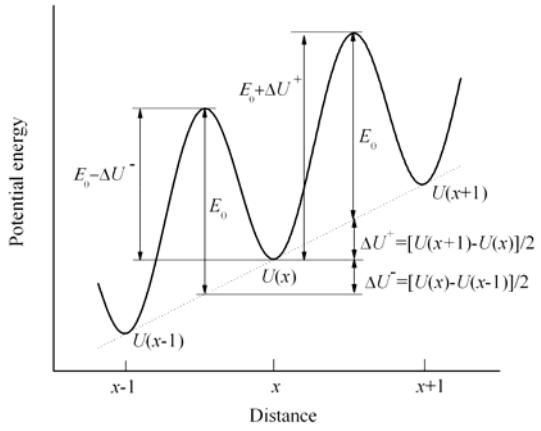

FIG. 2. Schematic diagram illustrating calculation of energy barriers.

C. Results for 1-D triangular wells

Calculations similar to those described above for a square well were performed for triangular symmetrical wells, i.e. when $|x_{\min}| = x_{\max}$ in Eq. (11). The statistics were accumulated for about 1,000,000 events. Eq. (12) for the mean dissociation time was reproduced within reasonable accuracy, usually about 1%. The distribution function of dissociation times is presented in Fig. 4. As can be seen, the distribution deviates from the exponential dependence much more significantly than for square wells. Similar to square wells, the deviation is stronger for shorter times and smaller ratio $\tau_{\text{diss}} / \tau_{\text{diff}}$. This is because of a high fraction of dissociation events occurring before particle visited the deep region of the well. It is evident that the higher the ratio $\tau_{\text{diss}} / \tau_{\text{diff}}$, the lesser the contribution of shallow regions to the mean time. Unlike that for the square well, the probability of short time dissociation in a triangular well is always high, even for deep and narrow wells, and the distribution at short times has quite different slope in logarithmic scale. This feature is due to geometry of the well, where shorter times correspond to smaller energy. At long times the distribution becomes exponential but with different slope, as shown in the comparison with exponential function plotted in Fig. 4.

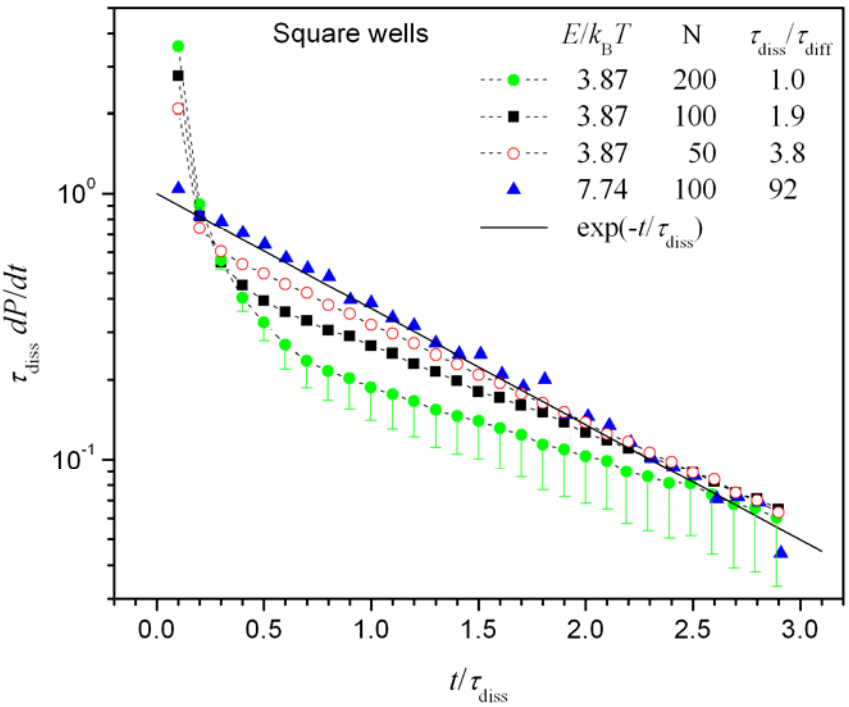

FIG. 3. Probability distribution of dissociation times of a migrating particle from wells of different depth *E* and width N. The typical error bars are shown for one set of calculations (the upper parts of errors bars are omitted in order to keep presentation clear).

Figure 5 shows the distribution of $1-P(t)$, i.e. the probability that a dissociation event does not occur before time *t*, for triangular wells of different width and depth. The error bars were very small for calculations of this type, not visible on the graph. One calculation for a square well (labelled 'Square') is also shown and it demonstrates a dependence which is close to exponential decay. In contrast, the distributions for triangular wells deviate from simple exponential dependence. The time dependence exhibits different behaviour at short and long times. The function at short times is steep and decreases quickly, while an exponential dependence evolves at long times. The curve for βE =3.87 and N =100, which is labelled '*x*=0', is the distribution of escape times from the bottom of the triangular well. That is, the trajectories of all the diffusing particles in this calculation started from $x=0$ corresponding to the deepest position in the well. In this calculation the mean dissociation time was about 15200 τ and more than an order of magnitude longer than that given by Eq. (12) and corresponding calculations, which is 1210 τ. We also note that this time was about twice higher than the corresponding value of 7230 τ for the square well of the same depth and width when all trajectories started from '*x*=0', i.e. the middle of the well. This does not seem trivial, since the simple average depth of the former well is smaller. As seen from Fig. 5, this calculation also shows the exponential decay. This indicates that the deviations from an exponential relationship are due to trajectories, which do not reach the bottom of the well. In addition, we make an important observation. When the time is equal to the mean dissociation time, the probability for the triangular wells is not equal to e^{-1} as expected for a random process, such as radioactive decay, described by Eq. (14). This means that the events are not randomly distributed, i.e. Eq. (14) is not applicable, and hence actual distribution function is required to characterise the process. It seems important to mention that, strictly speaking, such a process cannot be treated by chemical reaction equations, where the dissociation rate is the reciprocal of the mean dissociation time. These equations predict exponential decay for the trap concentration, thus describe random process. The work is currently in progress investigating possibility of overcoming these problems.

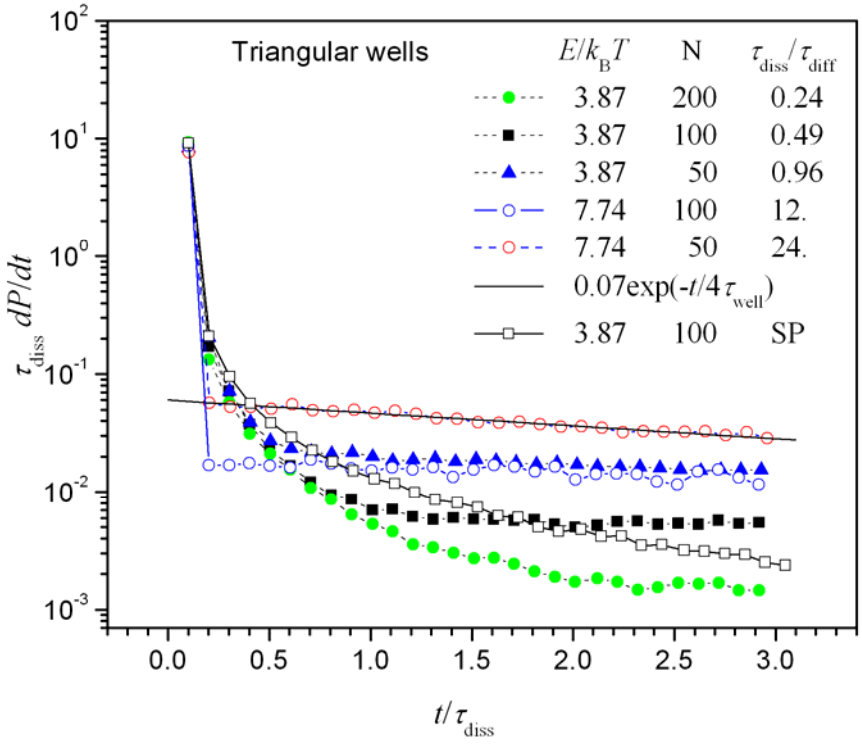

FIG. 4. Same as in Fig. 1 but for triangular wells. One curve, labelled 'SP' has been calculated for the energy profile where all saddle-point energies are equal.

D. Influence of saddle-point energy profile on time distribution

As has already been mentioned in Sec. II B, the mean dissociation time is independent of the saddle point energy profile within the well, and this follows from the general Eq. (7). We verified this statement by calculations for a triangular potential well where all saddle-point energies were taken to be the same and equal to those in perfect crystal. An example of such a well is shown in Fig.1b. In the calculations performed, the time delay was defined according to the actual saddle-point energy by including an additional Arrhenius factor. The results are presented in Fig. 4 in the curve labelled 'SP' for βE =3.87 and N =100. The mean dissociation time was the same as in corresponding calculation above for triangular well (see Sec. IV C) and given by Eq. (12) within accuracy of less than 2%. The probability distribution was different, however, with the probabilities of shorter-time dissociations increased. This is because there is no longer preference for a diffusing particle to jump towards deeper well regions. In other words, in this calculation, the well represents a region where only jump frequencies, but not the probabilities of different jumps, are affected.

Similar effect was studied in Ref. [9] for diffusion of vacancy and Cu atoms in a dilute Fe-Cu alloy. The analysis showed that the diffusion mechanism of Cu atoms, namely the crossover from 'exchange' (when a vacancy executes only exchange jumps with Cu atom) to 'drag' (when the vacancy co-migrates with Cu atom) mechanisms depends critically on the saddle-point energy profile of the vacancy around Cu atom (see Ref. [9], especially section 3.2).

V. Exchange Frequency between Wells

In the preceding sections we used the term 'dissociation', which can be inappropriate in some cases where the term 'escape' would be a better word. An important example is a dilute solution of traps. In this case, a migrating defect escaping from a trap has a high probability of returning to the same trap after a short-time migration in pure crystal. In diffusion-reaction kinetics, however, we are concerned mainly with events that result in complete dissociation in the sense that *the memory is lost* and the next reaction will occur with high probability at another trap. In other words, the quantity of interest is the frequency with which diffusing objects are exchanged between wells. This is the origin for the Eyring transmission factor in the reaction rate theory[10]. A clear distinction between escape and dissociation events can be seen in the example of vacancy evaporation from voids. The evaporation takes place at the void surface; hence, the total escape frequency is proportional to the surface area, i.e. the void radius squared. The well-known result of the diffusion-reaction theory gives proportionality to the void radius. Obviously and as demonstrated below, this difference is due to correlated absorption of vacancies by the same void they are emitted from. This indicates that accounting for correlated events can change even qualitative description of the process. Note also that the events contributed to the short-time non-exponential part in the distribution function of dissociation times, see Sec. IV C, can also be viewed as correlated events and thus part of the same problem. Below we consider this problem for two specific cases: vacancy evaporation from a void and de-trapping of interstitial cluster from dislocation.

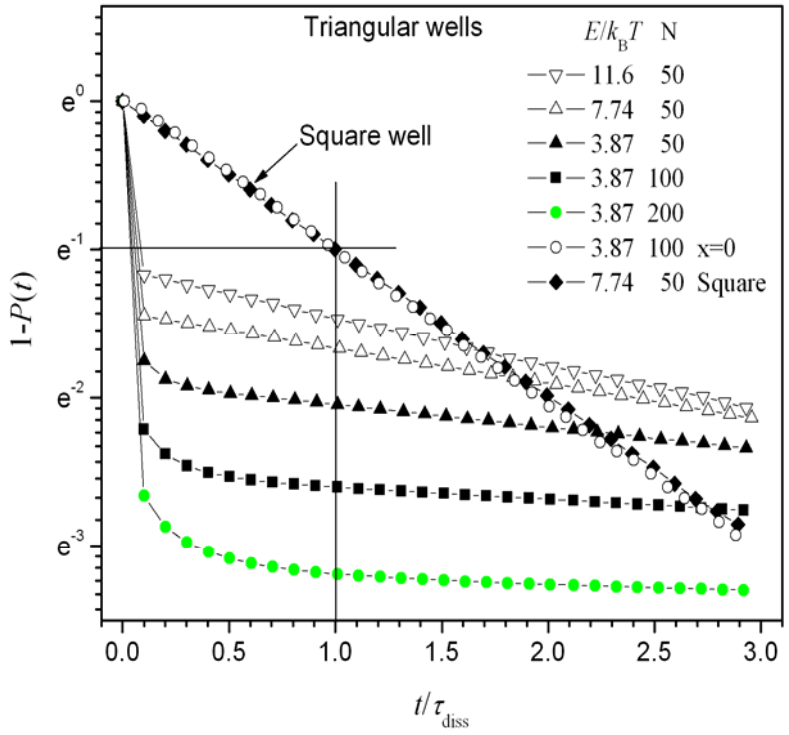

FIG. 5. Probability that a dissociation event does not occur before time *t* for the wells of triangular shape of different width and depth. One curve labelled as 'Square' was calculated for square well. The curve labelled as '*x*=0' shows the distribution of escape times from the bottom of the triangular well.

A. Vacancy evaporation from void

Consider a void of radius r_0, which emits τ_{diss}^{-1} vacancies per second per surface site, in a spherical coordinate system. Vacancies migrate three-dimensionally with the diffusion coefficient $D = a^2/6\tau$. The diffusion equation for vacancy concentration C is

$$\nabla^2 C = 0. \qquad (16)$$

To calculate the number of vacancies emitted from the void that reach some distance R from the void surface we use absorbing boundary conditions at this distance

$$C(R) = 0. \qquad (17)$$

One more boundary condition must specify the vacancy-void interaction process. Assuming that vacancies are absorbed by the void, which is a realistic scenario, the vacancy concentration at one jump distance *a* from the surface can be written as

$$C(r_0 + a)/\tau = \nu_{\text{diss}} + C(r_0 + 2a)/2\tau. \qquad (18)$$

The left-hand side of the equation describes the frequency with which vacancies leave the site. The first term on the right-hand side stands for the production of vacancies due to evaporation from the void. The last term on the right-hand side accounts for vacancies coming to this site from the sites further way from the void surface. After representing the latter term using Taylor series, in the limit of $r_0 >> a$, the boundary condition, Eq. (18), assumes the following form

$$C(r_0) = 2\tau\nu_{\text{diss}} + \nabla C(r_0)a. \qquad (19)$$

Using this condition, one finds the concentration to be equal to

$$C = 2\tau\nu_{\rm diss}\frac{r^{-1}-R^{-1}}{r_0^{-1}-R^{-1}}. \qquad (20)$$

It can readily be estimated using the last two equations that the gradient of concentration in Eq. (19) is smaller than the other terms by a factor of a/r_0 and does not contribute to Eq. (20). This means that most vacancies emitted from the void return back to it. As a result, the equilibrium condition for the concentration near the void surface is defined by the equality of frequencies of evaporation and jumps back to the surface and is not affected by the flux of vacancies away from the surface. The vacancy equilibrium concentration at the void surface is readily obtained from Eq. (20) as $C_{\rm V}^{\rm e} = C(r_0) = 2\tau\nu_{\rm diss}$.

The total number of vacancies passing through a spherical surface of radius R and area $S = 4\pi R^2$ per unit time is equal to

$$R_{\rm V}^{\rm a} = -\frac{SD}{\Omega}\nabla C(R) = \frac{DC_{\rm V}^{\rm e}}{\Omega}\frac{4\pi r_0}{1-r_0/R}, \qquad (21)$$

where superscript 'a' denotes absorbing boundary. There are three points to be made. First, Eq. (21) becomes independent of the distance R from the surface, when $R >> r_0$. Thus, vacancies reaching this distance lose their memory and can be counted as dissociated from the void. Second, despite the fact that the total vacancy emission frequency is proportional to the void surface area, the total vacancy flux far away from surface is proportional to the void radius. This is a well-known result of the reaction-diffusion theory (see, e.g. Ref. [11]). Third, as can be seen from Eq. (21), significant deviation from the proportionality to the void radius occurs at distances of the order of void radius.

As discussed above most vacancies emitted return to the void. The fraction of vacancies which do not return is equal to the ratio of the frequency defined by Eq. (21) and $\sim 4\pi r_0^2\nu_{\rm diss}/a^2$, which is for the total frequency of vacancy emission. It is thus equal to a/r_0. The same result can be demonstrated considering another, although unrealistic, scenario in which vacancies are reflected by the voids. In this case all vacancies produced contribute to the flux far away from the void. Indeed, in this case, we should multiply the left hand side of Eq. (18) by ½ to account for the fraction of unsuccessful jumps towards the void surface. Then, only the gradient and source terms remain in the boundary condition, Eq. (19):

$$\nabla C(r_0)a = -2\tau\nu_{\rm diss} \qquad (22)$$

and the vacancy concentration becomes

$$C = \frac{2\tau\nu_{\rm diss}r_0^2}{a}\left(\frac{1}{r}-\frac{1}{R}\right). \qquad (23)$$

The quantity defined by Eq. (21) modified for the case of reflecting boundary conditions (superscript 'r') is now proportional to the surface area:

$$R_{\rm V}^{\rm r} = \frac{4\pi r_0^2}{\Omega}\frac{2D\tau\nu_{\rm diss}}{a} = \left(\frac{r_0}{a}\right)R_{\rm V}^{\rm a}, \qquad (24)$$

and is higher than that for absorbing conditions by a factor of r_0/a.

We also note that the first non-vanishing correction to the proportionality of the vacancy flux to the void radius is positive and proportional to the void radius squared, see Eq. (21), where $r_0\left(1-r_0/R\right)^{-1} \approx r_0 + r_0^2/R$. This is the same result as obtained previously e.g. by Göselle (Ref. [12]) considering void capture efficiency. Thus, with increasing volume fraction more and more vacancies become absorbed at other voids and the proportionality to the void radius squared would be restored. The first correction term just shows the right tendency.

B. Interstitial cluster exchange between dislocations

Consider a random spatial arrangement of dislocations and interstitial clusters migrating one-dimensionally with the diffusion coefficient $D = a^2 / 2\tau$. This problem is similar to that considered above in Sec. V A. It is readily obtained that, with absorbing boundary conditions at the well boundary at $x = 0$, Eq. (18), and at distance L from the well, the cluster concentration is described by the following equation

$$C = 2\tau\nu_{\text{diss}}\left(1 - \frac{x}{L}\right). \qquad (25)$$

The distance L here can be interpreted as the mean distance between dislocations in 1-D and will be discussed further below. In this case, other dislocations absorb clusters passing this distance and, hence, the memory is lost. This process can be considered as cluster exchange between wells represented by dislocations. The total flux of clusters emitted from the well at distance L is

$$J^{\text{a}} = -D\nabla C(L) = \frac{D}{\Omega}\frac{2\tau\nu_{\text{diss}}}{L}. \qquad (26)$$

We note that, in contrast to 3-D diffusion, the total flux for 1-D diffusion always depends on the distance; namely, it decreases with increasing distance (decreasing dislocation density).

Similar to the problem of vacancy evaporation from a void considered above, one can show that, for reflecting boundary conditions, Eq. (22), the vacancy concentration and the flux of clusters are both L / a times higher. Hence, the fraction of clusters, which do not return to the well after escaping from the potential well, and, hence, the frequency with which clusters are exchanged between dislocations, f is equal to a / L:

$$f = \nu_{\text{diss}} a / L. \qquad (27)$$

Now let us make some estimates of the effect. The mean distance between randomly arranged dislocations in 1-D is described by the dislocation density ρ_{D} and capture radius d as $L = 2 / \pi\rho_{\text{D}} d$ (see, e.g. Ref. [13]). The jump distance in bcc lattice is the distance between atoms in <111> direction: $a = \sqrt{3}a_0 / 2$, where a_0 is the lattice parameter. Hence, the frequency of cluster exchange between dislocations is

$$f = \sqrt{3}\pi\nu_{\text{diss}}\rho_{\text{D}} d a_0 / 4. \qquad (29)$$

For typical dislocation density ρ_{D} =10^{12} m^{-2}, the capture radius d =100 nm estimated in Ref. [6] and a_0 =0.3 nm, the frequency is smaller than the rate of cluster emission from the well by about five orders of magnitude: $f \approx 4\times 10^{-5}\,\nu_{\text{diss}}$.

Thus, the exchange frequency for a diffusing particle between spatially separated wells may be many orders of magnitude smaller than the frequency of dissociation from a well, and this is due to correlated recapture of the particle by the same well. In addition, the effect depends strongly on the trap density.

ACKNOWLEGMENTS

A.V.B. acknowledges a research grant from the UK Engineering and Physical Sciences Research Council. Research at ORNL was partially sponsored by the Division on Materials Sciences and Engineering, U. S. Department of Energy.

REFERENCES

[1] A.V. Barashev, S.I. Golubov, D.J. Bacon, P.I.J. Flewitt, and T.A. Lewis, Acta Materialia **52,** 877 (2004).
[2] Yu.N. Osetsky, and A. Serra, Philos. Mag. A **73**, 249 (1996).
[3] Yu.N. Osetsky, and A. Serra, Philos. Mag. A **75**, 1097 (1997).
[4] A.C. Arokiam, A.V. Barashev, D.J. Bacon, and Yu.N. Osetsky, Philos. Mag. Lett. **85**, 491 (2005).
[5] A.C. Arokiam, A.V. Barashev, D.J. Bacon, and Yu.N. Osetsky, Philos. Mag. **87**, 925 (2007).
[6] H. Trinkaus, B.N. Singh, and A.J.E. Foreman, J. Nucl. Mater. **249**, 103 (1997).
[7] B.N. Singh, A.J.E. Foreman, and H. Trinkaus, J. Nucl. Mater. **249**, 91 (1997).
[8] G.S. Rushbrook, *Introduction to statistical mechanics* (Clarendon Press, Oxford, 1949).
[9] A.V. Barashev, and A.C. Arokiam, Philos. Mag. Lett. **86**, 321 (2006).
[10] P. Hanggi, P. Talkner, and M. Borkovec, Rev. Mod. Phys. **62**, 251 (1990).
[11] J.L. Katz, and H. Wiedersich, J. Chem. Phys. **55**, 1414 (1971).
[12] U.M. Gösele, in Progress in Reaction Kinetics **13**, 63 (1984).
[13] A.V. Barashev, S.I. Golubov, and H. Trinkaus, Philos. Mag. A **81,** 2515 (2001).

ATOMISTIC STUDIES OF PROPERTIES OF HELIUM IN BCC IRON USING THE NEW HE–FE POTENTIAL—David M. Stewart, Stanislav Golubov (Oak Ridge National Laboratory and the University of Tennessee), Yuri Ostesky, Roger E. Stoller, Tatiana Seletskaia, and Paul Kamenski (Oak Ridge National Laboratory)

SUMMARY

In fusion applications, helium caused by transmutation plays an important role in the response of RAFM steels to neutron radiation damage. The growth, migration and coalescence behavior of helium bubbles is very sensitive to the properties of individual He interstitials and helium-vacancy clusters [1]. We have performed atomistic simulations using a new 3-body Fe–He inter-atomic potential [2–4] combined with the Ackland [5] iron potential. With the ORNL potential, interstitial helium is very mobile and coalesces together to form interstitial clusters. The interstitial clusters show lower binding energy than with the Wilson potential [6], in agreement with the DFT calculations of CC Fu [7]. If the He cluster is sufficiently large the cluster can push out an Fe interstitial, creating a Frenkel pair. The resulting helium-vacancy cluster is not mobile. The ejected SIA is mobile, but is weakly trapped by the He-V cluster. If more helium atoms join the He-V cluster, more Fe interstitials can be pushed out, and they combine to form an interstitial dislocation loop. Such loops have been observed in experiment—for example in [8]. The reverse process is also studied. Multiple helium atoms can be trapped in a single vacancy, and if there are few enough, the vacancy can recombine with an Fe interstitial to create a helium interstitial cluster.

PROGRESS AND STATUS

Introduction

Helium produced in neutron irradiated iron plays an important part in its mechanical properties. A new He–Fe inter-atomic potential has been developed at ORNL, based on extensive fitting to first-principles calculations of point defects and clusters [2–4]. This potential has been used to investigate the properties of helium and helium-vacancy clusters in MD and MS simulations.

Potential

The ORNL 3-body potential is described in [2] and [3] and [4]. The potential was fitted to first principles calculations done in VASP. Fitted configurations included relaxed and unrelaxed defects, so that forces could be fitted as well as energies. A key result from the DFT calculations is that the tetrahedral interstitial site is more stable than the octahedral site. Reproducing this feature is difficult as the octahedral site has more volume. We achieved this by using a 3-body term. Later Juslin and Nordlund produced a pair potential [9] that also reproduced this feature.
The total energy of the He–Fe system has the following form:

$$E = E_{Fe-Fe} + E_{He-He} + \sum_{\substack{i \in He \\ j \in Fe}} \phi\left(r_{ij}\right) + \sum_{\substack{i \in He \\ j,k \in Fe,\, j \neq k}} Y\left(r_{ij}, r_{ik}, \Theta_{jik}\right) \tag{1}$$

The iron interatomic potential E_{Fe-Fe} can be the pair potential by Finnis and Sinclair [10], the EAM potential by Ackland and Bacon [5] or the EAM potential by Ackland and Mendelev [11, 12]. The helium potential E_{He-He} is the one from Aziz [13]. The repulsive pair term ϕ is given by:

$$\phi\left(r_{ij}\right) = p_1 \exp\left(-p_4\left(\frac{r_{ij}}{p_3} - i\right)\right) f_{cut}\left(r_{ij}\right) \tag{2}$$

This function has a cutoff of 4.4Å. The 3-body term Y is given by:

$$Y\left(r_{ij}, r_{ik}, \Theta_{jik}\right) = \cos^2\left(\Theta_{jik} - 0.44\right) f_{cut}\left(r_{ij}\right) f_{cut}\left(r_{ik}\right) \tag{3}$$

This function has a cutoff of 2.2Å. The angle 0.44 radians is chosen so that the $\cos^2$ function has a minimum at the angle in the centre of a tetrahedron.

Simulation Method

The general procedure followed is:
• Generate perfect BCC lattice.
• Introduce the defect(s) to be studied.
• Relax at constant volume using a mixture of conjugate gradient and simulated annealing, and save the atom positions in units of the lattice constant.
• Start the MD simulation.
The MD simulation uses NVE dynamics. The lattice constant and initial velocities are chosen to give close to zero pressure and the desired initial temperature. The boundary conditions are periodic in *X*, *Y* and *Z*, which are ⟨100⟩ directions. The velocity Verlet algorithm with a timestep of 0.3fs is used. As volume and temperature correction are not used, when processes that release energy are simulated the temperature and pressure both rise during the simulation.

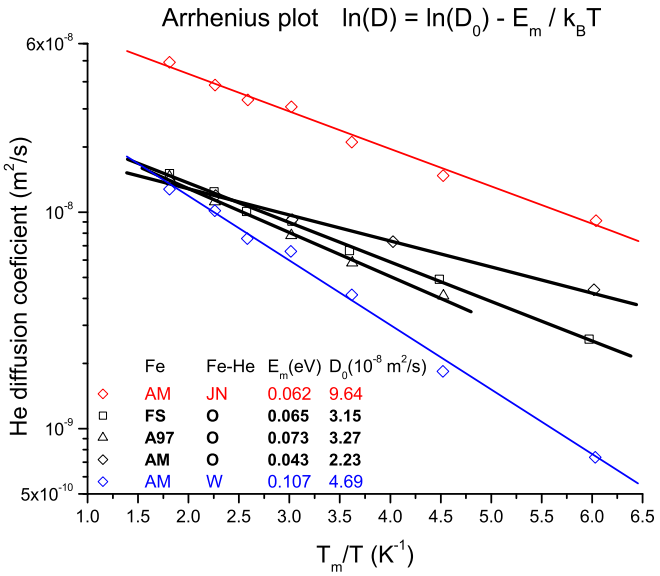

Figure 1. Arrhenius Plot for helium diffusion in iron matrix.

Single Helium Diffusion

Diffusion of an isolated interstitial He atom in a 10×10×10 BCC iron matrix (2,000 iron atoms) was simulated for several potentials at several temperatures. Arrhenius plots of the diffusion rates are shown in Fig. 1. The potentials used and fit parameters are shown in Table 1. The ORNL potential gives similar interstitial He migration barriers with three different iron matrices, all close to the 0.06eV value determined by DFT. The Juslin-Nordlund potential also gave a similar migration barrier, but much faster diffusion overall. The Wilson potential gave a higher barrier of 0.107eV. The diffusion rates are significantly more sensitive to the He-Fe potential used than to the iron matrix potential used.

Table 1. Migration barriers and diffusion rates of He in Fe for different potentials.

Symbol	Fe–Fe potential	Fe–He potential	E_m (eV)	D_0 ($10^{-8} m^2/s$)
◇	Ackland–Mendelev [11, 12]	Juslin–Nordlund [9]	0.062	9.64
□	Finnis–Sinclair [10]	ORNL [2–4]	0.065	3.15
△	Ackland–Bacon [5]	ORNL [2–4]	0.073	3.27
◇	Ackland–Mendelev [11, 12]	ORNL [2–4]	0.043	2.23
◇	Ackland–Mendelev [11, 12]	Wilson [6]	0.107	4.69

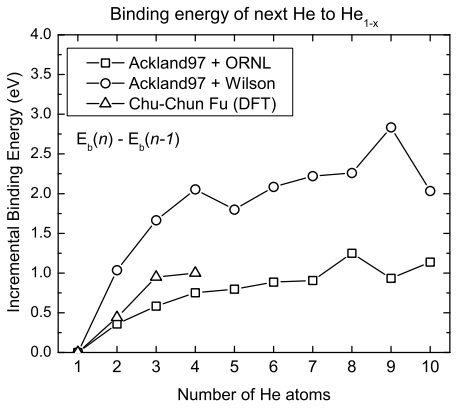

(a) He interstitial clusters

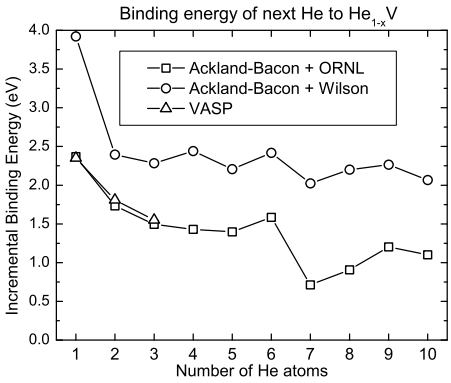

(b) Helium-Vacancy clusters

Figure 2. Cluster binding energies

Replacement Mechanism

Helium diffuses very fast in the matrix, but gets trapped in vacancies [14]. It is possible for a self-interstitial to recombine with the vacancy, kicking the helium into an interstitial position. To test whether this is favorable with this potential we performed static and dynamic calculations. Static calculations give formation energies for He_{sub}, He_{int} and SIA of 3.7, 4.3 and 4.9 eV respectively. Unsurprisingly $E(He_{sub}) + E(SIA) > E(He_{int})$, so recombination releases energy and is therefore favorable.

Static calculations for situations with more helium atoms are shown in Fig. 2. Figure 2a shows the incremental binding energy of an interstitial helium cluster as helium atoms are added. Figure 2b shows the incremental binding energy of a helium vacancy cluster as helium atoms are added. The simulations are done either in a 10×10×10 lattice or, for bigger defects, a 15×15×15 lattice (6,750 iron atoms). Calculations using both our He-Fe potential and Wilson's one are shown. *Ab initio* calculations by C.C. Fu and T. Seletskaia are also shown on the graphs for comparison. The ORNL potential results are closer to the *ab initio* results than are the Wilson potential ones.

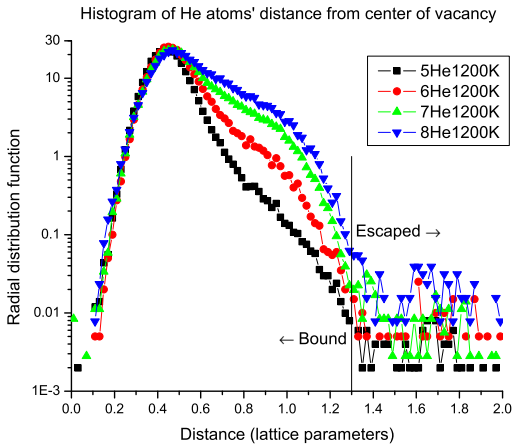

Figure 3. He atom location in HeV cluster

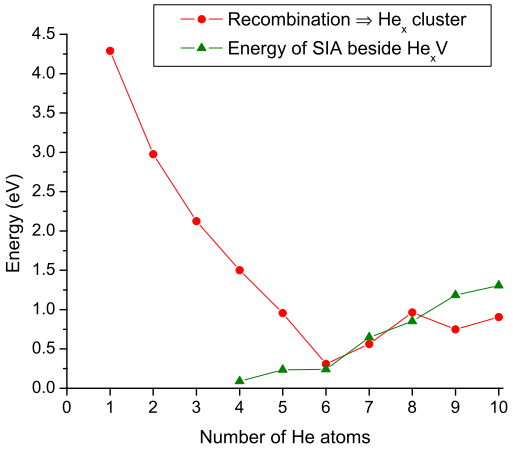

Figure 4. Energy differences for two processes

Dynamic simulations of helium-vacancy clusters are performed. The distribution of how far the He atoms are found from the centre of the vacancy is shown in Fig. 3. The most commonly observed configuration is an octahedron with the He atoms ~0.45 lattice parameters in the ⟨100⟩ directions, with any He atoms not part of the octahedron further out. As the helium is strongly bound to the vacancy, only results for 1200K are shown in order to observe helium atoms escaping within MD

timeframes. The results show that the helium atoms are bound out to a radius of 1.3 lattice parameters.

Dynamic simulations of an SIA and a helium-vacancy cluster at several temperatures are done to examine the replacement mechanism. Table 2 shows how many picoseconds it took for recombination to occur. As periodic boundary conditions and a small box were used, the SIA could not get away; if recombination is favorable it is likely to be observed in the simulation timeframe. For clusters with 5 or less helium atoms, recombination is observed at all temperatures tested. For He_6V, recombination is observed at 900K and 1200K but not at 600K, suggesting that recombination is favorable but has a high energy barrier to overcome. At 600K the SIA was trapped near the cluster but did not recombine. This was also observed for He_7V at both temperatures studied and for He_8V at 600K. For He_8V at 1200K a second SIA was ejected, creating an He_8V_2 cluster. The two SIAs were trapped next to it for 165ps, after which one of the SIAs recombined with the cluster, returning to the 1SIA + He_8V configuration.

Number of He atoms	300K	600K	900K	1200K
1	60.1	252.6	47.8	12.5
2		125.9		95.9
3		113.5		441.3
4	247.8	113.2		31.8
5	205.4	1363.6	320.7	35.4
6		didn't	4648.1	121.6
7		didn't		didn't
8		didn't		extra SIA

Table 2: Time in picoseconds for an SIA to recombine with a He_xV cluster

Using the results from Fig. 2, the amount of energy released when an SIA recombines with a He_xV cluster is calculated for different values of x and is plotted in Fig 4 (red circles). In some of the dynamic simulations an SIA was trapped close to a He-V cluster without recombining with it. Static calculations of this configuration are used to calculate the amount of energy released when an SIA moves into this position from far away. This is plotted as the green triangles in Fig. 4. If the vacancy contains 5 or less atoms, it is found to be energetically favorable for it to recombine with the SIA to form a helium interstitial cluster. For 6-8 atoms there is no clear winner, and for more than 8 it is more favorable for the SIA to be trapped nearby.

A dynamic simulation of a He_8 interstitial cluster at 600K showed that the reverse process can happen – an SIA was ejected, creating a He_8V cluster. The SIA was trapped beside the cluster.

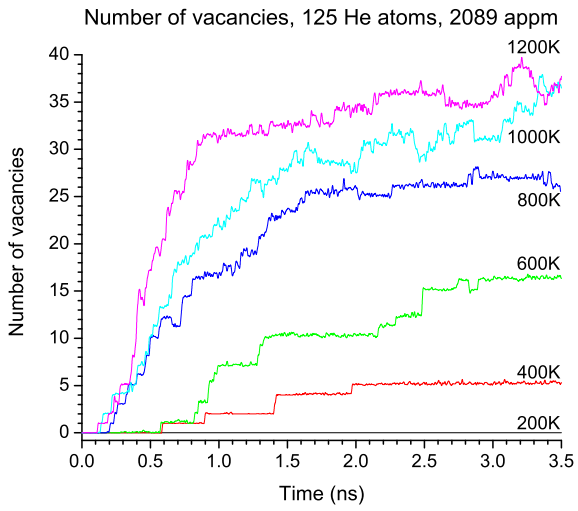

Figure 5. Vacancy production

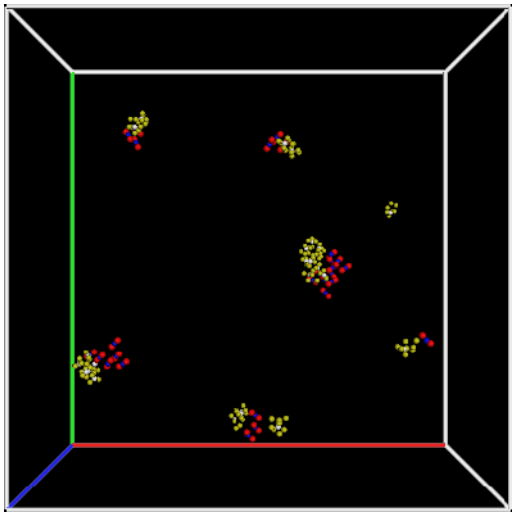

Figure 6. Clusters at 800K at t = 3.2ns

Coalescence

In order to see if helium interstitial clusters can form without a HeV + SIA recombination event, dynamic simulations were run with 125 helium atoms in a 31×31×31 BCC iron matrix (60,000 iron atoms). At 200K, there was insufficient kinetic energy to break up even a pair of He atoms, so the helium slowly and inexorably coalesced until it formed interstitial clusters too big to be mobile, He_4 or bigger. The largest observed cluster was He_7. No vacancies or SIAs were observed. At 400K, He_2 and He_3 were still mostly stable but more clusters were mobile so coalescence happened faster. When clusters reached 8 or 9 helium atoms, a single SIA was ejected. None of the ejected SIAs escaped their HeV cluster. At higher temperatures, smaller clusters like He_2 and He_3 were short lived, reducing the number of surviving clusters. The clusters that did form were bigger since the number of available He atoms was fixed at 125. The higher the temperature, the less He atoms were needed to eject an SIA. Higher temperatures also led to more SIAs escaping the HeV cluster where they were created. These SIAs were usually captured by other clusters that had SIAs. Groups of SIAs were observed to line up, forming dislocation loops.

The number of vacancies (equal to the number of SIAs ejected) is plotted as a function of time in Fig. 5. A snapshot of the 800K simulation after 3.2 nanoseconds is shown in Fig. 6. All the helium has coalesced into 9 clusters, all of which have pushed out from 1 to 6 SIAs. The SIAs have formed interstitial loops beside some of the clusters.

References

[1] S.I. Golubov, R.E. Stoller, S.J. Zinkle, and A.M. Ovcharenko, Kinetics of coarsening of helium bubbles during implantation and post-implantation annealing, Journal of Nuclear Materials 361 (2007), pp. 149–159.

[2] T. Seletskaia, Y. Osetsky, R.E. Stoller, and G.M. Stocks, Magnetic Interactions Influence the Properties of Helium Defects in Iron, Physical Review Letters 94 (2005), pp. 046403.

[3] T. Seletskaia, Y.N.Osetsky, R.E. Stoller, and G.M. Stocks, Calculation of helium defect clustering properties in iron using a multi-scale approach, Journal of Nuclear Materials 351 (2006), pp. 109–118.

[4] T. Seletskaia, Y.N. Osetskiy, R.E. Stoller, and G.M. Stocks, Development of a Fe He interatomic potential based on electronic structure calculations, Journal of Nuclear Materials 367 (2007), pp. 355–360.

[5] G.J. Ackland, D.J. Bacon, A.F. Calder, and T. Harry, Computer simulation of point defect properties in dilute Fe-Cu alloy using a many-body interatomic potential, Philosophical Magazine A-Physics Of Condensed Matter Structure Defects And Mechanical Properties 75 (1997), pp. 713–732.

[6] W. Wilson and R. Johnson, Rare Gases in Metals, Interatomic Potentials and Simulation of Lattice Defects, Battelle Institute Materials Science Colloquia, 1972, 375-390 (1972).

[7] C.C. Fu and F. Willaime, Ab initio study of helium in ®-Fe: Dissolution, migration, and clustering with vacancies, Physical Review B 72 (2005), pp. 064117.

[8] J.H. Evans, A. Van Veen, and L.M. Caspers, Direct Evidence for Helium Bubble Growth in Molybdenum by the Mechanism of Loop Punching, Scripta Metallurgica 15 (1981), pp. 323–326.

[9] K. Nordlund and S. Dudarev, Interatomic potentials for simulating radiation damage effects in metals, Comptes rendus-Physique (2008).

[10] M.W. Finnis and J.E. Sinclair, A simple empirical N-body potential for transition metals, Phil. Mag. A 50 (1984), pp. 45–55.

[11] M.I. Mendelev, S. Han, D.J. Srolovitz, G.J. Ackland, D.Y. Sun, and M. Asta, Development of new interatomic potentials appropriate for crystalline and liquid iron, Philosophical Magazine 83 (2003), pp. 3977–3994.

[12] G.J. Ackland, M.I. Mendelev, D.J. Srolovitz, S. Han, and A.V. Barashev, Development of an interatomic potentia for phosphorus impurities in agr-iron, Journal of Physics Condensed Matter 16 (2004), pp. 2629.

[13] R. Aziz, A. Janzen, and M. Moldover, Ab Initio Calculations for Helium: A Standard for Transport Property Measurements, Physical Review Letters 74 (1995), pp. 1586–1589.

[14] H. Trinkaus and B. Singh, Helium accumulation in metals during irradiation–where do we stand? Journal of Nuclear Materials 323 (2003), pp. 229–242.